MODELS OF OBSERVATIONAL SIGNATURES OF BLACK HOLES

A Thesis Submitted for the Degree of Doctor of Philosophy (Science) of Bengal Engineering and Science University, Shibpur

Submitted by

Prashanth Mohan

Department of Chemistry
Bengal Engineering and Science University
Shibpur, Howrah-711 103

September 2013

BENGAL ENGINEERING AND SCIENCE UNIVERSITY, SHIBPUR
Department of Chemistry, Howrah - 711103

This is to certify that the thesis entitled, **"Models of Observational Signatures of Black Holes"** *submitted by* **Mr. Prashanth Mohan** *to* **Bengal Engineering and Science University, Shibpur, India** *for the award of the degree of Doctor of Philosophy of Science is absolutely based upon his own work under the joint supervision of* **Dr. Arun Mangalam** *and* **Dr. Sudip Kumar Chattopadhyay**, *and that neither this thesis nor any part of it has been submitted for any degree/diploma or any other academic award anywhere before.*
We hereby forward the thesis for fulfilling the requirements for the award of the degree Doctor of Philosophy in accordance with the regulations of the University.

Dr. Arun Mangalam
Indian Institute of Astrophysics,
Sarjapur Road,
2nd Block, Koramangala,
Bangalore - 560034, India.

Dr. Sudip Kumar Chattopadhyay
Department of Chemistry,
Bengal Engineering & Science University,
Shibpur, Howrah - 711103, India.

Acknowlegements

I thank my guide from Indian Institute of Astrophysics (IIA), Dr. Arun Mangalam for helping me with the theoretical physics and statistical analysis work in this thesis.

I thank my guide from Bengal Engineering and Science University, Dr. Sudip Kumar Chattopadhyay, Dr. Alok C. Gupta and Prof. P. J. Wiita for helping me with the various aspects of the thesis. I also thank Dr. Rajat Chaudhuri from IIA for helping me in the PhD registration process and for offering helpful suggestions at each stage.

I thank IIA for providing the hostel, library and computing facilities.

I thank my parents, my brother and my extended family for being a constant source of encouragement in my academic pursuits, supportive of the most important decisions I have made.

I thank all my friends, both from IIA as well as from outside for their constant support and encouragement in bringing out my best.

Publications

In Refereed Journals

1. *Re-Analysis of QPO in 3C 273 Light Curve.*
   P. Mohan, A. Mangalam, H. Chand and A. C. Gupta
   Journal of Astrophysics and Astronomy, 32, 117M, 2011.

2. *Orbital signatures from observed light curves of blazars.*[*]
   A. Mangalam and **P. Mohan**.
   Journal of Astrophysics and Astronomy, 2013 (Accepted for publication).

3. *Parametric models of the periodogram.*[*]
   P. Mohan, A. Mangalam and S. Chattopadhyay,
   Journal of Astrophysics and Astronomy, 2013 (Accepted for publication).

4. *Multiwavelength intraday variability of the BL Lacertae S5 0716+714.*[†]
   A. C. Gupta, T. P. Krichbaum, P. J. Wiita, B. Rani, K. V Sokolovsky, **P. Mohan**, A. Mangalam et al.
   Monthly Notices of the Royal Astronomical Society, 425, 1357G, 2012.

[*]: Journal versions of these papers are not available as the final proofs are not ready.
[†]: Only the part related to the time series analysis of the optical light curve in this published paper is included in Chapter 4

Under Preparation

5. *Quasi-periodic behaviour in AGN light curves.*
   P. Mohan, A. Mangalam, A. C. Gupta and P. J. Wiita (2013). *Presented in part in Chapters 3 and 4.*

6. *Break frequency and constraints on AGN black hole mass and spin.*
   P. Mohan and A. Mangalam (2013). *Presented in part in Chapters 3 and 5.*

7. *Accretion disk variability models for AGN.*
   P. Mohan and A. Mangalam (2013). *Presented in part in Chapter 6.*

8. *Jet variability models for AGN.*
   P. Mohan and A. Mangalam (2013). *Presented in part in Chapter 7.*

Contents

List of Figures

List of Tables

Chapter 1

Introduction to AGN

Active galactic nuclei (AGN) are the compact central regions of certain galaxies whose luminosity ranges between $\sim 10^{42}$ - 10^{48} erg/s is much greater than that of their host galaxies. The emission from this central region spans a wide range of wavelengths from the infra-red to γ-rays unlike regular galaxies where the emission typically is from infra-red (dust), optical (stars) and UV (nebulae, stars). A canonical model of an AGN consists of the following constituents: the central super-massive black hole, whose mass can range from between 10^6 $M_\odot$ (e.g. for Seyfert galaxies) to 10^9 $M_\odot$ (e.g. for blazars); surrounding this is the accretion disk which is the main source of optical, UV and soft X-ray emission; an obscuring torus shaped region spanning a size > 0.1 pc consisting of gas and dust and is much further away from the black hole and is hence more cooler; a region consisting of broad line emission from gas clouds which are gravitationally bound by the central black hole spanning a typical size of $\sim$ 10 light days with a number density of 10^8 to 10^{11} particles/cm^3, known as the broad line region (BLR) and another region consisting of orbiting gas clouds with narrow emission lines, known as the narrow line region (NLR) which spans a size of 1 to 1000 pc from the central region with a number density of 10^2 to 10^6 particles/cm^3. These components are supplemented by models of radio loud AGN where powerful jets consisting of accelerated particles aligned with the axis of rotation of the black hole are observed. Various observational properties from AGN are believed to arise due to the observer line of sight passing through any of the above mentioned components. A simple model of an AGN with the above components is presented in Fig. 1.1.

AGN possess the following properties:

- Broadband spectrum: the distribution of spectral flux with frequency, the spectral energy distribution (SED) of an AGN indicates strong and continued non-thermal emission in a wide range of wavelengths from radio and infra-red to X-rays and γ-rays e.g. [1]. The spectrum is typically characterized by the energy flux (erg/cm^2/s in C.G.S. units) per unit frequency (Hz), F_ν expressed as a function of the frequency ν (Hz). The spectrum of the AGN is broad compared to stars whose spectrum is typically black body dominated and spans a decade in frequency in the optical wavelengths. A schematic of typical SEDs for different types of AGN is shown in Fig. 1.2.

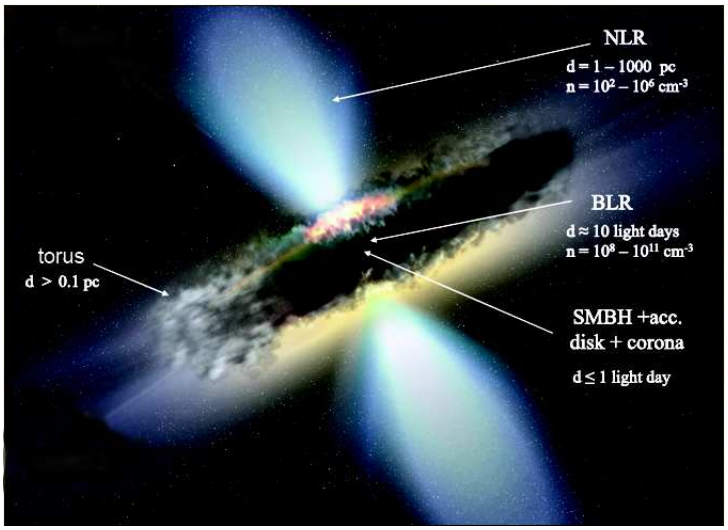

Figure 1.1: Simple representation of an AGN model showing the main features: supermassive black hole, accretion disk, BLR and NLR regions and the obscuring torus. Image courtesy: Mike Crenshaw.

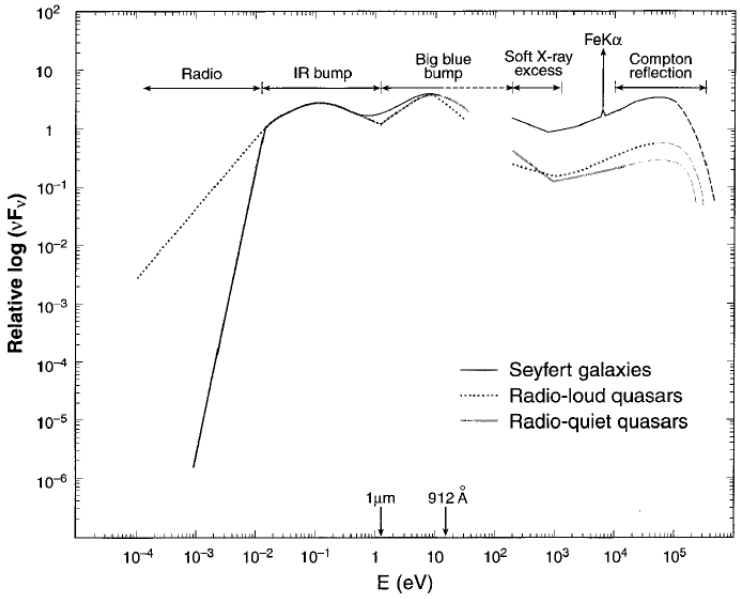

Figure 1.2: Typical SED of an AGN showing emission from the radio to γ-rays with the various contributing components in each of the wavelength bands. Image courtesy: [2].

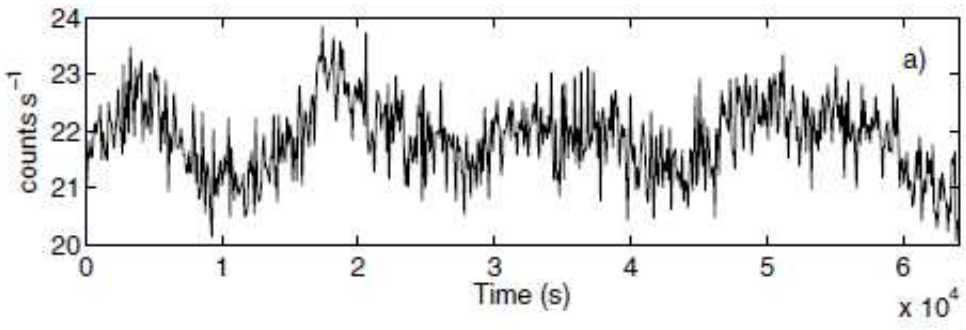

Figure 1.3: X-ray light curve of the blazar PKS 2155-304 (0.3 keV to 10 keV) indicating strong variability with a possible QPO. Image courtesy: [11]

- Rapid variability: the light curve which is the measured band or total integrated flux as a function of receiving time indicates rapid short timescale variability with small to large amplitude fluctuations which are generally aperiodic e.g. [3]. Variability occurs over a wide range of timescales: $\sim$ 100 s to a few 100 s in the γ-rays e.g. [4] where a 600 s variability is inferred from the TeV emission based power spectrum and well resolved bursts are observed at regular intervals of $\sim$ 200 s; $\sim$ 1000 s to a few hours in the optical/UV and X-rays e.g. [5, 6], (see analysis of light curves of blazars in Chapter 4 or that of the Seyfert galaxies in Chapter 5) where typical aperiodic variations are present with moderate to strong variability as characterized by the variability amplitude (for optical) or the excess fractional variability amplitude (for X-rays); less than a day to a few days in the optical e.g. [7] and radio e.g. [8] and months to years in the optical and radio e.g. [9, 10] depending on the type of AGN thus allowing us to ascribe these timescales to either disk or jet based physical processes. A figure showing typical short timescale variability ($\sim$ few hours) is shown in Fig. 1.3.

- Size of emitting region: emission from AGN dominates that from the background host galaxy if observed at lower redshifts. Upper limits to the size of source of the broadband spectrum and rapid variable emission can be placed using the light crossing time argument, $\Delta r = c\Delta t$. This typically yields a broad line region (BLR) size of around a few to tens of light days e.g. [12]. In addition, the angular size of the AGN is very small compared to the host galaxy, again owing to the emission being dominated by it. Effects due to the cosmological redshift and the wavelength of observation play an important role in enhancing this contrast. These must be taken into consideration after a careful study of the luminosity of the AGN as a function of redshift and the properties of the host galaxy. The flux (F)- luminosity (L) relation for the flux from an AGN at an effective distance d_{eff} and redshift z is given by

$$F = \frac{L}{4\pi d_{eff}^2} \frac{1}{(1+z)^2}. \tag{1.1}$$

  The factor $(1+z)^2$ arises due to the frequency shift of a single light ray coupled with the time delay between two pulses getting redshifted in the observer frame. The effective distance is

given by

$$d_{eff} = \frac{1}{H_0 \Omega_c^{1/2}} \begin{Bmatrix} \sin\chi \\ \chi \\ \sinh\chi \end{Bmatrix} \tag{1.2}$$

depending on whether the universe is closed, flat or open. For a cosmological scale factor $\tilde{a}$,

$$\chi(\Omega_v, \Omega_r, \Omega_m) = (\Omega_c)^{1/2} \int_{1/(1+z)}^{1} \frac{d\tilde{a}}{\tilde{a}[\Omega_c - 2U_{eff}(\tilde{a})]^{1/2}} \tag{1.3}$$

where Ω_v,Ω_r, Ω_m are the vacuum, radiation and matter energy densities. $\tilde{a} = a(t)/a(t_0)$ is the scale factor re-scaled in terms of the initial value $a(t_0)$ and the effective potential $U_{eff} = -(1/2)\ (\Omega_v \tilde{a}^2 + \Omega_m/\tilde{a} + \Omega_r/\tilde{a}^2)$ with Ω_c satisfying the relation $\Omega_v + \Omega_m + \Omega_r + \Omega_c = 1$. Once the above integral is carried out for measured energy densities and H_0, $d_{eff}(z)$ can be determined. For a source with a physical size r, the angular size subtended measured by an observer is $\theta = r/d$. Using the above relation and

$$L = 4\pi r^2 \sigma T_{Eff}^4, \tag{1.4}$$

a rough expression for the angular size [13] is given by

$$\theta = 87(1+z)^2 \left(\frac{F}{10^{-11}\ \mathrm{erg\ cm^{-2}\ s^{-1}}} \right)^{1/2} (T_{\mathrm{Eff}}/10^3\ \mathrm{K})^{-2} \tag{1.5}$$

where F roughly corresponds to the bolometric flux from the AGN and T_{eff} is the effective temperature of the inner region, typically $\sim 10^3$ K to 10^5 K. For a known or measured T_{eff} and z, the angular size of the AGN scales as $F^{1/2}$ such that apparently bright AGN also subtend a larger angular size.

- Bi-directional jets in radio to X-ray wavelengths: highly relativistic components which are confined within narrow opening angles (bulk Lorentz factor Γ between $\sim$ 3 - 30 and opening angles 0.5° - 10° e.g. [14]) over large distances from the central region ($\sim$ a few kpc). This is illustrated in a false colour image in Fig. 1.4.

- High luminosity: a balance between the outward bound radiation pressure built up through Thomson scattering on free electrons with the gravitational collapse yields an upper luminosity limit, the Eddington luminosity, $L_{Edd} \sim 1.3 \times 10^{46} M_8$ erg/s where $M_8 = M/(10^8 M_\odot)$. The luminosities of typical AGN range between $10^{42} - 10^{48}$ erg/s which is in the close vicinity of the Eddington luminosity indicating a powerful, active source of emission within the compact emitting region. This luminosity is $\sim$ 0.01 to 10^4 times the luminosity of $\sim 10^{44}$ erg/s observed for a typical field galaxy distribution indicating that the energy output from this small nuclear region is quite large.

  Mechanisms which can generate and sustain such a large luminosity output in a wide variety of wavelengths over long durations of time are very few. Using a similar argument as that in

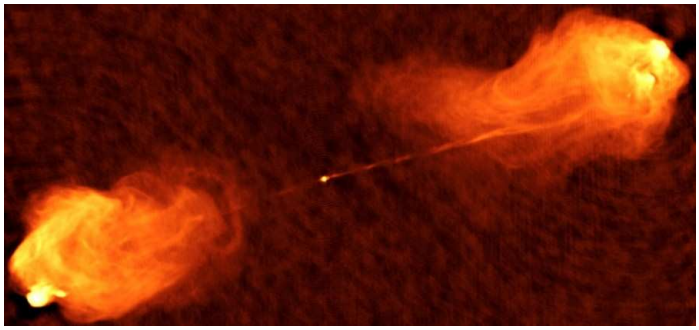

Figure 1.4: Multiconfiguration VLA observations of Cygnus A at 1.4 GHz and 5 GHz have been used to produce detailed maps of exceptional dynamic range. A radio jet extends from the core into the northwest lobe. The pressure of the cluster gas in which Cyg A is embedded appears to be insufficient to confine either the jet or the filamentary structures within them. From the necessarily high mechanical luminosity of the jet and the high energy densities of the hot spots, it is concluded that the jet is probably relativistic. Image courtesy: NRAO/AUI and studied by [15].

[16], the available accretion based energy due to a mass m is $\Delta E_{acc} \sim GMm/R \sim 0.5mc^2$ for a Schwarzschild black hole with a mass M and radius $R = 2GM/c^2$ and the nuclear burning process based energy $\Delta E_{nuc} \sim 0.007mc^2$ indicating that the accretion energy yield per unit mass is $\sim$ 2 orders of magnitude greater.

1.1 Classification of AGN

AGN are known to show a varying set of observationally distinct and unique characteristics. This has led to many proposals for classification schemes.

1.1.1 Optical spectra and line widths

The presence of lines with a broad profile can be used to demarcate various objects into classes. Early classification schemes were based on Seyfert galaxies where the host galaxy was visible and a certain population, the type 2 objects indicated narrow emission lines while another population, the type 1 objects indicated multiple broad as well as narrow emision lines. Currently classification schemes for the Seyfert galaxies have also used sub-classes [17] such as types 1, 1.2, 1.5, 1.8, 1.9 and 2 based on more well resolved spectroscopic observations which reveal more detailed features measured in the narrow Balmer lines. Seyfert galaxies are typically have an absolute B magnitude $M_B >$ -21.5, a bolometric luminosity between 10^{43} erg/s and 10^{45} erg/s. The broad permitted emission lines possess a full width at half maximum (FWHM) ranging between 800 km/s and 8000 km/s while the narrow emission lines which includes both permitted as well as forbidden lines possess a FWHM ranging between 200 km/s and 500 km/s. In addition, the Seyfert type 1 galaxies indicate a strong non-stellar continuum emission in their spectrum while the Seyfert type 2 galaxies indicate a weak stellar continuum. Another set of objects, the narrow line Seyfert 1 galaxies indicate a typical FWHM ranging between 800 km/s and 2000 km/s with strong Fe II

ionized emission. There is a strong excess emission contributing at and below the 1 keV to 2 keV soft X-rays accompanied by a rapid X-ray variability.

1.1.2 Radio power (radio loud or radio quiet)

Some of the first AGN were identified through various surveys, beginning with those conducted in the radio wavelengths due to the availability of large sky coverage, good instrumental sensitivity and a strong emission by AGN in radio. The third Cambridge (3C) catalogue consisted of $\sim$ 500 sources with a flux $>$ 9 Jy at 178 MHz and the third Cambridge revised (3CR) catalogue [18] consisted of 328 sources with declination $\delta >$ -5° and flux $>$ 9 Jy. These and the fourth Cambridge (4C) catalogue [19, 20] which covered a large part of the northern sky with source flux $>$ 2 Jy were compiled during the 1950s and 1960s using observations on a 178 MHz radio telescope at Cambridge University. This was followed by the Parkes survey (PKS) and others.

Radio power, which was measured in many of these surveys played an important role in the identification of two distinct populations of AGN e.g. [21]. The radio loudness parameter is defined as

$$R_L = \mathrm{Log}\frac{f_{5\ \mathrm{GHz}}}{f_{\mathrm{B}}} \tag{1.6}$$

where $f_{5\ \mathrm{GHz}}$ is the radio flux measured at 5 GHz and f_{B} is the optical B band flux measured at 4400 Å. AGN with a measured $R_L \geq 1$ are classified as radio loud and those with $R_L < 1$ are classified as radio quiet.

Each of these are further sub-divided into types 1 and 2. Type 1 radio loud AGN which show a low luminosity and indicate the presence of broad emission lines are known as broad line radio galaxies (BLRGs) while those with high luminosity are known as radio loud quasars. Steep spectrum radio quasars (SSRQs) and the flat spectrum radio quasars (FSRQs) are types of radio loud quasars, bifurcated based on the slope of their radio spectrum which if represented by a power law can be written as $F_\nu \propto \nu^{-\alpha}$. For the radio spectral index α being ≥ 0.5, the AGN is known as a SSRQ. For flatter α, typically < 0.5, the AGN is known as a FSRQ. Type 2 radio loud AGN are those where optical emission lines are narrow and are known as the narrow line radio galaxies (NLRGs) which are further classified into the Fanaroff-Riley type 1 and type 2 galaxies [22] based on their morphological properties and the environment surrounding the jet. Blazars are another set of radio loud AGN where the emission across all wavelengths of study are strongly variable on time-scales $\sim$ 1 day e.g. [23, 24, 25]. They indicate a strong polarization of 1 % to 4 % and are moderate to strongly radio loud. They can be further sub-divided into BL Lacertae objects where emission lines are generally absent or very weak with typical equivalent widths of $<$ 5 Å[26, 27], optically violently variable quasars which indicate a high polarization and have broad emission lines and the FSRQs. The BL Lacertae objects can be further sub-divided into the high-frequency BL Lacs (HBLs) where the synchrotron emission peaks in the X-rays and the low-frequency BL Lacs (LBLs) where the synchrotron emission peaks in radio wavelengths. Radio quiet AGN include the Seyfert galaxies, sub-divided into the Seyfert types 1 and 2 based on the earlier mentioned observability of narrow as well as broad emission lines from their optical spectra.

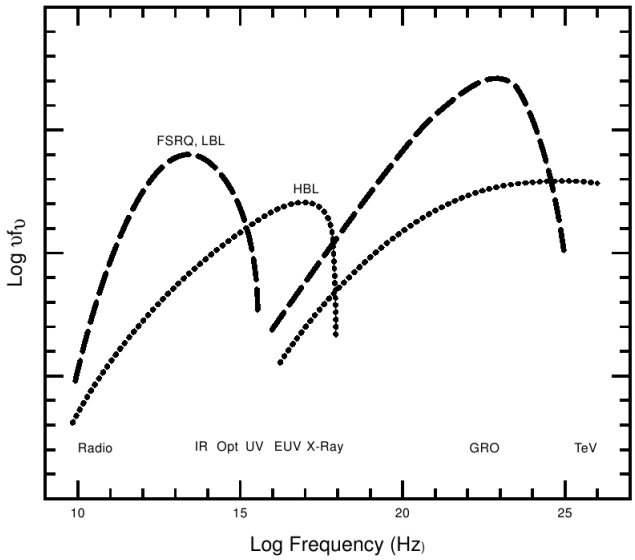

Figure 1.5: Spectral energy distributions for three kinds of blazars. The synchrotron power of strong emission line blazars (FSRQ) and low-frequency peaked blazars (LBL) peaks at submillimeter to infrared wavelengths, while that of high-frequency peaked blazars (all known HBL are BL Lac objects) peak at UV to X-ray wavelengths. The Compton powers peak at GeV energies for FSRQ and LBL and at much higher (TeV) energies for HBL. In general, FSRQ and LBL (dashed lines) are more luminous than HBL (dotted lines). Figure courtesy: [28]

Quasars are AGN with typical high luminosities ranging between 10^{45} erg/s and 10^{47} erg/s which have been observed to redshifts ~ 7, obtained from their strongly redshifted emission lines. They typically have strong blue continuum emission constituting their spectra with broad emission lines and strong variability in optical and X-ray wavelengths. In addition, their spectra resemble those from Seyfert 1 galaxies though with an absence or weakly detected stellar absorption features with weak, narrow lines. Interestingly, only 5 to 10 % of the quasars studied till date indicate a clearly marked radio loudness e.g. [29], which is ≥ 10, much more powerful than other radio loud objects with suggestions of disruption of jets by gas from tidal disruption of stellar material [30], the black hole spin affecting the magnetic field structure in the jet launching and collimation region [31] and others.

1.1.3 Morphology of the AGN, its jet or the host galaxy

The NLRGs, as mentioned above can be sub-divided into the Fanaroff-Riley type 1 (FR I) and type 2 (FR II) galaxies. FRI galaxies are those when studied in the radio wavelengths indicate a strong emission from the nucleus with diffuse lobes indicating a decrease in the brightness towards their edges, suggesting that they are present in a host galaxy enviroment rich in gas and dust. FR II galaxies meanwhile indicate powerful emission near the edges of a bi-directional outflowing lobe structure. They are generally observed in environments containing minimal contamination by gas and dust surrounding the host galaxy.

1.2 Unification and a physical AGN model

Proposals have been made in literature e.g. [32, 33] that the various classes of AGN can be explained by ascribing their differing properties to the viewing angle of the observer towards the AGN. According to this paradigm, the AGN can be described by the canonical model presented earlier.

Early unification models arose from the study of Seyfert galaxies and their subsequent classification into the Seyfert 1 and 2 observation. As mentioned earlier, Seyfert type 2 galaxies emit narrow emission lines while the Seyfert type 1 galaxies emit both narrow as well as broad emission lines. Polarization studies of Seyfert type 2 galaxies in the optical reveal an obscured broad line region, which is not observed in the regular optical spectrum e.g. [34, 35]. Such studies suggest that obscuration by a dusty torus indeed prevent us from observing the inner region, possible due to observer line of sight effects and thus adding evidence to unification schemes. The same suggestion is also carried over to the description of the variety of observational results for radio loud AGN where there is an astrophysical jet in addition. In these too, it is believed that the observer line of sight decides the object being viewed. The NLRGs, similar in their properties to Seyfert type 2 galaxies, except for the inability to resolve a host galaxy in them has an observer line of sight intersection through the dusty torus, thus obscuring the inner broad line region. The BLRGs, similar to the Seyfert type 1 galaxies though, with a poorly resolved host galaxy have an observer line of sight which intersects through both the broad as well as a portion of the narrow line clouds. They typically have Balmer profiles which are broader with weaker Fe II emission lines and a higher Hα/Hβ line ratio. The radio loud quasars which includes the SSRQs and FSRQs are believed to have an observer line of sight intersecting through the narrow line clouds at a smaller angle to the line of sight perpendicular to the accretion disk axis. Finally, the blazars, where emission is highly variable in multiple wavelengths is believed to be observed due to the observer looking almost head on into the heart of the AGN through the jet. The inclination angle towards the observer line of sight which is the polar or co-latitudinal angle, defining the opening angle of the jet is highly constrained, typically $\leq 10^{\circ}$ for these objects. Thus, if the material along the jets is moving at special relativistic velocities, these will be beamed towards the observer. Thus, even small disturbances in the jet get amplified due to beaming and the jet based emission dominates the observed spectrum of these objects. The unification schemes for the radio loud and radio quiet galaxies are presented as a schematic in Fig. 1.6.

A physical model of AGN emerges from all the previous discussion involving their classification and the proposal of unification modes. The canonical model of an AGN can be supplemented by finer detailed features and possible explanations for the origin of emission in the various wavelengths constituting the SED as well as their strong variability in both spectra as well as in their light curves.

A schematic showing a physical model of a quasar is shown in Fig. 1.7. When the nucleus of the AGN is not spatially resolved as is the case for typical radio quiet AGN, the components giving rise to emission in various wavelengths are inferred through multiple schemes. The optical, UV and the soft X-ray continuum emission is believed to arise from the accretion disk. A striking

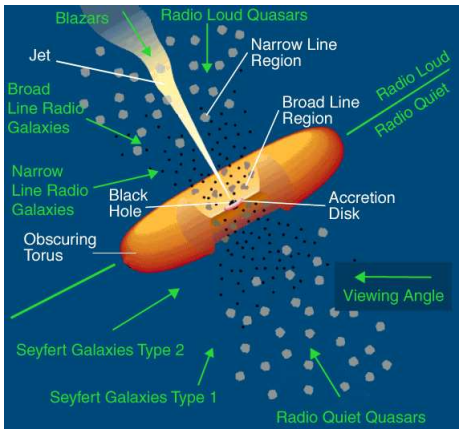

Figure 1.6: Schematic showing the observation angle related dependence of the type of AGN. Radio loud and radio quiet AGN along with the various components of a canonical AGN model are presented. Image courtesy: Adapted from [33].

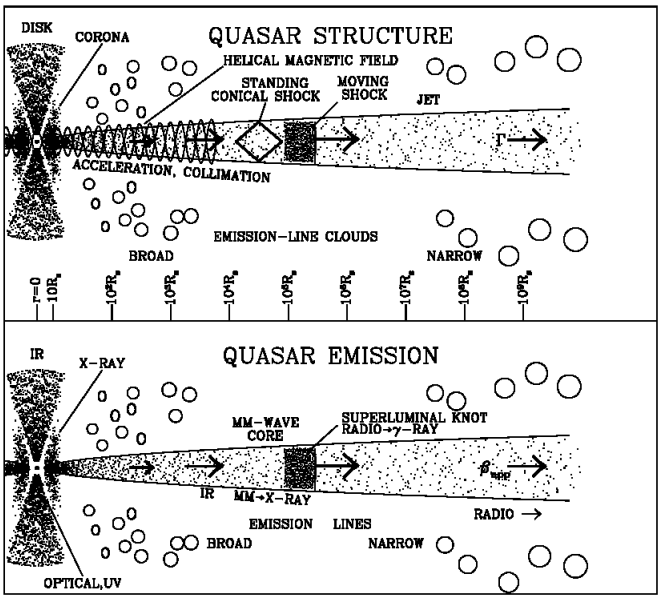

Figure 1.7: Physical model of a quasar showing multiple components beginning with the accretion disk, the corona surrounding it, the inner and expanding jet to large scales. Image courtesy: [36].

feature in the SED known as the big blue bump is often observed in Seyfert galaxies, especially the type 1s and is believed to offer evidence for the existence of the accretion disk e.g. [37]. The hard X-ray continuum is believed to arise from a corona sandwiching the disk consisting of relativistic thermal population of electrons. The infra-red emission can be ascribed to the re-processed thermal emission from the dusty torus and the NLR dust. In the case where the AGN is better resolved, especially in radio loud AGN where the morphology including the presence of a jet is discernable, the components giving rise to emission in a particular wavelength can be identified better. Radio emission is clearly observed from the core, jets and lobes of features of the AGN.

1.3 Determination of black hole mass in AGN

There is growing evidence from observational studies based on multiple physical schemes to support the hypothesis that these complex phenomena can be explained by a canonical model of an actively accreting central supermassive black hole (SMBH). These include direct astrometric measurements, gas dynamics based tests, stellar dynamical tests, studies on water maser emission, reverberation mapping and searches for interesting features such as quasi-periodic signals.

Recent advancements in observational techniques have allowed us to infer the SMBH in our galaxy. Direct astrometric imaging measurements tracing the highly elliptical orbit of a star close to the compact core in Sagittarius A* indicate a Keplerian orbital period of 15.2 years and a pericentric distance of $\sim$ 17 light hours with the best fit to the observations requiring a mass of $\sim 10^6$ $M_\odot$ [38]. As similar studies are not currently possible to conduct in other galaxies, alternate schemes have been developed.

1.3.1 Water maser emission

H2O maser emission at $\lambda = 1.35$ cm ($\sim$ 22 GHz) can be used to trace single gas clouds orbiting massive black holes in galactic nuclei. Radio interferometers such as the VLBA which can reach a high spatial and velocity resolution compared to optical and near-IR instruments can be used in the detection and the tracking of such features from an extended disk. As the motion of the maser sources is gravitationally bound to the central black hole, the mass of the SMBH can be precisely measured. For a disk inclined at an angle i towards the observer line of sight and a radial distance s to the center of the galaxy, the velocity of the source on the disk can be written as

$$v_{\rm obs} = \left(\frac{G\ M_{BH}}{s}\right)^{1/2} \sin i. \tag{1.7}$$

The velocity towards and away from the observer line of sight will be oppositely directed. For a source with velocity directed towards and then away from the observer line, a schematic plot of v versus $s_{\rm obs}$ is shown in Fig. 1.8.

A strong signature was observed in NGC 4258 where a SMBH mass of 3.6×10^7 $M_\odot$ was inferred in [39]. A black hole mass of $(8.0 \pm 0.3) \times 10^6$ $M_\odot$ is obtained for NGC 1068 where the disk is modelled as self gravitating [40]. A VLBI study of emission from seven galaxies is used to obtain a black hole mass in the range of 0.75×10^7 to 6.5×10^7 $M_\odot$ [41]. A compilation of known sources and the inferred SMBH masses is presented in [42].

1.3.2 Gas and stellar dynamics based measurements

The dynamical motion of gas and stars in the nuclear region of a galaxy are studied in a statistical manner to derive their average velocity v from the velocity distribution and the dispersion σ in the velocity. The stellar continuum emission is used in the determination of v and σ. Though, the parameters obtained from stellar kinematics are not as accurate owing to effects on the emission

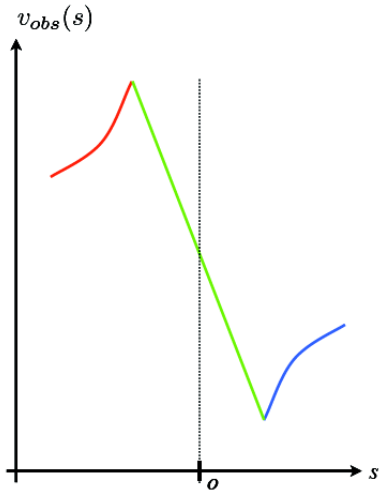

Figure 1.8: The rotation curve showing the velocity of a water maser emission source as a function of the radial distance from the central black hole. The disk, likely to be the outer portion or an extension of an accretion disk is gravitationally bound to the central black hole. Image courtesy: Alessandro Marconi.

lines due to contributions from magnetic fields in the galaxy and contamination by gas and dust. The surface brightness of the galaxy is then determined, modelled using a de Vacouler's profile or a general Sersic profiles, expressing it as a function of the radial distance from the center of the galaxy. This can then be used in combination with the to infer the contribution to the gravitational potential of the galaxy from the stellar components.

The study of the dynamics of the orbiting gas clouds, assumed to be in close proximity to the central black hole are used to determine their v and σ from observed emission lines. Just as in the case of the emitting source on Keplerian orbits in the case of the water maser emission, the emission is believed to originate from gas in Keplerian orbits around the central potential. This can then use similar a similar relation between v and the radial distance r from the central black hole to determine the SMBH mass. As an estimate of σ for the gas is available in many cases and the relationship between σ and r is known ($\sigma \sim 0$ at the edges and slowly increases to a maximum of 2 v at exactly the observer line of sight), there is an additional advantage in the use of gas motion as a tracer as the profile of v can also be confirmed with that of σ. Absorption lines from orbiting gas are studied with a measurement of the characteristics of their profile. Spectroscopic and narrowband observations of the region near the core of the galaxy are used to infer the kinematics such as radial velocity and the mass to light ratio, which are then compared with models of the gas kinematics to infer the presence and mass of the central SMBH. Hubble Space Telescope (HST) studies on M 87, a giant elliptical galaxy indicate a SMBH mass of $\sim 2.4 \pm 0.7 \times 10^9$ $M_\odot$ from narrowband Hα imaging [43] and O [III] 4959 Å line [44] and another consistent estimate of $3.2 \pm 0.9 \times 10^9$ $M_\odot$ from the O [II] 3727 Å line [45]. A similar HST narrowband Hα imaging study on another giant elliptical galaxy, NGC 6251 indicates a SMBH mass of $4 - 8 \times 10^8$ $M_\odot$ [46] and HST based spectroscopic study in the S [III] 9533 Å line of the nearby radio galaxy Centaurus A indicates a

SMBH mass of $\sim 10^8$ $M_\odot$ [47].

1.4 The M-σ relation

Dynamical measurements involve the study of the distribution and evolution of stellar parameters near the central region of various types of galaxies [48]. The SMBH mass is correlated with the measured velocity dispersion of the bulge as $M_{BH} \propto \sigma^{\alpha}$ with estimates of α in the range of ~ 4 - 5 [49, 50]. Physical motivations for the existence of this observed relationship have been probed in terms of the relationship between the SMBH and their host galaxies [51] by simulating galaxy mergers through the inclusion of contributing effects such as gas dissipation, cooling, star formation, and the accretion and feedback by the SMBH. It has been suggested here that the $M_{BH} - \sigma$ relation may be part of a black hole fundamental plane based relation where $M_{BH} \propto \sigma^{3.0\pm0.3} R_e^{0.43\pm0.19}$ and $M_{BH} \propto M_{Stellar}^{0.54\pm0.17} \sigma^{2.2\pm0.5}$. If we use a suitable R_e such that $M_{BH} \propto \sigma^4$, then we recover the Magorrian relation $M_{BH} \propto M_{Stellar}$.

1.5 Reverberation mapping and virial estimation

Reverberation mapping of the broad line region (BLR) clouds e.g. [52] is currently a much favoured technique owing to it being almost independent of the angular resolution, making it effectively useful over a wide span of distances. For a virialized gas cloud,

$$M = frv^2/G \tag{1.8}$$

where f is a covering fraction which must be used to account for the shape of the BLR clouds and other geometrical effects, r is the size of the emitting region and v^2 is the average velocity of the gas. The expression for the virial mass thus contains three parameters f, r and v^2 which must be constrained from observational studies.

Continuum emission from the inner accretion disk could experience fluctations caused by the detailed flow in this region. These fluctuations will be imprinted on the outgoing radiation. The BLR clouds which lie close to the inner region will then re-processes the incoming variable radiation over a very small timescale before it reaches the observer. BLR clouds lying on iso-delay surfaces will indicate the same time delay. Due to the geometrical alignment of these clouds, there will be a time delay between the variations in the line flux as compared to that in the continuum flux. For an iso-delay surface, $\Delta t = (r/c)(1 + \cos\theta)$ where r is the distance from the central BH. The $\Delta\tau$ between continuum and line variations are used to place upper limits on r as $r = c\Delta\tau$. A cross correlation of the continuum light curve $L_c(t)$ with an emission line light curve $L_e(t)$ gives $\Delta\tau$ for that pair. $\Delta\tau$ is obtained for different emission lines. Thus, a statistical determination of the time delay for each pair of line variability with respect to the continuum variability maps out a structure of the broad line region at each radius.

In the absence of reverberation based time delay measurements, r can be determined through

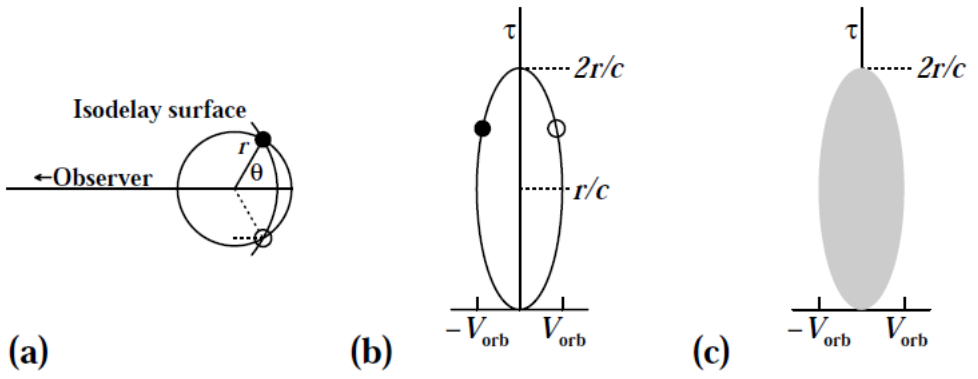

Figure 1.9: (a) In this illustrative model, the BLR clouds are distributed along a counter-clockwise circular orbit centered on the central continuum source at inclination $i = 90°$. Emission-line clouds respond to a continuum fluctuation with delay $\Delta\tau$, which compared with the photons from the central source that travel directly to the observer, is the additional path length this signal must travel to the distant observer to the left, as shown by the dotted line. At the $\Delta\tau$ shown, two clouds are responding, the upper one approaching the observer and the lower one receding. (b) The points on the circular orbit in (a) project to an ellipse in the velocity - time-delay plane. The locations of the two clouds in (a) are shown. (c) For circular orbits at inclinations less than 90°, the axes of both ellipses are decreased by a factor $\sin i$ and the center remains at $v = 0$, $\Delta\tau = r/c$. Thus, for a random distribution of inclinations, the response of the BLR occurs over the full range of radial velocities and time delays limited by the $i = 90°$ case. Image courtesy: [53].

a virial relationship between the broad line region radius for the Hβ or C[IV] emission line and the bolometric luminosity. $r \propto L^{0.6\pm0.1}$. The line width from multiple emission lines are used to measure v^2 by considering the full width at half maximum. Once these are known, the only unknown quantity is the covering fraction f. An estimation of f is generally carried out by comparing the estimated M/f with the black hole mass obtained from the $M - \sigma$ relation. It is found to be a fairly accurate manner of estimation and the value of f is typically constrained to ~ 0.75 to 1. Thus, M_{BH} can then be determined. This technique can be used to deduce the mass of the SMBH and kinematic properties of the inner BLR region close to the center e.g. [12, 54].

1.6 Quasi-periodic signals

The SMBH mass and spin can also be inferred from arguments based on observational signatures from disk based orbital features, specifically a quasi-periodic oscillation or a break frequency in the power spectrum. If a statistically significant quasi-periodic oscillation (QPO) is detected in the light curve of an AGN, e.g. a QPO centered at 3733 s in the narrow line Seyfert 1 galaxy REJ 1034+396 [55], then, based on the type of AGN (disk or jet dominated emission) and on the wavelength it was detected in (optical/UV or X-ray), it can be argued that the QPO arises due to an orbital feature in the inner disk close to the SMBH. Even if the physical origin is due to disk oscillations or other physical mechanisms, the above argument can be used to place upper limits

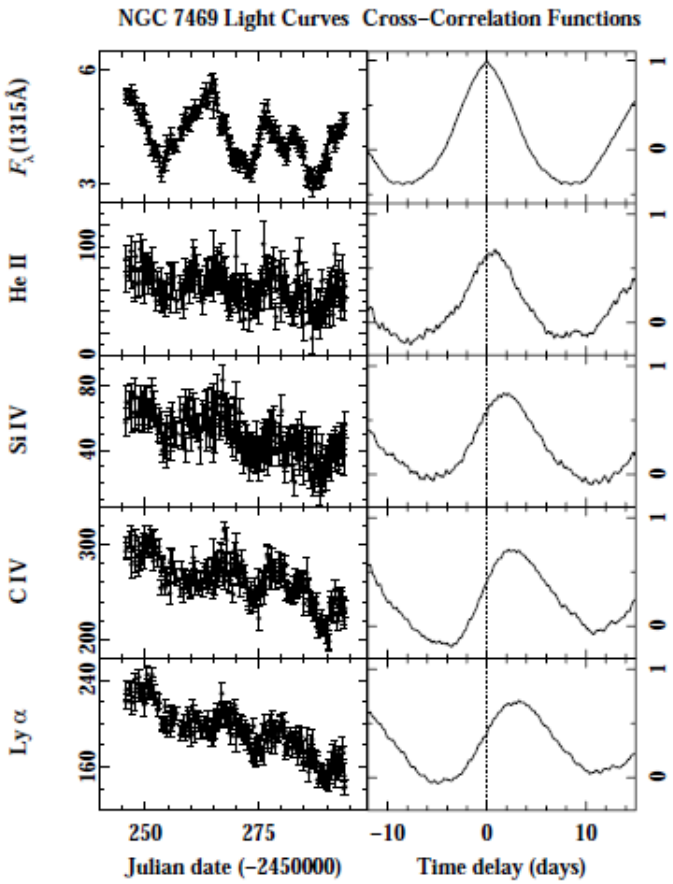

Figure 1.10: The left-hand columns show the light curves of NGC 7469 obtained with IUE during an intensive AGN Watch monitoring campaign during the summer of 1996. The right-hand column shows the result of cross-correlating the light curve immediately to the left with the 1315 Å. A light curve at the top of the left column; the panel at the top of the right column thus shows the 1315 Åcontinuum autocorrelation function. Image courtesy: [53].

on the SMBH mass. If a break is detected in the power spectrum e.g. [56], it is possible that its physical origin is due to matter infall into the SMBH from the innermost stable circular orbit (ISCO) or any characteristic disk based inner radius, which would still be close to the ISCO.

As these physical schemes can be used to infer and set constraints on the SMBH mass and spin and on the region of emission of the observational signatures, it merits further detailed theoretical studies complemented by the analysis of observational data. The location of these phenomena is in the inner accretion disk and developing jet in the close vicinity of the central SMBH.

1.7 Determination of black hole spin in AGN

For many Seyfert type 1 galaxies, the observer line of sight intersects through the inner region which includes the accretion disk as proposed by the unification models. These objects are also

a source of strong emission in the soft to hard X-rays (0.1 keV to a few 100 keV). Once the soft X-ray spectrum below 1 keV is fit, accounting for various sources of absorption such as gas clouds towards the observer line of sight, the remaining portion is a falling power law with a spectral index $\sim$ -0.9 which extends into the hard X-ray region of the spectrum (20 keV to 100 keV) with a high energy bump. This entire region is well fit through a model involving a large distribution of cold gas which takes part in the Compton scattering of X-rays to lower energies. As this material must cover a large region, there is indirect evidence for the presence of a disk which could be constituted by it. Further, in the soft X-rays (0.1 keV to 10 keV), a striking emission line in the spectrum at 6.4 keV is identified as a fluorescence emission line due to the excitation of iron where the K-shell electron is ejected due to an interaction with an incoming high energy photon. This line emission is very broad as indicated by its measured FWHM and its measurement at 6.4 keV implies that the temperature of the gas taking part in the fluorescence is cold and is getting irradiated by high energy X-rays from the inner-most region. Thus, the region containing this colder population of gas is likely to exist on a disk very close to the black hole. If the black hole has a sufficient intrinsic spin, it can influence the rotation rate of the surrounding disk through frame dragging and other effects. Further, the shape of the 6.4 keV FeKα line profile will then be influenced by strong gravitational effects such as black hole spin, Doppler shifts, gravitational red-shift, light bending and others. One can then take into account all these parameters which influence the shape and model it in order to compare them with spectral studies in these energies, possible due to a good coverage from X-ray missions such as the XMM Newton (0.1 keV to 10 keV), Chandra (0.1 keV to 10 keV), Suzaku (0.2 keV to 700 keV) and recent interest due to high resolution spectroscopy possible from NuSTAR (3 keV to 79 keV).

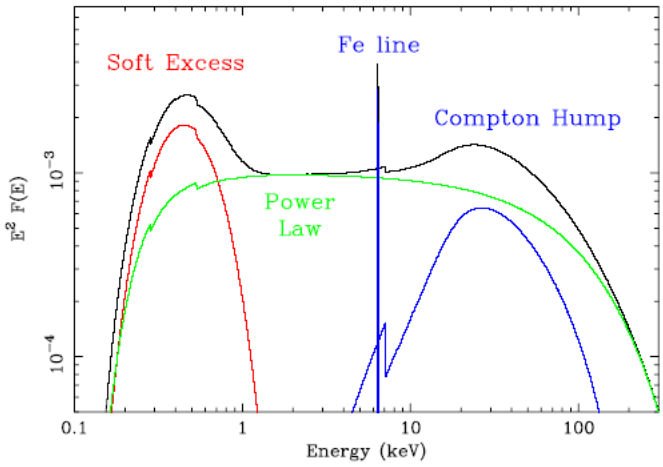

Figure 1.11: The main components of the X-ray spectra of unobscured accreting BH are shown: soft X-ray emission from the accretion disc (red); power law from Comptonization of the soft X-rays in a corona above the disk (green); reflection continuum and narrow Fe line due to reflection of the hard X-ray emission from dense gas (blue). Image courtesy: [57].

The SMBH mass and spin can be inferred from arguments based on orbital signatures from

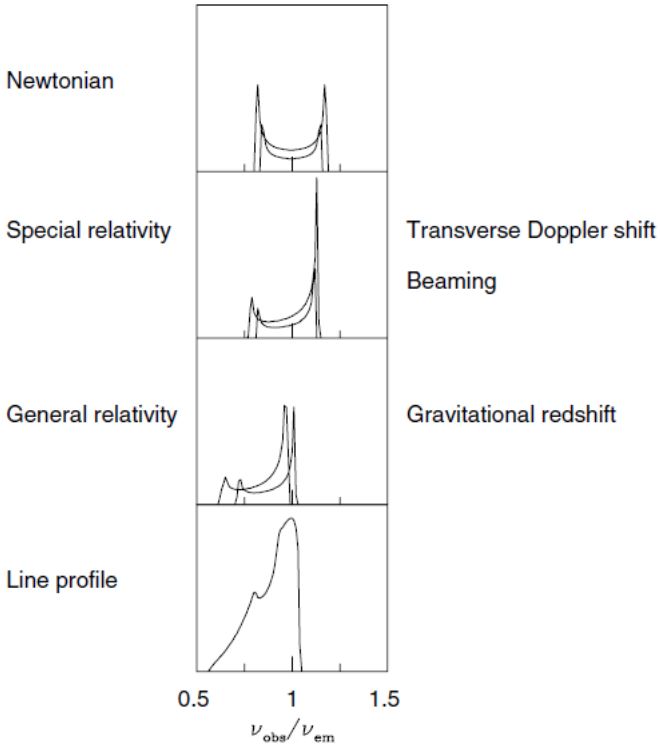

Figure 1.12: The profile of a narrow emission line is modified by the interplay of Doppler/gravitational energy shifts, relativistic beaming, and gravitational light bending occurring in the accretion disc (from Fabian et al. 2000). The upper panel shows the symmetric double-peaked profile from two annuli on a non-relativistic Newtonian disc. In the second panel, the effects of transverse Doppler shifts (making the profiles redder) and of relativistic beaming (enhancing the blue peak with respect to the red) are included. In the third panel, gravitational redshift is turned on, shifting the overall profile to the red side and reducing the blue peak strength. The disc inclination fixes the maximum energy at which the line can still be seen, mainly because of the angular dependence of relativistic beaming and of gravitational light bending effects. All these effects combined give rise to a broad, skewed line profile which is shown in the last panel, after integrating over the contributions from all the different annuli on the accretion disc. Image courtesy: [57].

the accretion disk by means of a QPO or a break frequency in the power spectrum as briefly discussed in the previous section. If the black hole mass is independently measured through any of the previously described techniques such as reverberation mapping, one can then reduce the free parameters in the theoretical description to the region of emission and the black hole spin. If we assume that the region of emission is very close to the inner-most stable circular orbit (ISCO), the description can then be cast only in terms of spin as the ISCO radius is related to the spin. Further, a cut-off break time-scale is expected if the accretion disk has a well defined inner edge. This timescale is imprinted onto the power spectral density shape and is identifiable by a fit to the observed periodogram. Spin of the black hole can then be constrained based on the mass and time-scale based constraints. This method of determination of black hole spin is purely from timing

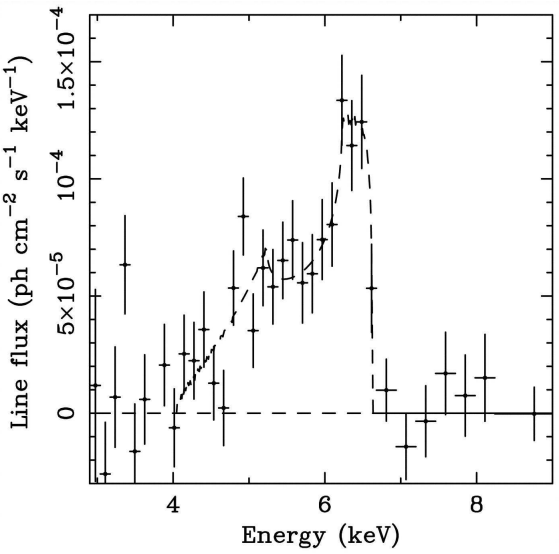

Figure 1.13: The line profile of iron K emission in the ASCA SIS spectrum of the Seyfert 1 galaxy MCG-6-30-15. The emission line is very broad, with full width at zero intensity of $\sim$ 100,000 km/s. The line shape is skewed toward energies lower than the rest energy of the emission line (6.35 keV at the source with $z = 0.008$). The dotted line shows the bestfit line profile from the model of [58], an externally illuminated accretion disk around a Schwarzschild black hole. Image courtesy: [59].

analysis and is further developed in Chapter 5.

1.8 Models of accretion disk and jet based variability

Any detailed theoretical study must involve specific models of variable emission and the development of the spectrum and its evolution at different wavelengths. Commonly used physical models for accretion disks include:

- Standard thin disks [60, 61] which are geometrically thin (i.e. the ratio of the disk height, z to its radial extent r, $z/r \ll 1$) and optically thick, rendering them radiatively efficient thus emitting a modified black body spectrum. The physical quantities representing the disk structure are vertically averaged, only possessing a radial dependence. The dominant flow velocity is the azimuthal component which can tend to relativistic speeds. These disks can be used to model emission and its variability from objects with disk dominated emission such as Seyfert Type 1s and NLS1s where the big blue bump feature is inferred from the SED in the optical/UV portion.

- Thick disks [62] are geometrically thick (i.e. $z/r > 1$) and optically thick. As radiative pressure is dominant in the inner region over the gas pressure, the disk gets "puffed" up and resembles a "Polish Doughnut". These could be used to model emission from objects with high luminosities such as radio loud quasars e.g. [63].

- Slim disks [64] are geometrically thick (i.e. $z/r \sim 1$) and optically thick. These can be used

to represent scenarios when the observed luminosity is significant compared to the Eddington luminosity e.g. $L \sim 0.3 L_{Edd}$. In these conditions, the radial velocity also becomes important and cooling can occur by a combination of radiation and advection of matter into the black hole. They can be applied to quasars [65] as X-ray emission is possible from them and to X-ray binaries [66].

- Advection dominated accretion flow [67] where the flow in the inner region becomes optically thin and a large portion of it is advected into the hole. It results in a quasi-spherical distribution of material around the black hole whose emission luminosity is very low. This mechanism is believed to power the SMBH in quiescent galaxies such as the Milky Way, e.g. [68]; and in FR I galaxies, e.g. [69]. Studies have indicated that the disk in many AGN such as the low-luminosity active galactic nuclei (LLAGN) may be truncated [70]. In these phenomenological models, the optical/UV spectra of these systems indicate that the inner edge of a standard thin disk is at $\sim 50\ M$, truncated at a characteristic radius. Inside this, leading to the central SMBH is an ADAF inferred from X-ray radiation.

The types of disk models and their characteristics and applicability are discussed in [71]. Some general properties of the disk can be illustrated by the use of the thin disk model.

Short timescale variability ranging between a few 1000 s and a few 10000 s in optical and ultraviolet emission is expected in from the accretion disk. Strong X-ray emission spanning from soft X-rays ($\sim$ 0.3 - 10 keV) to hard X-rays ($>$ 10 keV) contributes a power law portion with an exponential cut-off in AGN SEDs e.g. [72]. If virial equilibrium is established in an optically thin population of electrons surrounding the disk, the virial temperature, $kT = GMm_e/R = m_e c^2/r$ where m_e is the electron rest mass, $r = R/(GM/c^2)$ is the dimensionless radial distance in geometrized units. For $r = r_{ISCO} = 6$, $kT \sim 85.4$ keV, the effective accretion energy per electron. Emission and variability in the soft to hard X-rays is then expected from this optically thin, thermally energetic corona where disk based seed photons (UV photons) are inverse-Compton (IC) scattered to higher energies e.g. [73].

Typical variability due to disk based processes and time-scales over which the disk structure can change include the dynamical time-scale, thermal time-scale and the viscous time-scale. Using the α prescription for a geometrically thin disk [60] which represent a Newtonian disk rotating with a Keplerian velocity around the central black hole, for an orbital velocity $v_\phi = (GM/r)^{1/2}$, Mach number $\mathcal{M} = v_\phi/c_s$, kinematic viscosity ν, radial velocity v_r and surface density $\Sigma(r)$, typical timescales for disk based physical processes include:

- Viscous timescale due to the radial evolution of the surface density, $\Sigma(r)$ of a ring of gas through viscous torque action, given by $t_{visc} \sim r/v_r$. It can be interpreted as the timescale over which matter diffuses radially through the disk due to the viscous torque action. Here, $v_r \ll v_\phi$ due to which, this is the longest timescale.

- Dynamical timescale due to orbital processes and inhomogeneities in inner disk and jet such as flares, given by $t_\phi \sim r/v_\phi$. This is the shortest timescale as it is associated with events which occur at high velocities v_ϕ which could be relativistic.

- Hydrostatic balance timescale over which there is a smoothing of deviations from hydrostatic equilibrium in the vertical direction (along the disk height z), given by $t_z \sim z/c_s \sim r/v_\phi = t_\phi$.

- Thermal timescale over which there is a smoothing of deviations from thermal equilibrium, given by $t_{th} = \frac{\text{heat content per unit area}}{\text{dissipation rate per unit area}}$. For a gas in thermal equilibrium, the heat content per unit area $\sim \Sigma(r)c_s^2$ and the dissipation rate per unit area $D(r) = \frac{9}{8}\nu\Sigma(r)\frac{GM}{r^3}$ $\sim t_{visc}/\mathcal{M}^2$.

Thus, $t_\phi \sim t_z \sim \alpha t_{th} \sim \frac{\alpha}{\mathcal{M}^2}t_{visc}$. For typical physical conditions $\alpha \sim 0.01 - 0.001$, $\mathcal{M} = v_\phi/c_s \gg 1 \implies t_\phi < t_{th} \ll t_{visc}$, $t_\phi \sim 0.86\ M_8 r^{3/2}$ hour ~ 12.6 hour for $M_8 = 1$ and taking $r = R/M = r_{ISCO} = 6$. Thus, the smallest timescale, t_ϕ is likely to represent physical processes which lead to short time-scale variability over a few thousands of seconds to a day. It is then important to study orbital signatures which can cause variability in the emission over these timescales.

Preliminary models of disk based microvariability in X-ray and optical/ultra-violet wavelengths are discussed in [74, 75, 76, 77] and references therein. Here, emission from orbital features (hotspots and flares) with Keplerian motion on the disk in Schwarzschild space-time are modelled as the cause for the variability. Time delay, gravitational and Doppler shift, disk structure, eclipsing based effects and intrinsic disk based variability are some of the effects considered in these models. They provide a good match when compared to observational data. Some of the results predicted include a power law red noise portion $P(f) \propto f^{-\alpha}$ in the observed periodogram for reasonable choices of physical parameters, a low frequency flattening possibly due to decrease in the physical and emission coherency of orbital features and a high frequency cut-off due to the presence of an inner edge of the disk beyond which orbital features are absent. Simulations considering all the above general relativistic effects are carried out in [77] and show a good agreement with observed UV based power spectra for short durations, predicting a power law with slope between -1.1 and -2.4. In a recent model [78], an analytic approximation for light bending [79] is considered in the calculation of the effective redshift factor g as measured by an observer in the local static frame. The g factor used in [76, 77] is given by

$$g = \sqrt{\frac{r-2M}{r(r-3M)}}(M^{1/2}\sin i \sin\phi + \sqrt{r-2M}) \tag{1.9}$$

Where r is the radial distance in units of the geometrized mass M, i is the inclination angle towards the observer line of sight and ϕ is the azimuthal coordinate describing the orbital motion. The quantity g^4 represents the ratio of the observed intensity to the emitted intensity of radiation in a particular wavelength band such as optical/UV or X-rays. Changes in g^4 as a function of the proper time due to orbital motion of the emitting source and a combination of general relativistic effects thus represent the variability and hence, the observed light curve.

Radial or vertical perturbations to the orbit of test particles on Keplerian trajectories on the disk can be studied as additional sources of observed time-scales. As the disk can be thought of as being

composed by a population of cold accreted gas ($T < 10^5$ K), thermodynamical properties of this gas such as its pressure, density, entropy and equations of state can be identified in the relativistic regime. As this gas is composed of plasma, interacting in the presence of magnetic fields and could be highly turbulent, there could be perturbations produced in the thermodynamical parameters during their orbital motion. Time-scales for dynamic, vertical and the radial oscillation modes [80, 81] include

$$T_D(M_6, r, a) = 30.93\ (r^{3/2} + a)\ M_6\ (1 + z)\ s \tag{1.10}$$

$$T_V(M_6, r, a) = T_D(M_6, r, a)/(1 - 4a/r^{3/2} + 3a^2/r^2)^{1/2} \tag{1.11}$$

$$T_\kappa(M_6, r, a) = T_D(M_6, r, a)/(1 - 6/r + 8a/r^{3/2} - 3a^2/r^2)^{1/2} \tag{1.12}$$

where $T_D(M_6, r, a)$ is the orbital time period of timelike particles on Keplerian trajectories, $T_V(M_6, r, a)$ is the time period induced by vertical perturbations and $T_\kappa(M_6, r, a)$ is the time period induced by radial perturbations. For a Schwarzschild black hole, $T_D(M_6, r, a) = T_V(M_6, r, a) < T_\kappa(M_6, r, a)$. The time-scales in general ($a > 0$) are related by $T_D(M_6, r, a) < T_V(M_6, r, a) < T_\kappa(M_6, r, a)$. Contour plots of these time-scales for a fixed $r = 6M$ are plotted in Fig. 1.14. The black hole mass M_6 is taken in the range 1 - 10 (M_6 - M_7), typical for Seyfert galaxies. The spin range is assumed to be from 0 - 1. Dynamic and vertical time-scales of the order $\sim$ 1000 - 10000 s are calculated for these parameter ranges. The radial oscillation time-scales are $\sim$ 5 times this as seen in Fig. 1.14.

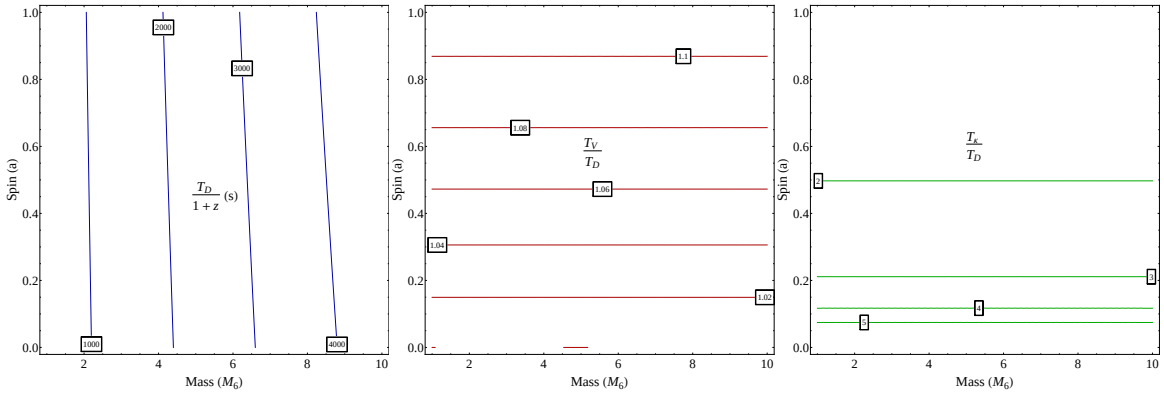

Figure 1.14: A comparison of the vertical and radial oscillation time-scales to the dynamic time-scale is presented for a given radial distance $r = 6\ M$. Left plot: Dynamic time-scale. Middle plot: ratio of vertical oscillation time-scale to dynamic time-scale. For $a = 0$, these are identical; Right plot: ratio of radial oscillation time-scale to dynamic time-scale. Typical dynamic time-scales range between $>$ 1000 s and $\sim$ 10000 s. The dynamic time-scale is seen to be the least of the three.

In addition, the Brunt-Vaisala frequency due to the vertical perturbation of the stratified gas which leads to buoyancy of the gas due to the presence of the gravitational potential is given by [80]

$$N_Z^2 = -\Omega_V^2(r, a)\left(z\frac{\partial \mathcal{A}}{\partial z}\right) \tag{1.13}$$

where z is the vertical height and $\mathcal{A}$ is a factor related to the equation of state prescribed for the gas and is given by $\mathcal{A} = \ln(p/\rho^{\Gamma})$ where Γ depends on the type of gas, typically taken to be 5/3 for a relativistic gas. Together, these frequencies will decide the oscillation modes of the disk. It has been argued that QPOs determined in X-ray binaries [82] could have a time-scale which corresponds to any of the above frequencies.

Vertical perturbations to the gas on equatorial orbits with a frequency $\Omega_V(M_6, r, a) = 2\pi/T_V(M_6, r, a)$ is also known as the Lense-Thirring frequency which is a gravito-magnetic phenomenon. In the case of X-ray binaries where the accretion disk extent is likely to be small, such a perturbation could lead to distortions in the shape of the disk [83, 84]. The material on the disk then begins to precess with this frequency along their orbital motion. The time-scale associated with $\Omega_V(M_6, r, a)$ ranges between $\sim$ 1000 s and 10000 s as discussed above.

In the inner disk where radiation pressure is dominant over gas pressure and the opacity is contributed to mainly by Thomson scattered radiation, the temperature of the disk and magnetic field strength, relevant to the current discussion are given by

$$T = 2.3 \times 10^5 \alpha^{-1/4} M_8^{-1/4} r^{-3/4} \text{ (K)} \tag{1.14}$$

$$B \leq 10^4 M_8^{-1/2} r^{-3/4} \text{ (Gauss)} \tag{1.15}$$

where α is the viscosity parameter used to characterize the scale of turbulent motions due to the dynamics in the disk, $M_8 = 10^8 M_\odot$ is the mass of the SMBH in units of the solar mass $M_\odot$ with a Schwarzschild radius R_{Sch} and $r = R/(3R_{Sch})$. Taking $\alpha = 0.01$, $M_8 = 1$ and $r = 1$, we obtain $T = 7.27 \times 10^5$K and $B \leq 10^4$ Gauss. From the calculated T, we can infer that the radiation is peaked in the UV band as $\lambda_{max} \sim 4$ nm from Wien's displacement law, applicable to blackbody radiation. The magnetic field is expected to be chaotic and confined to small scales due to the action of the differentially rotating disk. Though, if the magnetic field strength generated by dynamo action in the inner disk is in equipartition with the gas pressure as inferred from numerical simulations e.g. [85], a reasonably well developed vertical structuring can occur [86].

The inner region consisting of the disk and the developing jet is dominated by effects due to plasma flow and its interactions, magnetic field structures, differential rotation of the disk and radiative structuring. For P and ρ being the gas pressure and density, if the magnetic field is strong enough to resist perturbations due to gas pressure (in a region where the Alfvén speed $v_A = B/(4\pi\rho)^{1/2}$ is much greater than the sound speed $c_s = (P/\rho)^{1/2}$) as in the external portion of the disk, stable magnetic structures can develop. This could be shown to arise due to the advection of externally dynamo generated magnetic fields into the inner region [87] or a self-generated field in the inner region due to dynamo action [88]. For an axi-symmetric flow with a velocity v in a magnetic field B, the flux freezing condition $\nabla \times (\mathbf{v} \times \mathbf{B}) = 0$ leads to $\mathbf{v}$ being parallel to $\mathbf{B}$. Hence, the $v_P \parallel B_P$ and $v_\phi \parallel B_\phi$ [89]. But, there is a slippage in the sense that the angular velocity of the flow and the field lines differ, known from Ferraro's law. In the inner portions of the disk, if we

assume that vertical hydrostatic balance holds good, then

$$\frac{1}{\rho}\frac{\partial P}{\partial z} = \frac{\partial}{\partial z}\left(\frac{GM}{(r^2+z^2)^{1/2}}\right) \tag{1.16}$$

where M is the mass of the central black hole and (r, z) are the radial and height coordinates of the disk. For the thin disk, we can make the assumptions that $z \ll r$. For this condition to hold good, the sound speed $c_s \ll v_\phi$ where $v_\phi = (GM/r)^{1/2}$ is the orbital speed. The Alfvén speed v_A also satisfies $v_A \ll v_\phi$ in the inner disk when ρ is large. Then, the structured magnetic field lines in the inner disk can be considered to be rooted with foot points on the disk and rotating with a Keplerian angular velocity $\Omega = r_o^{-3/2}$ where r_o is the radial distance from the center to the foot point [13]. It could then be expected that material from the disk can be advected into an ordered flow along the vertically structured rotating field lines which would contribute to the loss of angular momentum in addition to magnetized winds and the disk viscosity, allowing for the in-spiralling of disk material.

Simplified models treating the flow in terms of test particles (bead on a wire model) assume their ballistic motion along open magnetic field structures e.g. [86] where there is an initial centrifugal acceleration of the flow which dies down as its velocity reaches the local Alfvén speed. Confinement at this stage is brought about by the co-rotation enforced by the rotating magnetic field lines in the expanding region of the jet. For radiation pressure dominated disks, there is a combination of acceleration from the centrifugal force action and the radiation pressure from the disk based outward flux [90]. Variability in the emission is expected from the inner jet at this stage, when the material has not yet attained asymptotic relativistic velocities (such as those close to the light cylinder and beyond) and the flow is constrained by the expanding vertical magnetic field component.

Astrophysical jets as mentioned earlier are generally observed as bi-directional and indicate a high degree of collimation to large distances. The processes of launching and collimation of the jet are believed to have an origin in the interaction between the disk, strong magnetic fields on the disk near the black hole and the availability of material through a process of active accretion. Variability in blazars is strong and occurs over rapid time-scales typically $\sim$ a few minutes to a few hours. As blazar emission is believed to be strongly dominated by the jet component leading to the identification of specific physical mechanisms that can give rise to variability.

Relativistic beaming and Doppler boosting play an important role in the amplification of variability in the jet due to the jet material moving at special relativistic velocities towards the observer line of sight. If S_ν is the spectral flux density observed and $S^{'}$ is the spectral flux density in the comoving frame, these are related by the expression

$$S_\nu(t) = \delta(t)^n S^{'}_\nu \tag{1.17}$$

where $n = 3+\alpha$ for a resolved blob of plasma and $n = 2+\alpha$ for a continuous flow and a spectral index α which is defined by $S_\nu \propto \nu^{-\alpha}$. δ is the Doppler factor given by

$$\delta = \frac{1}{\gamma_b(t)[1 - \beta_b(t)\cos\theta(t)]} \tag{1.18}$$

where θ(t) is the angle between the velocity $\beta_b(t) = \dot{x}_b(t)/c$ of the emission region and the observer line of sight and $\gamma_b(t) = 1/(1-\beta_b(t)^2)^{1/2}$ is the corresponding bulk Lorentz factor. In our jet models presented in Chapter 7, we have presented a full general relativistic form of the above used Doppler factor.

Early models of outbursts and associated variability invoked the propagation of a shock wave through an adiabatic, conical, relativistic jet [91]. The propagating shock front in this model accelerates electron populations in the jet to relativistic velocities. These electrons then undergo cooling through the emission of synchrotron and the inverse Compton process. In a simple model of a shock propagation through a relativistically moving fluid with energy density E, gas pressure density p and having a particle number density n e.g. [13], the post shock fluid can be accelerated to a maximum velocity of $c/3$ and the ratio of the number density in the post shock region to the pre-shock region the compression ratio $\propto (E_2/E_1)^{1/2}$ where E_2 is the energy density in the post shock region and E_1 is the energy density in the pre-shock region such that $E_2 > E_1$. Thus, the shock front compresses the material in the jet leading to an increased energy density and velocity. With R and x being characteristic sizes of the magnetic field B perpendicular and along the observer line of sight and ν_M being the frequency at which at turnover occurs in the spectrum ($\sim$ 300 GHz), the angular size of the emitting region and the variability timescale are given by [91]

$$\theta \sim 0.04 H_0^{0.6}(R/R_0) \text{ mas}, \tag{1.19}$$

$$\Delta t_{var} \sim 0.03 H_0^{-4}(\nu/\nu_M)^{-1/2} \text{ days} \tag{1.20}$$

where H_0 is the Hubble constant, assumed to be $\sim$ 70 km/s/Mpc, R_0 is the radius at which a component is injected into the flow thus inducing the shock. For $R \sim R_0$, $\theta = 0.05$ mas. For 3C 273, $\nu_M = 70$ GHz is measured and a typical timescale of $\sim$ few days is predicted from this model.

Rapid variability is produced in the total and polarized flux density over time-scales of hours to days due to changes in relativistic aberration are produced when there is a non-uniform propagation of shocks down relativistic jets [92]. As emission is beamed and boosted due to special relativistic effects, small variability features in the co-moving frame of the propagating jet are amplifed in the observer frame of reference. It can also be caused when emission from orbital material on helical trajectories gets beamed when their local angle is close to the angle to the observer line of sight e.g. [93, 94, 95]. This is likely to be quasi-periodic in nature as the number of cycles over which beaming occurs will be less (≤ 6). Also, if the flow is sourced from a hot corona, there is an expectation of observing this variability in X-ray wavelengths.

In models of swinging jets or when there is an internal rotation of the fluid e.g. [93, 95], the fluid is spun up to large relativistic Mach numbers by the time it reaches the light cylinder radius

R_L. The proper time interval $\Delta\tau^2$ can be related to the coordinate time and the polar spatial coordinates for a special relativistic fluid by

$$c^2 d\tau^2 = c^2 dt^2 - (dr^2 + r^2 d\theta^2 + r^2 \sin^2\theta d\phi^2). \tag{1.21}$$

Re-arranging the terms, we obtain

$$(\frac{dt}{d\tau})^2 - u_P^2 - u_\phi^2 \implies \gamma_{jet}^2 = \gamma_\phi^2(1 + u_P^2). \tag{1.22}$$

Using the above relation, one can determine γ_{jet} at large R. Using this in the Doppler factor eqn. 1.18, light curves showing a QPO can be simulated e.g. [93]. For typical $\gamma_{jet} \sim 5$ - 15 [96], a time-scale of $\sim$ a few days can be simulated [95] for Quasars and BL Lacertae objects. In Chapter 7, we make use of a full general relativistic jet model in Schwarzschild geometry to calculate γ_{jet} for the inner developing jet upto the light cylinder distance. $R > R_A$ where $R_A = x_A R_L$ is the Alfven point and $x_A \leq 1$, the specific angular momentum l is conserved with $v_\phi = l/(Rc)$. The angular velocities of the fluid Ω and that due to rotating field lines Ω_F differ due to slippage of the fluid. At and beyond the Alfven point, these coincide with the relation

$$l = R^2\Omega \sim R_A^2\Omega_F, \tag{1.23}$$

ignoring the contribution from the angular momentum of the field. The quantities R_A and Ω_F can thus be identified as the asymptotic, constant l can be calculated from specific models.

Jet based variability over long time-scales (days - years) can be caused by three important processes: nonballistic helical motion due to orbital motion in a binary black hole system with time-scale T_{orb}, ballistic or nonballistic helical motion due to precession of the jet with time-scale T_{prec} and nonballistic helical motion due to an internally rotating jet flow with a time-scale T_{int}. The time-scales for orbital motion T_{orb} and the internally rotating jet T_{int} are similar. For an inclination angle to the observer i and a half-opening angle of the precession cone α such that $\alpha \leq i$, the time-scales involved in each of these processes [95] are

$$T_{orb} = (1+z)\left(1 - \frac{v_z}{c}\cos i\right) T_K, \tag{1.24}$$

$$T_{prec} = (1+z)\left(1 - \frac{v_z}{c}\cos i - \frac{v_z}{c}\tan\alpha \sin i\right) T_P, \tag{1.25}$$

where $T_K = 2\pi/\Omega_K = \sqrt{\dfrac{2\pi d^3}{G(M+m)}}$ for a binary system with masses M and m seperated by a distance d, $T_P = 2\pi/\Omega_P = \dfrac{4\pi d c^2}{(3m+\mu)G\Omega_K}$ for a precession driven in a system with reduced mass μ and v_z is the velocity of the bulk flowing plasma in the vertical direction. Typical timescales are $T_{orb} \sim T_{int}$ = few days and T_{prec} = few years.

Strong variability is often observed in a wide variety of wavelengths ranging from radio to optical to γ-ray from AGN with strong jet components such as blazars. Perturbations produced on the disk can be advected into relativistic jets and amplified there via Doppler boosting e.g. [97]. It is thus important to study the inner region composed of the disk and developing jet with footpoints on the disk. Variability can occur only if the flow is mass dominated. Poynting flux can develop in the inner jet (spine) to further accelerate the mass loaded in the outer sheath through radiation pressure. The magnetic field based pressure and tension can also contribute to the developing kinetic energy of the jet. Ejected material may not be able to travel to large distances (few light cylinder radii) due to inertial effects, interaction with external earlier expelled gas and Compton drag from radiation pressure, at which time the flow could become Poynting flux dominated.

1.9 Aims of this thesis

- Theoretical modelling of orbital signatures from AGN in optical/UV and X-ray wavelengths, relevant to the physics of the accretion disk and developing jet close to the SMBH.
- Use these disk and jet models to place constraints on physical parameters such as black hole mass and spin.
- Development of a suite of time series analysis techniques to analyze light curves from AGN in the above wavelengths and to aid in the extraction of physically relevant quantities to aid theoretical models including constraining the shape of the PSD, inference of break frequencies, QPO detection and its properties.

This thesis aims at addressing the understanding of the above described complex phenomena using two complementary approaches: the construction of theoretical models and statistical analysis of observational data.

1.10 Thesis constituents

The structure of this thesis is arranged into the next seven chapters. Chapter 2 introduces and develops a suite of time series analysis techniques which will be used in the subsequent analysis of optical and X-ray light curves from AGN. Chapter 3 presents an analysis methodology which includes analytic and MC simulations based significance testing with key inputs from numerical experiments, conducted with the analysis suite on synthetic light curves with varying properties. A data characterization and search strategy is then formulated for application to AGN light curves. Chapter 4 presents an analysis of variability from optical and X-ray light curves of a sample of blazars as an application of the developed analysis suite and data characterization and search strategy. Chapter 5 first presents the development of a break frequency model applicable to the inner region of an accretion disk followed by a model for the QPO quality factor Q for a radially infalling bulk flow on the disk. This is followed by an analysis of variability from X-ray light

curves of Seyfert galaxies which are believed to be dominated by disk contributions. Then, we apply the models to the analysis of the light curves to present revised constraints on the black hole mass, spin and region of emission. Chapter 6 presents a theoretical model of accretion disk based variability, formulated in Kerr geometry and incorporating the properties of a bulk flowing plasma. A g-factor is calculated which includes Doppler and gravitational shifts, aberration and time delay. Simulations are carried out for a range of parameters and the development of a power law PSD shape and a QPO are discussed. Chapter 7 presents a theoretical model of jet based variability, formulated in Schwarzschild geometry and incorporating the properties of a bulk flowing plasma in helical motion along a funnel shaped surface. The g-factor is calculated including Doppler and gravitational shifts, aberration, light bending and time delay. Simulations are carried out for a range of parameters and the development of a power law PSD shape and a QPO are discussed. The role of the beaming effect on the appearance of the QPO and its number of cycles as inferred by a distant observer is discussed. Chapter 8 then presents a summary of the conclusions from all chapters. This is followed by a section on novel aspects of the current body of work with its impact. Then, we present future work which includes papers under preparation.

Chapter 2

Time series analysis

2.1 Introduction

The light curve is a time series, the ordinate generally being the variable flux from the emitting source which is ordered along the abscissa based on the time of reception.

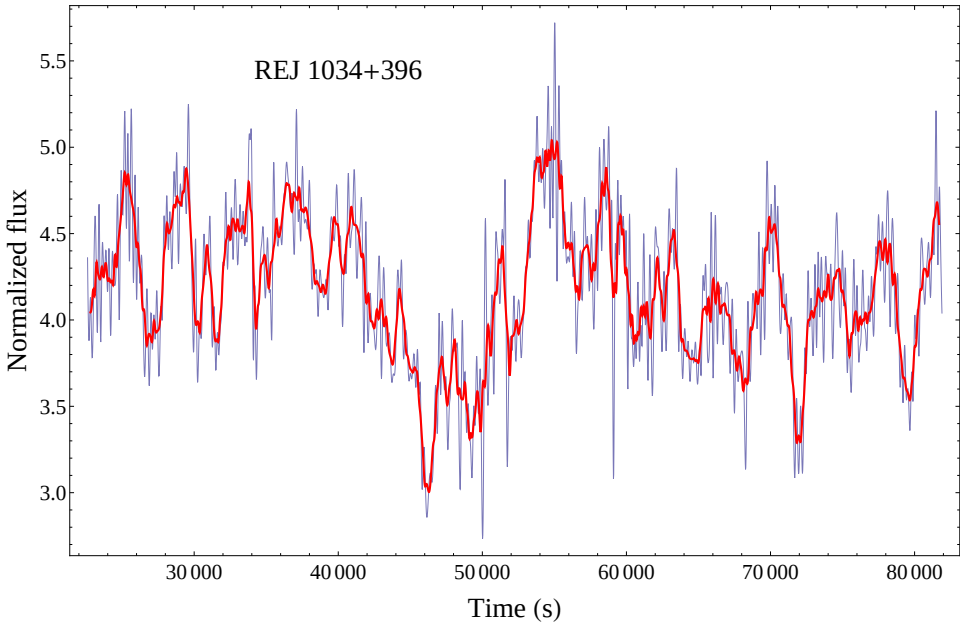

Figure 2.1: Illustration of variability: X-ray light curve in the 0.3 keV to 10 keV energy range from the narrow line Seyfert 1 AGN REJ 1034+396. This light curve was analyzed in [55] where the presence of a quasi-periodic oscillation centered at $\sim$ 3700 s was reported.

Properties of light curves from AGN can be classified broadly into intrinsic source based properties due physical processes at the emission source and measurement induced properties which the light curve acquires due to instrumental effects in the observation of these sources.

The variability of a light curve is the changes in flux as a function of the reception time. The light curve in Fig. 2.1 has a mean of $\sim$ 4.2 counts/s and varies between a minimum of 2.77 counts/s

and a maximum of 5.64 counts/s during the observation duration. There are many instances in this duration where the flux variation is rapid within a short interval of time. As an illustration, the flux at the start of the light curve is 4.36 counts/s. This flux increases to 5.17 counts/s within 25200 s and then falls to 3.64 counts/s within the next 1700 s. The variability in the light curve can be rapid and short as in the illustrated example in Fig. 2.1 where flux variations occur on timescales of a few 1000 s to a few 10000 s or can be long term with large changes in amplitudes occurring over long durations of time e.g. [98] where variability in the optical light curve of the blazar S5 0716+714 is observed on timescales of a day or more.

The variability amplitude can be quantified in terms of the fractional excess rms variability amplitude $F_{\rm var}$ [99]. If $\sigma_{{\rm err},k}$ is the uncertainty or measurement error for each point of the light curve $x(t_k)$ evaluated at times t_k, then, $\hat{\sigma}^2_{\rm err} = \frac{1}{N}\sum_{k=1}^{N}\sigma_{{\rm err},k}$ is the mean square error. If σ^2 is the variance and μ is the mean of the light curve evaluated from the points of the light curve,

$$F_{\rm var} = \sqrt{\frac{\sigma^2 - \hat{\sigma}^2_{\rm err}}{\mu^2}} \tag{2.1}$$

The variable light curve shows smaller fluctuations superimposed on a larger, longer duration background trend. The light curve in Fig. 2.1 shows a roughly parabolic trend between the start of the observation and $\sim$ 46000 s and no major trend if we consider the light curve as a whole. Trends in an AGN light curve could occur before and after a flaring phase. If this phase lasts for some time and the data is obtained during this time, we would observe a slowly decaying trend. One could also possibly observe the rising portion just before the maximum of the flare for a continuously monitored source.

The above mentioned properties relating to variability and trends depend on the observation wavelength and the type of AGN from which the light curve is obtained. For an AGN such as a Seyfert 1 galaxy, the unified model of AGN [33] suggests that the observer is measuring the flux emanating from possibly the inner region close to the central super-massive black hole. Thus, variability will be strong in the optical/UV emission which is believed to be the black body radiation from an optically thick disk. Variability is also strong in the soft and hard X-rays (0.1 - few 10s of keV) which could be re-processed black body radiation from a external corona consisting of thermally supported electrons surrounding the disk.

The measurement of the flux emitted at the source by the detector could occur at even intervals of time with constant time steps Δt or at uneven times. Depending on the reception times at which the flux is measured, the former is an evenly sampled light curve while the latter is unevenly sampled. The light curve illustrated in Fig. 2.1 was obtained using the X-ray Multi-Mirror Mission - Newton (XMM Newton) space based observatory in the 0.3 - 10 keV energy range [55].

An emission source can be observed continuously only for certain durations of time due to constraints imposed by the observing instruments and their properties. The final light curve could be made up of a set of segments obtained during consecutive days or a few days each month. Thus, light curves could have small duration (upto a day) to long duration (few days to a month) gaps.The

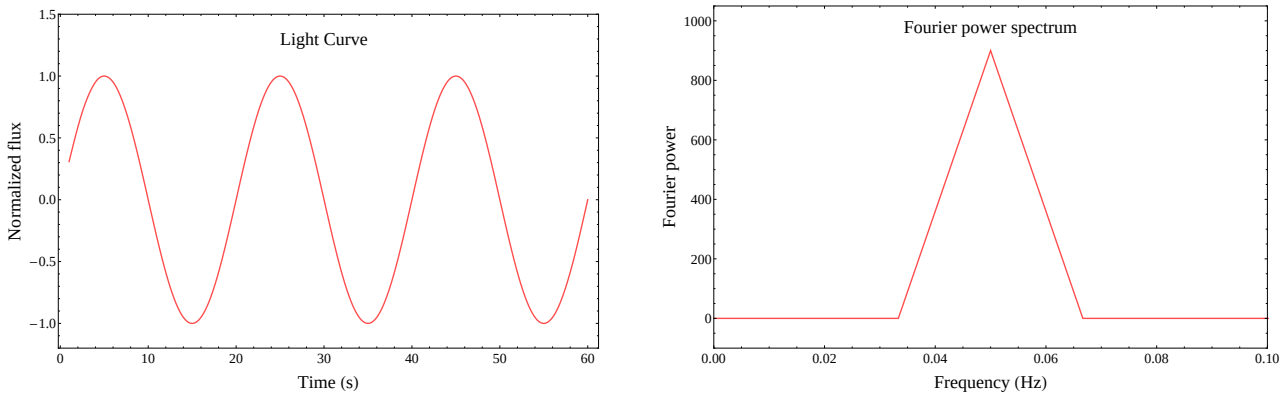

Figure 2.2: Left plot: synthetic sinusoidal light curve of duration 60 s with a periodicity of 20 s. Right plot: Fourier power spectrum $|F(f_j)|^2$ evaluated in the positive frequencies indicating a strong peak centered at 0.05 Hz.

finite observation duration in the obtained light curve segment must be taken into consideration while analyzing the light curve using frequency domain time series analysis techniques.

In this chapter, we describe the motivation for and the development of a suite of time series analysis techniques which can be employed in the analysis of light curve properties from AGN in relevant wavelengths such as optical/UV and X-rays. They can extract physically relevant properties such as variability characteristics of the source, presence of a quasi-periodic oscillation and its evolution, duration and number of cycles, breaks in the Fourier power spectrum; results from this analysis would aid in developing and constraining parameters in theoretical models of variability in emission.

These techniques include: the periodogram, Lomb-Scargle periodogram (LSP), multi-harmonic analysis of variance (MHAoV) and wavelet analysis. Brief descriptions of the development, application and advantages of each of the above techniques are discussed in [100, 98, 101].

2.2 Periodogram

This technique is the primary component of the developed analysis suite owing to its computational efficiency, though being applicable only to evenly sampled light curves. If an interesting, prominent feature is detected, a detailed analysis can then be carried out with the periodogram and the other components of the analysis suite: LSP, MHAoV and wavelet analysis.

2.2.1 Definition and evaluation frequencies

The discrete Fourier transform (DFT) of an evenly sampled, mean subtracted light curve $x(t_k)$, k spanning N points with a time step size between consecutive points of Δt is given by,

$$F(f_j) = \sum_{k=1}^{N} x(t_k) e^{i2\pi f_j t_k} \tag{2.2}$$

evaluated at frequencies $f_j = j/(N\Delta t)$ with $j = 1, 2, .., (N/2)$ such that the evaluation is carried out upto the Nyquist frequency $f_{N/2}$. Any evenly sampled time series will not contain information on $x(t)$ at intermediate points $< \Delta t$. The Fourier transform of this then samples only the discrete time step grid thus omitting contributions with frequencies higher than $1/\Delta t$. Also, sampling a time series is equivalent to a convolution with a Comb function which in the Fourier domain will show contributions at integer multiples of the sampling frequency. The contributions to the power spectrum would thus come from analyzed frequencies f_j and other frequencies that differ from f_j by an integer multiple of the sampling frequency. Higher frequencies outside this range will alias or mix into the sampled power spectrum. The maximum frequency upto which aliasing effects are negligible is the Nyquist frequency, $f_{N/2}$. The periodogram is the normalized Fourier power spectrum and is given by:

$$P(f_j) = \frac{2\Delta t}{\mu^2 N} F(f_j).F^*(f_j) = \frac{2\Delta t}{\mu^2 N} |F(f_j)|^2 \tag{2.3}$$

Where μ is the mean of the light curve evaluated before subtraction from $x(t_k)$. The normalization $\frac{2\Delta t}{\mu^2 N}$ is used to express $P(f_j)$ in units of (rms^2/mean^2) Hz^{-1} = (σ^2/μ^2) Hz^{-1} such that the integrated periodogram over the limits $f_1 = 1/(N\Delta t)$ and $f_{N/2} = 1/(2\Delta t)$ yields the fractional variance of the time series [99]. The Fourier power spectrum is illustrated with an application to an evenly sampled sinusoidal light curve in Fig. 2.2.

2.2.2 Least squares fit and properties

The power spectrum $P(f_j)$ is obtained by the least squares fit of the light curve $x(t_k)$ with the model

$$x_M(t_k) = \alpha \cos 2\pi f_j(t_k) + \beta \sin 2\pi f_j(t_k) \tag{2.4}$$

Let the square of the residue be R^2.

$$R^2 = \sum_{k=1}^{N} (x(t_k) - \alpha \cos 2\pi f_j(t_k) - \beta \sin 2\pi f_j(t_k))^2 \tag{2.5}$$

The extrema of R^2 with respect to the parameters α and β are then determined. If we use the following representation

$$\begin{aligned} C^2 &= \sum_{k=1}^{N} \cos^2 2\pi f_j(t_k) \\ S^2 &= \sum_{k=1}^{N} \sin^2 2\pi f_j(t_k) \\ SC &= \sum_{k=1}^{N} \sin 2\pi f_j(t_k) \cos 2\pi f_j(t_k) \\ XC &= \sum_{k=1}^{N} x(t_k) \cos 2\pi f_j(t_k) \\ XS &= \sum_{k=1}^{N} x(t_k) \sin 2\pi f_j(t_k) \end{aligned} \tag{2.6}$$

(2.7)

then, the extrema equations can be represented by the matrix equation

$$\begin{pmatrix} C^2 & SC \\ SC & S^2 \end{pmatrix} \begin{pmatrix} \alpha \\ \beta \end{pmatrix} = \begin{pmatrix} XC \\ XS \end{pmatrix}$$

We then invert the above equation to obtain

$$\begin{pmatrix} \alpha \\ \beta \end{pmatrix} = \frac{1}{C^2S^2 - (SC)^2} \begin{pmatrix} S^2XC - SCXS \\ SCXC - C^2XS \end{pmatrix}$$

Let $2\pi f_j(t_k) = \theta_{jk} = 2\pi \dfrac{j}{N\Delta t}(\Delta t)k = 2\pi \dfrac{jk}{N}$. Then

$$\begin{aligned} SC &= \sum_{k=1}^{N} \sin\theta_{jk} \cos\theta_{jk} = \frac{1}{2} \sin 2\theta_{jk} \\ &= \frac{1}{2} Im \left(\sum_{k=1}^{N} e^{i2\theta_{jk}} \right) = \frac{1}{2} Im \left(\sum_{k=1}^{N} e^{i2\pi \frac{jk}{N}} \right) = 0 \end{aligned} \tag{2.8}$$

for 1<j<$N/2$ and $k < N$. For $k \geq N$, the above quantity goes as $2\pi j$.

Thus, by a suitable choice of the sampling length (< reciprocal of the Nyquist frequency), the cross term $SC = 0$ for all t_k.

The power spectrum is given by

$$P_N(f_j) = \begin{pmatrix} XC & XS \end{pmatrix} \begin{pmatrix} \alpha \\ \beta \end{pmatrix}$$

=

$$\left(XC/C^2 XS/S^2\right)$$

then reduces to the expression in eqn. (2.3)

$$P(f_j) = \frac{XC^2}{C^2} + \frac{XS^2}{S^2} \tag{2.9}$$

The expressions C^2 and S^2 from eqn. (2.7) can be evaluated for all t_k.

$$\begin{aligned} C^2 &= \sum_{k=1}^{N} \cos^2 2\pi f_j(t_k) = \sum_{k=1}^{N} \cos^2 2\pi \frac{jk}{N} \\ &= \sum_{k=1}^{N} \frac{1}{2}(1 + \cos 4\pi \frac{jk}{N}) = (N/2) + \frac{1}{2}\sum_{k=1}^{N}(e^{4\pi i \frac{jk}{N}} + e^{-4\pi i \frac{jk}{N}}) \\ C^2 &= N/2 \end{aligned} \tag{2.10}$$

$$\begin{aligned} S^2 &= \sum_{k=1}^{N} \sin^2 2\pi f_j(t_k) = \sum_{k=1}^{N} \sin^2 2\pi \frac{jk}{N} \\ &= \sum_{k=1}^{N} \frac{1}{2}(1 - \cos 4\pi \frac{jk}{N}) = (N/2) - \frac{1}{2i}\sum_{k=1}^{N}(e^{4\pi i \frac{jk}{N}} - e^{-4\pi i \frac{jk}{N}}) \\ S^2 &= N/2. \end{aligned} \tag{2.11}$$

Using these, the expression for the power spectrum becomes

$$P(f_j) = \frac{2}{N}(XC^2 + XS^2) \tag{2.12}$$

It is to be noted here that the reduction $C^2 = S^2 = N/2$ can only occur when the light curve is evenly sampled such that the exponential terms in their expressions sum to 0.

2.2.3 The power spectral density (PSD)

The PSD which we represent here as $\hat{P}(f)$ is the underlying, true power spectrum which is presumed to be shaped by the physical process leading to the emission of the light curve. A primary objective in the analysis of a light curve is the characterization and constraining of the shape of this PSD. This would then lead to us being able to constrain in turn theoretical models of variable emission which gave rise to it. The shape of the PSD can be deduced from $P(f_j)$ using non-parametric procedures such as smoothing it by using a kernel function, weights or by binning as well as parametric procedures which fit the averaged periodogram with a model such as a power law, broken power law or bending power law. Details regarding the procedure we adopt to determine the PSD are presented in the Chapter 3.

2.2.4 Statistical properties of the periodogram

For a time series constructed from normal random variables, the periodogram $P(f)$ at a given frequency is exactly χ^2_2 distributed about the underlying constant PSD as the real and imaginary parts of the Fourier transform of the evenly sampled time series are normally distributed for a stochastic process e.g. [16], and the sum of two squared normally distributed variables is a χ^2_2 distributed variable. Thus, $P(f)$ is χ^2_2 distributed about the underlying constant PSD,

$$\hat{P}(f) = \text{Constant} = \sigma^2. \tag{2.13}$$

The periodogram is generally evaluated upto the Nyquist frequency. For an unevenly sampled time series, timescales corresponding to frequencies above the Nyquist frequency can contribute to the power at longer time-scales and hence influence the slope of the periodogram. Power is thus aliased to lower frequencies as described in §2.2.1. For processes whose spectrum deviates from a flat, constant value, $P(f)$ is still approximately χ^2_2 distributed about $\hat{P}(f)$, though, N must be large with small aliasing and biasing effects. i.e.

$$P(f) = \hat{P}(f)\chi^2_2/2. \tag{2.14}$$

Its expectation, $E(\chi^2_2/2) = \sigma^2$ and variance, $V(\chi^2_2) = \sigma^4$ when $\hat{P}(f) = \sigma^2$ suggesting that $P(f)$ is an inconsistent estimator of $\hat{P}(f)$ as this constant variance will not tend to zero under the limit of large N [16, 102]. This issue can be addressed by averaging the periodogram by binning in the frequency domain. Further, if the binning is carried out in the log-log space, the convergence towards a consistent estimator of the PSD occurs even for reasonable N [102].

2.2.5 Periodogram: the algorithm

1. Determine the frequencies at which the periodogram is to be calculated.
2. Determine the periodogram of a light curve using eqn. (2.3).
3. Express $P(f_j)$ in the log-log space.
4. Bin this log-log periodogram and average over the bins to obtain a smoothed periodogram. Typical number of points per bin is ~ 10.
5. The smoothed periodogram can now be used to determine and constrain the PSD shape.

The definition used for the periodogram and an illustration of a simple fit procedure to determine significant features is discussed in [103]. Non-parametric smoothing using binning and averaging the periodogram in the log-log space in order for it to converge faster to the underlying PSD is discussed in [102]. The normalization used in our definition of the periodogram in eqn. (2.3) is useful for the current problem under study in this thesis. A discussion on other normalizations in use and their context of use is discussed in [99]. The periodogram is computationally the simplest

amongst the time series techniques discussed in the preceding sections. Though, it is applicable only to evenly sampled light curves. When applied to unevenly sampled light curves, it could introduce spurious features. It is also noisy for real astrophysical light curves and techniques have to be developed in order to smooth it to get a better estimate of the true underlying PSD, either by parametric or non-parametric methods. For a light curve of finite length N, the expression for its DFT can be thought of as containing the light curve convolved with a rectangular window function. This causes spurious ringing features in the frequency domain when the DFT and hence the peridogram are determined. The finite length also leads to cyclic behaviour which results in spurious features at low frequencies. When the periodogram is binned and averaged in the log-log space, the scatter due to all the above intrinsic sources and external sources of noise reduces in turn reducing the variance estimate. The periodogram estimate at a given frequency is then χ^2 distributed about the underlying PSD. Once the shape of the PSD is well constrained, an analytic significance test (presented in Chapter 3) can be carried out to eliminate spurious features in the periodogram. The advantage is that once we account for all sources of intrinsic noise that are present in the periodogram, the noise due to external sources can be identified and studied.

2.3 Lomb-Scargle Periodogram (LSP)

The LSP is used as a primary technique when the input light curve is unevenly sampled. The LSP reduces the contributions from spurious, noisy features as it is independent of the time step Δt and hence changes in it.

2.3.1 Definition and evaluation frequencies

The power spectrum for the LSP evaluated from a light curve $x(t_k)$, k spanning N points is determined by a least squares fit to a mean subtracted time series using

$$x(t_k) = \alpha \sin 2\pi f_j(t_k - \tau) + \beta \cos 2\pi f_j(t_k - \tau) \tag{2.15}$$

and is given by [104]

$$\begin{aligned} P_N(f_j) &= \frac{1}{2\sigma^2}\left[\frac{(\sum_{k=1}^{N}(x(t_k)-\mu)\cos 2\pi f_j(t_k-\tau))^2}{\sum_{k=1}^{N}\cos^2 2\pi f_j(t_k-\tau)}\right. \\ &\quad \left. + \frac{(\sum_{k=1}^{N}(x(t_k)-\mu)\sin 2\pi f_j(t_k-\tau))^2}{\sum_{k=1}^{N}\sin^2 2\pi f_j(t_k-\tau)}\right], \end{aligned} \tag{2.16}$$

where τ is a time shift parameter and is given by

$$\tan(4\pi f_j \tau) = \frac{\sum_{k=1}^{N}\sin(4\pi f_j t_k)}{\sum_{k=1}^{N}\cos(4\pi f_j t_k)} \tag{2.17}$$

where μ is the mean of the light curve and $P_N(f_j)$ is evaluated at frequencies $f_j = j/(t_N - t_1)$ where $j = 1, 2, .., N/2$ and $(t_N - t_1)$ is the total duration of the observation. The LSP power spectrum [105, 106, 104] is constructed using the algorithm presented in [107] in order to achieve fast computational speeds. Using the simplifications,

$$S_h = \sum_{k=1}^{N} (x(t_k) - \mu) \sin 2\pi f_j t_k \tag{2.18}$$

$$C_h = \sum_{k=1}^{N} (x(t_k) - \mu) \cos 2\pi f_j t_k$$

$$S = \sum_{k=1}^{N} \sin 4\pi f_j t_k$$

$$C = \sum_{k=1}^{N} \cos 4\pi f_j t_k$$

The components of $P_N(f_j)$ can be expressed as:

$$\sum_{k=1}^{N} (x(t_k) - \mu) \cos 2\pi f_j (t_k - \tau) = C_h \cos 2\pi f_j \tau + S_h \sin 2\pi f_j \tau \tag{2.19}$$

$$\sum_{k=1}^{N} (x(t_k) - \mu) \sin 2\pi f_j (t_k - \tau) = S_h \cos 2\pi f_j \tau - C_h \sin 2\pi f_j \tau \tag{2.20}$$

$$\sum_{k=1}^{N} \cos^2 2\pi f_j (t_k - \tau) = (N/2) + (C/2) \cos(4\pi f_j \tau) + (S/2) \sin(4\pi f_j \tau) \tag{2.21}$$

$$\sum_{k=1}^{N} \sin^2 2\pi f_j (t_k - \tau) = (N/2) - (C/2) \cos(4\pi f_j \tau) - (S/2) \sin(4\pi f_j \tau) \tag{2.22}$$

The LSP is illustrated with an application to an unevenly sampled sinusoidal light curve in Fig. 2.3.

2.3.2 Least squares fit and properties

This method of deriving the LSP power spectrum was presented in [105]. An alternative approach was adopted in [106] where the LSP power spectrum was derived from statistical considerations applied to a generalized Fourier transform of a time series. This was shown to be equivalent to the earlier result. The power spectrum $P_N(f_j)$ is obtained by the least squares fit of the light curve $x(t_k)$ with the model

$$x(t_k) = \alpha \cos 2\pi f_j (t_k - \tau) + \beta \sin 2\pi f_j (t_k - \tau) \tag{2.23}$$

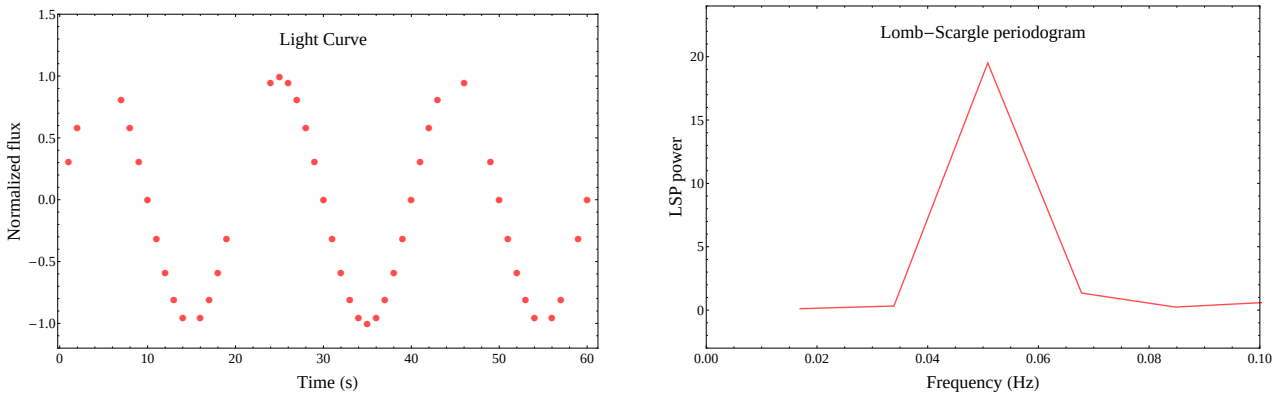

Figure 2.3: Left plot: synthetic unevenly sampled sinusoidal light curve of duration 60 s with a periodicity of 20 s. Right plot: LSP evaluated in the positive frequencies indicating a strong peak centered at ~ 0.05 Hz.

Let the square of the residue be R^2.

$$R^2 = \sum_{k=1}^{N} (x(t_k) - \alpha \cos 2\pi f_j (t_k - \tau) - \beta \sin 2\pi f_j (t_k - \tau))^2 \tag{2.24}$$

The extrema of R^2 with respect to the parameters α and β are then determined. If we use the following representation

$$\begin{aligned} \tilde{C}^2 &= \sum_{k=1}^{N} \cos^2 2\pi f_j (t_k - \tau) \\ \tilde{S}^2 &= \sum_{k=1}^{N} \sin^2 2\pi f_j (t_k - \tau) \\ \tilde{SC} &= \sum_{k=1}^{N} \sin 2\pi f_j (t_k - \tau) \cos 2\pi f_j (t_k - \tau) \\ \tilde{XC} &= \sum_{k=1}^{N} x(t_k) \cos 2\pi f_j (t_k - \tau) \\ \tilde{XS} &= \sum_{k=1}^{N} x(t_k) \sin 2\pi f_j (t_k - \tau) \end{aligned} \tag{2.25}$$

then, the extrema equations can be represented by the matrix equation

$$\begin{pmatrix} \tilde{C}^2 & \tilde{SC} \\ \tilde{SC} & \tilde{S}^2 \end{pmatrix} \begin{pmatrix} \alpha \\ \beta \end{pmatrix} = \begin{pmatrix} \tilde{XC} \\ \tilde{XS} \end{pmatrix}$$

We then invert the above equation to obtain

$$\begin{pmatrix}\alpha\\ \beta\end{pmatrix} = \frac{1}{\tilde{C}^2\tilde{S}^2 - \tilde{SC}^2}\begin{pmatrix}\tilde{S}^2\tilde{XC} - \tilde{SC}\tilde{XS}\\ \tilde{SC}\tilde{XC} - \tilde{C}^2\tilde{XS}\end{pmatrix}$$

For the choice of τ from eqn. (2.17), the cross term $\tilde{SC}$ vanishes.

The power spectrum

$$P_N(f_j) = \begin{pmatrix}\tilde{XC} & \tilde{XS}\end{pmatrix}\begin{pmatrix}\alpha\\ \beta\end{pmatrix}$$

then reduces to the expression in eqn. (2.16)

$$P_N(f_j) = \frac{\tilde{XC}^2}{\tilde{C}^2} + \frac{\tilde{XS}^2}{\tilde{S}^2} \tag{2.26}$$

The use of a τ makes the power spectrum independent of a shift in all t_k by a constant, i.e. $P_N(f_j)$ is rendered invariant under time translation. If the light curve is evenly sampled, then, $\tau = 0$ and $P_N(f_j)$ reduces to the periodogram $P(f_j)$ in eqn. (2.3). The LSP can thus be employed in the detection of regular sinusoidal signals in both evenly and unevenly sampled data. The LSP for unevenly sampled data must be preferably determined without conversion to evenly sampled data. By performing such a conversion, one introduces additional artificial sampling frequencies whose power contributions lead to the suppression of any actual significant peaks.

2.3.3 Statistical properties of the LSP

For a light curve $x(t_k)$ whose ordinates are normally distributed with zero mean and variance $= \sigma^2$, the components $\frac{\tilde{XC}^2}{\tilde{C}^2}$ and $\frac{\tilde{XS}^2}{\tilde{S}^2}$ are also normally distributed with zero mean and variances σ^2. The power spectrum $P_N(f_j)$ is then χ^2_2 distributed provided that the correct normalization by σ^2 is used in the expression for $P_N(f_j)$.

2.3.4 LSP: the algorithm

1. Determine the frequencies at which the LSP is to be calculated.
2. Determine the time shift factor τ using eqn. (2.17).
3. Determine the power spectrum $P_N(f_j)$ using the eqn. (2.16) and the above calculated value of τ.

The LSP power spectrum is derived in [105] by a model fit to the time series which is then solved using the method of least squares. An alternative approach demonstrating the independence of the polynomials components $\tilde{XC}^2/\tilde{C}^2$ and $\tilde{XS}^2/\tilde{S}^2$ of $P_N(f_j)$ was used to show an equivalence to the former in [106]. The correct normalization and its statistical implications are discussed in [104].

An algorithm which can be used to speed up the numerical procedure of evaluation of the LSP is presented in [107].

The LSP can be used to detect sinusoidal signals in both even and unevenly sampled light curves due to time shift property (not dependent on a constant time step Δt) and frequency sampling. Since the polynomials components $\tilde{XC}^2/\tilde{C}^2$ and $\tilde{XS}^2/\tilde{S}^2$ of the LSP are orthogonal, their statistical properties are independent of each other. The LSP evaluation is fast owing to the simplifications made in the evaluation expressions as presented earlier. The LSP reduces and is identical to the periodogram for $\tau = 0$ when the light curve is evenly sampled.

2.4 Multi-Harmonic Analysis of Variance (MHAoV)

The MHAoV periodogram is used for the following reasons: confirm the results from the periodogram/LSP if the analysis is carried out on an evenly sampled light curve; confirm the results from the LSP if the analysis is carried out on an unevenly sampled light curve; stronger detection of non-sinusoidal signals which may be present in the light curve.

2.4.1 Definition and evaluation frequencies

The multi-harmonic analysis of variance (MHAoV) is constructed using the algorithm presented in [108]. The mean subtracted light curve $x(t_k)$, k spanning N points is fit with a Fourier series with M harmonics, $F^{(M)}(t_k)$. A complex polynomial $\psi_M(z)$ of order $2M$ given by

$$\psi_{2M}(z) = z^M F^{(M)}(k) \tag{2.27}$$

is generated such that its constituents are expressed in an orthogonal basis.

$$\psi_M(z) = \sum_{n=0}^{M} c_n \phi_n(z) \tag{2.28}$$

where c_n are the coefficients of the complex, orthogonal polynomials, $\phi_n(z)$ are the unique orthonormal base vectors, $z = e^{i\omega k}$ and n is the index of the polynomial. $\phi_n(z)$ can be generated by the recurrence relation [108],

$$\tilde{\phi_0}(z) = 1 \tag{2.29}$$

$$\tilde{\phi}_{n+1}(z) = z\tilde{\phi_n}(z) - \alpha_n z^n \tilde{\phi}^*_n(z) \tag{2.30}$$

$$\phi_n(z) = \frac{\tilde{\phi_n}(z)}{\sqrt{\sum_{k=1}^{N} \tilde{\phi_n}(z)\ \tilde{\phi_n}^*(z)}} \tag{2.31}$$

where $\tilde{\phi}^*_n(z)$ are the complex conjugates of the polynomials, $\tilde{\phi_n}(z)$. The coefficients c_n and α_n are determined by the use of the polynomial expansion equation and the above recurrence relations

respectively.

$$\alpha_n = \frac{\sum_{k=1}^{N} z\ \tilde{\phi_n}(z)\tilde{\phi_n}^*(z)}{\sum_{k=1}^{N} z\ (\tilde{\phi_n}^*(z))^2} \tag{2.32}$$

$$c_n = \frac{\sum_{k=1}^{N} \psi\ \tilde{\phi_n}^*(z)}{\sqrt{\sum_{k=1}^{N} \tilde{\phi_n}(z)\ \tilde{\phi_n}^*(z)}} \tag{2.33}$$

where, $\psi = z^N x(k)$. For $n = -1$, $\tilde{\phi}_{-1}(z) = \frac{1}{z}$ and $\alpha_{-1} = 0$ are set from which further c_n and α_n are generated using the above relations. c_n are representative of the normalized Fourier transform of the light curve and can be thought of as a measure of the data variance when fit with a polynomial of order n. From the application of Parseval's theorem

$$\sum_{k=1}^{N}(F^{(M)}(t_k))^2 = \sum_{n=0}^{2M}|c_n|^2 \tag{2.34}$$

The MHAoV statistic, $\Theta(f)$ is used as the power spectrum. It is a comparison of the variances of the data to that of the noise. The MHAoV periodogram is given by

$$\Theta(f_j) = \frac{(N-2M-1)\sum_{n=0}^{2M}|c_n(f)|^2}{(2M)[(N-1)\sigma^2 - \sum_{n=0}^{2M}|c_n(f)|^2]} \tag{2.35}$$

where σ^2 is the variance of the data and $\Theta(f_j)$ is evaluated at frequencies $f_j = j/(t_N - t_1)$ where $j = 1, 2, .., N/2$ and $(t_N - t_1)$ is the total duration of the observation.

The MHAoV is illustrated with an application to an unevenly sampled sinusoidal function in Fig. 2.4 and an unevenly sampled square tooth wave in Fig. 2.5.

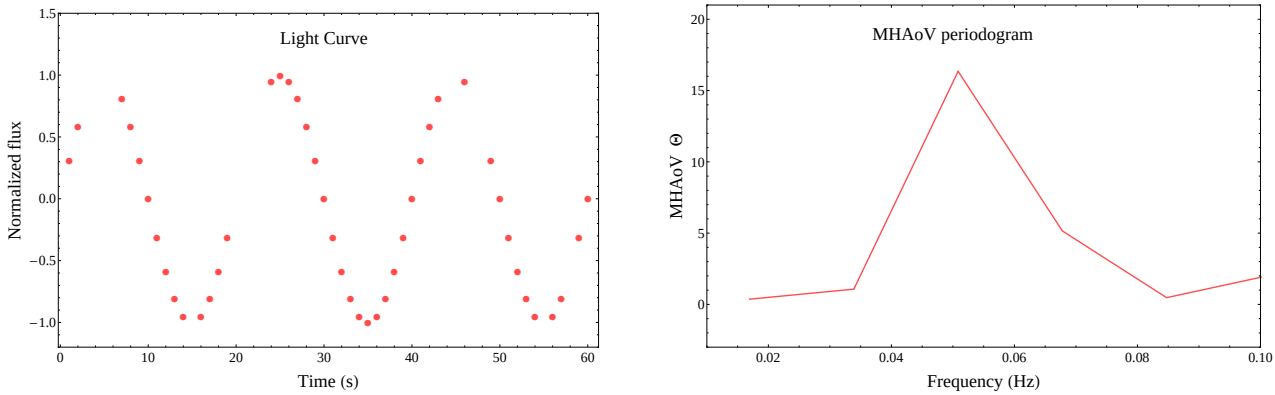

Figure 2.4: Left plot: synthetic unevenly sampled sinusoidal light curve of duration 60 s with a periodicity of 20 s. Right plot: MHAoV periodogram evaluated in the positive frequencies indicating a strong peak centered at ~ 0.05 Hz.

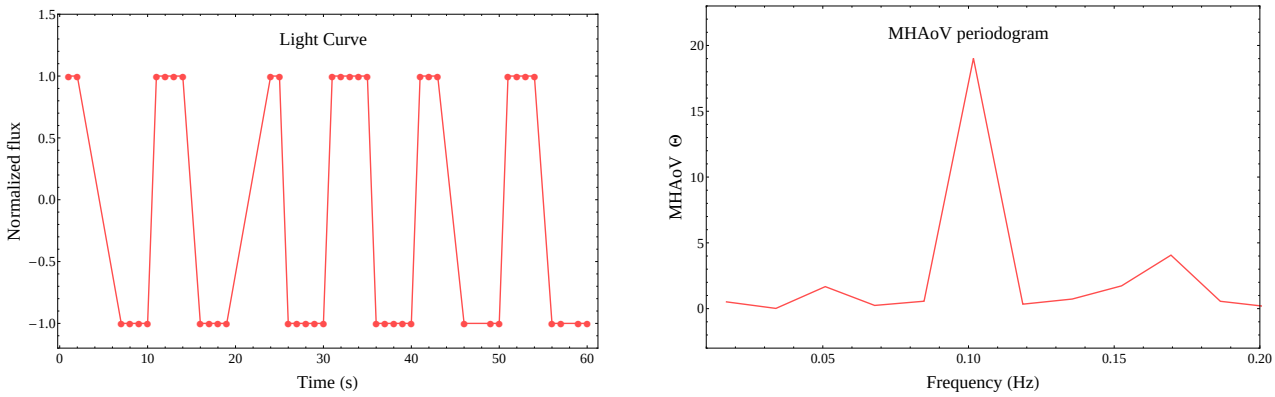

Figure 2.5: Left plot: synthetic unevenly sampled square wave based light curve of duration 60 s with a periodicity of 10 s. Right plot: MHAoV periodogram evaluated in the positive frequencies indicating a strong peak centered at ~ 0.1 Hz.

2.4.2 Statistical properties

The orthogonal polynomial generation based approach is an extension of that used in the LSP as even there, the orthogonal sinusoidal polynomials are obtained after setting the cross terms to zero by the use of the time shift operator τ. For $M = 1$, $|c_n|^2$ reduces to the LSP power spectrum $P_N(f_j)$. Though, in this case, the periodogram is the statistic $\Theta(f_j)$. This periodogram follows the Fischer's F probability distribution given by $F(2M, N - 2M - 1)$. In the periodogram and LSP, the normalization is the variance of the data which is related to the harmonic components of the power spectrum. Hence, the distribution of the ratio of the harmonic components of the power spectrum to the variance does not follow the Fischer's probability distribution.

2.4.3 MHAoV periodogram: the algorithm

1. Determine the frequencies at which the MHAoV periodogram is to be calculated.

2. Use the recursion procedure to generate the basis polynomial vectors $\phi_n(z)$ and the coefficients c_n.

3. Use the above generated c_n in the expression for the periodogram in eqn. (2.35).

The construction of the MHAoV periodogram and its statistical advantages over other techniques such as the LSP are presented in [108]. The MHAoV periodogram can also be used to detect sinusoidal signals in both even and unevenly sampled light curves due to frequency sampling. In addition, it can be used to detect even non-sinusoidal signals in light curves owing to its construction making use of higher order orthogonal polynomials. The MHAoV periodogram reduces to the LSP for order of polynomial $M = 1$. The MHAoV technique has many advantages over the discrete Fourier transform (DFT) and the LSP [108, 109]. Some of them include the ability to better handle periodic variations that are non sinusoidal and an improvement in computational efficiency as the

number of steps for computing a MHAoV is $\propto M$ compared to $\propto M^3$ for the LSP, where M is the number of harmonics considered.

2.5 Wavelet Analysis

Wavelet analysis is used to analyze evenly sampled light curves which indicate possible quasi-periodicity as characterized by the other techniques. This can be used to add to the existing set of properties of the data set and could offer new insights into the physics of the process causing the quasi-periodicity if the evolution of the interesting feature is studied in a statistical manner.

2.5.1 Definition and evaluation frequencies

The DFT of an evenly sampled, mean subtracted light curve $x(t_k)$, k spanning N points is given by $F(f_j)$ as expressed in eqn. (2.2).

The wavelet transform can be expressed in the time domain as the convolution of $x(t_k)$ with a wavelet analysing function $\psi(n - t_k, s)$ which can be scaled in size at any given position n in the time series by means of a scaling parameter s to sample a variable number of points in its immediate neighborhood as well as at a distance which can be as large as half the length of the data set. This can be repeated at all points of the time series by the use of the time shift parameter n and yields

$$W_n(s) = \sum_{k=1}^{N} x(t_k)\psi(n - t_k, s). \tag{2.36}$$

In our analysis, we make use of the Morlet wavelet function as the wavelet analysing function. In the time domain, it has the functional form

$$\psi(t_k/s) = \pi^{-1/4} e^{i(\omega_0 t_k/s) - (t_k/s)^2/2}. \tag{2.37}$$

where Morlet wavelet is a sinusoidal wave modulated by a Gaussian envelope and ω_0 is the frequency of oscillations contained within the Gaussian envelope. The wavelet transform can be carried out in the Fourier space due to computational advantages. It is then given by the inverse Fourier transform of the product of the Fourier transform of the time series with the normalized Fourier transform of the wavelet function

$$W_n(s) = \sum_{j=1}^{N/2} F(f_j)\psi^* \left(\frac{2\pi s j}{N}\right) e^{i\frac{2\pi j}{N}n}. \tag{2.38}$$

Where $\hat{\psi}^* \left(\frac{2\pi s j}{N}\right)$ is the complex conjugate of the Fourier transform of the Morlet analyzing function which is given by

$$\hat{\psi} \left(\frac{2\pi s j}{N}\right) = \pi^{-1/4} e^{-(\frac{2\pi s j}{N} - \omega_0)^2/2} \tag{2.39}$$

The term inside the summation in eqn. (2.38) is evaluated at frequencies $f_j = j/(N\Delta t)$ with

$j = 1, 2, .., (N/2)$ such that the evaluation is carried out upto the Nyquist frequency. Δt is the time step size between consecutive points of $x(t_k)$. The wavelet power spectrum (WPS) is then given by

$$WPS(n, s) = W_n(s).W_n^*(s). \tag{2.40}$$

The global wavelet power spectrum (GWPS) which is the analogue of the Fourier power spectrum is given by

$$GWPS(s) = \frac{1}{N}\sum_{n=1}^{N} W_n(s).W_n^*(s). \tag{2.41}$$

The GWPS gives an indication of the various periodic oscillations present in the data by means of power. It is a sum of the power at all the times n from the wavelet power spectrum and is a function of scale, s. Wavelet analysis is applied to an evenly sampled sinusoidal function for which $GWPS(n, s)$ and $WPS(n, s)$ are evaluated as illustrated in the bottom row of Fig. 2.6.

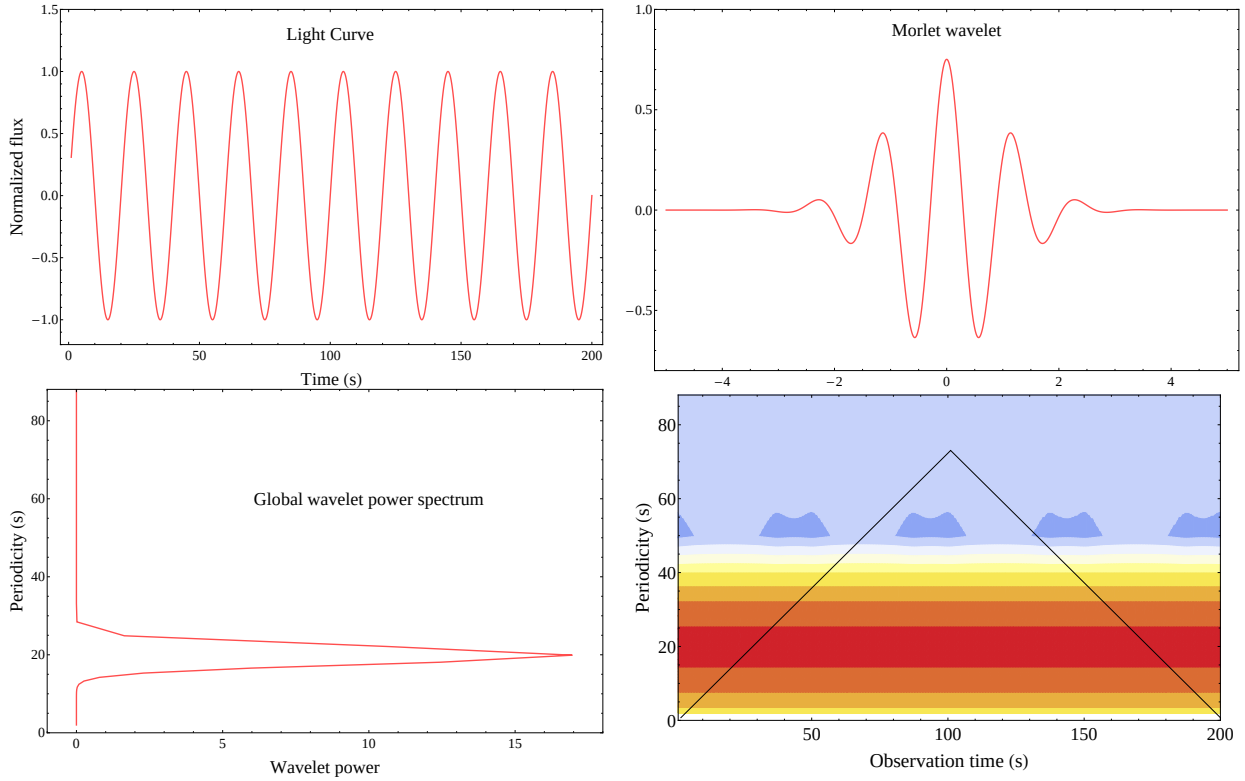

Figure 2.6:]

Top row: the left plot is a synthetic unevenly sampled sinusoidal light curve of duration 200 s with a periodicity of 20 s; the right plot is the Morlet sampling wavelet function. Bottom row: the left plot is the global wavelet power spectrum (GWPS) indicating a strong peak centered at 20 s; the right plot is the wavelet power spectrum $WPS(n, s)$. The $WPS(n, s)$ has the following components: the ordinates are the sampled frequencies converted to the Fourier wavelength space (in s), the abscissas are the observation times (in s), the cone of influence is defined here as the region inside the triangular region which can be used to interpret accurate results. The $WPS(n, s)$ indicates a strong feature at 20 s which lasts for the entire observation duration.

2.5.2 Shift and scale parameters

The time shift parameter $n = k\Delta t$ is taken from and is in the same units as the observation times t_k. The scale parameter s is also in the same units as the observation times t_k. For convenience and comparison with the power spectrum results from other techniques, we express it as the inverse of the evaluation frequencies. The relationship between the Fourier wavelength λ (time period) and the shift parameter s is given by

$$\lambda = \frac{4\pi s}{\omega_0 + \sqrt{2 + \omega_0^2}} \tag{2.42}$$

The numerical algorithm constructed based on the equations in the previous section incorporates the result from eqn. (2.42) and expresses $WPS = WPS(n, \lambda)$ and $GWPS = GWPS(\lambda)$.

2.5.3 Cone of influence (COI)

The Fourier transform of the light curve $F(f_j)$ treats the light curve $x(t_k)$ of finite length N as a cyclic quantity in order to evaluate the sinusoidal coefficients. As $F(f_j)$ is used in the evaluation of the wavelet transform $W_n(s)$, the wavelet power spectrum $WPS(n, s)$ will indicate this at the beginning and near the end. In order to reduce these edge effects, $x(t_k)$ is padded with zeroes such that its length is now equal to the closest power of two. Though, this has the effect that the amplitude of the wavelet power in $WPS(n, s)$ decreases with increasing scale s as the sampling wavelet function will pick up more zeroes in the evaluation. There will thus be a gradual increase in the size of the edge with scale s.

The COI is the region in the wavelet power spectrum $WPS(n, s)$ which serves as a demarcation between the amplitudes at a particular (n, s) which are evaluated with least error and those close to the edge which suffer from the above mentioned errors. An e-folding time in the current context is used to specify the time at which the wavelet power falls off by a factor $1/e^2$ near the edge. The COI contour includes all points $COI = COI(n_e, s_e)$ near the edge at which this transition occurs. This demarcation contour is illustrated in the right plot of the bottom row of Fig. 2.6 which is the wavelet power spectrum $WPS(n, s)$. It is defined here as the region inside the triangular region which can be used to interpret accurate results.

2.5.4 Statistical properties

For a time series whose constituents are Gaussian distributed, the power spectrum $= |F(f_j)|^2$ is approximately χ_2^2 distributed about the true spectrum, which was referred to as the PSD in the context of the periodogram. As the wavelet power spectrum $WPS(n, s)$ is the convolution of $x(t_k)$ with a wavelet analysing function $\psi(n - t_k, s)$, in the frequency domain, it is effectively smoothed by this window function and is hence a reasonable, though smooth approximation of the underlying PSD. Thus, $WPS(n, s)$ is also χ_2^2 distributed about the underlying PSD or the mean spectrum.

2.5.5 Wavelet analysis: the algorithm

1. Determine the frequencies at which WPS and GWPS are to be calculated.

2. Use eqn. (2.40) to determine the WPS of the light curve which can be represented by a contour plot as $WPS = WPS(n, s)$.

3. Use eqn. (2.41) to determine the GWPS of the light curve which is the equivalent of a smoothed Fourier power spectrum.

We have developed a numerical realization of the wavelet analysis technique based on the algorithm presented in [110]. Various types of wavelet sampling functions, their contexts of use and general properties of the discrete and continuous wavelet transform with their applications are discussed in [111]. The wavelet analysis can be used to detect sinusoidal signals in evenly sampled light curves only. In a similar manner as the periodogram, it could lead to the presence of spurious peaks in the wavelet power spectrum $W_n(s)$. This technique, though lacking in the strong characterization of a feature when compared to the other discussed techniques offers a much more information than them. The strength of a possible quasi-periodicity in the light curve can be determined by both visual inspection of the wavelet power spectrum $W_n(s)$ which is a contour plot as well as by automating the algorithm in order to identify all features which are above a desired amplitude threshold. The times during which this feature is present in the data can be determined. Further, the time duration of the existence of this feature and hence, the number of cycles the feature is present for can also be determined.

Chapter 3

Implementation of statistical techniques

3.1 Introduction

In this chapter, we first develop a statistical procedure to estimate the true underlying power spectral density (PSD) from the periodogram technique by using parametric models in §3.2. This procedure can be used to determine the PSD and constrain the model parameters. The procedure and its application are briefly discussed in [112].

Noise present in the data is generally coloured. i.e. the periodogram indicates a white noise region (flat portion) at high frequencies which evolves into a red noise region (power law portion) and their properties and statistical inferences are well studied in the context of the periodogram. We make use of the parametric model procedure to develop an analytic significance test, applicable to the periodogram in order to rule out spurious detections and study realistic cases in more detail in §3.3.1.

The statistical interpretation from other techniques have generally addressed only Gaussian distributed white noise. Thus, there is a necessity for the development of an alternate strategy for the statistical significance test while using the other techniques. The strategy here involves the use of Monte-Carlo (MC) simulated synthetic periodograms to find the best fit PSD model and are described in §3.4.

A comparison of the applicability and usage of the time series techniques by means of numerical experiments is then presented is §3.5. This demonstrates the applicability of each technique, their complementary properties and the use of the significance tests developed. The procedure and its development are briefly discussed in [101].

An overall strategy for the usage of the time series techniques tool box along with the significance testing is then presented. Here, we formulate a search-data characterization strategy for the extraction and to quantify information from any given light curve. In case the light curve indicates an interesting quasi-periodic feature of high significance, its properties and evolution can be studied.

3.2 Parametric models of the periodogram

Broadband flux variability in AGN light curves can be attributed to the orbital signatures from disk and jet based phenomena and the measured periodogram from the X-ray or optical/ultra-violet flux will be implicitly dependent on their physics. Parametric models of the periodogram can be used to estimate the underlying PSD shape that broadly mimics the effects of these physical phenomena. The maximum likelihood estimator (MLE) based fit procedure of the periodogram proves to be better suited in determining model parameters as compared with the traditionally used least squares fit where the uncertainties are large and the parameter estimates are biased [113]. Model selection using the Akaike information criteria [114] then yields the best fit model following which the analytic significance test can be carried out to determine the presence of any substantive quasi-period. Also, the choice of a statistically appropriate PSD model is useful in the development of theoretical models of variability and constrain the model parameters.

We first summarize the definition and important properties which will be used in the further discussion of the parametric models. The normalized periodogram, described in detail in Chapter 2 is given by,

$$P(f_j) = \frac{2\Delta t}{\mu^2 N}|F(f_j)|^2 \tag{3.1}$$

Where Δt is the time step size, μ is the mean of an evenly sampled, mean subtracted light curve $x(t_k)$ of length N points and $|F(f_j)|$ is its discrete Fourier transform evaluated at frequencies $f_j = j/(N\Delta t)$ with $j = 1, 2, .., (N/2 - 1)$. With this normalization, the integrated periodogram gives the fractional variance of the time series [99] and $P(f)$ is in units of (rms/mean)^2 Hz^{-1}. The periodogram is binned in the log-log space to enable its probability density function to tend to Gaussian and to render its variance a constant [102].

The power law model of the periodogram is given by

$$I(f_j) = A f_j^{-\alpha}, \tag{3.2}$$

where α is the red-noise slope, often found in the range of -1 and -2.5 in the periodograms of AGN. This model fits optical/ultra-violet and X-ray data reasonably well and could represent broadband variability across a wide range of Fourier frequencies due to collective and random processes on the disk or jet.

The broken power law model is given by

$$\begin{aligned} I(f_j) &= A(f_j/f_{Brk})^{-\alpha_{hi}}, f_j > f_{Brk} \\ &= A(f_j/f_{Brk})^{-\alpha_{low}}, f_j < f_{Brk} \end{aligned} \tag{3.3}$$

where f_{Brk} is the break frequency, α_{hi} is the slope of the high frequency region and α_{low} is the slope of the low frequency region. This model is motivated from its application to the low state hard X-ray emission based power spectrum from the black hole X-ray binary Cyg X-1 which indicates a flattening of the power spectrum at low frequencies [115]. In this state, the emission is dominated

by physical processes in a jet as there is a correlation between the radio and X-ray intensities [116].

The bending power law or knee model is given by

$$I(f_j) = A(1 + (f_j/f_{Knee})^2)^{-\alpha/2}, \tag{3.4}$$

where f_{Knee} is the knee frequency and α is the slope in the high frequency region above the knee frequency. This model is used when a sharp break in the power spectrum is not expected and is applied to similar data as the broken power law model.

The power law with Lorentzian quasi-periodic oscillation (QPO) model is given by

$$I(f_j) = A f_j^{-\alpha} + \frac{R^2 Q f_0^2/\pi}{f_0^2 + Q^2(f_j - f_0)^2} \tag{3.5}$$

where α in the first term is the red-noise slope and the second term is a Lorentzian function with amplitude R, central frequency f_0 and quality factor Q defined as $f_0/\Delta f$ where Δf is the frequency spread in the bin hosting the central frequency. This model is motivated from the QPOs observed in galactic black holes [117, 118]. The fit parameters can be used as inputs to disk and jet based theoretical models of quasi-periodicity from orbital signatures or from plasma processes.

3.2.1 Fit procedure, model selection and significance testing

The periodogram of the evenly sampled light curve is first evaluated. Binning is carried out in the log-log space in order to reduce the scatter of the ordinates. The region dominated by white noise (flat portion at higher frequencies) and that dominated by red noise (approximate power law at lower frequencies) are identified. Then, parametric fit models are applied to only the red noise portion. For the power law model, the normalization is first fixed using a linear fit to the red noise portion. Then, slopes α of the power law portion in the red noise region ranging between -1.00 and -2.50 in steps of 0.01 are used to generate a set of test models. For the bending power law model, the normalization used is the mean of the red noise portion. A range of bend frequencies are generated in an evenly sampled grid varying between the lowest frequency and highest frequency in the red noise portion. Half the difference between the first set of consecutive frequencies representing the central frequency in the periodogram bins is used as the step size to generate the test bending frequencies. One can use smaller step sizes if required to get a more finely refined grid. The slopes α representing the power law portion in the red noise region ranging between -1.00 and -3.00 in steps of 0.01 are used along with the bending frequencies to generate a two dimensional grid of test models. For the broken power law model, the normalization used is the mean of the red noise portion. A range of break frequencies are generated in an evenly sampled grid varying between the lowest frequency and highest frequency in the red noise portion. One sixth the difference between the first set of consecutive frequencies representing the central frequency in the periodogram bins is used as the step size to generate the test break frequencies to get a finely sampled grid. Slopes $\alpha_{\rm Low}$ representing the power law portion in the frequencies lower than (to the right of) the break frequency ranging between -0.50 and -1.00 in steps of 0.01 and $\alpha_{\rm Hi}$ representing the power law

portion in the frequencies higher than (to the left of) the break frequency ranging between -1.00 and -2.50 in steps of 0.01 are then generated. The slopes along with the break frequencies are used to generate a three dimensional grid of test models.

The likelihood and log-likelihood functions are defined to be

$$L(\theta_k) = \prod_{j=1}^{(n-1)} \frac{1}{I(f_j, \theta_k)} e^{-P(f_j)/I(f_j,\theta_k)}, \tag{3.6}$$

$$S(\theta_k) = 2\sum_{j=1}^{n-1} (\ln(I(f_j, \theta_k)) + P(f_j)/I(f_j, \theta_k)), \tag{3.7}$$

where $L(\theta_k)$ is the likelihood function, $I(f_j, \theta_k)$ are parametric models, θ_k are the parameters of $I(f_j, \theta_k)$ to be estimated and $P(f_j)$ is the periodogram of data. Determining θ_k which minimize S yields the maximum likelihood values. Confidence limits are determined in a similar manner as that described in [119] for the $\Delta\chi^2$ method.

The log-likelihood S is determined for a large number of combinations spanning the test parameter space θ_k for a given model. The minimum log-likelihood value $S_{\min}$ is determined. The parameter combination yielding this minimum is unique and can be easily identified. These parameters can be used to construct the best fit model. Now, a space of ΔS values is constructed using $\Delta S = S_i - S_{\min}$ where the S_i corresponds to each unique combination of the parameters θ_k. The differences, ΔS are approximately χ^2_k distributed with the degrees of freedom k corresponding to the number of parameters in the model. For example, a power law model with a fixed normalization has only the slope α as a parameter. Hence, in this case, $k = 1$. Confidence intervals can then be set based on the cumulative distribution function of the χ^2_k distribution. One can determine the 1 σ or 2 σ confidence intervals. These would correspond to a given value of ΔS. Thus, the ΔS determined from the parameter combinations within a set confidence interval are grouped. The parameter ranges that they span can thus be determined using which one can specify the confidence intervals of all parameters θ_k used in a given model. This procedure is repeated for all parametric models. In each case, the best fit model, best fit parameter values and the confidence interval of each of those parameters is determined.

Model selection is carried out using the Akaike information criteria (AIC) and the relative likelihood (RL). The AIC is a measure of the information lost when a model is fit to the data. The model with least information loss (least AIC) is assumed to be the null model and the tentative best fit. The likelihood of other models describing the data as well as the null is determined using the likelihood ratio and the relative likelihood e.g. [114]. The AIC, likelihood ratio and the relative

likelihood are defined by

$$\begin{aligned} AIC &= S(\theta_k) + 2p_k, \\ \Delta_i &= AIC_{\min(\text{model i})} - AIC_{\min(\text{null})}, \\ L(\text{model i}|\text{data}) &= e^{-\Delta_i/2}, \text{and} \\ RL &= 1/L(\text{model i}|\text{data}), \end{aligned} \tag{3.8}$$

where p_k is a penalty term and is the number of parameters θ_k used in the model, $L(\text{model i}|\text{data})$ is the likelihood of model i given the data, RL is the likelihood ratio of model i relative to that of the null model. L and RL are determined for each competing model. Models with $\Delta_i \leq 2$ can be considered close to the best fit, those with $4 \leq \Delta_i \leq 7$ are considerably less supported and those with $\Delta_i > 10$ and $RL > 150$ cannot be supported [114]. For large RL, the null thus remains the best fit model. When the PSD is subtracted from the periodogram, it would consist ideally of only χ^2_2 distributed noise whose light curve ordinates are normally distributed e.g. [16]. The residue from the best fit to the data is tested against the χ^2_2 distribution using a goodness of fit test such as the Kolmogorov-Smirnov test. Significance levels such as 99% based on the cumulative distribution function of the χ^2_2 distribution can be used to reveal a statistically significant QPO.

3.2.2 Application, results and inferences

The procedure of constructing the periodogram, applying fit models, model selection and analytic significance testing is applied to the XMM X-ray light curve (0.3 keV - 10 keV) of REJ 1034+396, the periodogram of which revealed a QPO of $\sim$ 3733 s [55]. We wish to illustrate the usefulness of our method in the identification of the QPO component. The periodogram with 296 data bins is constructed and fit models are applied to it (Fig. 3.1). The power law with QPO model serves as the best fit model with an AIC = 149.8 and a significance of the QPO $>$ 99.94 %. The other results are presented in Table 3.1.

Parameter estimation with MLE and model selection with AIC is computationally efficient, minimizing the dependence on more intensive procedures based on Monte-Carlo simulations [115]. Any other parametric model can be easily incorporated into this procedure. If a statistically significant QPO is detected, a lower limit to the black hole mass and constraints on its spin can be placed assuming that the QPO is from an orbital signature. Phenomenological models considering the imprints of general relativistic effects and structure of the emitting region on the outward bound emission can be used to simulate PSDs with varying physical parameters and are carried out in Chapters 6 & 7.

Fit model	Properties	Results
Power law	(AIC, RL)	(170.1, 25.3 $\times$ 10^3)
Fit parameters	Power law slope (α)	(-1.33 $\pm$ 0.013)
	Significance (%)	>99.99
Broken power law	(AIC, RL)	(172.1, 68.1 $\times$ 10^3)
Fit parameters	Break frequency f_{Brk} (Hz)	0.00032 $\pm$ 0.000074
	High frequency region slope α_{hi}	-1.6 $\pm$ 0.42
	Low frequency region slope α_{low}	-1 $\pm$ 0.33
	Significance (%)	>99.99
Bending power law	(AIC, RL)	(198.4, 3.5 $\times$ 10^{10})
Fit parameters	Knee frequency f_{Knee} (Hz)	0.00084 $\pm$ 0.00018
	High frequency region slope α	-3.9 $\pm$ 0.74
	Significance (%)	>99.99
Power law & QPO	(AIC, RL)	(149.8, 1)
Fit parameters	Central frequency f_0 (Hz)	0.000269
	Amplitude R	0.05 $\pm$ 0.014
	Quality factor Q	32 $\pm$ 6.5
	Significance (%)	>99.94

Table 3.1: Periodogram analysis with fit models: results

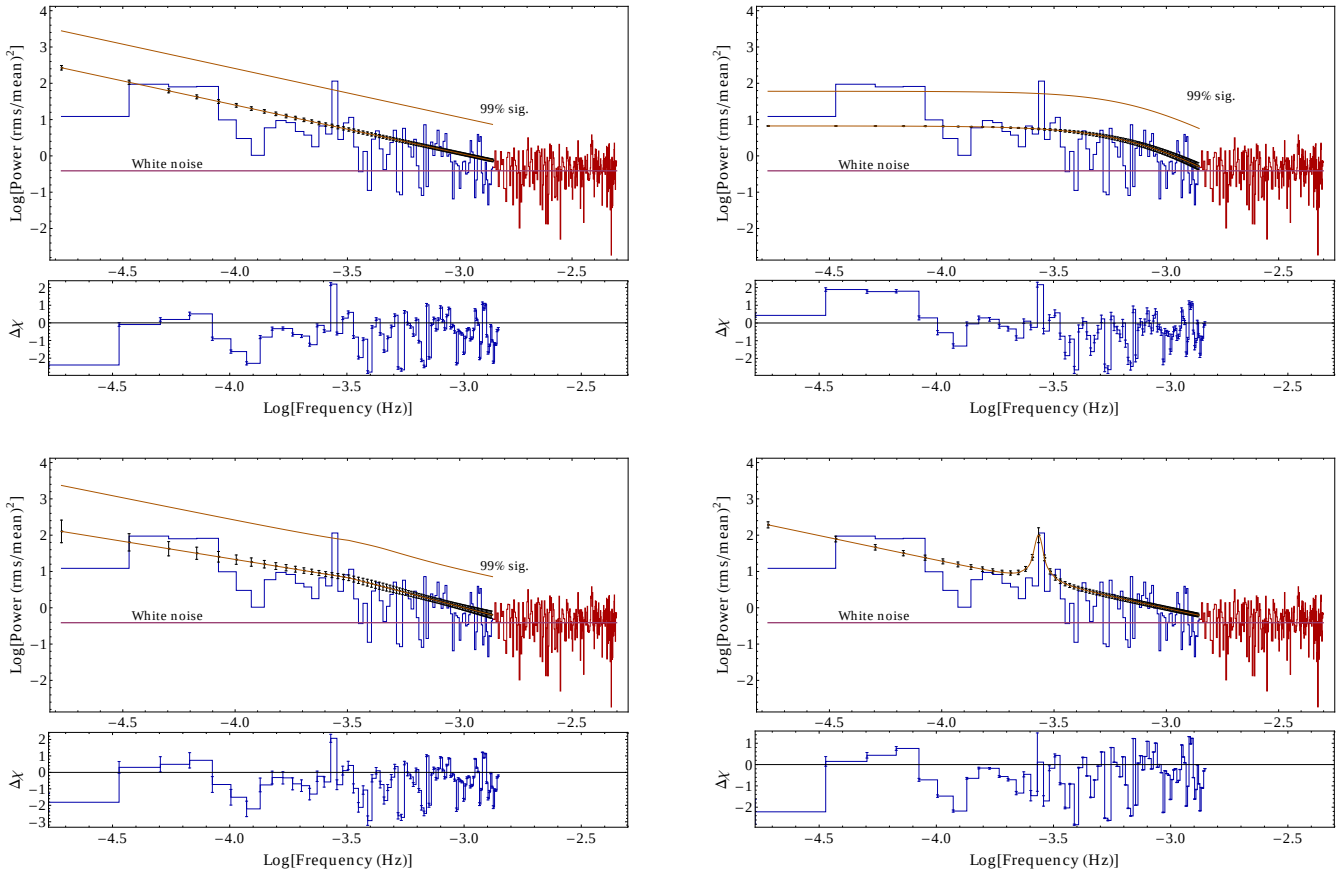

Figure 3.1: The binned periodogram with the white noise level is shown in all the plots. Fit portion is in blue and white noise region is in red. The fit residue $\Delta\chi$ =(data-model)/σ is shown below all plots with error bars. Top left plot: fit with power law model. Top right plot: fit with bending power law or knee model. Bottom left plot: fit with broken power law model. Bottom right plot: fit with power law and Lorentzian QPO model. The fit model in all cases is plotted with error bars. A 99% significance contour is also plotted to distinguish the QPO component.

3.3 Significance testing

Once information is extracted from a light curve by the application of the analysis suite developed in the Chapter 2, it is essential to make use of statistical significance testing in order to test the relevance of the information in aiding physical models. Significance testing includes the comparison of the computed data with the expected probability distribution using which one can rule out spurious features which may appear in these techniques due to the previously described source or measurement based effects. It can also be used to set confidence limits once the statistical distribution of noise is known and constrained. In the analysis of time series relevant to AGN light curves, we are interested in the search for quasi-periodic signals which may be present and buried in systematic and instrumental noise. Outside of the distribution of the computed data, we are interested in any possible statistically significant outliers. Significance testing identifies these outliers which can then be analysed further to extract important inputs to theoretical models.

In the following portion, we use the PSD shape which was determined through a parametric fit to the smoothed periodogram to develop analytic significance tests using the periodogram. This is then extended to the development of significance tests for all the techniques in the analysis suite using a Monte-Carlo simulation procedure.

3.3.1 Analytic significance test

The goodness of fit is quantified by the use of the Kolmogorov-Smirnov test [119] which compares the cumulative distribution function of the scatter $\gamma(f_j)$ in the linear space which is the data/model ratio ($\gamma(f_j) = 2P(f_j)/I(f_j)$) to the cumulative distribution function of the χ^2_2 distribution. A large p-value from this test indicates a good fit. Now, confidence limits can be set in the log-periodogram space in order to determine outliers in the periodogram which are the periodic variations that we are interested in. The area under the tail of the probability density function of the χ^2_2 distribution (which is equivalent to a gamma density $\Gamma(1, 1/2) = \exp(-x/2)/2)$ gives the probability ϵ that the power deviates from the mean at a given frequency and is measured in units of standard deviation given by γ_ϵ. For K number of trial frequencies used to construct the best fit model, we can specify a $(1-\epsilon)$ 100 percent confidence limit on $\gamma(f_j)$ [103] by means of

$$\gamma_\epsilon = -2\ln[1-(1-\epsilon)^{\frac{1}{K}}]. \tag{3.9}$$

After the specification of an ϵ such as 95 % or 99.99 %, γ_ϵ is calculated, and the quantity, $\log(\gamma_\epsilon/2)$ is added to the expression for $\log(I(f_j))$. This new $\log(I(f_j))$ ensures that only peaks in the data periodogram above a certain specified level of confidence, $1-\epsilon$ are really present corresponding to the periodicities in the data.

As an example of the above developed analytic significance test, we now illustrate an application to a periodogram which indicates a red noise power law portion. In AGN light curves, the background power fluctuations or noise is coloured, i.e. the periodogram is not flat as in the case of Gaussian distributed noise but has a finite slope α which suggests that the periodogram

$P(f_j) \propto f_j^{-\alpha}$. If we now assume that the underlying $I(f_j)$ can be described by a power law model,

$$I(f_j) = C f_j^{-\alpha} \tag{3.10}$$

expressed in the logarithm space as

$$\log(I(f_j)) = \log(C) - \alpha \log(f_j) \tag{3.11}$$

The logarithm of the periodogram estimate $P(f_j)$ is then given by

$$\log(P(f_j)) = \log(I(f_j)) + \log(\chi_2^2/2) = \log(C) - \alpha \log(f_j) + \log(\chi_2^2/2) \tag{3.12}$$

Then, the expectation value of the periodogram is given by,

$$< \log(P(f_j)) >= \log(C) - \alpha \log(f_j) - 0.25068 \tag{3.13}$$

Thus, the data log-periodogram is fit with a power law model in the log space and the parameters of the fit, $\log(C)$ and α are determined for the best fitting region.

3.4 Monte-Carlo (MC) simulations based significance testing

The procedure adopted in the previous section can be summarized as follows: fit the red noise dominated region of the periodogram, $P(f_j)$ with the parametric models (power law, power law with Lorentzian QPO, knee, break). Use the Akaike information criteria and relative likelihood to determine the best fit model and hence the best fit parameters and their error bars.

The PSD shape obtained using the above procedure does not account for the biases introduced by the light curve properties which include effects due to aliasing, red noise leakage and that due to the re-binning and interpolation (for un-evenly sampled light curves). We make use of a modified version of the MC simulations based procedure, the power spectrum response (PSRESP) technique described in [115]. The PSRESP technique allows us to to account for the above biases in the simulated PSD shape as well as offers a goodness of fit test which measures the rejection probability of the simulations based distorted model PSD.

If the rejection probability of the simulated model PSD (mean of all the simulated PSDs) is less (< 5 %), it is accepted as the PSD describing the data. The error at each frequency bin is the root mean square value of the simulated PSDs about the mean. The errors on the fit parameters obtained previously for the best fit model are corrected taking into account the simulated model PSD. The analytic significance test described in the previous section can then be carried out with the corrected simulations based model PSD.

In our procedure, the MC simulations are carried out based on the algorithm prescribed in [120] as applied to the best fit PSD model obtained from the AIC and RL procedure described in §3.2.1. A large number (typically $N >1000$) of synthetic periodograms are generated. It must be ensured that the sampling frequencies are sufficiently large so as to produce long duration light curves (at

least 10 times the duration of the original light curve) to account for red noise leakage, also taking into account aliasing effects and those introduced due to re-binning and interpolation [115]. These periodograms are re-binned and truncated to the frequency region relevant to the study of red noise in the original data based periodogram. The mean of the simulated periodograms $\bar{P}_{\rm sim}(f_n)$ and the root mean squared deviation from the mean $\Delta P_{\rm sim}(f_n)$ are determined at each frequency f_n. Then, the particular value of the normalization A which minimizes $\chi^2_{\rm dist.}$ defined by [115]:

$$\chi^2_{\rm dist.} = \sum_{f_n=f_{\rm min}}^{f_{\rm max}} \frac{(A\bar{P}_{\rm sim}(f_n) - P(f_n))^2}{(\Delta P_{\rm sim}(f_n))^2} \tag{3.14}$$

is determined where $f_{\rm max}$ and $f_{\rm min}$ correspond to the bounding frequency bins representing the red noise region. The normalized model then corresponds to the best fit model accounting for effects due to the described biases.

The goodness of fit of the determined best fit model is similar to that described in [115]. From the simulated periodograms, a random sample of 500 is chosen at a time. These periodograms are subjected to the same re-binning and truncation as followed previously. For this sample, the mean periodogram and the root mean squared deviation from the mean are determined at each frequency f_n. The $\chi^2_{\rm dist.,i}$ is determined for a given realization i. This procedure is repeated for i upto 1000, each time with a randomly sampled set of 500 simulated periodograms. The 1000 values of $\chi^2_{\rm dist.,i}$ can thus be used as an empirical distribution function for the statistical characterization of $\chi^2_{\rm dist.}$. The generated $\chi^2_{\rm dist.,i}$ values are sorted in order and the rejection probability of a given model is given by the number of $\chi^2_{\rm dist.,i} < \chi^2_{\rm dist.}$.

The MC simulations were used above to determine an accurate PSD model. These simulations can also be used for significance testing. From the N simulated periodograms, one can sample a specific portion of each periodogram and extract N light curves which have the same mean, standard deviation, time bin size, flux binning and length as the original observed AGN light curve. An important consequence of using the above procedure is that we are now able to describe the statistical distribution of the periodogram at any given frequency f provided this point is in the red noise region, generally at lower frequencies. At each frequency f, there are thus N synthetic periodogram based estimates for the ordinate.

The periodogram is constructed from each of the N simulated light curves and the number of instances, p in which the original data based power exceeds that obtained from the random simulations divided by N is reported as a significance value. This serves as a strong statistical criterion for confirming or ruling out nominal quasi-periods. A typical N of 1000 simulations can yield significance values of up to 0.999 and if a stronger claim of significance level seems possible, N can be increased. The procedure of identifying the number p as described above is then the manner in which the empirical cumulative distribution function at each point is estimated.

The above procedure is also applicable to test the significance of detection of QPOs in other techniques such as the MHAoV, wavelet analysis and the LSP. In some of these, an analytic significance test is not available when the data indicates the presence of red noise. The significance

of a detection can be obtained by feeding the simulated LCs into each of the above techniques. For each technique one determines the number of instances in which the power in the original LSP, MHAoV or global wavelet power spectrum exceeds the power at the same position from the simulated LCs to provide direct significance values. This serves the following purposes:

1. To confirm independently in each technique the presence of a QPO.

2. To obtain a stronger significance as compared to the analytic significance test which is applicable only to the Fourier periodogram.

3. In case the light curve is unevenly sampled, the Fourier periodogram is constructed from a light curve which is re-binned into evenly spaced bins. In case a quasi-periodic feature exists in the light curve, the periodogram amplitude of this feature may be under-estimated. In this case, the light curve in the un-evenly sampled form can be directly analysed using the LSP and MHAoV techniques which offer a better estimate. Thus, the periodogram can be used to determine the correct PSD shape and its properties which can then be used in the MC simulations based significance testing procedure for the LSP and MHAoV techniques to give a stronger estimate of p.

In the next section, we perform a set of numerical experiments which can provide a handle on a statistically desirable quantitative estimate of the significance.

3.5 Numerical experiments

A series of exercises are carried out to compare the efficacy of various time series analysis techniques and to test their robustness in detection and characterization of the properties of data sets regardless of their sampling and the nature of the signal. This is done by a comparison of their power spectrum obtained by the analysis of synthetic test light curves. The toolbox consists of four time series analysis techniques: periodogram, Lomb-Scargle periodogram (LSP), multi-harmonic analysis of variance (MHAoV) and wavelet analysis. This procedure is used to highlight the areas in which they can provide useful information when analysing a light curve.

The types of possible light curves is first described. These have differing properties such as the sampling and the signal properties both including and without noise. Then, the development of the synthetic light curves which will be used for the experiments is described in §3.5.1. The methodology followed in the extraction of the properties from each of these light curves is then presented in §3.5.2. The results are presented in §3.5.3 and are summarized in Tables 3.1 and 3.3. Inferences are then drawn on the effectiveness of each analysis technique and on the Monte-Carlo simulations based significance test.

We take periodic signals with the following differing properties:

- Nature of the signal: sinusoidal, S or non-sinusoidal, $\bar{S}$.

- Sampling of the signal: evenly, E or unevenly sampled, U.

- Life-time of a signal is taken as a fraction f of the observation duration. If t_P is the duration of existence of the periodicity P, the quantity $n_P = (t_P/P)$ indicates the number of cycles that a signal lasts during the observation.

- Number of signals in the light curve, n_S.

- Effects of noise in the test light curves which we denote by r.

3.5.1 Data preparation

A combination of all the above factors will impact the results. Here we aim to study the utility of a particular technique in detecting a periodic signal in the presence of a given combination of the above properties. Hence, we aim to demonstrate the relative importance of each technique for a given signal. The detection of periodicities in all techniques is carried out by determining the power spectrum. The following synthetic light curves are used in the experiments:

Experiments without noise

The following combinations are used to illustrate the utility of each technique:

$S\ E$, $S\ U$, $\bar{S}\ E$, $\bar{S}\ U$ for the combination $n_S = 1$ and $f = 1$.

$S\ E$ for $n_S = 1$ and $f < 1$.

$S\ E$ for $n_s = 2$ and $f = 1$.

$S\ E$ is an evenly sampled ($\Delta t = 1$ s) light curve containing a sinusoidal waveform of period 20 s. The periodicity lasts for a duration of 200 s ($n_P = t_P/P = 10$, $f = 1$).

$S\ U$ is an un-evenly sampled light curve containing a sinusoidal waveform of period 20 s. The periodicity lasts for a duration of 200 s ($n_P = t_P/P = 10$, $f = 1$).

$\bar{S}\ E$ is an evenly sampled ($\Delta t = 1$ s) light curve containing a non-sinusoidal (saw-tooth) waveform of period 20 s. The periodicity lasts for a duration of 200 s ($n_P = t_P/P = 10$, $f = 1$).

$\bar{S}\ U$ is an un-evenly sampled light curve containing a non-sinusoidal (saw-tooth) waveform of period 20 s. The periodicity lasts for a duration of 200 s ($n_P = t_P/P = 10$, $f = 1$).

$S\ E\ n_s = 1$ is an evenly sampled (Δt =1 s) light curve consisting of three sections. The first lasts for a duration of 50 s is populated with standard Gaussian white noise (mean = 0, standard deviation = 1). A sinusoidal waveform of period 20 s which lasts for the next 100 s ($n_P = 5$) follows this section. Another section of standard Gaussian white noise then lasts for the remaining duration of 50 s. The total duration sums up to 200 s ($f = 0.5$).

S, E, $n_S = 2$ is an evenly sampled (Δt =1 s) light curve consisting of two sections. A sinusoidal waveform of 50 s periodicity which lasts for a duration of 200 s ($n_{P1} = 4$) is followed by another sinusoidal waveform of 100 s periodicity which lasts for the next 300 s ($n_{P2} = 3$), the total duration summing up to 500 s ($f = 0.4$ for the 50 s periodicity and $f = 0.6$ for the 100 s periodicity).

Experiments with noise

The following combinations are generated to compare the detection efficacy of each technique, to demonstrate the utility of the Monte-Carlo simulations in significance testing and in order to place a statistically sound significance limit which can be used to identify a strong signal. They include:

$S\ E\ r$, $S\ U\ r$, $\bar{S}\ E\ r$, $\bar{S}\ U\ r$ for the combination $n_S = 1$ and $f = 1$.

In the above light curves, a red noise power spectrum (slope = -2) is generated using the algorithm prescribed in [120]. This is then inverse Fourier transformed to obtain a light curve with length equal to the original light curve containing the signal. This is added to the light curve containing the signal.

$S\ E\ r$ is an evenly sampled ($\Delta t = 1$ s) light curve containing a sinusoidal waveform of period 20 s with red noise. The periodicity lasts for a duration of 200 s ($n_P = t_P/P = 10,\ f = 1$).

$S\ U\ r$ is an un-evenly sampled light curve containing a sinusoidal waveform of period 20 s with red noise. The periodicity lasts for a duration of 200 s ($n_P = t_P/P = 10,\ f = 1$).

$\bar{S}\ E\ r$ is an evenly sampled ($\Delta t = 1$ s) light curve containing a non-sinusoidal (saw-tooth) waveform of period 20 s with red noise. The periodicity lasts for a duration of 200 s ($n_P = t_P/P = 10,\ f = 1$).

$\bar{S}\ U\ r$ is an un-evenly sampled light curve containing a non-sinusoidal (saw-tooth) waveform of period 20 s with red noise. The periodicity lasts for a duration of 200 s ($n_P = t_P/P = 10,\ f = 1$).

3.5.2 Methodology

The methodology of the experiments without noise is as follows:

1. The synthetic light curve with the desired combination of the properties described earlier is generated.

2. If the light curve is evenly sampled, the periodogram, LSP, MHAoV and the wavelet analysis based power spectra are determined.

3. For uneven sampling, a certain number of points are removed from the light curve before its analysis. The evenly sampled light curve is first constructed (200 points). 80 randomly chosen points are then removed such that the final unevenly sampled light curve has 120 points.

4. For this unevenly sampled light curve, the LSP and MHAoV based power spectra are first determined. The light curve is then made evenly sampled by re-binning the points in evenly spaced bins and determining the mean of each bin. For empty bins, a linear interpolation considering the nearest neighbours is used to determine an estimate. The periodogram and wavelet analysis are applied to this re-binned, evenly sampled light curve to obtain their corresponding power spectra.

5. The power spectrum of each technique is normalized by the total power under it. This aids in the comparison between the power amplitudes indicated by each technique.

The methodology of the experiments including noise is as follows:

1. Noise with a χ^2_2 distribution is added to each frequency bin of a synthetic periodogram with a slope $\alpha = -2$ (red noise). This is then inverse Fourier transformed to obtain a light curve which contains both the signal and red noise. This particular noise model is adopted for this exercise as it is often observed in the optical/UV and X-ray light curves from AGN. It hence mimics an actual signal.

2. For uneven sampling, a certain number of points are removed from the light curve before its analysis. The evenly sampled light curve is first constructed (200 points). 100 randomly chosen points are then removed such that the final unevenly sampled light curve has 100 points.

3. For this unevenly sampled light curve, the LSP and MHAoV based power spectra are first determined. The light curve is then made evenly sampled by re-binning the points in evenly spaced bins and determining the mean of each bin. For empty bins, a linear interpolation considering the nearest neighbours is used to determine an estimate. The periodogram and wavelet analysis are applied to this re-binned, evenly sampled light curve to obtain their corresponding power spectra.

4. The power spectrum of each technique is normalized by the total power under it. This aids in the comparison between the power amplitudes indicated by each technique.

5. Monte-Carlo (MC) simulations are carried out by generating a set of 1000 random light curves using the algorithm prescribed by [120] accounting for red noise leakage by generating first red-noise light curves which are 20 times the length of the original light curve and then re-sampling them to match the bin sizes and times of the original light curve. The bias at each frequency is also estimated for each synthetic periodogram and is added to it before a final synthetic light curve is generated.

6. These simulated light curves are analysed using all techniques to determine the significance p.

7. A criterion for identifying a true detection is $p > 0.99$ from the MC simulations for the periodogram, LSP and MHAoV which are the main detection techniques. If P_1 is the amplitude of the power at the indicated periodicity, μ and σ are the mean and standard deviation of the noise obtained from Monte-Carlo simulations, we define $N_\sigma = (P_1 - \mu)/\sigma$.

3.5.3 Results

Here, we discuss the results of the experiments carried out with the various combinations of synthetic light curves. Brief inferences are drawn from the test results. All results are summarized in Tables 3.3 and 3.4.

For the experiments without noise, the following are the results:

Experiment 1 ($S\ E\ n_S = 1$): The peak at a frequency of 0.05 Hz (20 s) is well detected by all techniques. The normalized periodogram, LSP and MHAoV yield the same amplitude of 1.00. The GWPS power amplitude is lower at 0.33. The LSP and periodogram amplitudes are equal as the LSP reduces to the periodogram when the light curve is evenly sampled. The GWPS is lower than the others as sampling with wavelets can be thought of as smoothing the raw periodogram with a window function. The light curve and the power spectra are plotted in Fig. 3.2. The wavelet power spectrum (bottom row of Fig. 3.2) is used to infer that the periodicity of 20 s lasts for the entire observation duration.

Experiment 2 ($\bar{S}\ E\ n_S = 1$): The peak at a frequency of 0.10 Hz (10 s) is well detected by all techniques. The normalized periodogram and LSP yield the same amplitude of 0.65. The MHAoV yields the highest amplitude of 0.71 which is ~ 8 % better than the periodogram and LSP estimates indicating that it is well suited for the analysis of non-sinusoidal light curves. The GWPS yields the lowest amplitude of 0.11. The light curve and the power spectra are plotted in Fig. 3.3. The wavelet power spectrum (left plot of the bottom row of Fig. 3.3) is used to infer that the periodicity of 20 s lasts for the entire observation duration.

Experiment 3 ($S\ U\ n_S = 1$): The LSP and MHAoV analysis of the unevenly sampled light curve detect the signal frequency of 0.05 Hz (20 s) and yield normalized power amplitudes of 0.63 and 0.29 respectively, shown in the right plot of the top row of Fig. 3.4. The periodogram and wavelet analysis of the evenly sampled binned light curve yields normalized power amplitudes of 0.91 and 0.50 respectively, shown in the right plot of the bottom row of Fig. 3.4. The wavelet power spectrum (left plot of the bottom row of Fig. 3.4) is used to infer that the periodicity of 20 s lasts for the entire observation duration.

Experiment 4 ($\bar{S}\ U\ n_S = 1$): The LSP and MHAoV analysis of the unevenly sampled light curve detect the signal frequency of 0.10 Hz (10 s) and yield normalized power amplitudes of 0.45 and 0.51 respectively, shown in the right plot of the top row of Fig. 3.5. The periodogram and wavelet analysis of the evenly sampled binned light curve yields normalized power amplitudes of 0.21 and 0.13 respectively, shown in the right plot of the bottom row of Fig. 3.5. The MHAoV amplitude is once again the highest, $\sim$ 12 % higher than the LSP and $\sim$ 59% higher than the periodogram, once again indicating that it is a good estimator of the periodic component when the signal is unevenly sampled. The wavelet power spectrum (left plot of the bottom row of Fig. 3.5) is used to infer that the periodicity of 20 s lasts for the entire observation duration.

Experiment 5 ($S\ E\ n_S = 1\ f = 0.5$): The peak at a frequency of 0.05 Hz (20 s) is detected by all techniques. The normalized periodogram and LSP yield the same amplitude of 0.17. The MHAoV yields the highest amplitude of 0.21 while the GWPS yields the lowest amplitude of 0.10. The light curve and the power spectra are plotted in Fig. 3.6. From the wavelet power spectrum (left plot of the bottom row of Fig. 3.6), one can infer that the periodicity of 20 s lasts only for the duration between 50 s and 150 s during the observation.

Experiment 6 ($S\ E\ n_S = 2$): The peaks at the frequencies 0.05 Hz ($20\ s^1$) and 0.02 Hz ($50\ s^2$) are detected by all techniques. The normalized periodogram and LSP yield the same amplitudes of 0.25^1 and 0.25^2 respectively. The MHAoV yields amplitudes of 0.26^1 and 0.26^2 while the GWPS

yields amplitudes of 0.13[1] and 0.21[2] respectively. The light curve and the power spectra are plotted in Fig. 3.7. From the wavelet power spectrum (left plot of the bottom row of Fig. 3.7), one can infer that the 20 s periodicity lasts for the duration between the start and 100 s while the 50 s periodicity lasts between 101 s and 200 s during the observation.

For the experiments with red noise added to the light curve (slope of red noise power spectrum = -2), the following are the results:

Experiment 7 ($S\ E\ r\ n_S = 1$): The peak at a frequency of 0.05 Hz (20 s) is well detected by all techniques. The normalized periodogram and LSP yield the same amplitude of 0.52. The MHAoV power amplitude is the highest at 0.81 while the GWPS power amplitude is lower at 0.16. The MHAoV power is $\sim$ 36 % higher than the periodogram and LSP estimates indicating that it is well suited for detection of signals buried in noise. The light curve and the power spectra are plotted in Fig. 3.8. The wavelet power spectrum (bottom row of Fig. 3.8) is used to infer that the periodicity of 20 s lasts for the entire observation duration which is stronger after 80 s during the observation.

Experiment 8 ($\bar{S}\ E\ r\ n_S = 1$): The peak at a frequency of 0.10 Hz (10 s) is detected by all techniques. The normalized periodogram and LSP yield the same amplitude of 0.30. The MHAoV yields a higher amplitude of 0.43 and the GWPS yields the lowest amplitude of 0.05. The light curve and the power spectra are plotted in Fig. 3.9. The 10 s periodic feature is weakly detected near the beginning and towards the end of the observation duration by the wavelet power spectrum (left plot of the bottom row of Fig. 3.9) is used to infer that the periodicity of 10 s lasts for the entire observation duration.

Experiment 9 ($S\ U\ r\ n_S = 1$): The LSP and MHAoV analysis of the unevenly sampled light curve detect the frequency of 0.05 Hz (20 s) yielding normalized power amplitudes of 0.38 and 0.96 respectively, shown in the right plot of the top row of Fig. 3.10. The periodogram and wavelet analysis of the evenly sampled binned light curve yields normalized power amplitudes of 0.52 and 0.09 respectively, shown in the right plot of the bottom row of Fig. 3.10. The MHAoV power is $\sim$ 46 % greater than the periodogram estimate and is $\sim$ 60 % greater than the LSP estimate indicating that it is well suited for the analysis of un-evenly sampled light curves with noise. The wavelet power spectrum (left plot of the bottom row of Fig. 3.10) is used to infer that the periodicity of 20 s lasts for the entire observation duration.

Experiment 10 ($\bar{S}\ U\ r\ n_S = 1$): The LSP and MHAoV analysis of the unevenly sampled light curve detect the frequency of 0.10 Hz (10 s) yielding normalized power amplitudes of 0.23 and 0.22 respectively, shown in the right plot of the top row of Fig. 3.11. The periodogram and wavelet analysis of the evenly sampled binned light curve ($\Delta t = 5$ s) yields normalized power amplitudes of 0.26 and 0.03 respectively, shown in the right plot of the bottom row of Fig. 3.11. The signal is weak and is not detected with wavelet power spectrum (left plot of the bottom row of Fig. 3.11). Though, the GWPS in the right plot of the top row of Fig. 3.11 indicates that there is a detection with a small bump at the 0.10 Hz frequency.

3.5.4 Inferences and discussion

All techniques are able to detect the signal in the synthesized light curves fairly accurately in a majority of cases with and without noise added to the light curve.

The periodogram and LSP are well suited in the detection of the periodic signal in evenly sampled sinusoidal light curves as inferred from the experiments $S\ E$ (experiment 1), $S\ E\ n_S = 1\ f = 0.5$ (experiment 5) and $S\ E\ r\ n_S = 1$ (experiment 7) where the detection amplitude is reasonably high in order to clearly identify the periodicity.

The LSP is also well suited in the detection of the periodic signal in un-evenly sampled sinusoidal light curves as inferred from the experiment $S\ U$ (experiment 3) where it yields an amplitude of 0.63, higher than the MHAoV.

The MHAoV power spectrum amplitude is fairly high as inferred from the experiments $\bar{S}\ E$ (experiment 2), $\bar{S}\ U$ (experiment 4), $S\ E\ r\ n_S = 1$ (experiment 7), $\bar{S}\ E\ r\ n_S = 1$ (experiment 8) and $S\ U\ r\ n_S = 1$ (experiment 9) where it consistently yields the highest corresponding power amplitudes of 0.71, 0.51, 0.81 and 0.96 respectively. It can thus be inferred that it is well suited for the detection of both sinusoidal as well as non-sinusoidal signals in both even and un-evenly sampled light curves.

The wavelet analysis can be used for reasonable detection amplitudes. The power amplitude estimates of the GWPS are consistently lower than the rest of the techniques as sampling with wavelets is equivalent to the convolution in the Fourier space of the analyzing spectrum with a wavelet window function. This tends to have the effect of reducing noise, though, at the cost of diminishing the estimated true power amplitudes. This is not a serious drawback though as the MC simulations carried out can be used to identify strong features as measured by the significance p of a given frequency. Also, the main utility of this technique comes from the wavelet power spectrum. This can be used for the identification of a periodicity and its duration of existence and hence the number of cycles it lasts for. In case a QPO is present in a real AGN light curve, the power spectrum can also yield information on its evolution.

There is a power loss to other frequencies in all techniques including harmonics of the primary frequency due to spectral leakage effects which can arise due to:

1. the light curve being considered to be truncated as it is of finite length.

2. the light curve being considered to be convolved with a rectangular window of duration equal to that of the light curve.

3. the sampling being carried out at periods different from P.

The power loss is the least in the MHAoV technique in a majority of the experiments.

We demonstrated that the proposed methodology is used to make strong and reliable statistically sound conclusions on detected periodicities, number of cycles and its phase of existence.

These experiments show that the techniques that have been developed as part of the analysis toolbox work in a complementary manner contributing in different ways to the finally available

information which cannot be obtained using any single technique. This is the main objective behind the use of multiple techniques.

The underlying noise is treated in the same manner across all techniques in the MC significance testing. Hence, if multiple techniques indicate a strong p-value, we can conclude that the periodic signal definitely exists. In the experiments, the significance p of certain spurious detections are much smaller compared to 0.99 which is the criteria used to detect the periodicity P.

3.6 Data characterization and search strategy

The following procedures are used in the formulation of a data characterization and search strategy which can be used to extract light curve properties and aid in the detection of a quasi-periodic feature in it through a rigourous statistical procedure:

The identification of a statistically appropriate PSD model from §3.2 followed by MC simulations based constraints on the chosen model through a goodness of fit test as well as significance testing of detected signals as described in §3.4.

The results from the numerical experiments which can be used to gauge the collective strengths of each time series technique in the analysis suite and their mode of application to analyze a variety of light curves with differing properties.

The data characterization and search strategy is as follows:

1. If the light curve is un-evenly sampled, re-bin it into equally spaced bins and perform a linear interpolation over empty bins in order to obtain an evenly sampled light curve with a fixed Δt.

2. Construct the periodogram and fit with an appropriate model (power law, power law with Lorentzian QPO, knee, break) using the Akaike information criteria and relative likelihood to determine the best fit model. If a QPO is detected, determine its analytic significance.

3. Use the MC simulations with the above best fit model parameters to construct the PSD accounting for biases and red noise leakage.

4. MC simulations based significance testing: Use the algorithm prescribed by [120] with the periodogram best fit model parameters and generate a large number (N $>$ 1000) of LCs. These are analyzed using all techniques. The number of instances in which the original power exceeds that obtained from random simulations divided by N is reported as a significance value p.

5. Use wavelet analysis to determine the phases during which the QPO exists, its evolution if any and the number of cycles of existence.

6. Construct the LSP (if applicable: e.g. to unevenly sampled light curves) and MHAoV to confirm the detected QPO.

Technique	Advantages	Significance Testing
Fourier periodogram	Primary detection technique	Analytic & MC sims.
Lomb-Scargle periodogram (LSP)	Applicable to unevenly sampled LCs	MC sims.
Multi-harmonic analysis of variance (MHAoV)	Applicable to unevenly sampled LCs, non-sinusoidal signals	MC sims.
Wavelet analysis	phase of existence of the QPO, duty cycle	MC sims.

Table 3.2: Summary of the applicability of each time series technique. In LSP, MHAoV and wavelet analysis, we are currently working on analytic significance testing.

7. Based on numerical experiments results, we suggest the criteria for detection of a strong feature (quasi-period) to be a significance > 0.99.

A summary of the abilities and drawbacks of each time series analysis technique is given in Table 3.2.

Expt. No. & factors	Technique	Periodicity P (s)	Peak power amplitude
1. $S\ E\ n_S = 1$ Total duration $t_P = 200$ s $n_P = 10$, $f = 1$	Periodogram LSP MHAoV Wavelet	20 20 20 20	1.00 1.00 1.00 0.33
2. $\bar{S}\ E\ n_S = 1$ Total duration $t_P = 200$ s $n_P = 20$, $f = 1$	Periodogram LSP MHAoV Wavelet	10 10 10 10	0.65 0.65 0.71 0.11
3. $S\ U\ n_S = 1$ total duration $t_P = 200$ s, 100 points removed $n_P = 10$, $f = 1$ $\Delta t = 5$ s (for periodogram and wavelet)	Periodogram LSP MHAoV Wavelet	20 20 20 20	0.91 0.63 0.29 0.50
4. $\bar{S}\ U\ n_S = 1$ Total duration $t_P = 200$ s, 100 points removed $n_P = 20$, $f = 1$ $\Delta t = 5$ s (for periodogram and wavelet)	Periodogram LSP MHAoV Wavelet	10 10 10 10	0.21 0.45 0.51 0.13
5. $S\ E\ n_S = 1$ with $f = 0.5$ in segment 2 segment 1 (1 - 50 s) & segment 3 (150 s - 200 s) populated with N(0,1) random noise total duration of 200 s ($n_P = 5$)	Periodogram LSP MHAoV Wavelet	20 20 20 20	0.17 0.17 0.21 0.10
6. $S\ E\ n_S = 2$ total duration of 200 s $f = 0.5$, $n_P = 5$ for 20 s periodicity $f = 0.5$, $n_P = 2$ for 50 s periodicity	Periodogram LSP MHAoV Wavelet	20^1, 50^2 20^1, 50^2 20^1, 50^2 20^1, 50^2	0.25^1, 0.25^2 0.25^1, 0.25^2 0.26^1, 0.26^2 0.13^1, 0.21^2

Table 3.3: Summary of the results from the first six experiments which do not include noise addition to the light curve. [1]results for P_1; [2]results for P_2.

Expt. No. & factors	Technique	Periodicity P (s)	Peak power amplitude	MC sims. sig.
7. $S\ E\ r\ n_S = 1$	Periodogram	20	0.52	> 0.99
Total duration $t_P = 200$ s	LSP	20	0.52	> 0.99
$n_P = 10$, $f = 1$	MHAoV	20	0.81	> 0.99
	Wavelet	20	0.16	> 0.99
8. $\bar{S}\ E\ r\ n_S = 1$	Periodogram	10	0.30	> 0.99
Total duration $t_P = 200$ s	LSP	10	0.30	> 0.99
$n_P = 20$, $f = 1$	MHAoV	10	0.43	> 0.99
	Wavelet	10	0.05	> 0.99
9. $S\ U\ r\ n_S = 1$	Periodogram	20	0.52	> 0.99
total duration $t_P = 200$ s, 100 points removed	LSP	20	0.38	> 0.99
$n_P = 10$, $f = 1$	MHAoV	20	0.96	> 0.99
$\Delta t = 2$ s (for periodogram and wavelet)	Wavelet	20	0.09	> 0.99
10. $\bar{S}\ U\ r\ n_S = 1$	Periodogram	10	0.26	> 0.99
Total duration $t_P = 200$ s, 100 points removed	LSP	10	0.23	> 0.99
$n_P = 20$, $f = 1$	MHAoV	10	0.22	> 0.99
$\Delta t = 2$ s (for periodogram and wavelet)	Wavelet	10	0.03	> 0.99

Table 3.4: Summary of the results from the next four experiments which include red noise which is added to the light curve.

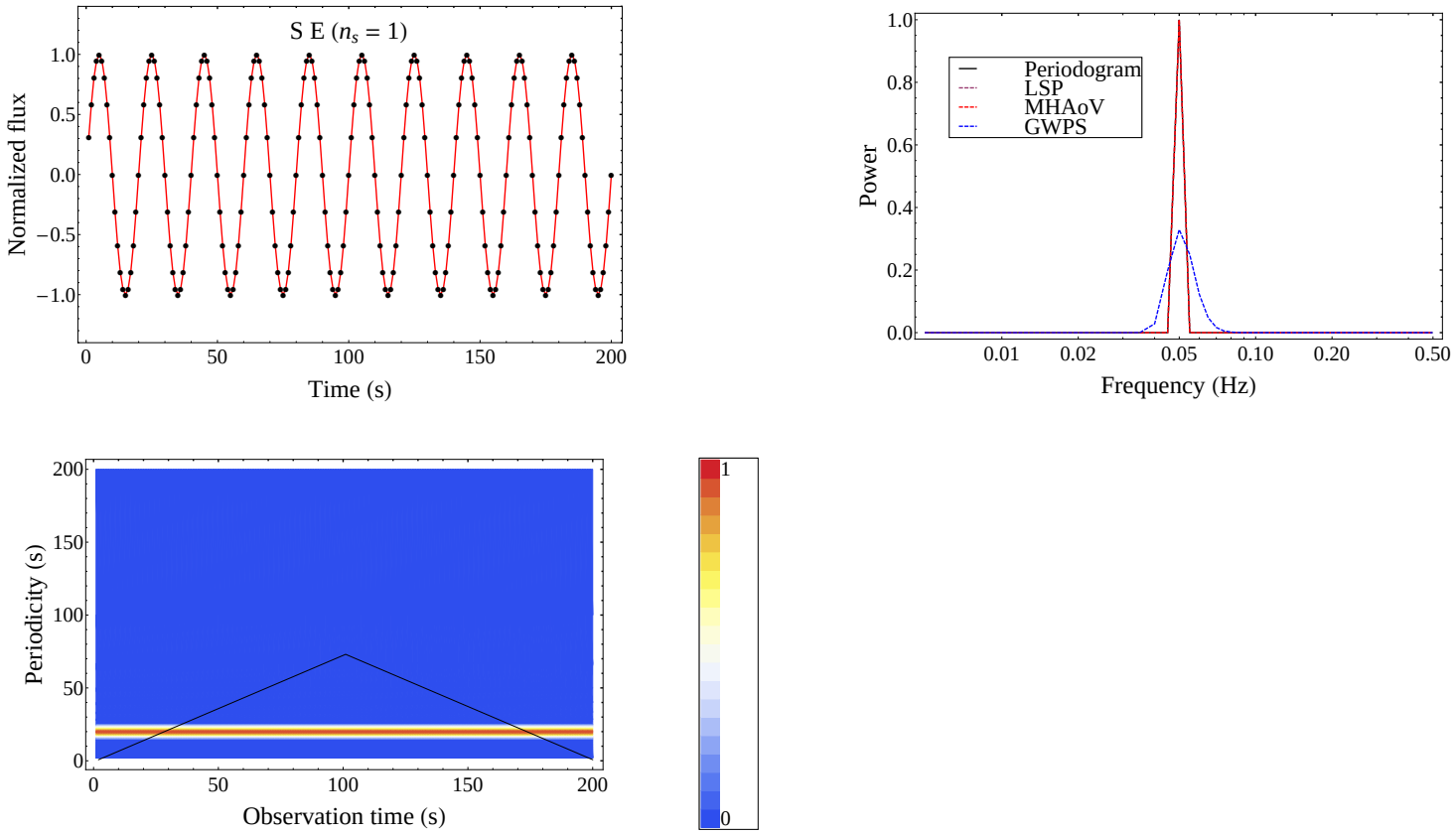

Figure 3.2: Experiment 1: Top row: left panel: evenly sampled sinusoidal light curve; right panel: combined plot showing the normalized power spectra of all techniques. The peak amplitude at a frequency of 0.05 Hz (20 s) is equal for the periodogram, LSP and MHAoV. Bottom row: left panel: contour plot showing the wavelet power spectrum. The periodicity of 20 s lasts throughout the observation duration.

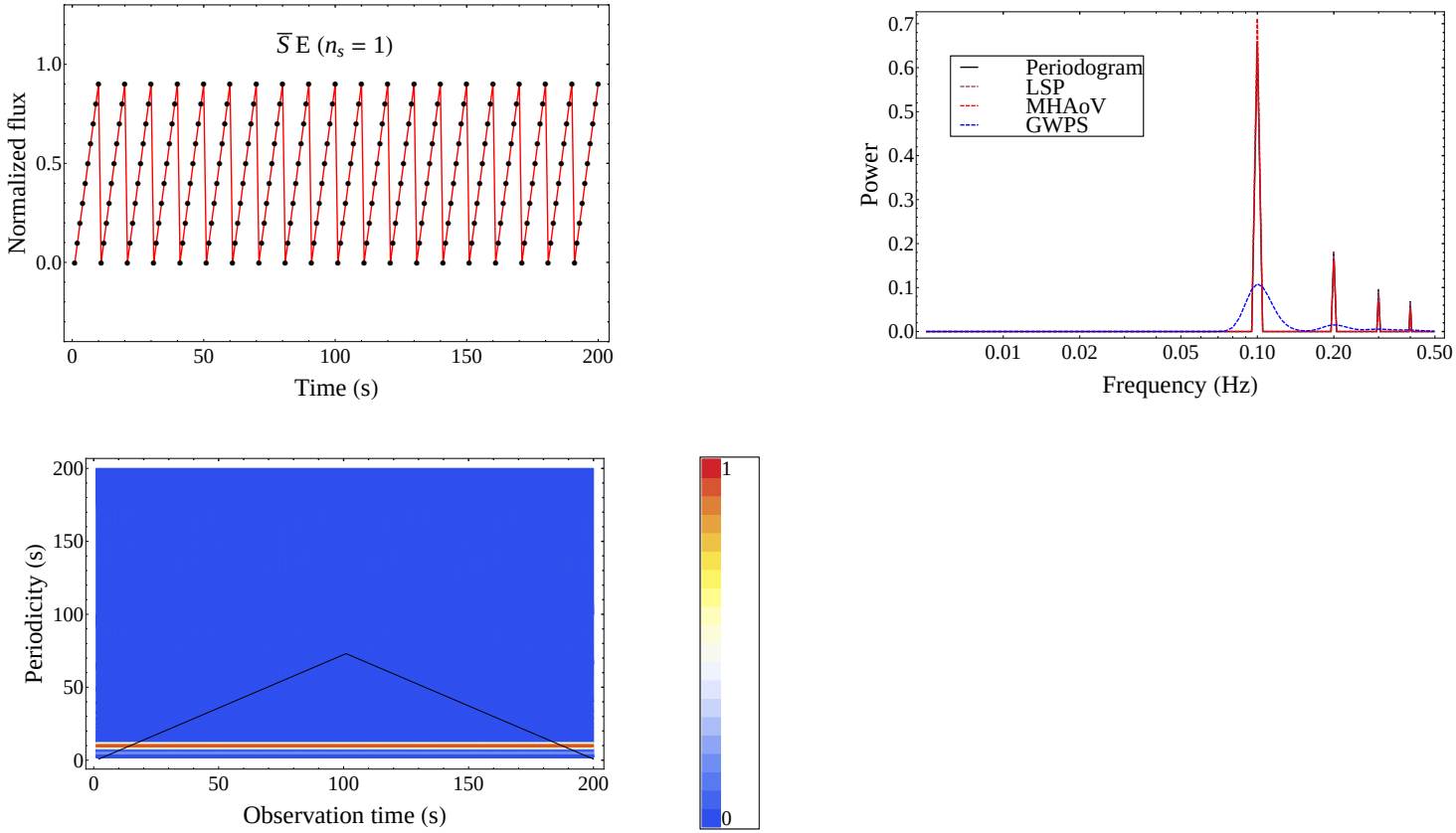

Figure 3.3: Experiment 2: Top row: left panel: evenly sampled saw-tooth light curve; right panel: combined plot showing the normalized power spectra of all techniques. The normalized peak amplitude at a frequency of 0.10 Hz (10 s) is 0.65 for the periodogram and LSP (both are the same for an evenly sampled light curve). The MHAoV shows a higher amplitude at 0.71. Bottom row: left panel: contour plot showing the wavelet power spectrum. The periodicity of 20 s lasts throughout the observation duration.

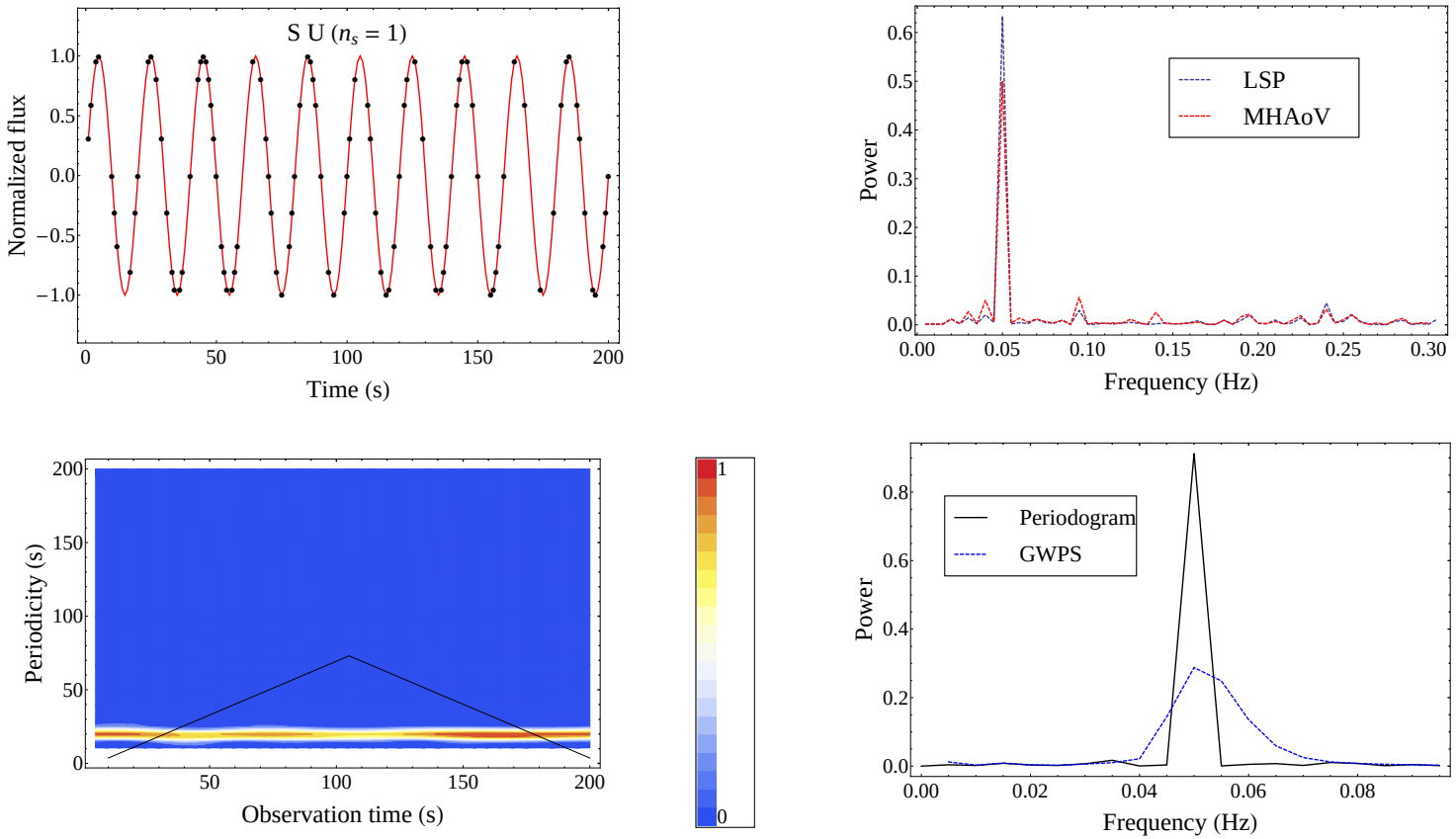

Figure 3.4: Experiment 3: Top row: left panel: un-evenly sampled sinusoidal light curve; right panel: combined plot showing the normalized power spectra of the LSP and MHAoV. The corresponding peak amplitudes at the frequency of 0.05 Hz (20 s) are at 0.63 and 0.29 respectively. Bottom row: left panel: contour plot showing the wavelet power spectrum. The periodicity of 20 s lasts throughout the observation duration; right panel: combined plot showing the normalized periodogram and GWPS. These have been plotted seperately as they are constructed from an evenly sampled light curve.

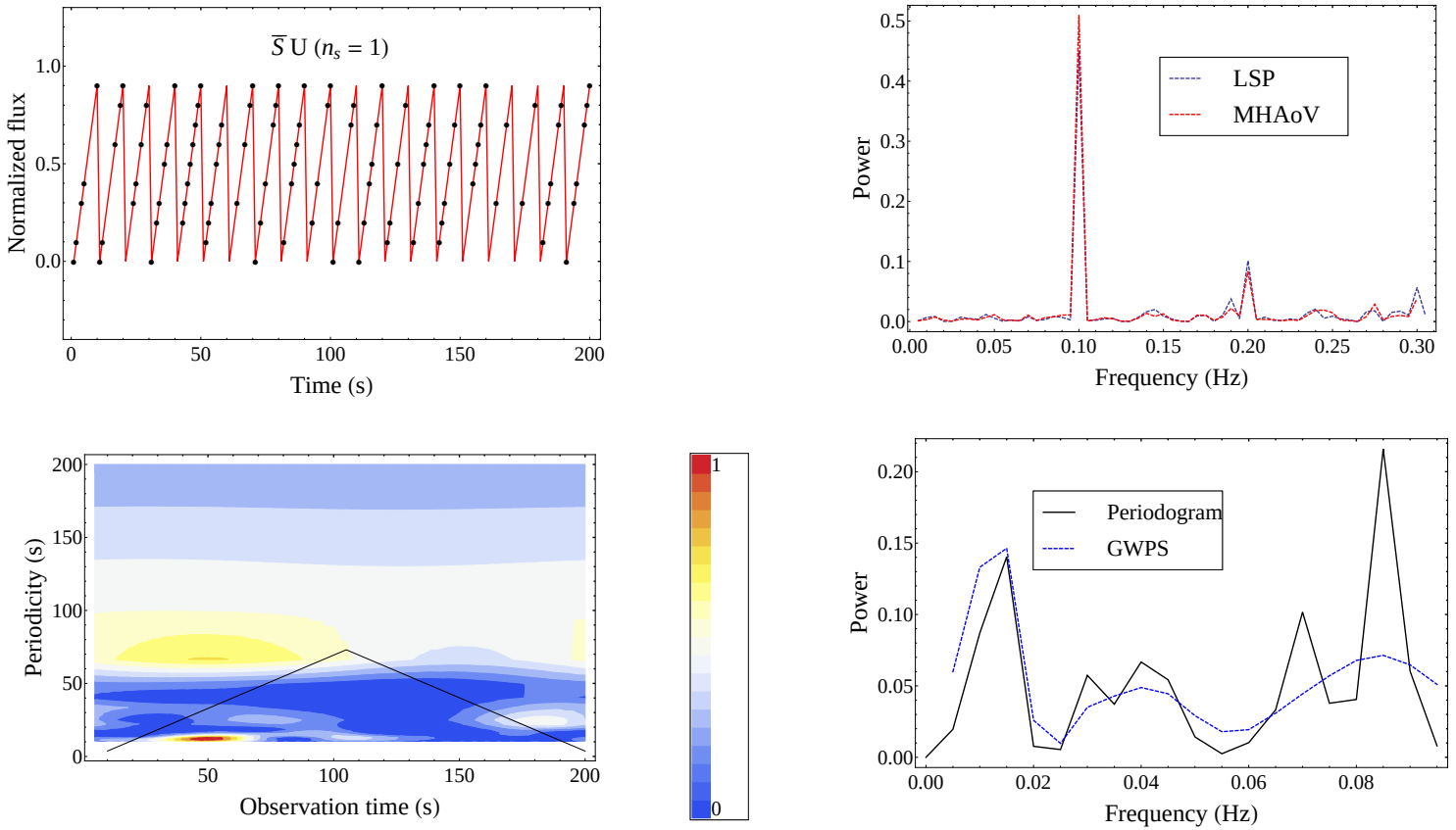

Figure 3.5: Experiment 4: Top row: left panel: un-evenly sampled saw-tooth light curve; right panel: combined plot showing the normalized power spectra of the LSP and MHAoV. The corresponding peak amplitudes at the frequency of 0.10 Hz (10 s) are at 0.45 and 0.51 respectively. Bottom row: left panel: contour plot showing the wavelet power spectrum. The periodicity of 10 s is well detected only between $\sim$ 40 s and $\sim$ 70 s; right panel: combined plot showing the normalized periodogram and GWPS. These have been plotted seperately as they are constructed from an evenly sampled light curve.

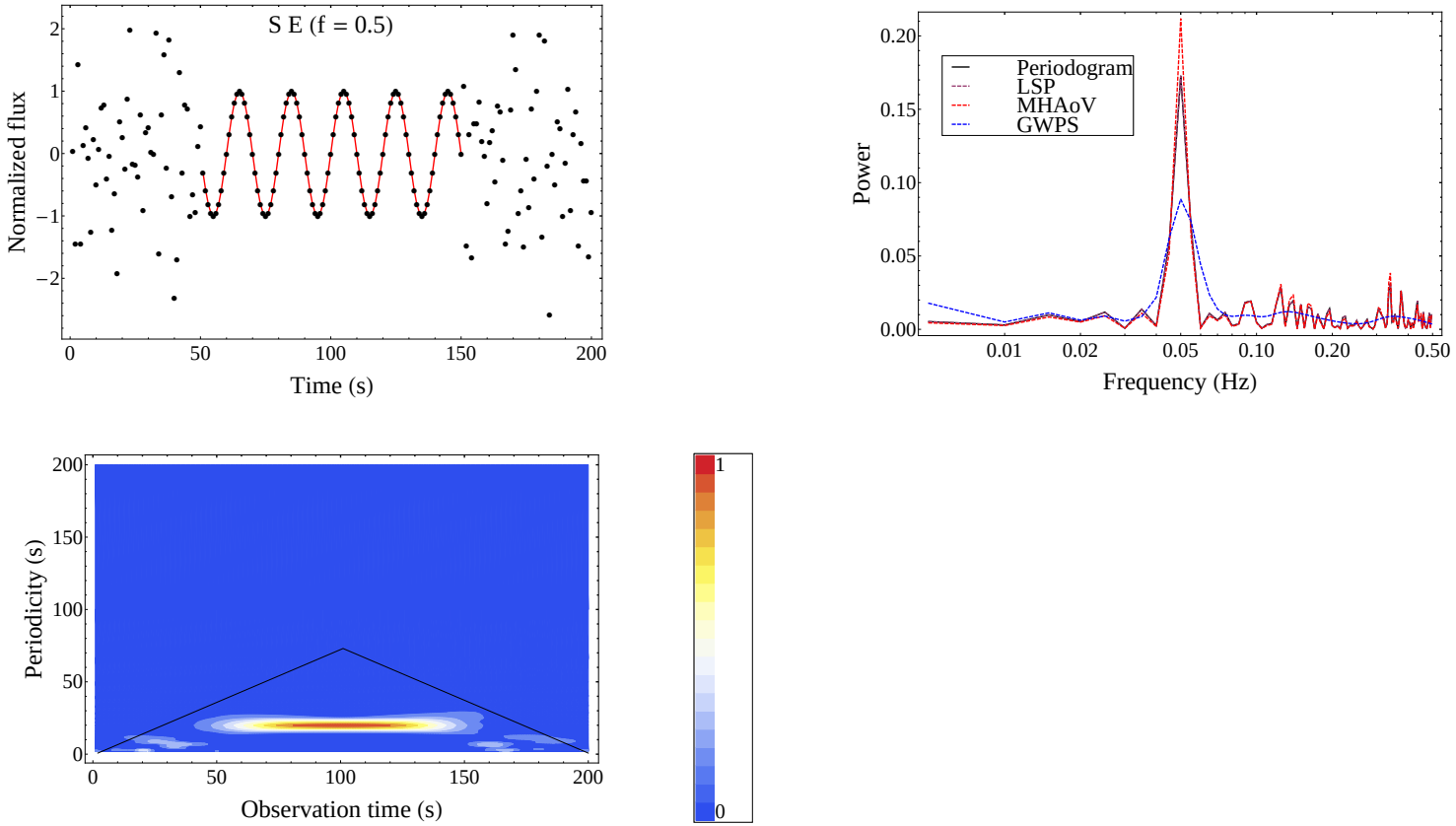

Figure 3.6: Experiment 5: Top row: left panel: evenly sampled sinusoidal light curve sandwiched between two sections of standard Gaussian noise; right panel: combined plot showing the normalized power spectra of all techniques. The frequency of 0.05 Hz (20 s) is well detected by all techniques. Bottom row: left panel: contour plot showing the wavelet power spectrum. The periodicity of 20 s is seen to last within the cone of influence between the periodicities of 50 s and 150 s, exactly following the duration of existence of the sinusoid in the light curve.

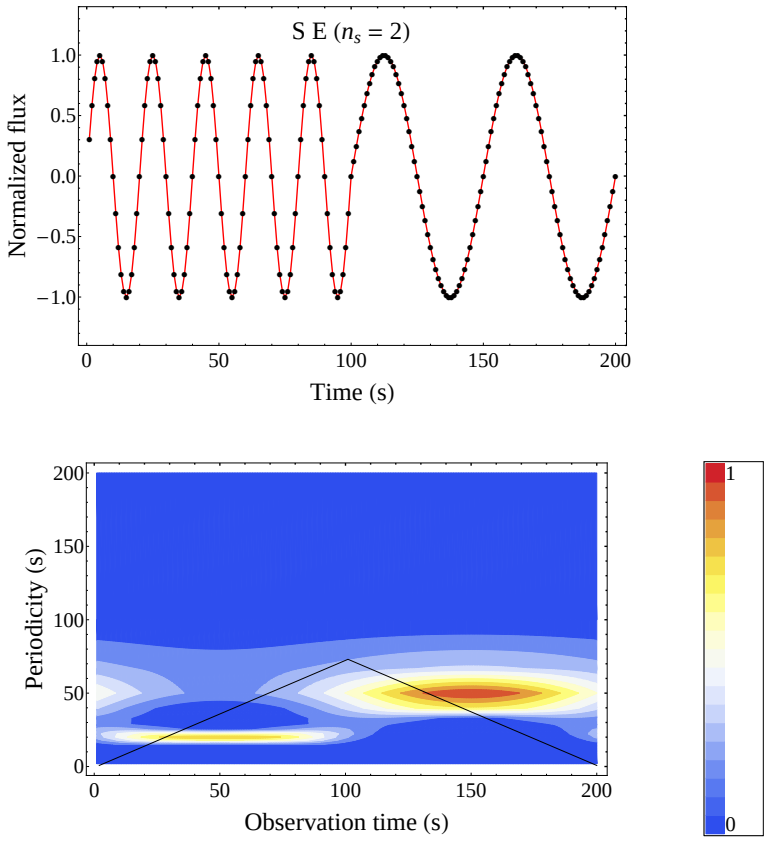

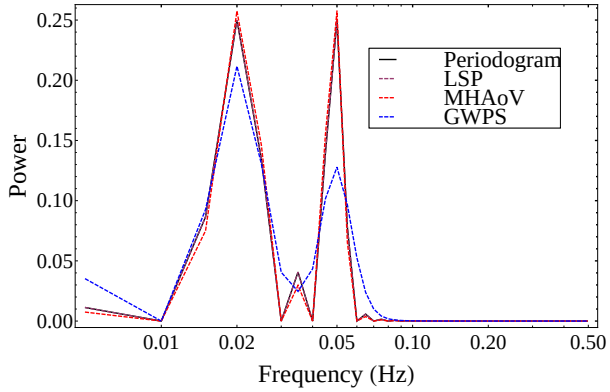

Figure 3.7: Experiment 6: Top row: left panel: evenly sampled sinusoidal light curve composed of two sinusoidal components. The first has a period of 20 s and lasts for 100 s. The second has a period of 50 s and lasts for 100 s; right panel: combined plot showing the normalized power spectra of all techniques. The frequencies of 0.05 Hz (20 s) and 0.02 (50 s) are well detected by all techniques. Bottom row: left panel: contour plot showing the wavelet power spectrum. The 20 s periodicity lasts between the start and 100 s. The 50 s periodicity lasts between 100 s and 200 s. They exactly follow the duration of existence of the corresponding sinusoids in the light curve.

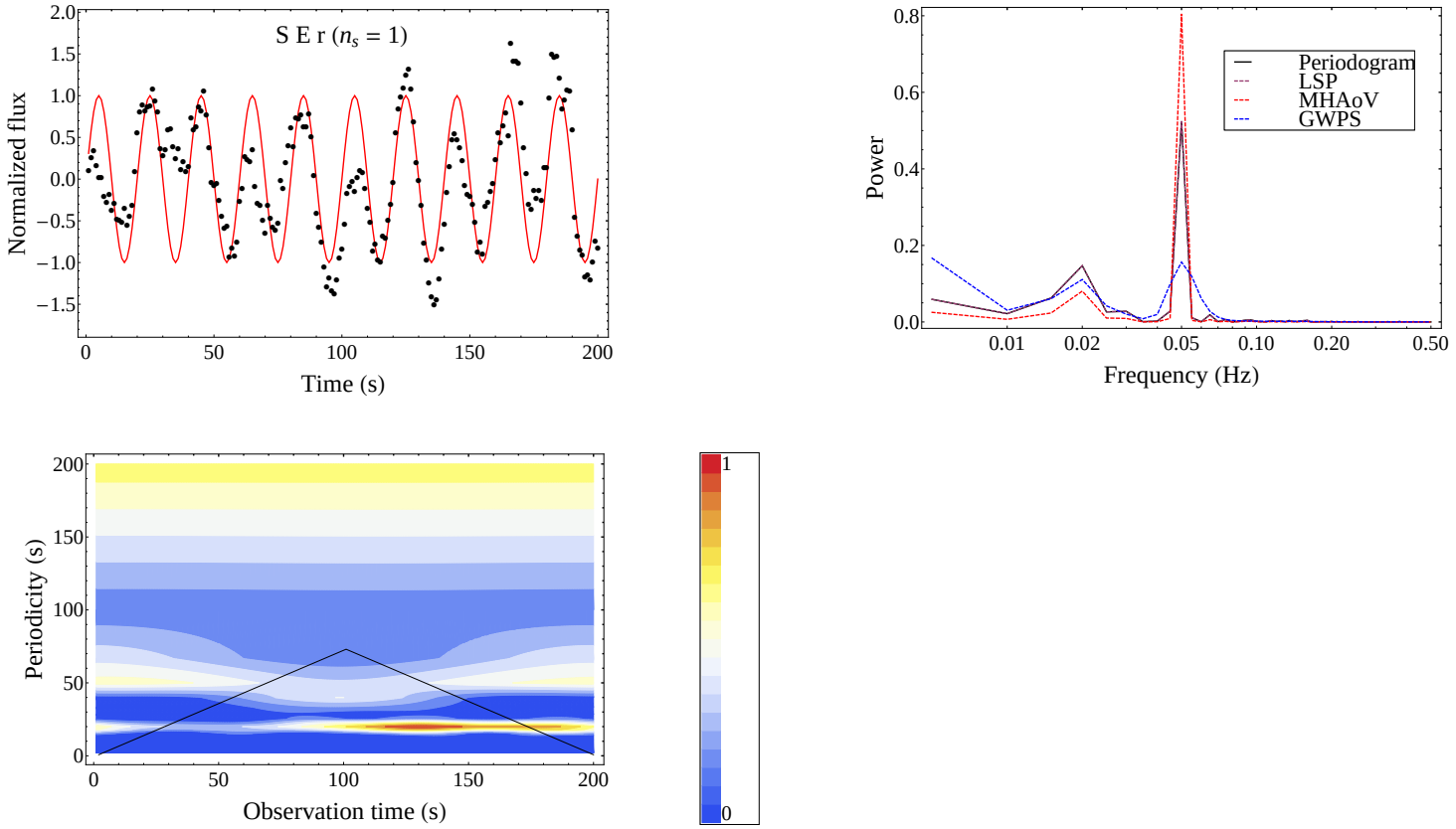

Figure 3.8: Experiment 7: Top row: left panel: evenly sampled sinusoidal light curve with red noise; right panel: combined plot showing the normalized power spectra of all techniques. The peak amplitude at a frequency of 0.05 Hz (20 s) is equal for the periodogram and LSP. The MHAoV has the highest amplitude of 0.81. Bottom row: left panel: contour plot showing the wavelet power spectrum. The periodicity of 20 s is detected reasonably well only after the first 60 s.

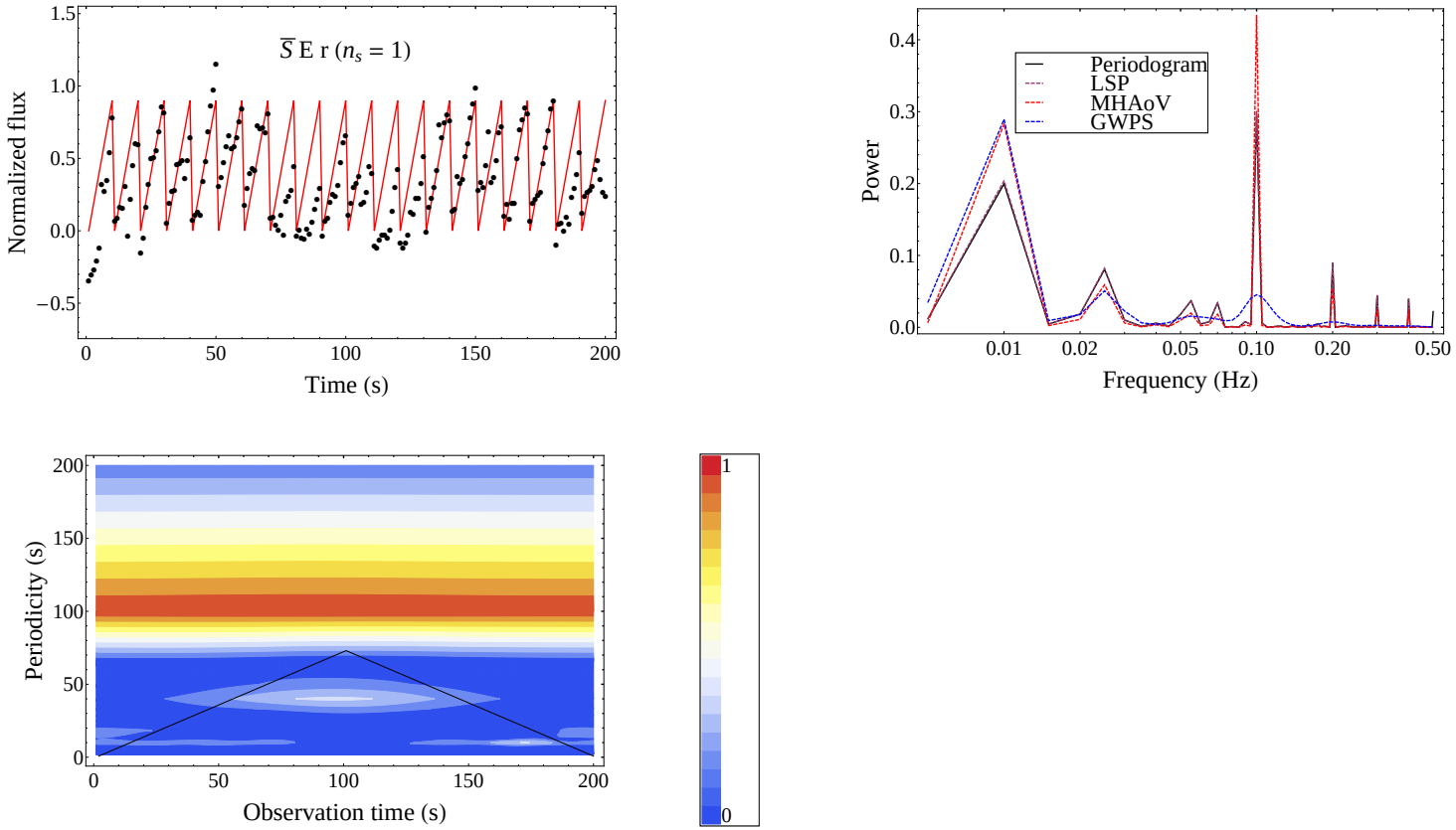

Figure 3.9: Experiment 8: Top row: left panel: evenly sampled saw-tooth light curve with red noise; right panel: combined plot showing the normalized power spectra of all techniques. The normalized peak amplitude at a frequency of 0.10 Hz (10 s) is 0.30 for the periodogram and LSP. The MHAoV shows a higher amplitude at 0.43. Bottom row: left panel: contour plot showing the wavelet power spectrum. The periodicity of 10 s is weakly detected near the end of the observation duration.

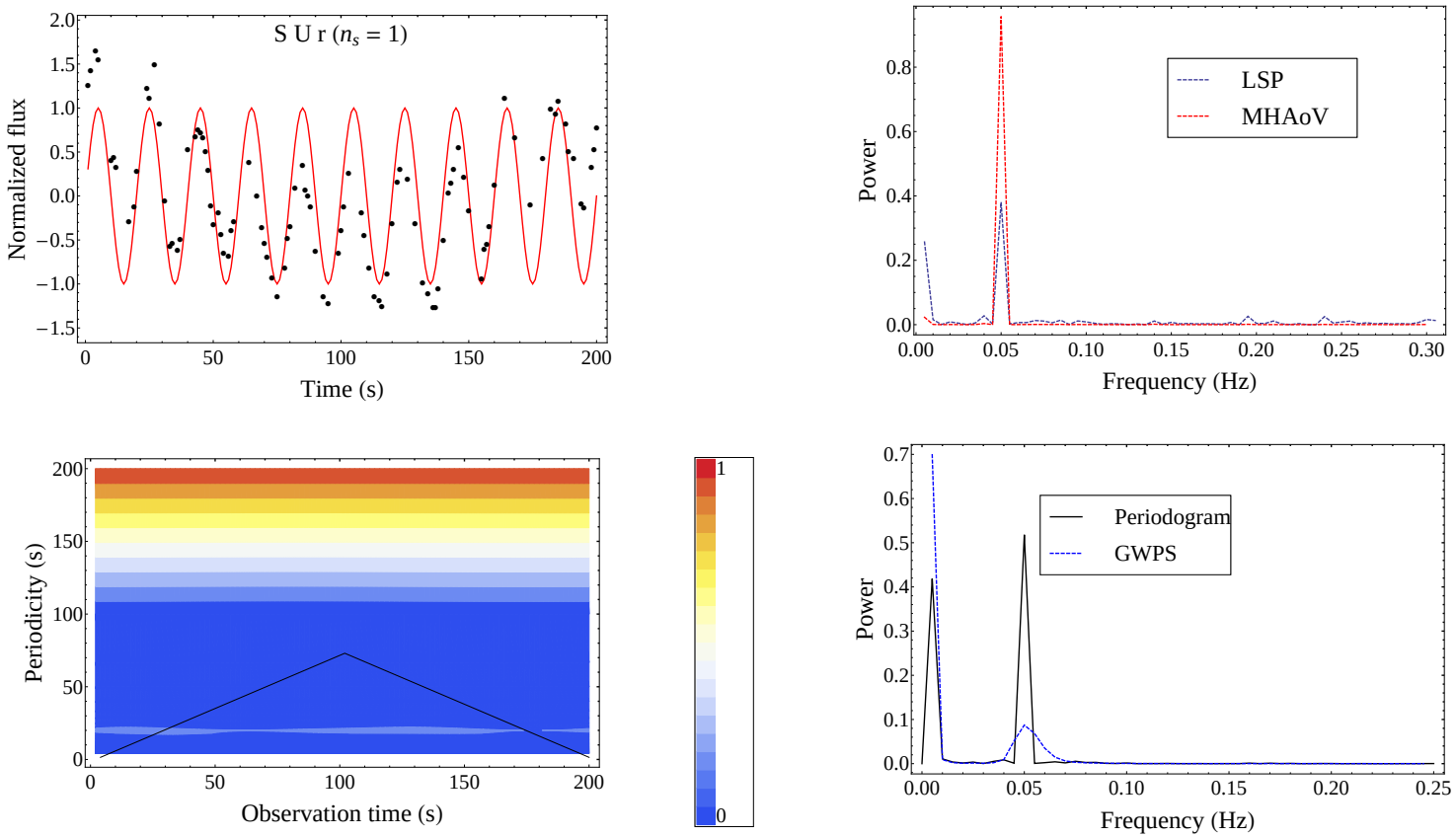

Figure 3.10: Experiment 9: Top row: left panel: un-evenly sampled sinusoidal light curve with red noise; right panel: combined plot showing the normalized power spectra of the LSP and MHAoV. The corresponding peak amplitudes at the frequency of 0.05 Hz (20 s) are at 0.38 and 0.96 respectively. Bottom row: left panel: contour plot showing the wavelet power spectrum. The periodicity of 20 s is weakely detected throughout the observation duration; right panel: combined plot showing the normalized periodogram and GWPS.

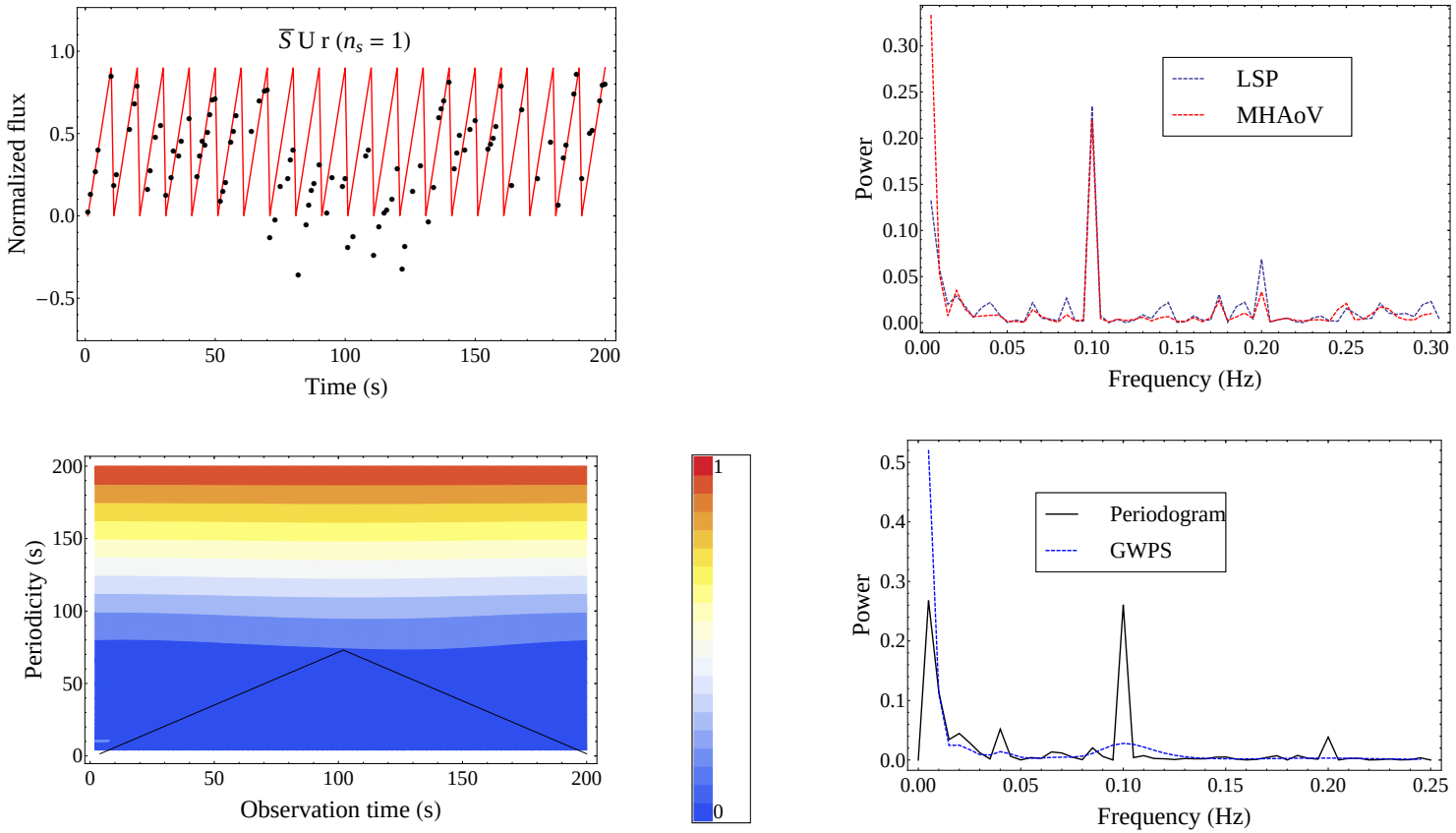

Figure 3.11: Experiment 10: Top row: left panel: un-evenly sampled saw-tooth light curve with red noise; right panel: combined plot showing the normalized power spectra of the LSP and MHAoV. The corresponding peak amplitudes at the frequency of 0.10 Hz (10 s) are at 0.23 and 0.22 respectively. Bottom row: left panel: contour plot showing the wavelet power spectrum. The periodicity of 10 s does not show up prominently; right panel: combined plot showing the normalized periodogram and GWPS. The periodicity at 0.1 Hz (10 s) shows up as a small bump in the GWPS plot.

Chapter 4

Analysis of variability in blazars

4.1 Introduction

Variability is often observed in emission from AGN with strong jet components such as blazars, inferred from the domination of synchrotron processes in radio to optical light curves and spectra from regions at parsec scales as well as close to the base of the jet e.g. [121, 98]. Theoretical models are often applicable to emission from regions which are some distance away from the central region where structures are resolvable. Some of these include Doppler beaming of a stream or blobs of plasma accelerated to relativistic velocities along helical paths, the entire structure being oriented in a direction very close to the observer line of sight [93, 94, 95] observed recently in the blazar BL Lacertae [122], shocks propagating along the relativistic jet [91] which explains the variability in some blazars e.g. [123, 124] and relativistic aberration effects due to small deviations from linearity in the propagating shock front could also lead to variability in overall flux and polarization [92]. Rapid variability has been observed in TeV emission from blazars [4], the time-scales of which are a few times or much shorter than the light crossing time. Explanations have invoked instabilities in the jet e.g. [125, 126] as well as the presence of layering in the jet with randomly oriented substructures contributing to the overall observation [127, 128].

4.2 Data selection

In this section, we detail the selection criteria employed in the extraction of the optical light curves obtained from ground based observational facilities and X-ray (0.3 keV to 10 keV) light curves obtained from archival data available from the XMM Newton Science Archive. The identification of the region of emission from the above light curves can help in advancing theoretical models of variability.

4.2.1 Optical light curves of the blazar S5 0716+714

Our criteria include a combination of long duration observations with good time resolution and nearly uniform sampling. This is satisfied by the data published by [129] on S5 0716+714. These

observations were made on 102 nights between 1999 and 2003 and are presented in the SIMBAD astronomical database[1]. First, 37 light curves with observational gaps during a night are rejected. Then, 5 light curves with median errors more than 0.015 mag. are rejected. For the remaining 60 light curves the intra-day variability amplitude, A [23] is determined as:

$$A = 100 \times \sqrt{(A_{\rm max} - A_{\rm min})^2 - 2\,\sigma^2}\ \%, \tag{4.1}$$

where A_{max} and A_{min} are the maximum and minimum magnitudes in the calibrated light curve of the blazar and σ is the averaged measurement error of that light curve. From this reduced sample, we accept a set of 30 light curves with A >10%. Finally, we reject 9 light curves with time duration less than 7.5 hours. This is done so that if a QPO with a typical duration of $\sim$ 1 hour exists in the light curve which lasts for the entire observation duration, a minimum of 6 cycles can be inferred. If we use the analysis suite to analyse these light curves, the developed statistical description can confirm the presence of a real signal as opposed to one caused due to random noise.

A set of 21 light curves in the V and R magnitudes (optical bands) are thus obtained for the analysis.

The criteria used here for extraction and a wavelet analysis of additional light curves with the results are discussed in [130].

4.2.2 X-ray light curves of blazars

We chose a set of eight blazars: MS 0205.7+3509, AO 0235+164, S5 0716+714, S5 0836+710, OJ 287, 1ES 1028+511, 3C 273 and 3C 454.3 which indicated mild to strong variability. Then their light curves were extracted based on the following criteria:

Their time duration must be 7 hours or greater to ensure that if a QPO with a typical duration of $\sim$ 1 hour is present in the light curve, it can last for a minimum of 6 cycles. We next ensured that these light curves had not earlier been probed for the presence of QPOs or intra-day variability time-scales. We had to reject some of these light curves when EPIC-PN detector based observations were not available because the remaining MOS1 and MOS2 detector observations are likely to suffer from event pile-up. Additional light curves were dropped when there were multiple proton flaring events in the middle of the observation duration that contributed to data with gaps rendering the final time duration less than 7 hours. These cannot be analysed effectively as an interpolation across large patches would introduce false features in the frequency domain analyses. Also, light curves having poor S/N (source counts/s being low compared to the error bars) were rejected as the estimates from them of various parameters would be highly uncertain. Using all the above criteria, a set of 15 X-ray LCs for 8 blazars were obtained using SAS v 10.0.0 tools.

A set of 20 blazar light curves in the soft X-ray band (0.3 keV to 10 keV) are thus obtained for the analysis.

[1] http://simbad.u-strasbf.fr/simbad/

4.2.3 Other data sets

A possible QPO was reported by [131] for 3C 273 based on XMM Newton data taken in the 0.75 keV - 10 keV, with time bin of 5s (ObsID 126700301). The light curve was analysed using our analysis suite with the result that the statistical significance of the reported feature being very low across all techniques. We ruled out the presence of a 3300 s periodicity in this data set with strong statistical significance in [100]. In §4.4, we present a more extended analysis of this light curve.

A one week multi-wavelength campaign to study the variability and the spectral properties of the blazar S5 0716+714 was conducted during December 9-16, 2009 [98]. Nine ground-based telescopes at widely separated longitudes and one space-based telescope aboard the *Swift* satellite collected optical data.

Ground based observations:

Optical data was obtained using the U, B, V, R and I filters. Observations during 9, 10, 11 and 12 December 2009 were carried out with the 1.3 m McGrawHill telescope (Kitt Peak, Arizona, U.S.A.). Observations during the period of 9, 11, 12, 14, 15 and 16 December 2009 were also carried out at the Abastumani Observatory using the 70 cm f/3 meniscus telescope. Observations on 11, 13 and 15 December 2009 were carried out on the 1.04 m f/13 Sampuranand telescope at Nainital (India). Observations on 12 December 2009 were carried out with the 23.5 cm f/10 Schmidt-Cassegrain telescope at LaSapienza University (Roma, Italy) with simultaneous observations being made with the 31 cm f/4.5 Newtonian telescope at Crever in Chianti (near Florence, Italy). It was also observed during 12 December 2009 at the 0.9 m optical SARA telescope at the Kitt Peak National Observatory (USA). Observations on 13 December 2009 were carried out with the 50/70 cm Schmidt telescope at the Rozhen National Astronomical Observatory (Bulgaria). Observations were also carried out on 13 December 2009 using the 61 cm Boller and Chivens reflector at Sobaeksan Optical Astronomy (Korea). On 2009 December 12, 13 and 14, the source was observed with the 1.2 m Cassegrain telescope at the Michael Adrian Observatorium of Astronomie Stiftung Trebur (Germany). Observations were also carried out on 10 and 16 December 2009 at the 2.56 m Nordic Optical Telescope (NOT), Canary Islands (Spain) using ALOFSC (December 10) and MOSCA (December 16).

Space based observations: The S5 0716+714 also was observed by the Ultraviolet Optical Telescope (UVOT) aboard the Swift satellite in the V band during 54 pointings between 11 - 15 December 2009.

In §4.4.3, we present an analysis and discussion of the optical light curve of this blazar.

4.3 Data reduction and preparation

4.3.1 Optical light curves of the blazar S5 0716+714

The obtained optical V and R band light curves are un-evenly sampled. These can be analyzed directly after mean subtraction using the LSP and MHAoV techniques which are well suited for this purpose. These light curves are also converted to an evenly sampling for their analysis using the

periodogram and wavelet analysis. Another important reason for this conversion is the use of the periodogram in determining the PSD shape. This must be constrained in order that MC simulations based significance testing can be made available for use across all techniques of the analysis suite. The un-evenly sampled light curves are re-binned into bins of equal temporal spacing and the mean flux in each bin is estimated. For empty bins, a linear interpolation is used to obtain the flux estimate. The light curve is now evenly sampled.

4.3.2 X-ray light curves of blazars

The light curve for the energy range > 10 keV was first observed and manually truncated to a good time interval (GTI) by eliminating regions of the light curve dominated by proton flaring events. Then, we placed a circular aperture of size ranging from $35''$ to $45''$ around the object depending on the specific data set. The light curve of the object was then extracted with a time bin size of 100 s in the GTI for the energy range 0.3 keV to 10 keV. By placing a circular aperture of the same size as the object slightly away (about $200''$) from the source to prevent contamination by source photons, we extracted the light curve of the background in the same energy range with the same bin size in the GTI. The size of the apertures around the object and the background are tailored for each data set in order to avoid dark regions or patches with no counts. The object light curve with time bin size of 100 s was then obtained by subtracting the background from the source. Where small data gaps (< 10 points) were present in an object light curve, caused due to the removal of flaring portions, we performed a linear interpolation in this region and used these estimates to obtain the final analysable light curve with time bin size of 100 s, similar to the procedure followed in [132].

4.3.3 Other data sets

The optical data from the campaign observations of S5 0716+714 were reduced using IRAF reduction software. This included bias correction, flat fielding and cosmic ray subtraction and was carried out for each of the observations carried out. Aperture photometry was then carried out using aperture sizes ranging between $3''$ - $7''$ depending on the instrument. For a more detailed description of the entire set of observations made during the campaign, including the observational facilities used (optical, radio and X-ray observations) and individual reduction procedures see [98].

4.4 Results and discussion

The analysis of the light curves follows the procedure detailed in §3.2.1 of Chapter 3.

4.4.1 Optical light curves of the blazar S5 0716+714

Table 4.1 summarizes the properties of the optical light curves of S5 0716+714 and the main results of the periodogram analysis. A sample of the analysis conducted is presented in Fig. 4.1. Here, light curves, their periodogram with the best fit PSD model and the results of the LSP, MHAoV

and wavelet analysis are presented. The PSD shape in all 21 data sets analysed are estimated to be of a power law form. Once the PSD shape is constrained, MC simulations are carried for each of the data sets to determine the goodness of fit of the model. The rejection probability ranges between < 0.1 % and 99.70 %. Of these, for 16 data sets (76 %), the rejection probability ranges between < 0.1 % and 29.50 % while the slope varies between -1.68 and -2.00. An average slope of -1.86 $\pm$ 0.11 indicates that the power law model is a good approximation of the PSD shape, not changing considerably over a large span of the observation period, which lasted during the years 1996 - 2003. The MC simulations based significance test of detected peaks in the LSP, MHAoV and wavelet analysis periodograms do not indicate any statistically significant QPO. Table 4.2 summarizes the results of the bending power law PSD model fit to the periodograms. The bending power law model is not a good candidate for the description of the underlying PSD as inferred from the relative likelihoods (RL) in Table 4.2 which vary between 1.19×10^{-8} and 1.90×10^{-2}. Bend timescales vary between 3349^{+540}_{-408} s and 11731^{+7396}_{-3272} s, often with large errors, the errors quoted being the 68% confidence intervals. The slope α in the frequencies higher than the bend frequency varies between -1.90 and -3.00. Table 4.3 summarizes the results of the broken power law PSD model fit to the periodograms. It is not a good estimate of the PSD shape as inferred from the relative likelihoods (RL) in Table 4.3 which vary between 6.77×10^{-2} and 1.54×10^{-1}. Break timescales vary between 4638^{+881}_{-639} s and 13652^{+10458}_{-4130} s with large errors, the errors quoted being the 68% confidence intervals. The slope $\alpha_{\rm Hi}$ in the frequencies higher than the break frequency ranges between -1.90 and -2.50, the slope -2.50 likely arising in multiple data sets due to the limit in sampling slopes set in our numerical procedure. These slopes are likely to be steeper if the test range for $\alpha_{\rm Hi}$ is decreased beyond -2.50. The slope $\alpha_{\rm Low}$ of the power law region in the frequencies lower than the break frequency is -1.00 for all data sets. This is once again a consequence of the limit in sampling slopes set in our numerical procedure. These slopes are likely to be steeper if the test range for $\alpha_{\rm Low}$ is increased above -1.00.

A search for IDV timescales in the above set of light curves indicated quasi-periodicities with timescales between 25 minutes and 73 minutes which were then used to draw conclusions on the black hole mass [130]. The wavelet analysis procedure which we have used does indicate the presence of some of these features. Though, our more rigourous statistical analysis using Monte-Carlo simulations for significance testing of the data does not support these conclusions of the timescales obtained. For blazars, the optical emission is mostly dominated by the jet component. Hence, it is unlikely that these time-scales are caused by disk based orbital signatures. Variability in the jet could occur due to the propagation of multiple shocks due to disk based processes in the inner region e.g. [133], selective beaming of flow material along the observer line of sight for short durations, irregular propagation of the shock front [92]. The rapid changes in the slope of the power law and the extent of variation could be explained by multiple processes causing the variability in the light curve at the same time with some dominating over the others during a particular observation duration. If the dominating processes are those that cause variability over longer time durations, they would tend to cause the slope to steepen while if they cause variability over shorter time scales, they would tend to flatten the slope.

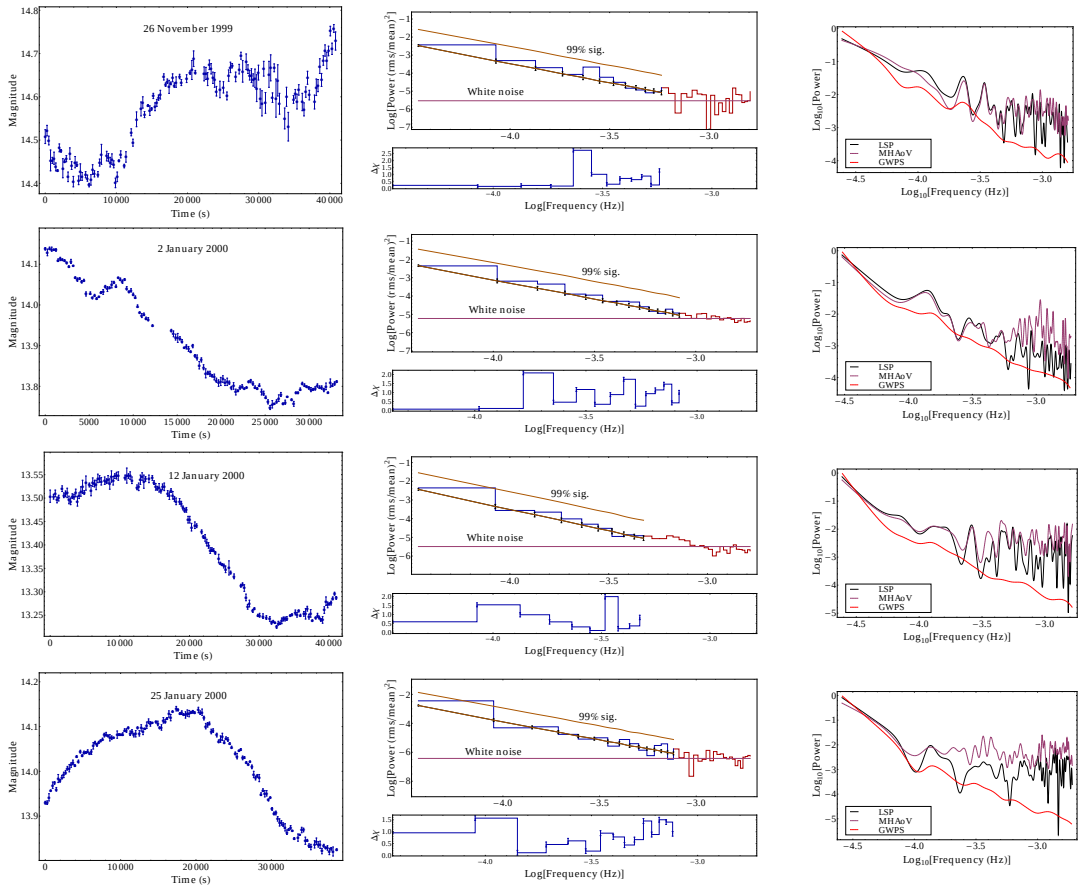

Figure 4.1: A subset of the analysis results is plotted in these figures to illustrate the power law PSD shape in these light curves. Detailed results are presented in Tables 4.1, 4.2 and 4.3. Left plot: Optical V and R band plot of the blazar S5 0716+714. Middle plot: binned periodogram: fit portion is in blue and white noise region is in red. The best fit model is plotted over the fit portion and the residue $\Delta\chi$ =(data-model)/σ is shown below it. Right plot: LSP, MHAoV periodogram and global wavelet power spectrum results.

Observation Date	Time Duration (s)	Variability Amplitude %	Best fit PSD shape	MC sims. Rejection Prob. (%)	Fit parameters
26 November 1999	40807	36.15	Power law	2.40	α = -1.85 $\pm$ 0.09
2 January 2000	33134	39.10	Power law	< 0.1	α = -1.85 $\pm$ 0.10
12 January 2000	41057	32.29	Power law	< 0.1	α = -1.91 $\pm$ 0.10
25 January 2000	38681	31.89	Power law	53.40	α = -2.12 $\pm$ 0.09
27 October 2000	27795	19.37	Power law	4.00	α = -1.98 $\pm$ 0.10
14 February 2001	37982	10.76	Power law	94.20	α = -1.70 $\pm$ 0.07
26 February 2001	35994	28.58	Power law	0.25	α = -1.84 $\pm$ 0.08
3 November 2001	36158	15.37	Power law	1.20	α = -1.83 $\pm$ 0.10
1 February 2002	29473	12.24	Power law	< 0.1	α = -1.79 $\pm$ 0.09
13 March 2002	31579	10.31	Power law	73.75	α = -2.02 $\pm$ 0.08
15 March 2002	33213	13.84	Power law	< 0.1	α = -1.82 $\pm$ 0.10
20 March 2002	33540	10.22	Power law	29.50	α = -2.03 $\pm$ 0.10
25 March 2002	33703	18.36	Power law	16.70	α = -2.00 $\pm$ 0.10
1 April 2002	31994	12.86	Power law	0.05	α = -1.98 $\pm$ 0.11
22 April 2002	27665	22.47	Power law	0.05	α = -1.76 $\pm$ 0.12
28 October 2002	30145	10.47	Power law	73.60	α = -1.79 $\pm$ 0.10
29 December 2002	44098	53.26	Power law	99.70	α = -1.80 $\pm$ 0.07
18 February 2003	39295	20.63	Power law	6.25	α = -1.84 $\pm$ 0.10
25 February 2003	39589	19.96	Power law	< 0.1	α = -1.68 $\pm$ 0.13
4 March 2003	33843	39.39	Power law	< 0.1	α = -1.81 $\pm$ 0.10
18 March 2003	31070	14.71	Power law	20.45	α = -2.00 $\pm$ 0.10

Table 4.1: Results from the PSD fit with the best fit model to the optical V and R band light curves of S5 0716+714. Columns 1 – 6 give the source observation date, its observation duration during that night, variability amplitude as defined in eqn. (4.1), the best fit PSD shape obtained from the Akaike Information Criteria, MC simulations based goodness of fit quantified as a model rejection probability and the best fit model parameters with their errors based on the 68 % confidence intervals obtained from the contours of the differences of the log-likelihood function ΔS.

Observation Date	Bending power law model parameters		AIC	Δ_i	Relative Likelihood (RL)
	T_{Ben} (s)	α		= AIC_i-AIC_{Null}	
26 November 1999	5441^{+1256}_{-860}	-3.00 ± 0.12	-243.51	18.60	9.16×10^{-5}
2 January 2000	5098^{+1411}_{-909}	-2.90 ± 0.11	-240.07	21.60	2.04×10^{-5}
12 January 2000	11731^{+7396}_{-3272}	-2.40 ± 0.12	-244.78	24.38	5.10×10^{-6}
25 January 2000	9670^{+5300}_{-2528}	-3.00 ± 0.11	-311.17	27.83	9.07×10^{-7}
27 October 2000	6177^{+2294}_{-1317}	-2.20 ± 0.13	-193.35	17.34	1.72×10^{-4}
14 February 2001	4468^{+1368}_{-848}	-2.00 ± 0.09	-607.20	36.49	1.19×10^{-8}
26 February 2001	7199^{+3167}_{-1685}	-2.50 ± 0.10	-336.12	29.18	4.60×10^{-8}
3 November 2001	6574^{+2203}_{-1319}	-2.60 ± 0.12	-284.74	21.59	2.05×10^{-5}
1 February 2002	5895^{+2580}_{-1376}	-2.10 ± 0.11	-364.77	26.30	1.95×10^{-6}
13 March 2002	5263^{+1841}_{-1083}	-2.80 ± 0.10	-428.39	29.85	3.30×10^{-7}
15 March 2002	5536^{+1411}_{-935}	-3.00 ± 0.13	-222.13	14.35	7.65×10^{-4}
20 March 2002	9583^{+6018}_{-2668}	-1.90 ± 0.12	-296.74	22.35	1.40×10^{-5}
25 March 2002	4815^{+1179}_{-792}	-3.00 ± 0.12	-269.36	19.10	7.12×10^{-5}
1 April 2002	9141^{+4291}_{-2213}	-2.70 ± 0.14	-210.25	17.64	1.48×10^{-4}
22 April 2002	7904^{+2971}_{-1696}	-2.90 ± 0.16	-131.36	10.92	4.25×10^{-3}
28 October 2002	3349^{+540}_{-408}	-3.00 ± 0.13	-233.17	11.07	3.94×10^{-3}
29 December 2002	5880^{+1825}_{-1127}	-2.60 ± 0.09	-377.37	34.54	3.15×10^{-8}
18 February 2003	6045^{+1626}_{-1057}	-2.70 ± 0.12	-257.05	20.21	4.09×10^{-5}
25 February 2003	7180^{+3419}_{-1751}	-3.00 ± 0.17	-132.79	7.93	1.90×10^{-2}
4 March 2003	5641^{+1633}_{-1035}	-2.80 ± 0.12	-200.78	19.32	6.38×10^{-5}
18 March 2003	4780^{+1324}_{-852}	-2.90 ± 0.11	-304.41	22.89	1.07×10^{-5}

Table 4.2: Results from the PSD fit with the bending power law model for the optical V and R band light curves of S5 0716+714. Columns 1 – 6 give the observation date, the bend timescale in s (converted to temporal domain from a bend frequency in the binned periodogram), the slope α of the power law region at frequencies lower than the bend frequency, the AIC value, the difference Δ_i which is used to calculate the likelihood and the relative likelihood which quantifies the probability of the bending power law model being chosen over the null model as a best fit PSD model.

Object	Broken power law model parameters			AIC	Δ_i	Relative Likelihood (RL)
	T_{Brk} (s)	α_{Hi}	α_{Low}		= AIC_i-AIC_{Null}	
26 November 1999	7419^{+1996}_{-1297}	-2.50 ± 0.09	-1.00 ± 0.06	-257.76	4.35	1.14×10^{-2}
2 January 2000	7100^{+2407}_{-1434}	-2.40 ± 0.09	-1.00 ± 0.06	-256.30	5.38	6.77×10^{-2}
12 January 2000	12965^{+7465}_{-3469}	-2.30 ± 0.09	-1.00 ± 0.06	-261.50	7.66	2.18×10^{-2}
25 January 2000	13652^{+10458}_{-4130}	-2.50 ± 0.08	-1.00 ± 0.06	-330.61	8.38	1.51×10^{-2}
27 October 2000	7580^{+2875}_{-1634}	-2.00 ± 0.10	-1.00 ± 0.07	-204.34	6.34	4.19×10^{-2}
14 February 2001	5558^{+1838}_{-1106}	-2.00 ± 0.09	-1.00 ± 0.05	-636.89	6.81	3.33×10^{-2}
26 February 2001	8639^{+4001}_{-2078}	-2.30 ± 0.08	-1.00 ± 0.06	-357.56	7.74	2.09×10^{-2}
3 November 2001	8344^{+3040}_{-1758}	-2.30 ± 0.09	-1.00 ± 0.06	-300.25	6.09	4.77×10^{-2}
1 February 2002	6801^{+2861}_{-1553}	-2.00 ± 0.08	-1.00 ± 0.06	-383.71	7.35	2.53×10^{-2}
13 March 2002	7018^{+2953}_{-1604}	-2.40 ± 0.08	-1.00 ± 0.05	-450.74	7.50	2.35×10^{-2}
15 March 2002	7665^{+2293}_{-1435}	-2.50 ± 0.10	-1.00 ± 0.07	-232.86	3.62	1.63×10^{-1}
20 March 2002	10062^{+5237}_{-2566}	-1.90 ± 0.09	-1.00 ± 0.06	-311.74	7.35	2.54×10^{-2}
25 March 2002	6523^{+1993}_{-1172}	-2.50 ± 0.09	-1.00 ± 0.06	-283.033	5.42	6.65×10^{-2}
1 April 2002	11292^{+5697}_{-2836}	-2.50 ± 0.11	-1.00 ± 0.07	-221.39	6.50	3.88×10^{-2}
22 April 2002	10374^{+4350}_{-2366}	-2.50 ± 0.12	-1.00 ± 0.08	-138.67	3.62	1.64×10^{-1}
28 October 2002	4638^{+881}_{-639}	-2.50 ± 0.10	-1.00 ± 0.07	-240.50	3.74	1.54×10^{-1}
29 December 2002	7782^{+2875}_{-1653}	-2.20 ± 0.07	-1.00 ± 0.05	-405.043	6.87	3.22×10^{-2}
18 February 2003	8732^{+2967}_{-1766}	-2.20 ± 0.09	-1.00 ± 0.06	-270.68	6.57	3.74×10^{-2}
25 February 2003	10402^{+6307}_{-2850}	-2.50 ± 0.13	-1.00 ± 0.09	-139.47	1.25	5.36×10^{-1}
4 March 2003	7810^{+2678}_{-1589}	-2.30 ± 0.09	-1.00 ± 0.06	-214.36	5.74	5.67×10^{-2}
18 March 2003	6904^{+2483}_{-1444}	-2.30 ± 0.09	-1.00 ± 0.06	-320.28	7.02	2.98×10^{-2}

Table 4.3: Results from the PSD fit with the broken power law model for the optical V and R band light curves of S5 0716+714. Columns 1–7 give the observation date, the break timescale in s (converted to temporal domain from a break frequency in the binned periodogram), the slope α_{Hi} of the power law region at frequencies higher than the break frequency, the slope α_{Hi} of the power law region at frequencies lower than the break frequency, the AIC value, the difference Δ_i which is used to calculate the likelihood and the relative likelihood which quantifies the probability of the broken power law model being chosen over the null model as a best fit PSD model.

4.4.2 X-ray light curves of blazars

Table 4.4 summarizes the properties of the soft X-ray (0.3 - 10 keV) light curves of blazars and the main results of the periodogram analysis. A sample of the analysis conducted is presented in Fig. 4.2. Here, light curves, their periodogram with the best fit PSD model and the results of the LSP, MHAoV and wavelet analysis are presented. The excess fractional variability of the data sets ranges between 1.75 % and 16.79 % indicating that there is moderate to strong intrinsic variability. The PSD shape in 12 of 15 (80 %) data sets analyzed are a broken power law form with rejection probability ranging between 13.40 % and 95.60 %. The break frequency is in the frequencies dominated by white noise making the estimate unreliable. Only in three cases, for the same object 3C 273, the break frequency is sufficiently removed from the white noise region. The estimated $T_B = 1502^{+78}_{-72}$ is reliable due to the low rejection probability of the model fit to the data. It is interesting to note that the other two break timescales, even though not statistically significant are similar to the one discussed above within their corresponding error bars.

The MC simulations do not indicate any statistically significant feature. Table 4.5 summarizes the results of the power law PSD model fit to the periodogram of the blazar X-ray light curves. The power law model is a statistically valid candidate for only two data sets, 3C 454.3 and S5 0716+714. The rejection probability of the former is 44.05 % indicating that the goodness of fit is moderate and that of the later is 0.05 % indicating that the goodness of fit is very good and the model has a strong probability of describing the data. Their slopes are -1.13 and -1.79 and repectively (Table 4.5). For the rest of the data sets (12 out of 15), the power law model does not describe the PSD shape well as inferred from the relative likelihoods (RL) in Table 4.6 which vary between 5.25×10^{-13} and 6.54×10^{-2}. The power law slope α ranges between -0.50 and -1.79. The slope of the PSD shape for S5 0716+714 (obs. I.D.: 0502271401) of -1.79 in the X-rays is similar to the -1.86 obtained from the optical light curves. This could indicate that both optical and X-ray variability processes for this object are arising from similar regions. Table 4.6 summarizes the results of the bending power law PSD model fit to the periodograms. The bending power law model is a statistically valid candidate for only one data set (3C 273) where the bend timescale is $T_{\rm Ben} = 426^{+13}_{-13}$ s and the slope α in the frequencies lower that the bend frequency is -1.50. Though, as the timescale is very close to the white noise dominated region, it is unreliable. For the rest of the data sets (14 out of 15) the relative likelihoods (RL) vary between 1.04×10^{-12} and 9.57×10^{-1}. Bend timescales vary between 324^{+8}_{-8} s and 3623^{+605}_{-909} s, the errors quoted being the 68% confidence intervals. The slope α in the frequencies higher than the bend frequency varies between -1.00 and -2.80. The limit of -1.00 likely arises in multiple data sets due to the limit in sampling slopes set in our numerical procedure. These slopes are likely to be less steeper if the test range for α is increased above -1.00. Table 4.7 summarizes the results of the broken power law PSD model fit to the periodograms. The broken power law describes the PSD well in 80 % of the data sets. The relative likelihoods (RL) for the remaining 3 of 15 data sets are 8.04×10^{-1} (3C 273), 2.78×10^{-1} (3C 454.3) and 9.24×10^{-2} (S5 0716+714). Break timescales vary between 488^{+18}_{-16} s and 4486^{+1262}_{-808} s, the errors quoted being the 68% confidence intervals. The slope $\alpha_{\rm Hi}$ in

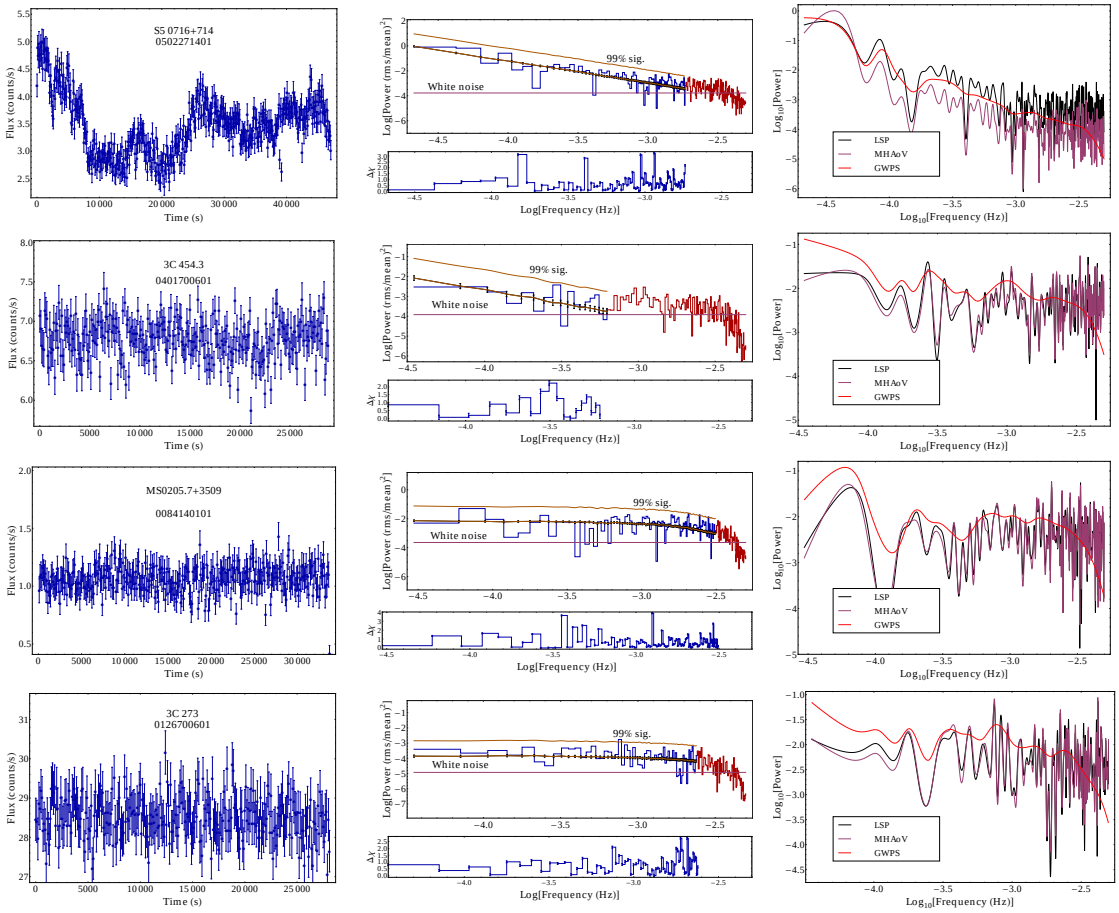

Figure 4.2: Left plot: X-ray light curve (0.3 keV to 10 keV) of the blazar. Middle plot: binned periodogram: fit portion is in blue and white noise region is in red. The best fit model is plotted over the fit portion and the residue $\Delta\chi$ =(data-model)/σ is shown below it. Right plot: LSP, MHAoV periodogram and global wavelet power spectrum results.

the frequencies higher than the break frequency ranges between -1.00 and -2.50 and the slope $\alpha_{\rm Low}$ in the frequencies lower than the break frequency ranges between -0.10 and -1.00. A value of -1.00 in $\alpha_{\rm Hi}$ likely arises in multiple data sets due to the limit in sampling slopes set in our numerical procedure. These slopes are likely to be less steeper if the test range for α is increased above -1.00.

The timescale indicated is typically low $<$ 1000 s which would lie in the white noise portion of the periodogram and cannot be relied upon; for the data sets which indicate larger timescales (1502 s, 1640 s and 1810 s for 3C 273), the slopes below and above the break timescale are either similar or are at the higher or lower limit of the sampling parameter space and are thus likely to change if we use a larger sampling grid of slopes. Further, the emission is likely to be dominated by jet based processes due to the objects being blazars. Hence, the variability based results obtained may not be directly applicable to infer the black hole spin or set constraints in this manner on the black hole mass.

Object	RA (J2000)	Dec. (J2000)	Redshift z	Observation ID	Time Duration	Fractional Variability $F_{\rm var}$	Best fit PSD shape	MC sims. Rejection Prob. (%)	Fit parameters
MS 0205.7+3509	02h08m38.2s	+35d23m12.7s	0.32	0084140101	33700	11.57	Broken power law	20.00	$T_{\rm Brk.} = 488^{+18}_{-16}$ s $\alpha_{\rm Hi}$ = -2.1 ± 0.05 $\alpha_{\rm Low}$ = -0.2 ± 0.03
AO 0235+16	02h38m38.9s	+16d36m59s	0.94	0206740101	27100	16.79	Broken power law	82.50	$T_{\rm Brk.} = 940^{+47}_{-43}$ s $\alpha_{\rm Hi}$ = -2.5 ± 0.08 $\alpha_{\rm Low}$ = -0.0 ± 0.05
S5 0716+714	07h21m53.4s	+71d20m36s	0.31	0502271401	47100	15.46	Power law	0.05	α = -1.79 ± 0.05
S5 0836+710	08h41m24s	+70d53m42s	2.17	0112620101	23000	5.15	Broken power law	86.95	$T_{\rm Brk.} = 590^{+30}_{-28}$ s $\alpha_{\rm Hi}$ = -2.0 ± 0.06 $\alpha_{\rm Low}$ = -0.2 ± 0.04
OJ 287	08h54m48.9s	+20d06m31s	0.31	0300480301	23700	16.67	Broken power law	14.25	$T_{\rm Brk.} = 519^{+23}_{-21}$ s $\alpha_{\rm Hi}$ = -2.4 ± 0.06 $\alpha_{\rm Low}$ = -0.1 ± 0.04
OJ 287				0401060201	44900	14.89	Broken power law	79.25	$T_{\rm Brk.} = 792^{+37}_{-33}$ s $\alpha_{\rm Hi}$ = -1.8 ± 0.04 $\alpha_{\rm Low}$ = -0.3 ± 0.03
1ES 1028+511	10h31m18.5s	+50d53m35.8s	0.36	0303720301	79900	4.57	Broken power law	39.85	$T_{\rm Brk.} = 722^{+24}_{-23}$ s $\alpha_{\rm Hi}$ = -1.0 ± 0.03 $\alpha_{\rm Low}$ = -0.3 ± 0.02
1ES 1028+511				0303720601	83100	6.08	Broken power law	27.50	$T_{\rm Brk.} = 919^{+39}_{-35}$ s $\alpha_{\rm Hi}$ = -1.0 ± 0.03 $\alpha_{\rm Low}$ = -0.4 ± 0.02
3C 273	12h29m06.7s	+02d03m09s	0.16	0126700601	28100	1.83	Bending power law	95.60	$T_{\rm Ben.} = 426^{+13}_{-13}$ s α = -1.5 ± 0.08
3C 273				0126700701	21400	1.75	Broken power law	39.55	$T_{\rm Brk.} = 690^{+37}_{-33}$ s $\alpha_{\rm Hi}$ = -2.2 ± 0.07 $\alpha_{\rm Low}$ = -0.2 ± 0.05
3C 273				0126700801	47300	3.86	Broken power law	13.40	$T_{\rm Brk.} = 1502^{+78}_{-72}$ s $\alpha_{\rm Hi}$ = -2.5 ± 0.07 $\alpha_{\rm Low}$ = -0.2 ± 0.05
3C 273				0136551001	27500	3.57	Broken power law	68.90	$T_{\rm Brk.} = 954^{+61}_{-55}$ s $\alpha_{\rm Hi}$ = -1.4 ± 0.06 $\alpha_{\rm Low}$ = -0.3 ± 0.04
3C 273				0414190101	59300	2.35	Broken power law	64.75	$T_{\rm Brk.} = 1640^{+142}_{-122}$ s $\alpha_{\rm Hi}$ = -1.0 ± 0.04 $\alpha_{\rm Low}$ = -0.6 ± 0.03
3C 273				0414190501	36200	1.83	Broken power law	73.45	$T_{\rm Brk.} = 1810^{+209}_{-170}$ s $\alpha_{\rm Hi}$ = -1.0 ± 0.06 $\alpha_{\rm Low}$ = -0.7 ± 0.04
3C 454.3	22h53m57.7s	+16d08m54s	0.86	0401700601	28800	3.71	Power law	44.05	α = -1.13 ± 0.12

Table 4.4: Results from the PSD fit with the best fit model for the X-ray light curves of blazars. Columns 1 – 10 give the object name, its right ascension (RA), declination (Dec.), cosmological redshift z, a unique observation I.D. assigned to each observation in the XMM Newton archives, its observation duration, fractional variability amplitude $F_{\rm var}$, the best fit PSD shape obtained from the Akaike Information Criteria, MC simulations based goodness of fit quantified as a model rejection probability and the best fit model parameters with their errors based on the 68 % confidence intervals obtained from the contours of the differences of the log-likelihood function ΔS as described in Chapter 3.

Object	Observation ID	Power law model parameters α	AIC	Δ_i = AIC_i-AIC_{Null}	Relative Likelihood (RL)
MS 0205.7+3509	0084140101	-1.17 ± 0.05	-418.19	20.86	2.95×10^{-5}
AO 0235+16	0206740101	-1.01 ± 0.08	-104.65	5.45	6.54×10^{-2}
S5 0716+714	0502271401	-1.79 ± 0.05	-391.19	0.00	1.00
S5 0836+710	0112620101	-1.36 ± 0.06	-377.90	12.18	2.26×10^{-3}
OJ 287	0300480301	-1.32 ± 0.06	-207.76	17.90	1.30×10^{-4}
OJ 287	0401060201	-1.51 ± 0.05	-391.18	22.59	1.24×10^{-5}
1ES 1028+511	0303720301	-1.32 ± 0.03	-1506.92	56.55	5.25×10^{-13}
1ES 1028+511	0303720601	-1.26 ± 0.04	-1199.48	37.07	8.93×10^{-9}
3C 273	0126700601	-1.44 ± 0.06	-480.56	15.27	4.84×10^{-4}
3C 273	0126700701	-1.49 ± 0.07	-349.99	10.10	6.42×10^{-3}
3C 273	0126700801	-0.50 ± 0.08	-253.25	38.25	4.95×10^{-9}
3C 273	0136551001	-1.60 ± 0.07	-333.12	11.89	2.61×10^{-3}
3C 273	0414190101	-1.42 ± 0.04	-997.12	20.35	3.81×10^{-5}
3C 273	0414190501	-1.32 ± 0.06	-528.59	4.72	9.45×10^{-2}
3C 454.3	0401700601	-1.13 ± 0.12	-104.97	0.00	1.00

Table 4.5: Results from the PSD fit with the power law model for the X-ray light curves of blazars. Columns 1 – 6 give the object name, its observation I.D., the slope α which is the only parameter used in this model, the AIC value corresponding to the particular parameter value for which the log likelihood S is a minimum, the difference Δ_i which is used to calculate the likelihood and the relative likelihood which quantifies the probability of the power law model being chosen over the null model as a best fit PSD model.

Object	Observation ID	Bending power law model parameters		AIC	Δ_i	Relative Likelihood (RL)
		T_{Ben} (s)	α		= AIC_i-AIC_{Null}	
MS 0205.7+3509	0084140101	324^{+8}_{-8}	-1.30 ± 0.06	-436.91	2.14	3.43×10^{-1}
AO 0235+16	0206740101	713^{+30}_{-27}	-1.00 ± 0.10	-110.02	0.09	9.57×10^{-1}
S5 0716+714	0502271401	3623^{+605}_{-909}	-1.80 ± 0.07	-336.00	55.19	1.04×10^{-12}
S5 0836+710	0112620101	329^{+9}_{-10}	-2.30 ± 0.07	-387.16	2.93	2.31×10^{-1}
OJ 287	0300480301	325^{+8}_{-9}	-1.60 ± 0.07	-223.50	2.16	3.40×10^{-1}
OJ 287	0401060201	401^{+9}_{-9}	-2.80 ± 0.06	-405.97	7.81	2.02×10^{-2}
1ES 1028+511	0303720301	354^{+6}_{-6}	-1.70 ± 0.04	-1539.91	23.57	7.62×10^{-6}
1ES 1028+511	0303720601	630^{+18}_{-16}	-1.00 ± 0.04	-1220.06	16.49	2.62×10^{-4}
3C 273	0126700601	426^{+13}_{-13}	-1.50 ± 0.08	-495.83	0.00	1.00
3C 273	0126700701	446^{+16}_{-15}	-1.70 ± 0.09	-359.71	0.37	8.29×10^{-1}
3C 273	0126700801	1391^{+69}_{-62}	-1.00 ± 0.10	-291.00	0.50	7.81×10^{-1}
3C 273	0136551001	492^{+17}_{-15}	-2.30 ± 0.08	-343.85	1.16	5.60×10^{-1}
3C 273	0414190101	1318^{+89}_{-79}	-1.00 ± 0.05	-983.26	34.21	3.73×10^{-8}
3C 273	0414190501	1420^{+124}_{-106}	-1.00 ± 0.07	-518.76	14.55	6.93×10^{-4}
3C 454.3	0401700601	1694^{+103}_{-91}	-2.70 ± 0.15	-102.38	2.59	2.73×10^{-1}

Table 4.6: Results from the PSD fit with the bending power law model for the X-ray light curves of blazars. Columns 1 – 7 give the object name, its observation I.D., the bend timescale in s (converted to temporal domain from a bend frequency in the binned periodogram), the slope α of the power law region at frequencies lower than the bend frequency, the AIC value, the difference Δ_i which is used to calculate the likelihood and the relative likelihood which quantifies the probability of the bending power law model being chosen over the null model as a best fit PSD model.

Object	Observation ID	Broken power law model parameters			AIC	Δ_i	Relative Likelihood (RL)
		T_{Brk} (s)	α_{Hi}	α_{Low}		= AIC_i-AIC_{Null}	
MS 0205.7+3509	0084140101	488^{+18}_{-16}	-2.1 ± 0.05	-0.2 ± 0.03	-439.05	0.00	1.00
AO 0235+16	0206740101	940^{+47}_{-43}	-2.50 ± 0.08	-0.00 ± 0.05	-110.11	0.00	1.00
S5 0716+714	0502271401	4486^{+1262}_{-808}	-1.60 ± 0.05	-1.00 ± 0.04	-386.42	4.76	9.24×10^{-2}
S5 0836+710	0112620101	590^{+30}_{-28}	-2.0 ± 0.06	-0.2 ± 0.04	-390.09	0.00	1.00
OJ 287	0300480301	519^{+23}_{-21}	-2.40 ± 0.06	-0.10 ± 0.04	-225.66	0.00	1.00
OJ 287	0401060201	792^{+37}_{-33}	-1.80 ± 0.04	-0.30 ± 0.03	-413.77	0.00	1.00
1ES 1028+511	0303720301	722^{+24}_{-23}	-1.00 ± 0.03	-0.30 ± 0.02	-1563.47	0.00	1.00
1ES 1028+511	0303720601	919^{+39}_{-35}	-1.00 ± 0.03	-0.40 ± 0.02	-1236.55	0.00	1.00
3C 273	0126700601	843^{+50}_{-45}	-1.00 ± 0.06	-0.2 ± 0.04	-495.39	0.43	8.04×10^{-1}
3C 273	0126700701	690^{+37}_{-33}	-2.20 ± 0.07	-0.2 ± 0.05	-360.09	0.00	1.00
3C 273	0126700801	1502^{+78}_{-72}	-2.50 ± 0.07	-0.20 ± 0.05	-291.49	0.00	1.00
3C 273	0136551001	954^{+61}_{-55}	-1.40 ± 0.06	-0.30 ± 0.04	-345.01	0.00	1.00
3C 273	0414190101	1640^{+142}_{-122}	-1.00 ± 0.04	-0.60 ± 0.03	-1017.47	0.00	1.00
3C 273	0414190501	1810^{+209}_{-170}	-1.00 ± 0.06	-0.70 ± 0.04	-533.31	0.00	1.00
3C 454.3	0401700601	2880^{+289}_{-241}	-2.50 ± 0.11	-0.40 ± 0.08	-102.41	2.56	2.78×10^{-1}

Table 4.7: Results from the PSD fit with the broken power law model for the X-ray light curves of blazars. Columns 1 – 8 give the object name, its observation I.D., the break timescale in s (converted to temporal domain from a break frequency in the binned periodogram), the slope α_{Hi} of the power law region at frequencies higher than the break frequency, the slope α_{Hi} of the power law region at frequencies lower than the break frequency, the AIC value, the difference Δ_i which is used to calculate the likelihood and the relative likelihood which quantifies the probability of the broken power law model being chosen over the null model as a best fit PSD model.

4.4.3 Other data sets

In [98], we had analyzed the unevenly sampled optical R band light curve from the campaign observations of S5 0716+714 using the periodogram, LSP, MHAoV and wavelet analysis techniques. The red noise portion of the periodogram was well fit with a power law with a slope α -2.00 ± 0.16. The fit was carried out using an earlier procedure which relied on the method of least squares to determine the fit parameters and the errors on the fit. An analytic goodness of fit test (the Kolmogorov-Smirnov test) yielded a p value of 0.99 indicating a good fit to the data.

In [100], we had analyzed an evenly sampled soft X-ray (0.75 - 10 keV) light curve of 3C 273 (obs I.D. 126700301) which was claimed previously to indicate a possible QPO [131]. We had shown using our analysis suite consisting of the structure function, periodogram, LSP, MHAoV and wavelet analysis that the statistical significance of this feature was very low and it did not appear consistently across all the power spectra.

Here, we analyze these light curves in more detail using our recently developed procedure which incorporates the fitting of data with multiple PSD model shapes and model selection using the Akaike information criteria. The goodness of fit of the best fit PSD model shape is then tested using of Monte-Carlo simulations. We also analyze these light curves using the LSP and MHAoV. Finally, the wavelet analysis is used to scan and identify regions where any possible QPO could be present along the observation duration.

Campaign data

The light curve, its periodogram with the best fit model representing the underlying PSD and the results of the LSP, MHAoV and wavelet analysis are plotted in Fig. 4.3. The light curve shows strong variability during the observation duration, confirmed by a strong variability amplitude of 77.11 %.

For the periodogram and wavelet analysis, the light curve of duration = 564032 s ($\sim$ 6.53 days) is first made evenly sampled with a time step size Δt of 420 s. The power law PSD model fit to the periodogram yields a slope α of -2.21 $\pm$ 0.04. It does not indicate any quasi-periodic feature above a 99 % analytic significance level. The AIC value is -1433.91. The slope α and AIC value above are based on the minimum log likelihood S obtained for the power law model applied to this data set. The bending power law PSD model fit to the periodogram yields a bend timescale $T_{\rm Ben}$ = 38269^{+24850}_{-10810} s. The slope α in the frequencies higher than the bend frequency is -2.40 $\pm$ 0.06 and the AIC value is -1324.63. The broken power law PSD model fit to the periodogram yields a break timescale $T_{\rm Brk}$ = 42180^{+27735}_{-11980} s. The slope $\alpha_{\rm Hi}$ in the frequencies higher than the break frequency is -2.30 $\pm$ 0.04 and the slope $\alpha_{\rm Low}$ in the frequencies lower than the break frequency is -1.00 $\pm$ 0.03. The AIC value is -1421.12. The AIC is least for the power law PSD model. It is then taken as the null model and the relative likelihoods for the bending power law and broken power law PSD models are determined to be 1.78 $\times$ 10^{-24} and 1.67 $\times$ 10^{-3} respectively indicating that the power law model is the best fit model.

A set of 5000 periodograms are simulated with the power law slope α = -2.21 using the procedure described in Chapter 3. These are then used to determine a rejection probability of 2.4 % indicating that the power law model is a good approximation to the underlying PSD shape. We thus see that the power law model is the best approximation of the underlying PSD. The slope α = -2.21 $\pm$ 0.04 is now well constrained.

The LSP and MHAoV are used to analyze the unevenly sampled light curve. They do not yield any statistically significant feature as inferred from the MC simulations based significance test. A possible quasi-periodicity of 141008 s $\sim$ 1.63 days with a MC simulation significance of 96.62 % is identified in the MHAoV. Though, since our detection criteria is at 99.9 % (see numerical experiments from Chapter 3), we cannot claim this to be a true feature. The wavelet analysis indicates a quasi-period centered at 112722 s $\sim$ 1.30 days with an MC simulations based significance of 90.15 %. Though, this feature is not observed stongly in the wavelet power spectrum. A broad, weak feature with a periodicity ranging between 50000 s $\sim$ 0.58 days and 100000 s $\sim$ 1.16 days is seen between 120000 s $\sim$ 1.39 days from the start of the observation and 220000 s $\sim$ 2.55 days from the start of the observation. The mean timescale is $0.87^{+0.29}_{-0.29}$ days and it lasts for $\sim$ 1.16 days.

The light curve thus does not indicate any strong quasi-periodic feature. Any features that are indicated are not detected consistently across all techniques and their MC simulations based statistical significance is too low to claim a detection. The slope of -2.21 $\pm$ 0.04 of the power law shaped PSD measured from this set of campaign observations is in rough agreement with the

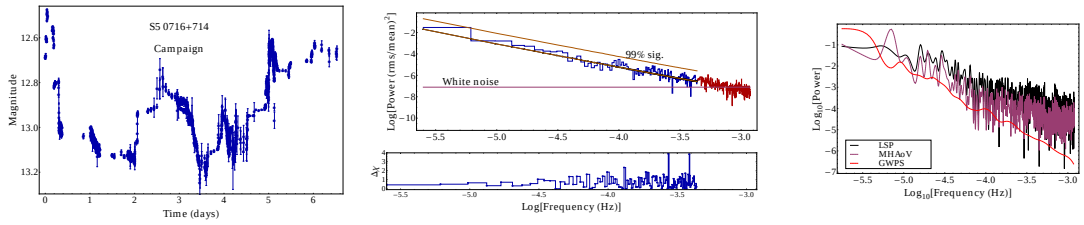

Figure 4.3: Left plot: Composite optical light curve of the blazar S5 0716+714 obtained from the campaign study. Middle plot: binned periodogram: fit portion is in blue and white noise region is in red. The best fit model is plotted over the fit portion and the residue $\Delta\chi$ =(data-model)/σ is shown below it. Right plot: LSP, MHAoV periodogram and global wavelet power spectrum results.

average slope of -1.86 ± 0.11 measured in §4.4.1 using the set of sixteen S5 0716+714 optical light curves which have moderate to high goodness of fit. We could also interpret this result as a steepening of the slope between the observation period of 1999 - 2003 and the campaign observations during 2011. In a period of $\sim$ 8 years, the slope has steepened by -0.35. This could indicate that physical processes occuring with lower frequency are gradually gaining prominence. If short timescale variability processes (few 1000 s) arise from jet based phenomena such as travelling shock fronts or orbital features in the jet, these longer timescales (few 100000 s) could arise from disk based viscous processes or the slow precession of the jet. In the context of the theoretical funnel model, the slopes are still similar.

X-ray light curve of 3C 273

The light curve, its periodogram with the best fit model representing the underlying PSD and the results of the LSP, MHAoV and wavelet analysis are plotted in Fig. 4.4. The light curve shows moderate variability during the observation duration with a excess fractional variability of 3.05 %. The light curve analyzed is of duration 57600 s and is evenly sampled with a time step size Δt of 100 s.

The power law PSD model fit to the periodogram yields a slope α of -0.73 ± 0.13. It does not indicate any quasi-periodic feature above a 99 % analytic significance level. The AIC value is -101.23. The bending power law PSD model fit to the periodogram yields a bend timescale $T_{\rm Ben}$ = 2305^{+160}_{-130} s. The slope α in the frequencies higher than the bend frequency is determined to be -1.50 ± 0.17. The AIC value is -98.93. The broken power law PSD model fit to the periodogram yields a break timescale $T_{\rm Brk} = 3297^{+307}_{-259}$ s. The slope $\alpha_{\rm Hi}$ in the frequencies higher than the break frequency is determined to be -2.50 ± 0.13 and the slope $\alpha_{\rm Low}$ in the frequencies lower than the break frequency is determined to be -0.20 ± 0.09. The AIC value is -98.44. The AIC is least for the power law PSD model. It is taken as the null model and the relative likelihoods for the bending power law and broken power law PSD models are determined to be 3.17 × 10^{-1} and 2.48 × 10^{-1} respectively indicating that the power law model is the best fit model. A set of 5000 periodograms are simulated with the power law slope α = -0.73 using the procedure described in Chapter 3. These are then used to determine a rejection probability of $<$ 0.1 % indicating that the power law

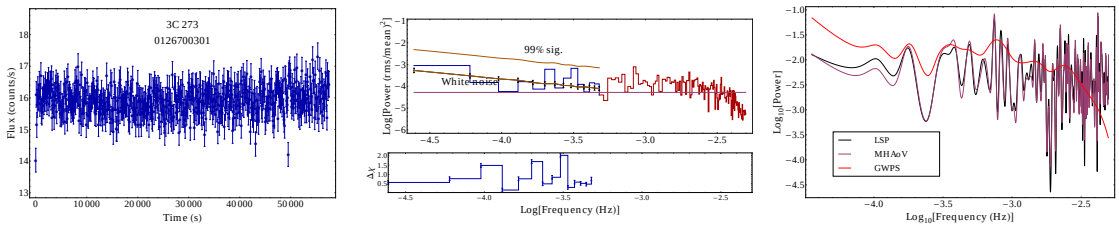

Figure 4.4: Left plot: X-ray light curve (0.3 keV to 10 keV) of the blazar 3C 273. Middle plot: binned periodogram: fit portion is in blue and white noise region is in red. The best fit model is plotted over the fit portion and the residue $\Delta\chi$ =(data-model)/σ is shown below it. Right plot: LSP, MHAoV periodogram and global wavelet power spectrum results.

model describes the PSD shape well. The LSP is used to analyze the light curve. It does not yield any statistically significant feature. The feature of $\sim$ 3300 s which was claimed to be present is not indicated with any strong significance. The MHAoV is then used to analyze the light curve. It too does not yield any statistically significant feature as inferred from the MC simulations based significance test. A quasi-periodic feature at 3032 s is indicated, though, its MC simulations based significance is very low at 2.19 %. The light curve is then analyzed using wavelet analysis. It does not indicate any statistically significant quasi-period. A quasi-periodic feature at 3382 s is indicated, though, its MC simulations based significance is very low at 7.39 %.

Thus, we rule out the presence of any statistically significant quasi-periodic feature in this data set. Any features that are indicated are not detected consistently across all techniques and their MC simulations based statistical significance is too low to claim a detection.

4.5 Conclusions

1. The time series analysis suite presented in Chapter 2 and the data characterization-search strategy developed in Chapter 3 were applied in the analysis of optical and X-ray light curves of blazars.

2. In the analysis of X-ray data, 80 % of the blazars show a broken power law. Though, all are ruled out based on strict statistical considerations.

3. The optical light curves of S5 0716+714 shows a power law PSD with a slope ranging between -1.86 (1999 - 2003 data) and -2.21 (2012 campaign data). This could be interpreted in terms of a larger emission region, possible in the context of an expanding jet.

4. A possible QPO reported in [131] for an X-ray LC of 3C 273 was ruled out based on our statistical analysis.

5. A weak time-scale of $\sim$ 1 day is seen in the optical light curve of S5 0716+714 from the campaign study.

6. The typical aperiodic variability time-scales over $\sim$ 1 day are consistent with expectations from orbital signatures in jets.

4.6 Appendix: Object description

4.6.1 Optical data: S5 0716+714

ROSAT observations in the soft X-rays (0.1 to 2.4 keV) indicates a rapid variability with the variation increasing by a factor of 7 in a duration of 2 days [134].

Variability studies at radio frequencies of 1.4 to 230 GHz, the data spanning over 20 years and in the optical U, B, V, R & I bands, the data spanning around 8 years indicate possible long term periodicities of 3.3 years in the optical wavelengths and 5.5 to 6 years in the radio frequencies of 5 GHz, 8 Ghz and 15 Ghz using the discrete Fourier transform, DCF and SF analyses [135]. A cross correlation between data in the radio wavelengths indicate that flux variations at lower frequencies lag those at higher frequencies with time delays ranging between a few days to several weeks, the interpretation of which is not constrained by the data. Possibilities include appealing to types of relativistic electron distributions: homogeneous or inhomogeneous populations. Cross correlation of radio with optical data indicates only weak features and no conclusion can be drawn from this.

A study aimed at determining a characteristic X-ray variability timescale from RXTE observations in soft X-rays (0.2 - 10 keV) makes use of an exponential timescale, defined in terms of the rising or decaying phase of the source observed during a major flare [136]. A timescale of $(0.147 \pm 0.052) \times 10^4$ is indicated. This cannot be directly connected to accretion disk based processes due to the source being a blazar and hence, the emission most likely arising from the jet.

A long term study of variability in optical B, V, R & I bands, the data spanning over 50 years between 1953 and 2003 indicates a periodic trend of 10 to 15 years, the B magnitudes ranging from a maximum of 14.2 ± 0.2 to a minimum of 17.99 ± 0.06 during this time [137]. The data suggests a precessing relativistic jet as it is inferred that the angle of the jet to the observer line of sight has decreased from 5.0° to 0.7°.

A comprehensive optical photometric campaign study lasting $\sim$ 7 years between 1996 - 2003 was carried out in the optical V, B, R & I bands with a majority of the ordinates ranging between 13.0 and 13.75 magnitudes [129]. A statistical study of the magnitute variation rate over different timescales indicated that its distribution was roughly exponential with a mean of 0.027 magnitude/hour which corresponds to a characteristic flux variation timescale of 37.6 hours. Some of these light curves (21 of 102) were analysed in §4.4.1 as part of our study on jet based variability processes.

A multiband optical monitoring indicates strong variability on 2 nights out 11 nights of observations in the V and R bands with amplitude changes of ≥ 0.2 magnitudes [138]. A possible time lag of $\sim$ 10 minutes is inferred between these two bands with the shorter wavelength leading the longer consistent with shock-in-jet models.

IDV studies in the optical R band were carried out for 5 nights during January - March, 2007 [139]. The observation durations range from 1.00 hour to 4.24 hours and indicate a variability

amplitude of 6.3 % and 5.2 % for 2 of the 5 observations. The source was caught in an outburst phase during this observation period with a maximum of R = 12.58 magnitude during 12 January 2007, close to earlier reported maxima of 12.75 magnitude in early 1995, 12.6 magnitude in late 1997, 12.55 magnitude in mid 2001 and another event in 2004. This event is thus consistent with the $\sim$ 3.3 year periodicity reported in [135].

Radio data from long term monitoring at 22 GHz (15.9 years), 37 GHz (16.74 years) and 90 GHz (8.82 years) indicates long term variability timescales of 5.5 years which lasts for 2.2 cycles and 4.3 years which lasts for 1.8 cycles in the 22 GHz and 37 GHz frequencies respectively [140].

A search for IDV timescales in archival data from [129] reveal quasi-periodicities ranging between 25 minutes and 73 minutes which suggest a black hole mass ranging between 2.47 and 7.35 x 10^6 $M_\odot$ for the case of a Schwarzschild black hole and 1.57 and 4.67 x 10^7 $M_\odot$ for a Kerr black hole [130]. These estimates could be taken as tentative lower limits on the mass.

Intra-night polarization variability studies indicate a polarization of 5.87 $\pm$ 0.1 % and a position angle of 116° with variability in both normalized Stokes parameters [141].

Structure function analysis applied to RXTE ASM based soft X-ray data (1.5 - 12 keV) of duration exceeding 12 years indicates possible quasi-periodic variability on a timescale of 347 $\pm$ 18 days [10].

Recent R band observations with a high cadence of 10 s reveal data with a 15 minute periodicity significant above the 3 σ level when analysed using the periodogram, SF and LSP time series analyses techniques [142].

Our multi-wavelength observation of this source in radio frequencies (2.7 GHz, 4.8 GHz, 4.85 GHz and 10.5 GHz) using 2 ground based facilities, optical wavelengths (U, B, V, R and I bands) using 9 ground based facilities and soft X-rays (0.2 to 10 keV) using the Swift space mission was carried out for a duration of 1 week in December 2011 [98]. The study was aimed at determining any possible correlation between the observed wavelength fluxes in order to identify the origin of the radio and optical emission in this source. A possible characteristic IDV on a timescale of $\sim$ 1 day was inferred from the optical data. Cross correlation between the 2.8 cm radio data with optical V band data indicates a moderate but not statistically significant feature, thus not allowing us to infer strongly the origin of the radio and optical emission.

A multi-wavelength study in radio frequencies (2.7 GHz to 345 GHz) using 9 ground based facilities, optical V band from 1 ground based facility and archival data from 2 other ground based facilities during the observation period, soft X-rays (0.3 to 10 keV) using the Swift space mission and γ-rays (100 MeV to 300 GeV) using the Fermi/LAT space mission in a survey mode was carried out between April 2007 to January 2011 to study flux variability, spectral properties of the source and to identify the origin of flaring activity [143]. During this period, the source was inferred to be highly active at optical and higher frequencies. A long-term variability trend ($\sim$ 350 days) is visible in the optical light curves. There are smaller variations on shorter time scales of $\sim$ 60 days within this.

4.6.2 X-ray data

Blazars

MS 0205.7+3509

Optical observations of a group of 33 X-ray selected samples includes MS 0205.7+3509 [144]. This study, aimed at determining IDV in these objects and to determine differentiating properties between radio selected BL Lac objects and X-ray selected BL Lac objects does not indicate variability (confidence = 4.5 %). A low variability amplitude of (4.8 ± 1.5) % is quoted.

Pointing observations of this source with XMM Newton on two occasions during 2001 and 2002 were used to study its spectrum in the soft X-rays (0.2 - 10 keV), determined to be synchrotron dominated and it is inferred that this object is likely to possess a low metallicity. The light curves of these two pointings (of durations $\sim$ 40000 s and $\sim$ 20000 s repsectively) do not show any strong variability with average flux being (2.80 ± 0.01) and (3.34 ± 0.02) $\times$ 10^{12} erg cm^2 s^1 respectively [145].

S5 0836+710

IDV studies in the 0.9 GHz, 2.8 GHz, 6.0 GHz and 11 GHz radio frequencies indicate weak variability during September 1995 and September 1998 with a maximum variability amplitude of 2 % measured over all the observation epochs between 1989 and 1999 [146].

BATSE/OSSE observations of this source in the 20 keV to 2 MeV energy range during December 1994 to October 1997 [147] indicate multiple flares and a maximum 20 keV to 100 keV flux of 3 $\times$ 10^{-10} erg cm^2 s^1 during January 1996 with a lag of $\sim$ 55 days compared to the maximum in the optical R band. The flux dies down to a mean of (1.32 ± 0.11) $\times$ 10^{-10} erg cm^2 s^1 in the next three months.

An optical photometric monitoring of γ-ray loud blazars in the B, V and R bands indicate a strong variability in the R band magnitude between 16.09 and 16.77 in the period between November 1995 and April 1996 [148].

A study of IDV and the description of the source properties including its compactness and strength of jet components in the 6 cm and 11 cm radio wavelengths characterizes variability in terms of a fluctuation index which depends on the root mean square deviation of the observed flux from the mean [149]. For this source, an index ranging between 0.68 % and 0.75 % in three observations during 1988 and 1989 in the 6 cm were measured with low significance and an index ranging between 0.44 % and 0.75 % in three observations during 1988 and 1989 in the 11 cm were measured, once again with low significance. These observations indicate that the source is in a low variability state.

Polarization measurements indicate a strong polarization of 6.59 ±0.23 % and 6.81 ±0.37 % based on two observations in the 3 cm wavelength [150], the corresponding flux being 1.771 ±0.029 Jy and 1.649 ± 0.06 Jy respectively.

Another study on the polarization with VLA observations in the 6 cm radio wavelength reveals a strong polarization of 9 % [151].

3C 273

A proposal to study strongly variable sources using the HST space based facility summarizes key results from historical monitoring of this source [152]. The B-magnitude ranges between 13.00 and 13.36 with an average of 13.20 and a variation of 0.36 in observations conducted during 1963 and 1980 [153] and between 12.59 and 13.46 with an average of 13.02 and a variation of 0.87 in observations conducted during 1974 and 1987 [154].

Multiwavelength archival data (few decades starting from $\sim$ late 1960s) and then recent data compiled upto 2006 are used to study the variability properties of the source in the radio frequencies (2.5 GHz to 37 GHz), infra-red wavelengths (0.35 mm to 3.3 mm), optical and UV (U, B, V, G, J, H, K, L, M, N and Q) bands, X-rays (0.5 keV to 430 keV) and γ-rays (3 MeV to 10 GeV), the data obtained from multiple ground based and space based facilities. The structure function technique is employed in the time series analysis to give periodic variability estimates [155] over these long timescales and the fractional variability amplitude $F_{\rm Var}$ which is the excess variance over and above the measurement noise is used to characterize the variability. Some periodicities include 4.4 $\pm$ 0.3 yr in the 8 GHz band observed by the University of Michigan Radio Astronomy Observatory (UMRAO) during 1963 to 2006 which also gives an average flux intensity of 0.29 x 10^{-11} erg cm^{-2} s^{-1} with $F_{\rm Var}$ = 0.157 $\pm$ 0.002, a 1.23 $^{+0.19}_{-0.03}$yr in the 37 GHz band observed by the Metsähovi Radio Observatory during 1970 to 2006 which also gives an average flux intensity of 0.92 x 10^{-11} erg cm^{-2} s^{-1} with a $F_{\rm Var}$ = 0.373 $\pm$ 0.007 , 3.9 yr in optical U, V and B bands, 0.5 yr in the UV wavelengths of 1300 Å , 1525 Å , 1700 Å and 1950 Å , 0.216 yr in the 4 to 9 keV X-ray energy range, 0.221 yr in the 9 to 20 keV X-ray energy range, 1.3 yr in the 20 to 70 keV energy range and 1.4 yr in the 70 to 430 keV energy range, the largest $F_{\rm Var}$ and the largest flux intensity being observed in the X-ray studies.

Archival radio data in the 4.8 GHz, 8 GHz and 14.5 GHz frequencies are studied for variability and possible correlation between variability and source brightness over long timescales [156]. The study uses the date-compensated discrete Fourier transform to analyze the time series and indicates periodicities of 8.8 $\pm$ 0.3 yr in 4.8 GHz with a false alarm probability of 0.001, 8.3 $\pm$ 0.2 yr in 8 GHz with false alarm probability of 0.006 and 8.2 $\pm$ 0.2 yr in 14.5 GHz with false alarm probability of 0.001.

GINGA archival data in the soft X-rays (2 keV to 10 keV) on five occasions between July 1987 and December 1988 (duration ranging between 5408 s and 31232 s) were studied for variability and to put constraints on the black hole mass [157]. Using the normalized power spectral density (NPSD), an estimate of a characteristic frequency of $9.61^{+2.65}_{-3.68} \times 10^{-6}$ Hz at which the product NPSD $\times$ frequency = 10^{-3} is determined. Assuming then that the AGN is a scaled version of the stellar mass black hole in Cyg. X1 (M = 10 M$_\odot$) whose characteristic frequency is 45 Hz, a black hole mass of $4.74^{+2.94}_{-1.02} \times 10^7$ is determined. This estimate is not very reliable though owing to the moderate goodness of fit of χ^2 = 43.6 with 11 degrees of freedom obtained for the power law model fit to the normalized power spectral density.

Archival X-ray data (2 keV to 20 keV) from RXTE observations of this source are used to study its time variability and spectral properties [158]. The study analyses data from 230 observations made between 1996 and 2000 which amounts a duration of 845 ks. The normalized power spectral

density (NPSD) and the structure function are used in the time series analysis. The NPSD was found to be well fit with a broken power law PSD model, the goodness of fit measured through a chi-square fit with $\chi^2 = 7.3$ with 6 degrees of freedom. A break frequency at $(4.7 \pm 1.5) \times 10^{-6}$ Hz corresponding to a timescale of $\sim$ 3 days, high frequency region slope $\alpha_{\rm High}$ = -2.6 $\pm$ 0.1 and low frequency region slope $\alpha_{\rm Low}$ = -1.4 $\pm$ 0.2 were determined. The spectral analysis indicates that the emission is well fit with a power law, consistent with other blazar spectra indicating that the obtained timing properties described previously are likely to arise from jet based processes which could include changes in acceleration of the electron population giving rise to the emission, in the magnetic field strength or in the beaming factor.

EGRET observations in the γ-rays (30 MeV to 50 GeV energy range) during 18 viewing periods lasting upto the end of the fourth cycle measure a flux ranging between 9.6 $\pm$ 4.2 x 10^{-8} photons cm^{-2} s^{-1} and 55.7 $\pm$ 11.9 x 10^{-8} photons cm^{-2} s^{-1} and a variability index of 3.48 which indicates that the object is strongly variable [159].

The Swift/BAT all sky survey in the hard X-rays (14 to 195 keV) to study variability in this energy band indicates a X-ray luminosity of $\log L_X = 46.26$, an average photon count rate for a 20 day binned light curve of 5.05 $\times$ 10^{-4} counts s^{-1} and a corrected intrinsic variability which is the excess variance over and above the measurement noise for a 20 day binned light curve of 15$\pm$ 5 % [160].

AO 0235+16

Two photometric observations of this object give high polarizations of the order of 10 % [161]. Compiled data along with polarimetric studies indicate a flux of 2.24 Jy in 5 Ghz band, an apparent V magnitude of 19 and a degree of polarization of 0.3 $\pm$ 0.1 % [162].

A WEBT based optical monitoring program [163] indicates large-amplitude outbursts in the B band, the minimum magnitude being 15.09 $\pm$ 0.18 and the maximum magnitude being 20.5 $\pm$ 0.05. R band magnitudes ranging between 14.03 $\pm$ 0.08 and 19.47 $\pm$ 0.06 are seen. The spectral index is seen to be almost a constant at ~ -2.8.

Characteristic timescales of 11.2 to 11.5 yr are revealed from the DCF of the optical data. Observations for micro-variability indicate a maximum change of 0.43 on a V magnitude of 17.02 $\pm$ 0.01 [164].

A periodicity search in 16 years of optical data using the discrete correlation function (DCF) and the Jurkevich method yields a possible periodicity of 2.95 $\pm$ 0.15 yr [25].

A compilation of optical data with a study on intra-night variability presents a absolute B magnitude of -27.6, a radio spectral index of 0.67 based on non linear fits to non-simultaneous data, a polarization of 14.9 %, periodicity timescales (using structure function) of $\sim$ 3.6 hrs and 3.4 hrs with the corresponding amplitudes being 12.8 % and 10.4 % [165].

Studies on IDV variability in the R band indicate variability amplitudes of 13.7 % and 9.5 % on 2 occasions. A search for IDV reveals amplitudes of 13.7 % and 9.5 % on two out of three occasions with confidence limits of $>$ 99 % [139].

Radio observations at a large number of frequencies (318 MHz, 430 MHz, 606 MHz, 880 MHz, 1.4 GHz, 4.8 GHz, 8 GHz and 14.5 GHz) over a period of 6 years indicate correlations between the

flux density variability in the different bands indicating an intrinsic variability in the source [166].

Another study involving a long term monitoring (14 years) in the 318 MHz and 430 MHz reveals variability in both frequencies but which are uncorrelated. Variability is characterized by means of visual inspection, usage of a modulation index and the structure function [167].

Variability studies at 5 Ghz indicate a flux density variation of 7.02 % with a timescale of 32 hours, the average flux being 0.47 Jy [168].

A long term study of variability and spectral characterization in the wavelengths of 21 cm, 18 cm, 11 cm, 6 cm, 3.6 cm, 2.8 cm, 2 cm, 1.3 cm 9 mm and 7 mm indicates modulation indices of 45.7 % with an associated average flux of 1.31 $\pm$ 0.56 Jy at 11 cm, 72.3 % with an associated average flux of 1.19 $\pm$ 0.84 Jy at 6 cm, an average flux of 2.48 $\pm$ 1.67 Jy at 3.6 cm, 73 % with an associated average flux of 1.83 $\pm$ 1.29 Jy at 2.8 cm and average flux of 2.04 $\pm$ 1.78 Jy at 1.3 cm [169].

OJ 287

Optical polarization studies (Visvanathan & Wills 1998) indicate an intrinsic source based polarization of 12.2 $\pm$ 0.1 % with radio (2.7 to 5 GHz) spectral index of 0.42. Intra-night polarization variability studies indicate a high polarization of 16 % and a position angle of 126^o with variability in both normalized Stokes parameters (Villforth et al. 2009). R band observations using the Vainu Bappu observatory (VBO) indicate a variability from a minimum of 14.763 $\pm$ 0.039 to a maximum of 15.725 $\pm$ 0.04 during 6 observations (Ghosh et al. 2002). A periodicity search in 104 years of optical data using the discrete correlation function (DCF) and the Jurkevich method yields possible periodicities of 5.53 $\pm$ 0.15 yr and 11.75 $\pm$ 0.5 yr (Fan et al. 2002). A large amplitude variation in the R band magnitude of 0.35 over a short timescale of 31 minutes is indicated in an optical photometric study in the V, R and I bands with the 1 m telescope at the Yunnan astronomical observatory (Zhang et al. 2007).

Variability studies on ASM data of $>$ 12 years from RXTE observations indicates periodicities of 148 $\pm$ 19 days and 337 $\pm$ 26 days from sturcture function analysis (Rani, Wiita & Gupta 2009).

3C 454.3

This object has been studied closely over the years for optical variability. A set of observations in the B band compiled over a period of 9 years indicates a steady fluctuation ranging from a minimum of 17.4 to a maximum of 16.35 [170]. Variability studies in the IR wavelengths of 2.7 mm and 1.5 cm indicate fluxes of 7687 $\pm$ 12 mJy and 10387 $\pm$ 57 mJy at 1.5 cm from 2 observations and 8086 $\pm$ 107 mJy at 2.7 mm with a 2.7 mm to 2.5 cm spectral index of -0.15 [171]. A study of the optical polarization properties indicates an approximate apparent V magnitude of 16.1, a polarization of 1.37 $\pm$ 0.46 and a polarization position angle of 166^o [172]. Radio observations that include polarization studies indicate a maximum polarization of 5.78 % at 8 GHz with an average polarization of 3.173 % and a spectral index of 0.129 encompassing the 4.8 GHz, 8 GHz and 14.5 GHz frequencies observed from UMRAO, the data being collected over a period of 33 years [173].

A long term variability study using data from the Einstein X-ray observatory in the energy range 0.2 to 3.5 keV indicates an average count rate of 0.117 counts s^{-1} but does not indicate variability durig the observation [174].

Chapter 5

X-ray variability and the break frequency in AGN

5.1 Introduction

X-ray emission and variability in Seyfert type 1s and the narrow line Seyfert 1s (radio quiet AGN) are believed to be dominated by the accretion disk in the context of unification models for AGN [32, 33] as the observer line of sight intersects the disk as discussed in Chapter 1. Short time-scale variability in the X-rays can be studied with the availability of almost contiguous light curves for some objects with small sampling intervals from multiple space based instruments such as XMM Newton, Chandra, Suzaku and others in the energy range of 0.1 keV - 100 keV. For variability over a time-scale Δt, the size of the emitting region can be at the most $c\Delta t$. Typical short time-scales from observed light curves range from $\sim$ 1000 s to a few hours. For a typical black hole mass of 5 $\times$ 10^6 $M_\odot$, this corresponds to an emitting region of size $\sim$ 41 M to a few 100 M. The inferred location of the emission region is between a few to a few tens of M from spectral modelling of the broad X-ray emission lines e.g. [175]. As this location corresponds roughly to the ISCO radius which depends on the black hole spin, it may lie closer to the black hole for high spins.

Observed UV to X-ray spectra from these AGN indicate the presence of a colder population of gas ($T \leq 10^5$ K) constituting the accretion disk sandwiched by another population at a much higher temperature, interpreted in terms of a layer of optically thin, thermally agitated relativistic electrons e.g. [176, 177]. As argued in the Chapter 1 (Introduction), soft X-rays can be produced either through direct accretion disk based black body emission or through the inverse-Compton scattering of low energy photons by the corona.

Spectral and timing studies in the X-rays can be used in a complementary manner to constrain the black hole mass, spin and the emission region properties. The results can be used as a qualitative indicator of these properties in radio loud AGN if one were to account for effects due to the relativistic jet during a quiescent phase.

In [178], an X-ray (0.5 keV to 10 keV) variability study is conducted with archival Advanced Satellite for Cosmology and Astrophysics (ASCA) data for 36 Seyfert 1 galaxies. A maximum root

mean square variance of $(78.4 \pm 8.80) \times 10^{-3}$ is inferred for MRK 766. The variance is found to be related to the Hβ FWHM as $\sigma_{rms} \propto (FWHM\ H\beta)^{-2.8}$, consistent with rapid variability and narrow lines leading to a small black hole mass. In RXTE (2 keV to 12 keV) based long term X-ray variability studies spanning 3 years ([179]) and 7 years ([180]), an anti-correlation between source luminosity and variability amplitude is measured on short time-scales and is found to be in agreement with previous studies e.g. [181, 182] and it is suggested that this could be due to either a positive correlation between the luminosity and a break time-scale or an inverse correlation between luminosity and overall amplitude. In [183], a one day study of simultaneous X-ray and optical variability is conducted for 8 nearby Seyfert 1 galaxies using XMM Newton. The X-ray variability amplitude is observed to be greater than that of the optical. In the optical, a maximum rms amplitude of 2.9 % is measured for NGC 3783. The rms amplitude for the X-ray light curves ranges between 2.0 % for Ark 120 and 47.6 % for NGC 4051. A cross correlation analysis between the optical and X-ray light curves does not indicate any significant correlation for three of the four objects showing a detectable optical variability, implying that re-processing of optical radiation may not be a dominant mechanism of production of the X-rays. In [184], a comparative study of the spectrum of 14 hard X-ray selected ($>$ 20 keV) NLS1 galaxies from the fourth INTEGRAL/IBIS catalogue is conducted in the 0.3 keV to 100 keV energy range using data from XMM Newton, Swift/XRT and INTEGRAL/IBIS. Black hole masses are calculated using the line width-luminosity-mass relation $M_{BH} \propto R_{BLR}v^2$ where R_{BLR} is the size of the broad line region (BLR) obtained from $R_{BLR} \propto L_{Bol}$ relating it to the bolometric luminosity, v^2 is the velocity of the virialized BLR clouds, measured as the full width at half maximum of the Hβ emission line for nearby sources. The study shows that NLS1 galaxies generally host low mass black holes, the calculated mass distribution of the objects peaking at $\sim 10^7$ $M_\odot$. It must however be noted that NLS1 black hole mass estimates consistently fall below the M_{BH} - σ relation as indicated by previous studies e.g. [185]. Hence, mass obtained from this method may be systematically underestimated by a small factor.

In [186], a compilation of Seyfert galaxies indicating evidence for relativistically broadened X-ray emission lines is made. The study includes an analysis of X-ray data (0.2 keV to 700 keV) from Chandra X-ray Observatory, XMM-Newton and Suzaku. Black hole spin for many of these objects, constrained through spectral fit procedure discussed in Chapter 1 is presented. Evidence suggested to support spectral studies include the observation that the disk extends to the ISCO for a given spin a above a threshold in the mass accretion rate and arguments which imply that free falling material inside of the ISCO is fully ionized thus emitting only weakly e.g. [187, 188]. In [189], an XMM Newton (2 keV to 10 keV) based statistical study of 149 Seyfert type 1 galaxies is conducted to collect evidence for a relativistically broadened Fe Kα line. The main interpretations are drawn from a flux limited sub-sample of 31 Seyfert type 1 galaxies. Strong evidence for a relativistically broadened Fe Kα line is inferred for 36 % of the flux limited sources (11 of 31), interpreted as a lower limit to the fraction of all possible sources which could provide such an evidence. Inferences include an average line equivalent width of $\sim$ 100 eV, an average disc inclination of 28°$\pm$ 5° and black hole spins of $0.86^{+0.01}_{-0.02}$ for MCG-6-30-15 and $0.74^{+0.03}_{-0.04}$ for MRK 509. [190] conduct a survey

of the Fe K emission lines from archival Suzaku and Swift-BAT (0.6 keV - 100 keV) spectra of nearby (z $\leq$ 2) Seyfert 1 galaxies. After accounting for probable sources of its emission such as obscuring warm absorption clouds or as a part of an outflow, the residual of the broad component is studied with a spectral fit. For a sample of 46 objects studied, 23 objects (50 %) are found to require relativistic effects to account for the observed emission with a statistical significance $>$ 99.5 %. An average disk inclination towards the observer line of sight of 33° $\pm$ 2° is inferred from 20 objects. A maximally spinning BH ($a = 0.998$) is ruled out for all objects with a confidence of 90 % with a ranging between 0 and 0.80.

In this chapter, we present theoretical models of observational signatures from dynamic processes, likely to be present in the inner accretion disk in §5.2. These include a discussion of dynamical processes, the QPO phenomenon and properties which can be extracted from a detected QPO followed by a discussion on the break frequency, its possible origin and related physics which can be inferred from observational results. We then apply the search-characterization strategy developed in Chapter 3 to X-ray light curves of Seyfert galaxies (Sy1s and NLSy1s). The details of the data reduction and light curve extraction are presented in §4.3. We then present the results of the analyses with a discussion on the possible theoretical implications alongside a comparison of results from literature in §5.3.1.

5.2 Theoretical models: dynamical processes

5.2.1 Dynamical time-scale and related physics

Dynamic processes yield the shortest characteristic time-scale over which orbital features and inhomogeneities in disk and jet such as flares could occur or cause perturbations and is given by $t_\phi \sim r/v_\phi$. Black hole mass and spin can be determined if observed light curves or spectra indicate the presence of these processes.

The Keplerian angular frequency of a test particle in circular motion around a Kerr black hole is given by (e.g. Frank, King & Raine)

$$\Omega = \frac{2\pi}{T} = \frac{M}{r^{3/2} + a}. \tag{5.1}$$

T is the orbital periodicity associated with the angular frequency and r is the radial distance from the black hole with a spin a. Using the above expression in C.G.S. units, T can be written as

$$T = 2\pi(r^{3/2} + a)\ (1+z)\ GM_{BH}/c^3\ s = 30.93(r^{3/2} + a)\ M_6\ (1+z)\ s \tag{5.2}$$

where T has been corrected to include the cosmological redshift factor z and the black hole mass is scaled in terms of the solar mass, $M_6 = M_{BH}/(10^6 M_\odot)$. T, M_{BH} and a are thus related through the above set of expressions. If there is evidence for a quasi-periodicity from light curves of AGN, depending on the relation to the dynamic time-scale, this could be caused by the orbital motion and radial drift of the flow in the disk.

A measure of the evolution of the periodicity or the orbital frequency is the quality factor of a QPO, $Q = \Omega/\Delta\Omega$ where $\Delta\Omega$ is the change in the angular frequency caused by the radial drift of the orbiting material during each orbit. The quantity, $\frac{\Delta T}{T} = \frac{\Delta\Omega}{\Omega} = Q^{-1}$. If a QPO is detected from the PSD analysis of the observed light curve of an AGN, its characteristics such as Δf, amplitude and peak frequency can be determined using a Lorentzian with a power law fit model [112] explained in detail in Chapter 3.

The quality factor can be expressed in terms of the physics in the inner accretion disk [191]

$$Q^{-1} = \frac{\Delta T}{T} = \frac{\Delta\Omega}{\Omega} = \frac{1}{\Omega}\frac{d\Omega}{dr}\frac{dr}{dt} \tag{5.3}$$

As we consider Δt to be the change in angular frequency due to radial drift over one orbit, $\Delta t = d\phi/\Omega = 2\pi/\Omega$. We can extend this idea to relativistic flows by

$$Q^{-1} = \frac{2\pi}{\Omega^2}\frac{d\Omega}{dr}\frac{u^r}{u^t} \tag{5.4}$$

where u^r and u^t are the four-velocity components of the orbiting flow. For a bulk flow of material in Kerr geometry, $u^r = \gamma_r\beta_r\sqrt{\frac{\Delta}{r^2}}$ and $u^t = \sqrt{\frac{A}{\Delta r^2}}\gamma_\phi\gamma_r$, obtained for a bulk flow in radial motion with a Lorentz factor γ_r and a velocity β_r as well as orbital motion with a Lorentz factor γ_ϕ on the disk as viewed by an observer in the local non-rotating frame (see Chapter 6 for its derivation); $A = (r^2 + a^2)^2 - a^2\Delta\sin^2\theta$ and $\Delta = r^2 + a^2 - 2Mr$ are quantities used in the expression for the Kerr metric. Thus,

$$\frac{u^r}{u^t} = \frac{\beta_r\Delta}{\sqrt{A}\gamma_\phi} \tag{5.5}$$

Using which Q can then be written as

$$Q^{-1} = \frac{2\pi}{\Omega^2}\frac{d\Omega}{dr}\frac{\beta_r\Delta}{\sqrt{A}\gamma_\phi} \tag{5.6}$$

Q thus depends of the radial distance r, the polar angle defining the plane of motion of the emitting source θ and the black hole spin a. The azimuthal Lorentz factor $\gamma_\phi = \sqrt{1-(v^\phi)^2}$ where v^ϕ is the azimuthal orbital velocity of the bulk flow. It is given by the expression $v^\phi = \frac{A\sin\theta}{\Sigma}\frac{\Omega-\omega}{\sqrt{\Delta}}$ where $\Sigma = r^2 + a^2\cos^2\theta$ and $\omega = 2ar/A$ is the rotational angular frequency due to the frame dragging effect of the spinning black hole. If we assume that the flow is along the equatorial plane ($\theta = \pi/2$) and for Keplerian angular velocity, $\Omega = \frac{M}{r^{3/2}+a}$ as in eqn. (5.1), the quantity Q then depends on the radial distance r, the spin of the black hole and the radial velocity of the bulk flow β_r:

$$Q = \frac{1}{3\pi r^{1/2}}\frac{\sqrt{A}}{\beta_r\Delta}\left(1 - \frac{(A - 2ar(r^{3/2}+a))^2}{\Sigma^2\Delta}\right)^{-1/2} \tag{5.7}$$

A simple estimate of β_r can be made. The local sound speed in the medium is $c_s \sim \sqrt{kT}m_e$ for a gas composed of electrons of mass m_e obeying the ideal gas equation. For a typical disk

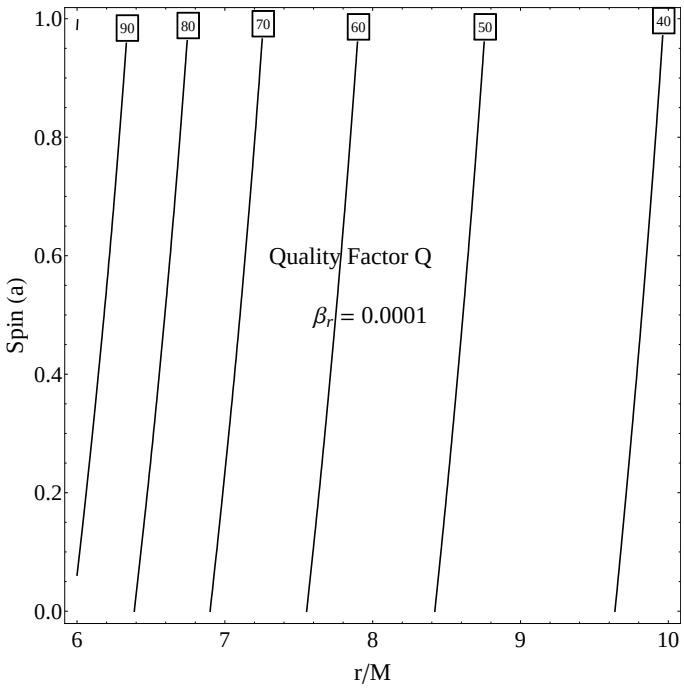

Figure 5.1: Contours of the quality factor $Q = Q(r, a)$ assuming a radial bulk flow velocity $\beta_r = 0.0001$. For a given spin a, Q decreases from 90 to 40 for the emission radius r increasing between $6M$ and $10M$. For a given radius, Q increases gradually when the spin increases from 0 to 0.998.

temperature $T \sim 10^5$ K as in the inner disk, $c_s \sim 1.23 \times 10^6$ m/s. From the discussion in Chapter 1, $v_r \ll c_s$. Thus, $\beta_r = v_r/c \ll 0.004$. In the current analysis, we use a $\beta_r = 0.0001$ to illustrate contours of $Q = Q(r, a)$ as plotted in Fig. 5.1. The quality factor evaluated increases with a decrease in β_r. When a bulk flow is radially drifting inward towards the central BH, if its radial velocity β_r is very low (~ 0.0001), any orbital feature present on the disk is likely to exist for a large number of cycles, a lower limit to which can be determined using the wavelet analysis in the analysis suite. Also, the change in orbital frequency $\Delta\Omega$ is very small for this β_r, thus in turn giving rise to a high Q and hence, a sharp QPO feature. If β_r is large (e.g. 0.1), then, there is insufficient time for the QPO to develop as the radial bulk motion is very fast leading to a broad QPO. In many cases, this would merge with the continuum of the PSD shape, rendering it difficult to statistically identify it. This could be a possible explanation for the absence of a QPO detection in the light curves of radio quiet AGN.

5.2.2 Break frequency and the region of emission

A break frequency in analyzed light curves is characterized by a clear demarcation in the power law slope of the periodogram in the frequencies lower than the break (flatter with slope ranging between 0 and -1) and that in the frequencies higher than the break (steeper with slope ranging between -1 and -2). The broken power law model is applied to the red-noise dominated portion of the periodogram in the log-log space. The fit procedure, identification of the best fit PSD models

among multiple competing models and the extraction of model parameters can be found in [112] and Chapter 3. The broken power law model is given by

$$\begin{aligned} I(f_j) &= A(f_j/f_{Brk})^{-\alpha_{hi}}, f_j > f_{Brk} \\ &= A(f_j/f_{Brk})^{-\alpha_{low}}, f_j < f_{Brk} \end{aligned} \tag{5.8}$$

If the power law break model is the best fit PSD model, the parameters from the fit include the break frequency f_{Brk}, the slope of the high frequency region, α_{hi} and the slope of the low frequency region α_{low}. Broken power law models can be used in the detection of large break time-scales (at low Fourier frequencies) such as 10^6 s or a few days from data spanning over a few years from satellite observations in the soft to hard X-rays. Such a break frequency could be associated with a typical size of the accretion disk and could arise due to a characteristic outer radius of the disk. In [192], RXTE (0.2 keV to 10 keV) light curves are obtained from continuously monitoring six Seyfert 1 galaxies (Fairall 9, NGC 5548, Ark 564, NGC 3783, NGC 3516 and NGC 4151) for a period of a few years. A variability study is then done for time-scales ranging between days and years. The excess fractional variance for these light curves ranges between (5.3 ± 0.4) % for the short time-scale light curve of NGC 5548 to (39 ± 1.8) % for the long time-scale light curve of Fairall 9. A broken power law model for the PSD shape is accepted as a good fit in one of the six sources (Ark 564) with an acceptance probability of 97.3 %. A break frequency at $1.59^{+4.73}_{-0.95}\times 10^{-6}$ Hz, a low frequency power law slope of $0.05^{0.55}_{-2.05}$ and a high frequency power law slope of $1.20^{+0.25}_{-0.35}$ are inferred. A study of the long term soft X-ray (2 keV to 10 keV) light curves of AGN from RXTE, XMM-Newton and ASCA is aimed at addressing the relation between the excess variance and the black hole mass [193]. A significant anti-correlation between the excess variance σ_{NXS} and black hole mass M_{BH} is determined in this study. A single value of the excess variance could correspond to a variety of PSD shapes. It is thus suggested that the assumption of a specific PSD shape can be used to infer the possible effects on the relation between σ_{NXS} and M_{BH} and compare it with the observation based relationship to make a claim on the validity of the PSD shape.

A sharp cut-off in the PSD shape at high frequencies ($\geq 10^{-4}$ Hz) above which is a power law portion could occur due to emitting bulk flow on the disk making a transition from tightly bound orbits on the disk to a free falling inward spiral towards the central black hole upon crossing the inner edge of the accretion disk. For Keplerian angular velocity, $\Omega = \dfrac{M}{r^{3/2}+a}$ as in eqn. (5.1), the break time-scale T_B is related to the location of r_{ISCO} and is given by

$$T_B = 30.93\ M_6(1+z)f(a)\ s \tag{5.9}$$

where

$$f(a) = (r^{\frac{3}{2}}_{ISCO}(a) + a) \tag{5.10}$$

and

$$r_{ISCO} = 3 + Z_2(a) - [(3 - Z_1(a))(3 + Z_1(a) + 2Z_2(a)]^{\frac{1}{2}} \tag{5.11}$$

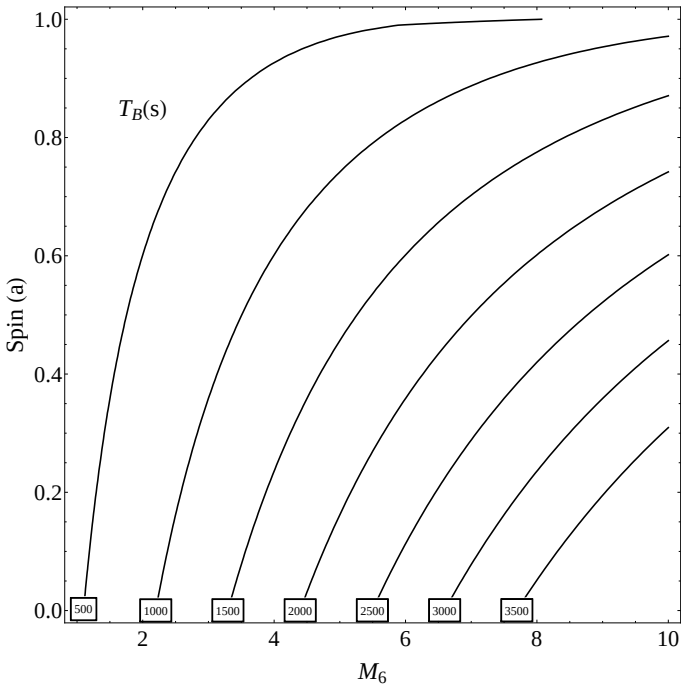

Figure 5.2: Contours of the break time-scale $T_B = T_B(r, a)$. The timescales indicated in the plot range between $\sim$ 500 s and 3500 s for the black hole mass in units of M_6 ranging between 1 and 10 and the spin a ranging between 0 and 0.998. The time-scales indicated in the plot are chosen such that they can be used in the direct comparison for T_B inferred from short time-scale X-ray light curves where it is expected to range between a few 100 s and a few 1000 s.

$$Z_1(a) = 1 + (1-a^2)^{\frac{1}{3}}[(1+a)^{\frac{1}{3}} + (1-a)^{\frac{1}{3}}]; Z_2(a) = (3a^2 + Z_1^2(a))^{\frac{1}{2}} \tag{5.12}$$

Thus, the break time-scale T_B, corrected to include the cosmological redshift factor is dependent on the black hole mass scaled in terms of the solar mass, $M_6 = M_{BH}/(10^6 M_\odot)$ and the black hole spin a. Contours of $T_B(M_{BH}, a)$ are plotted in fig. 5.2.

Emission could at the most arise from sources near the innermost stable circular orbit (ISCO) for a Keplerian disk around the SMBH. We can place constraints on the minimum size of the emitting region, spin of the SMBH and its mass using certain conditions. The constant spin Ω in a rotating metric must obey $\Omega_{\rm min} < \Omega < \Omega_{\rm max}$ where

$$\Omega_{\rm max,min} = \frac{-g_{t\phi} \pm (g_{t\phi}^2 - g_{tt}g_{\phi\phi})^{\frac{1}{2}}}{g_{\phi\phi}}. \tag{5.13}$$

For the Kerr case this leads to the condition that,

$$\begin{aligned} &4a^4 r + 8a^4 + 2a^3 r^{\frac{7}{2}} + 8a^3 r^{\frac{5}{2}} + 8a^3 r^{\frac{3}{2}} + a^2 r^5 \\ &-a^2 r^4 - 2a^2 r^3 + 2ar^{\frac{11}{2}} + 4ar^{\frac{9}{2}} + r^7 - 3r^6 > 0, \end{aligned} \tag{5.14}$$

where r and a are in units of M. In addition, the emitting region must lie outside the event horizon

r_+ of the hole given by,

$$r > r_+ = 1 + \sqrt{(1 - a^2)}. \tag{5.15}$$

The constraints above on the emission region and spin of the black hole along with information on the redshift z of the AGN can be used in $\frac{M_\bullet}{M_\odot} = \frac{3.23 \times 10^4 P}{[r^{\frac{3}{2}} + a](1+z)}$ to place upper limits on the SMBH mass $M_\bullet$ and a plot representing the above condition are presented in Fig. 5.3.

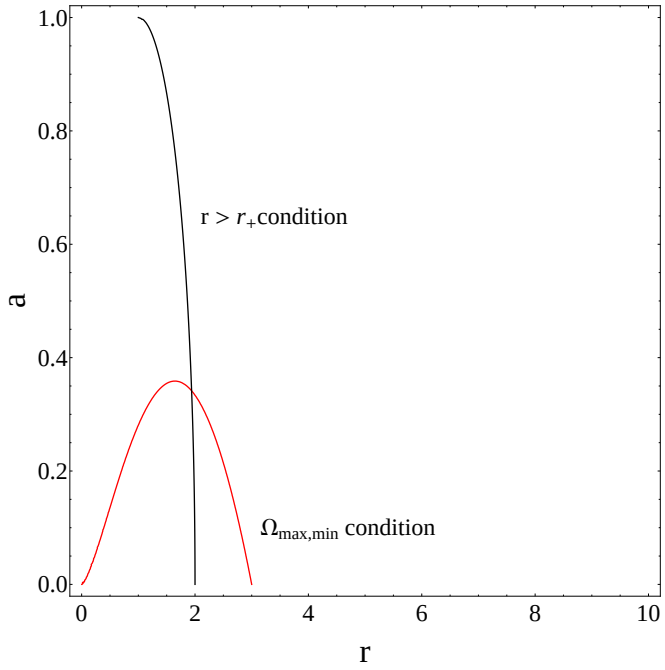

Figure 5.3: The equality in the inequalities from eqns. (5.14) and (5.15) are plotted as functions of r and a. The region to the right of both the contours is the allowed region for emission.

5.3 Data selection and reduction

To study models of variability through disk based processes, we first identified AGN which could be potential candidates to study the accretion disk. Then, those candidates indicating strong X-ray variability as gauged by their light curves using the excess fractional variability index F_{var} were identified. The time series analysis suite developed in Chapter 2 was then applied to extract information on the variability and its properties from their light curves.

We chose a set of 16 Seyfert galaxies: MRK 335, Q 0056-363, Fairall 9, 3C 120, ARK 120, MRK 79, NGC 3516, NGC 3783, NGC 4051, NGC 4151, MRK 766, MCG-6-30-15, IC 4329A, MRK 509 and NGC 7469 which indicated mild to strong variability. All the above objects have been studied for and indicate the presence of a relativistically broadend Fe K α 6.4 keV emission line measured by multiple instruments such as Chandra, XMM Newton and Suzaku in multiple observation epochs.

A set of 58 light curves from the 16 Seyfert galaxies in the soft X-ray band (0.3 keV to 10 keV)

are extracted and reduced for the analysis using SAS 12.0. Reduction, light curve extraction and pre-processing of the light curves are carried out as follows:

The light curve for the energy range > 10 keV was first observed and manually truncated to a good time interval (GTI) by eliminating regions of the light curve dominated by proton flaring events. Then, we placed a circular aperture of size ranging from $35''$ to $45''$ around the object depending on the specific data set. The light curve of the object was then extracted with a time bin size of 100 s in the GTI for the energy range 0.3 keV to 10 keV. By placing a circular aperture of the same size as the object slightly away (about $200''$) from the source to prevent contamination by source photons, we extracted the light curve of the background in the same energy range with the same bin size in the GTI. The size of the apertures around the object and the background are tailored for each data set in order to avoid dark regions or patches with no counts.

The object light curve with time bin size of 100 s was then obtained by subtracting the background from the source. Where small data gaps (< 10 points) were present in an object light curve, caused due to the removal of flaring portions, we performed a linear interpolation in this region and used these estimates to obtain the final analysable light curve with time bin size of 100 s, similar to the procedure followed in [132]. The data characterization and search strategy developed in the previous chapter is used to analyse the above optical and X-ray light curves.

5.3.1 Results and discussion

Information on basic properties of the studied Syefert galaxies is presented in Table 5.2. We perform a linear fit to F_{var} vs. M_{BH} data in the log-log space with and without the results of the NLSy1 population (MRK 335, NGC 4051 and MRK 766) due to suggestions from literature e.g. [194] which expect $F_{var} \propto M_{BH}^{-0.5}$ only when Seyfert type 1 galaxies are considered. The average $F_{\rm var}$ ranges between 3.12 (ARK 120) and 26.60 (MCG-6-30-15) for a reduced sample of 13 objects. We removed another point for Q 0056-363 as its black hole mass estimate is uncertain and the quoted value has not been confirmed using the multiple mass measurement procedures. The fit to the average $F_{\rm var}$ vs M_{BH} data in the log-log space for 12 objects yields a slope of -0.31, plotted in fig. 5.4, flatter compared to the expected -0.5. With the inclusion of the data from the NLSy1 galaxies, the fit for 15 objects yields a steeper slope of -0.39 plotted in fig. 5.5, within the error bars of previous studies.

MC simulations based significance testing of detected peaks in the LSP, MHAoV and wavelet analysis periodograms do not indicate any statistically significant QPO in any of the analyzed data sets.

For the X-ray light curve of REJ 1034+396, analyzed in Chapter 3, the power law with a Lorentzian QPO was determined to be the best fit PSD shape (QPO significance > 99.94 %) with an amplitude R of 0.05 ± 0.01 and a quality factor Q of 32.0 ± 6.5. If the QPO,peaked at 3733 s is due to orbital features in the inner disk, constraints can be placed on the black hole mass M_{BH} and spin a using eqn. (5.2) from §5.2.1. The region of variability and the emergence of the QPO feature in the light curve are likely to be close to r_{ISCO}. For a non-rotating black hole, if we assume an emission ring of radius $r = 10M$, slightly outside the ISCO though still within the inner region,

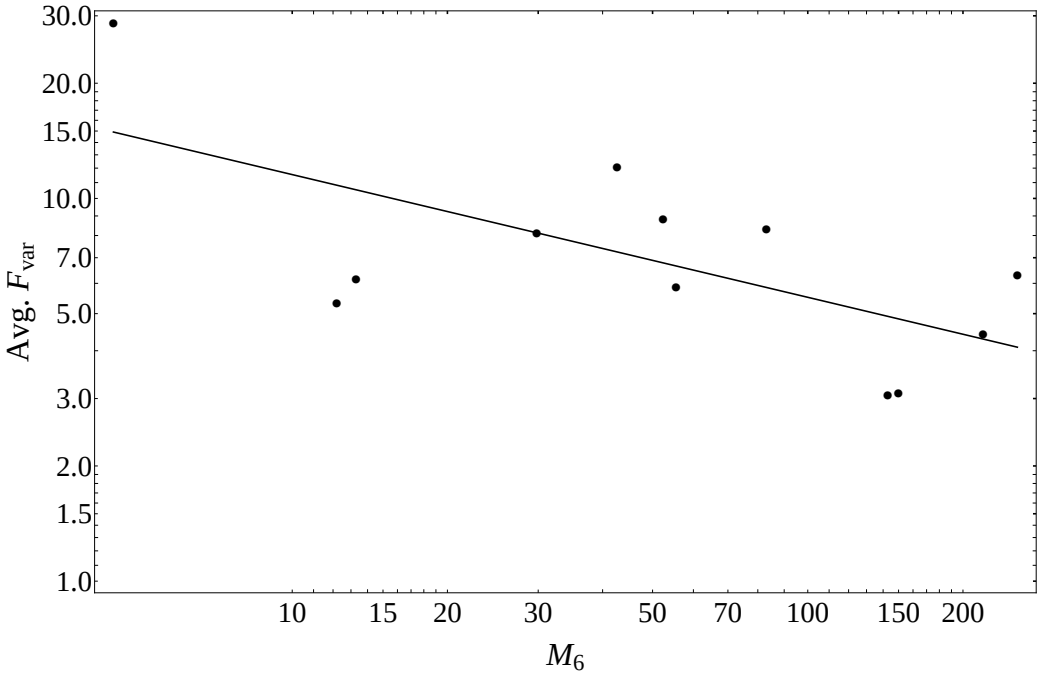

Figure 5.4: Linear fit in the log-log space to the $F_{\rm var}$ vs M_{BH} data for the Sy1 galaxies.

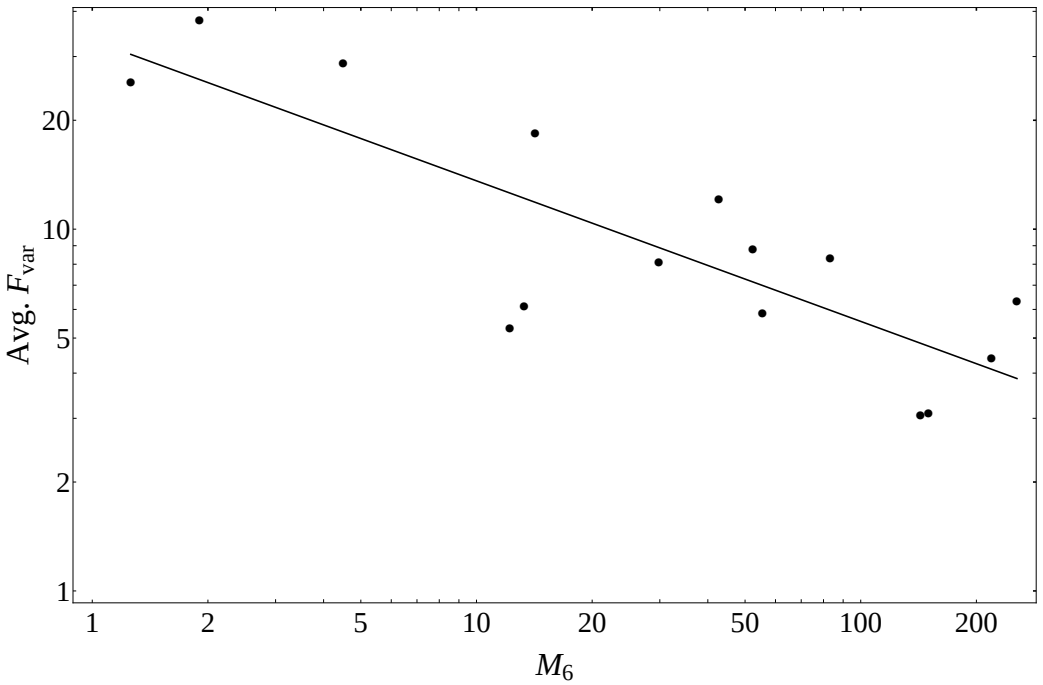

Figure 5.5: Linear fit in the log-log space to the $F_{\rm var}$ vs M_{BH} data for Sy1 and NLSy1 galaxies.

we obtain a BH mass of 3.7 M_6. The choice of $r = 10M$ could allow the orbital feature to exist for a few cycles before getting disrupted due to the physical processes in the disk such as radiation and convection. For a maximally rotating black, if we assume an emission ring of radius $r = 4M$, slightly outside the ISCO though still within the inner region, we obtain a BH mass of 13.0 M_6. If the emission arose from the ISCO $r = 1.236M$ for the maximally spinning black hole, the BH mass is 49.2 M_6. Hence, we can place a lower BH mass limit of $\geq 10^6$ $M_\odot$ and an upper limit of $\leq 5 \times 10^7$ $M_\odot$ from the current analysis. The inferred mass here is consistent within errors of an estimate of $(4^{+3}_{-2}) \times 10^6$ $M_\odot$ inferred from the relation between the excess variability amplitude and the black hole mass [195]. The determined mass in our study when compared to the above mentioned estimate implies that the black hole spin is likely to be low. From the inferred quality factor Q of 32.0 ± 6.5, eqn. (5.7) indicates a well constrained emission radius $r \sim 11$ M for a black hole with spin ranging between $a = 0$ and $a = 0.998$ assuming that the radial velocity of the bulk flow is 0.0001.

Table 5.4 summarizes the results from the periodogram analysis of each light curve. F_{var} for these light curves ranges between 2.30 % and 50.61 % indicating a moderate to strong variability. The PSD shape in 47 of 58 (81 %) data sets analyzed is estimated to be a power law with the rejection probability ranging between < 0.1 % and 76.15 %. The power law model of the PSD is a reasonable to good fit in 37 of 58 (64 %) of the data sets. It is not a good fit in 10 data sets where the MC simulations based rejection significance is high. The PSD shape in 10 of the 11 remaining data sets is estimated to be of a broken power law form. The rejection probability of these ranges between < 0.10 % and 90.45 %. For 5 of these 7 data sets indicating a good to strong goodness of fit, the break timescale varies between 2960^{+516}_{-382} s (MRK 766) and 9891^{+8726}_{-3157} s (3C 120), though, the latter indicates a large error bar and the result are unreliable. The slope $\alpha_{\rm Hi}$ in the frequencies higher than the break frequency ranges between -1.00 and -2.50 while the slopes $\alpha_{\rm Low}$ in the frequencies lower than the break frequency are all -1.00. This arises in multiple data sets due to the limit in sampling slopes set in our numerical procedure. These slopes are likely to be less steeper if the test range for α is increased above -1.00. The remaining data set for Q 0056-363 indicates a bending power law PSD model, though, with a large rejection probability of 83.5 %. Also, the bending timescale of 517^{+20}_{-19} is very close to the white noise dominated portion and hence, the result is unreliable. In the application of the theoretical break frequency model from §5.2.2, we reject data sets where the MC simulations based model rejection probability is high and where the break frequency is not clearly present. A group of 5 of 58 data sets (9 %) displaying a prominent break frequency and where the fit is good are now used in further analysis.

Table 5.4 summarizes the results of the power law PSD model fit to the periodograms. For 11 data sets, the relative likelihood compared to other best fit models ranges between 7.36×10^{-9} and 5.9×10^{-1}. The power law slope α for these data sets with lower relative likelihood (< 1) ranges between -1.25 and -2.53. In general, considering all data sets, α ranges between -1.25 and -2.57. Table 5.4 summarizes the results of the bending power law PSD model fit to the periodogram of the periodogram of the X-ray light curves. The bending power law model is a statistically valid candidate for only one data set (Q 0056-363) where the bend timescale is $T_{\rm Ben} = 517^{+20}_{-19}$ s and the

slope α describing the PSD shape in the frequencies lower that the bend frequency is -1.30. One other data set (NGC 4151 with obs. I.D. 0402660101) indicates the presence of a bend timescale of 430^{+16}_{-15} s due to its high relative likelihood of 9.91×10^{-1}. As these timescales are very close to the white noise dominated region, they are not reliable estimates. For the rest of the data sets (57 out of 58) the bending power law PSD model is not a good candidate for the description of the underlying PSD as inferred from the relative likelihoods (RL) in Table 5.4 which vary between 2.20 $\times 10^{-32}$ and 3.48×10^{-2}. Table 5.4 summarizes the results of the broken power law PSD model fit to the periodogram of the X-ray light curves. The relative likelihoods (RL) vary between 1.04×10^{-3} and 9.61×10^{-1}. Break timescales vary between 588^{+28}_{-26} s and 11353^{+9886}_{-3606} s with large errors, the errors quoted being the 68% confidence intervals. The slope $\alpha_{\rm Hi}$ in the frequencies higher than the break frequency ranges between -1.00 and -2.50. The slope $\alpha_{\rm Low}$ in the frequencies lower than the break frequency is -1.00 for 45 of 58 data sets (78 %). This is in a consequence of the limit in sampling slopes set in our numerical procedure. These slopes are likely to be steeper if the test range for $\alpha_{\rm Low}$ is increased beyond -1.00. For the remaining 13 data sets, the slope is -0.20 for two data sets, ranging between -0.20 and -0.90.

We make use of the BH mass M_{BH} and spin a ranges as quoted in literature and presented in Table 5.2 for the analysis. Since $T_B = T_B(M_{BH}, a)$ from eqn. (5.9), with these three constraints, we calculate the region of overlap of these quantities on the M_{BH}-a plane.

NGC 3516 with an inferred break timescale of 3830^{+676}_{-500} (from the current analysis) hosts a BH of mass $(42.7^{+14.6}_{-14.6})$ M_6 and a lower limit on the spin of ≥ 0.30. Contours of $T_B = T_B(r, a)$ are plotted in Fig. 5.6. The region of overlap of the constraints is marked in red colour. The current analysis helps in constraining the spin of the BH further. It results in an improved lower limit on the spin of ≥ 0.84.

NGC 4051 with an inferred break timescale of 3403^{+805}_{-547} (from the current analysis) hosts a BH of mass $(1.9^{+0.78}_{-0.78})$ M_6 and a lower limit on the spin of ≥ 0.30. Contours of $T_B = T_B(r, a)$ are plotted in Fig. 5.7. The overlap in this case is only between the contours of T_B and the spin a. Thus, an upper limit to the black hole mass of 57.6 M_6 (for a maximally spinning black hole with $a = 0.998$) can be inferred.

MRK 766 with two inferred break timescales of 3939^{+882}_{-609} and 2960^{+516}_{-382} (from the current analysis) hosts a BH of mass $(1.26^{+1.19}_{-0.61})$ M_6 and a lower limit on the spin of ≥ 0.30. Contours of $T_B = T_B(r, a)$ are plotted in fig. 5.8 and 5.9. The overlap in this case is only between the contours of T_B and the spin a. Thus, an upper limit to the black hole mass of 57.2 M_6 (for a maximally spinning black hole with $a = 0.998$) can be inferred.

MCG-6-30-15 with an inferred break timescale of 3181^{+806}_{-535} (from the current analysis) hosts a BH of mass $(1.9^{+0.78}_{-0.78})$ M_6 and a lower limit on the spin of ≥ 0.80. Contours of $T_B = T_B(r, a)$ are plotted in fig. 5.10. The overlap in this case is only between the contours of T_B and the spin a. Thus, an upper limit to the black hole mass of 53.9 M_6 (for a maximally spinning black hole with $a = 0.998$) can be inferred.

The results from the above discussion are presented in Table 5.1. The results of the time series analysis of the above light curves where a T_B is inferred are plotted in Fig. 5.11.

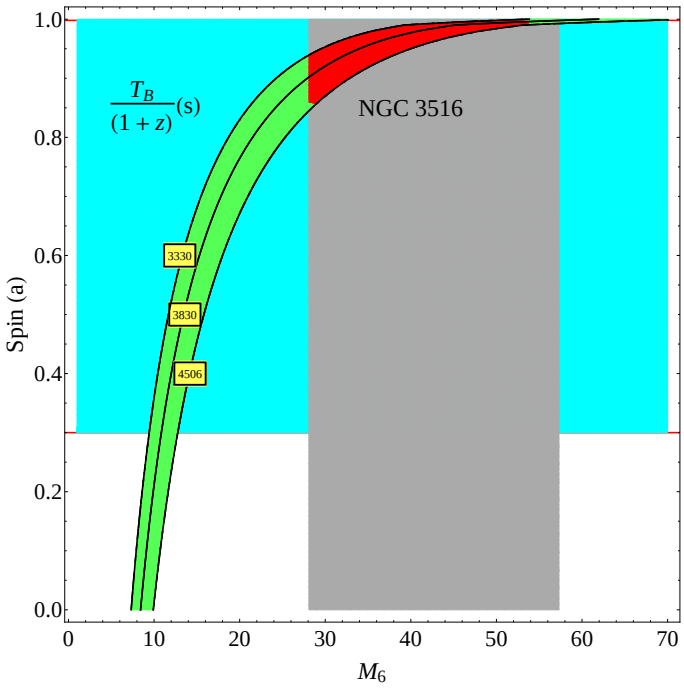

Figure 5.6: Contours of the break timescale $T_B = T_B(r, a)$ plotted for the Sy1.5 galaxy NGC 3516 (obs. I.D. 0107460601). Three constraint bands are plotted in the figure. The first is from the black hole mass of $42.7^{+14.6}_{-14.6}$ M_6, plotted as a grey coloured vertical band. The second is from the black hole spin ≥ 0.30, plotted as a cyan coloured horizontal band. The third is from the contours of T_B which is inferred from the current analysis to be 3830 s lying within a 68 % confidence interval from 3330 s and 4506 s, plotted as the green coloured contour bands. The three constraint bands intersect to provide a tighter constraint on the lower limit ot the black hole spin of ≥ 0.80, within the red coloured region.

Object	Break Timescale T_B (s)	Mass limits M_6	Spin limits a
NGC 3516	3830^{+676}_{-500}	$42.7^{+14.6}_{-14.6}$	≥ 0.84
NGC 4051	3403^{+805}_{-547}	≤ 57.6	0 - 0.998
MRK 766	3939^{+882}_{-609}	≤ 57.2	≥ 0.30
	2960^{+516}_{-382}		
MCG-6-30-15	3181^{+806}_{-535}	53.9	≥ 0.80

Table 5.1: Summary of the application of the theoretical break frequency model applied to the X-ray light curves of Seyfert galaxies. Properties extracted include upper limits on BH mass and spin using statistically inferred T_B.

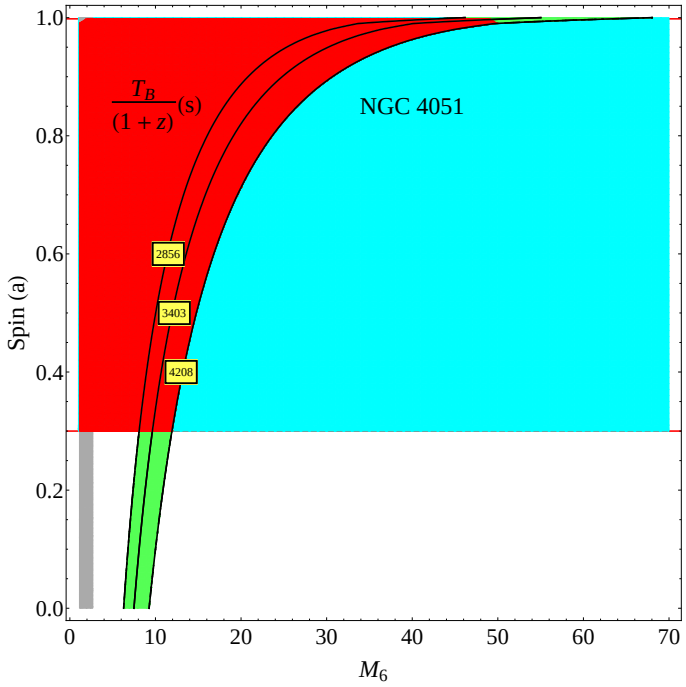

Figure 5.7: Contours of the break timescale $T_B = T_B(r, a)$ plotted for the NLSy1 galaxy NGC 4051 (obs. I.D. 0606321601). Three constraint bands are plotted in the figure. The first is from the black hole mass of $1.90^{+0.78}_{-0.78}$ M_6, plotted as a grey coloured vertical band. The second is from the black hole spin ≥ 0.30, plotted as a cyan coloured horizontal band. The third is from the contours of T_B which is inferred from the current analysis to be 3403 s lying within a 68 % confidence interval from 2856 s and 4208 s, plotted as the green coloured contour bands. Only two of the constraint bands intersect (spin and T_B) represented by the red coloured region. An upper limit on the black hole mass of 57.6 M_6 can be inferred from the current analysis.

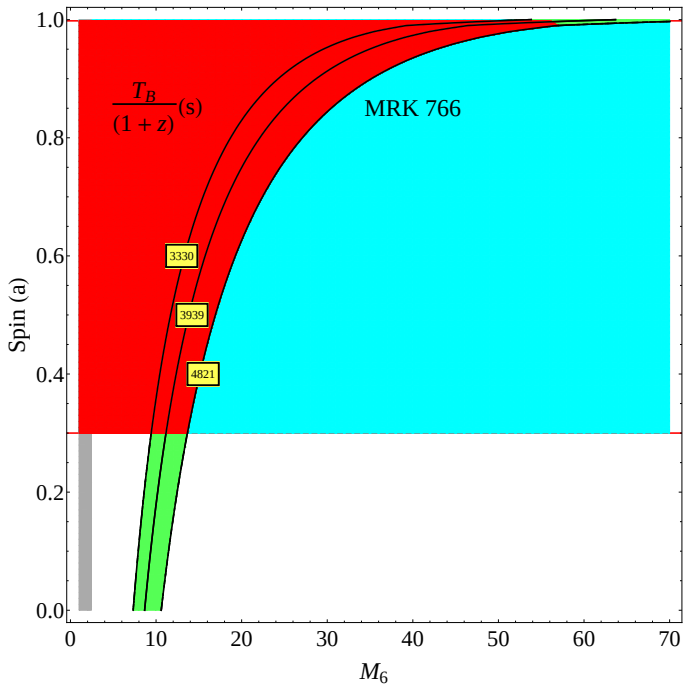

Figure 5.8: Contours of the break timescale $T_B = T_B(r, a)$ plotted for the NLSy1 galaxy MRK 766 (obs. I.D. 0304030401). Three constraint bands are plotted in the figure. The first is from the black hole mass of $1.26^{+1.19}_{-0.61}$ M_6, plotted as a grey coloured vertical band. The second is from the black hole spin ≥ 0.30, plotted as a cyan coloured horizontal band. The third is from the contours of T_B which is inferred from the current analysis to be 3939 s lying within a 68 % confidence interval from 3330 s and 4821 s, plotted as the green coloured contour bands. Only two of the constraint bands intersect (spin and T_B) represented by the red coloured region. An upper limit on the black hole mass of 57.2 M_6 can be inferred from the current analysis.

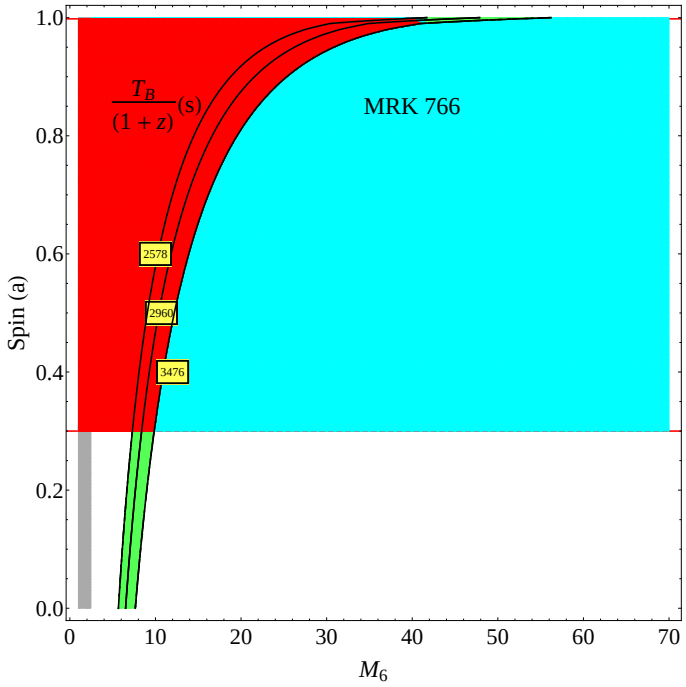

Figure 5.9: Contours of the break timescale $T_B = T_B(r, a)$ plotted for the NLSy1 galaxy MRK 766 (obs. I.D. 0304030501). Three constraint bands are plotted in the figure. The first is from the black hole mass of $1.26^{+1.19}_{-0.61}$ M_6, plotted as a grey coloured vertical band. The second is from the black hole spin ≥ 0.30, plotted as a cyan coloured horizontal band. The third is from the contours of T_B which is inferred from the current analysis to be 2960 s lying within a 68 % confidence interval from 2578 s and 3476 s, plotted as the green coloured contour bands. Only two of the constraint bands intersect (spin and T_B) represented by the red coloured region. An upper limit on the black hole mass of 57.2 M_6 can be inferred from the current analysis.

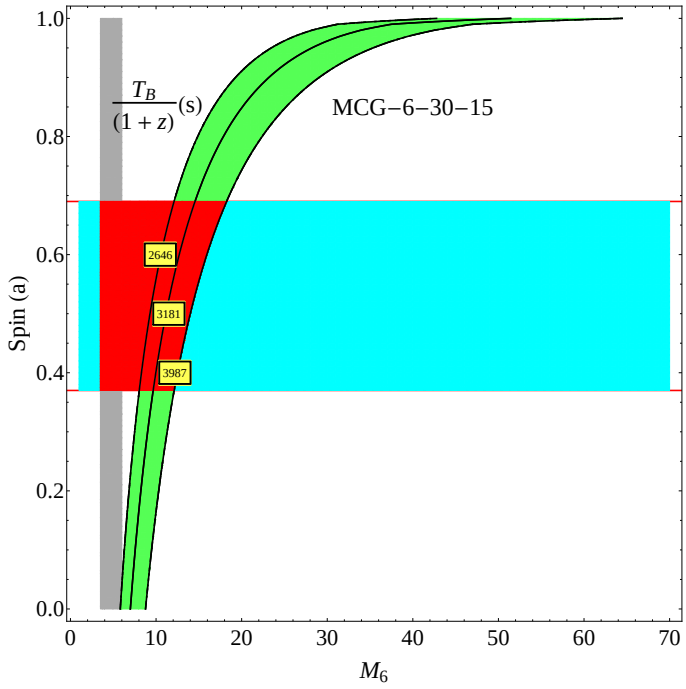

Figure 5.10: Contours of the break timescale $T_B = T_B(r, a)$ plotted for the Sy1 galaxy MCG-6-30-15 (obs. I.D. 0111570201). Three constraint bands are plotted in the figure. The first is from the black hole mass of $4.5^{+1.5}_{-1.0}$ M_6, plotted as a grey coloured vertical band. The second is from the black hole spin $0.49^{+0.20}_{-0.12}$, plotted as a cyan coloured horizontal band. The third is from the contours of T_B which is inferred from the current analysis to be 3181 s lying within a 68 % confidence interval from 2646 s and 3987 s, plotted as the green coloured contour bands. Only two of the constraint bands intersect (spin and T_B) represented by the red coloured region. An upper limit on the black hole mass of 18.2 M_6 can be inferred from the current analysis.

Object	AGN Type	RA	Dec.	Redshift z	Black hole mass M_{BH} (10^6 $M_\odot$); ref.	Black hole spin a; ref.	Average Fractional Variability $F_{\rm var}$
MRK 335	NLSy1	00h06m19.5s	+20d12m10s	0.258	$(14.2^{+3.7}_{-3.7})$; 1	$(0.83^{+0.09}_{-0.13})$; 7	18.52
Q 0056-363	Sy1	00h58m37.3s	-36d06m05s	0.164	610; 2	N	7.69
Fairall 9	Sy1.2	01h23m45.8s	-58d48m21s	0.047	(255^{+56}_{-56}); 1	$(0.82^{+0.09}_{-0.19})$; 7	6.35
3C 120	Sy1.5	04h33m11.1s	+05d21m16s	0.033	$(55.5^{+31.4}_{-22.5})$; 1	N	5.90
ARK 120	Sy1	05h16m11.4s	-00d08m59s	0.033	(150^{+19}_{-19}); 1	$(0.64^{+0.19}_{-0.11})$; 7	3.12
MRK 79	Sy1.2	07h42m32.8s	+49d48m35s	0.022	$(52.4^{+14.4}_{-14.4})$; 1	$(0.7^{+0.1}_{-0.1})$; 8	8.87
MCG-5-23-16	Sy1	09h47m40.1s	-30d56m55s	0.008	$(83.2^{+125.7}_{-50.1})$; 3	N	8.33
NGC 3516	Sy1.5	11h06m47.5s	+72d34m07s	0.009	$(42.7^{+14.6}_{-14.6})$; 1	≥ 0.30; 9	13.94
NGC 3783	Sy1.5	11h39m01.7s	-37d44m19s	0.010	$(29.8^{+5.4}_{-5.4})$; 1	≥ 0.20; 9	9.08
NGC 4051	NLSy1	12h03m09.6s	+44d31m53s	0.002	$(1.9^{+0.78}_{-0.78})$; 1	≥ 0.30; 9	37.99
NGC 4151	Sy1.5	12h10m32.6s	+39d24m21s	0.003	$(13.3^{+4.6}_{-4.6})$; 1	N	6.17
MRK 766	NLSy1	12h18m26.5s	+29d48m46s	0.013	$(1.26^{+1.19}_{-0.61})$; 4	≥ 0.30; 9	25.54
MCG-6-30-15	Sy1.2	13h35m53.7s	-34d17m44s	0.008	$(4.5^{+1.5}_{-1.0})$; 5	$0.49^{+0.20}_{-0.12}$; 10	26.60
IC 4329A	Sy1.2	13h49m19.2s	-30d18m34s	0.016	$(218.88^{+217.64}_{-109.65})$; 6	≥ 0.00; 9	4.43
MRK 509	Sy1.5	20h44m09.7s	-10d43m25s	0.034	(143^{+12}_{-12}); 1	$(0.78^{+0.03}_{-0.04})$; 7	3.34
NGC 7469	Sy1.5	23h03m15.6s	+08d52m26s	0.016	$(12.2^{+1.4}_{-1.4})$; 1	$(0.64^{+0.13}_{-0.20})$; 7	5.42

Table 5.2: BH Mass: [1]: [54] (virial mass using reverberation mapping with mass calibrated using the M_{BH}-σ relation); [2]: [196] ;[3]: [197] (M-σ relation); [4]: [198]; [5]: [199] (use of the scaling of the PSD break timescale with black hole mass and confirmation with reverberation mapping); [6]: [200] (M-σ relation); BH spin: [7]: [201]; [8]: [202]; [9]: [189]; [10]: [175]; N: not identified. Columns 1 - 8 give the object name, its right ascension (RA), declination (Dec.), cosmological redshift z, the mass of the SMBH it hosts M_{BH} in terms of 10^6 $M_\odot$, the spin of the black hole and the average excess fractional variability index $F_{\rm var}$ determined in the current study.

5.4 Summary and conclusions

1. A break frequency model and a model for the quality factor Q were developed in §5.2, both being cast in Kerr geometry.

2. An analysis of X-ray light curves (0.3 keV - 10 keV) from a group of Seyfert galaxies was conducted to infer any statistically significant break time-scale.

3. Break time-scales ranging between 2960 s and 3939 s were inferred from this analysis in 5 light curves from 4 Seyferts.

4. The break frequency model was applied to these light curves. In NGC 3516, a revised lower limit on the BH spin of ≥ 0.84 is inferred. In NGC 4051, MRK 766 and MCG-6-30-15, revised upper limits on BH masses of 57.6 M_6, 57.2 M_6 and 53.9 M_6 are inferred.

5. The Q-factor model is applied to the X-ray light curve of REJ 1034+396 where a statistically significant QPO at 3733 s was inferred. With the measured Q of 32.0 $\pm$ 6.5, an emission radius of $\sim$ 11 M is inferred. An upper limit on the BH mass of $\leq$ 50 M_6 is also inferred, consistent with estimates in literature [195].

Object	Observation ID	Time Duration (s)	Fractional Variability $F_{\rm var}$	Best fit PSD shape	MC sims. Rejection Prob. (%)	Fit parameters
MRK 335	0101040101	31500	11.07	Power law	< 0.10	α = -1.98 ± 0.09
	0306870101	13200	12.22	Power law	< 0.10	α = -2.05 ± 0.06
	0600540501	80600	24.05	Power law	< 0.10	α = -1.86 ± 0.06
	0600540601	111700	26.75	Power law	0.40	α = -1.74 ± 0.04
Q 0056-363	0205680101	101100	7.58	Broken power law	90.45	$T_{\rm Brk} = 740^{+31}_{-29}$ $\alpha_{\rm Hi}$ = -1.0 ± 0.04 $\alpha_{\rm Low}$ = -0.3 ± 0.03
	0401930101	44600	7.79	Bending power law	83.5	$T_{\rm Ben} = 517^{+20}_{-19}$ α = -1.3 ± 0.09
Fairall 9	0101040201	28900	3.96	Power law	42.30	α = -0.94 ± 0.09
	0605800401	129500	8.73	Broken power law	< 0.10	$T_{\rm Brk} = 8587^{+5524}_{-2415}$ $\alpha_{\rm Hi}$ = -1.1 ± 0.04 $\alpha_{\rm Low}$ = -1.0 ± 0.02
3C 120	0152840101	125500	5.90	Broken power law	< 0.10	$T_{\rm Brk} = 9891^{+8726}_{-3157}$ $\alpha_{\rm Hi}$ = -1.00 ± 0.04 $\alpha_{\rm Low}$ = -1.00 ± 0.03
ARK 120	0147190101	111500	3.12	Power law	0.20	α = -0.95 ± 0.05
MRK 79	0502091001	78200	8.87	Power law	44.8	α = -0.74 ± 0.06
MCG-5-23-16	0302850201	116900	8.33	Power law	< 0.10	α = -1.75 ± 0.05
NGC 3516	0107460601	126000	23.89	Broken power law	< 0.10	$T_{\rm Brk} = 3830^{+676}_{-500}$ $\alpha_{\rm Hi}$ = -1.8 ± 0.05 $\alpha_{\rm Low}$ = -1.0 ± 0.03
	0107460701	127900	8.84	Power law	3.70	α = -0.76 ± 0.04
	0401210401	51600	14.95	Power law	0.25	α = -1.97 ± 0.09
	0401210501	68500	8.37	Power law	< 0.10	α = -1.69 ± 0.07
	0401210601	68000	28.22	Power law	0.05	α = -2.27 ± 0.06
	0401211001	59400	9.31	Power law	< 0.10	α = -1.95 ± 0.08
NGC 3783	0112210101	36900	6.46	Power law	< 0.10	α = -1.58 ± 0.09
	0112210201	57100	8.14	Power law	< 0.10	α = -1.46 ± 0.07
	0112210501	136300	12.63	Power law	< 0.10	α = -1.61 ± 0.04
NGC 4051	0157560101	33600	21.47	Power law	76.15	α = -2.48 ± 0.09
	0606320101	45200	34.15	Power law	0.60	α = -2.57 ± 0.08
	0606320201	43500	45.73	Power law	< 0.10	α = -2.37 ± 0.07
	0606321601	41400	50.61	Broken power law	0.95	$T_{\rm Brk} = 3403^{+805}_{-547}$ $\alpha_{\rm Hi}$ = -2.2 ± 0.05 $\alpha_{\rm Low}$ = -1.0 ± 0.03
NGC 4151	0402660101	39800	5.42	Broken power law	52.9	$T_{\rm Brk} = 588^{+28}_{-26}$ $\alpha_{\rm Hi}$ = -2.5 ± 0.07 $\alpha_{\rm Low}$ = -0.2 ± 0.05
	0402660201	47400	6.92	Power law	< 0.10	α = -1.65 ± 0.07
MRK 766	0096020101	38900	19.05	Power law	< 0.10	α = -1.82 ± 0.09
	0109141301	128400	25.97	Power law	< 0.10	α = -1.97 ± 0.04
	0304030301	98400	37.63	Power law	< 0.10	α = -2.09 ± 0.05
	0304030401	94400	22.21	Broken power law	< 0.10	$T_{\rm Brk} = 3939^{+882}_{-609}$ $\alpha_{\rm Hi}$ = -2.4 ± 0.05 $\alpha_{\rm Low}$ = -1.0 ± 0.04
	0304030501	94200	19.39	Broken power law	< 0.10	$T_{\rm Brk} = 2960^{+516}_{-382}$ $\alpha_{\rm Hi}$ = -2.5 ± 0.05 $\alpha_{\rm Low}$ = -1.0 ± 0.03
	0304030601	98400	28.60	Power law	< 0.10	α = -2.08 ± 0.05
	0304030701	29100	25.93	Power law	1.05	α = -2.09 ± 0.09
MCG-6-30-15	0029740101	80500	28.82	Power law	0.40	α = -2.15 ± 0.06
	0029740701	12300	19.94	Power law	< 0.1	α = -2.01 ± 0.05
	0029740801	124100	35.57	Power law	< 0.1	α = -2.20 ± 0.06
	0111570101	43100	29.93	Power law	< 0.1	α = -2.20 ± 0.07
	0111570201	53400	18.74	Broken power law	< 0.10	$T_{\rm Brk} = 3181^{+806}_{-535}$ $\alpha_{\rm Hi}$ = -2.4 ± 0.07 $\alpha_{\rm Low}$ = -1.0 ± 0.05
IC 4329A	0147440101	132500	4.43	Power law	< 0.10	α = -1.15 ± 0.05
MRK 509	0130720101	29300	3.08	Power law	60.30	α = -0.85 ± 0.11
	0130720201	41500	2.59	Power law	27.70	α = -0.91 ± 0.08
	0306090201	85300	2.77	Power law	0.70	α = -0.87 ± 0.06
	0306090301	46300	2.41	Power law	20.40	α = -0.85 ± 0.07
	0306090401	69300	4.33	Power law	< 0.10	α = -0.85 ± 0.07
	0601390201	57000	2.81	Power law	0.65	α = -0.91 ± 0.07
	0601390301	63200	3.00	Power law	10.30	α = -0.76 ± 0.06
	0601390401	60300	2.30	Power law	0.40	α = -0.96 ± 0.06
	0601390501	60300	5.64	Power law	< 0.10	α = -1.04 ± 0.06
	0601390601	62200	3.41	Power law	< 0.10	α = -1.05 ± 0.06
	0601390701	62400	3.56	Power law	< 0.10	α = -1.13 ± 0.07
	0601390801	60200	4.46	Power law	< 0.10	α = -1.06 ± 0.07
	0601390901	60300	2.55	Power law	0.40	α = -0.97 ± 0.06
	0601391001	64800	4.08	Broken power law	< 0.10	$T_{\rm Brk} = 4508^{+1966}_{-1050}$ $\alpha_{\rm Hi}$ = -1.1 ± 0.06 $\alpha_{\rm Low}$ = -1.0 ± 0.04
	0601391101	62200	3.09	Power law	< 0.10	α = -0.96 ± 0.07
NGC 7469	0112170301	23000	5.15	Power law	3.6	α = -1.04 ± 0.12
	0207090101	84400	5.36	Power law	< 0.10	α = -1.16 ± 0.06
	0207090101	78500	5.76	Power law	< 0.10	α = -1.22 ± 0.07

Table 5.3: Results from the PSD fit with the best fit model. Columns 1 – 8 give the object name, a unique observation I.D. assigned to each observation in the XMM Newton archives, its observation duration, excess fractional variability index $F_{\rm var}$ of the individual light curves, the best fit PSD shape obtained from the Akaike Information Criteria, MC simulations based goodness of fit quantified as a model rejection probability and the best fit model parameters with their errors based on the 68 % confidence intervals obtained from the contours of the differences of the log-likelihood function ΔS as described in chapter 3.

Object	Observation ID	Power law model parameters α	AIC	Δ_i = AIC_i-AIC_{Null}	Relative Likelihood (RL)
MRK 335	0101040101	-1.98 ± 0.09	-178.07	0.00	1.00
	0306870101	-2.05 ± 0.05	-702.77	0.00	1.00
	0600540501	-1.86 ± 0.06	-348.02	0.00	1.00
	0600540601	-1.74 ± 0.04	-962.82	0.00	1.00
Q 0056-363	0205680101	-1.39 ± 0.04	-835.21	37.45	7.36×10^{-9}
	0401930101	-1.25 ± 0.07	-226.63	6.81	3.33×10^{-2}
Fairall 9	0101040201	-0.94 ± 0.09	-193.30	0.00	1.00
	0605800401	-1.7 ± 0.04	-860.00	14.19	8.28×10^{-4}
3C 120	0152840101	-1.49 ± 0.04	-954.16	4.62	9.95×10^{-2}
ARK 120	0147190101	-0.95 ± 0.05	-849.72	0.00	1.00
MRK 79	0502091001	-0.74 ± 0.06	-390.04	0.00	1.00
MCG-5-23-16	0302850201	-1.75 ± 0.05	-734.05	0.00	1.00
NGC 3516	0107460601	-1.87 ± 0.05	-348.89	0.00	1.00
	0107460701	-0.76 ± 0.04	-971.61	0.00	1.00
	0401210401	-1.97 ± 0.09	-180.69	0.00	1.00
	0401210501	-1.69 ± 0.07	-305.98	0.00	1.00
	0401210601	-2.27 ± 0.06	-334.43	0.00	1.00
	0401211001	-1.95 ± 0.08	-241.55	0.00	1.00
NGC 3783	0112210101	-1.58 ± 0.09	-165.54	0.00	1.00
	0112210201	-1.46 ± 0.07	-270.42	0.00	1.00
	0112210501	-1.61 ± 0.04	-920.01	0.00	1.00
NGC 4051	0157560101	-2.48 ± 0.09	-91.36	0.00	1.00
	0606320101	-2.57 ± 0.08	-130.00	0.00	1.00
	0606320201	-2.37 ± 0.07	-111.59	0.00	1.00
	0606321601	-2.51 ± 0.05	-233.05	3.41	1.82×10^{-1}
NGC 4151	0402660101	-1.35 ± 0.07	-270.18	10.21	6.08×10^{-3}
	0402660201	-1.65 ± 0.07	-319.04	0.00	1.00
MRK 766	0096020101	-1.82 ± 0.09	-124.85	0.00	1.00
	0109141301	-1.97 ± 0.04	-661.32	0.00	1.00
	0304030301	-2.09 ± 0.05	-418.58	0.00	1.00
	0304030401	-2.33 ± 0.05	-414.00	2.17	3.38×10^{-1}
	0304030501	-2.42 ± 0.05	-482.02	6.14	4.63×10^{-2}
	0304030601	-2.08 ± 0.05	-478.46	0.00	1.00
	0304030701	-2.09 ± 0.09	-104.99	0.00	1.00
MCG-6-30-15	0029740101	-2.15 ± 0.06	-328.18	0.00	1.00
	0029740701	-2.01 ± 0.05	-633.82	0.00	1.00
	0029740801	-2.20 ± 0.06	-569.05	0.00	1.00
	0111570101	-2.20 ± 0.07	-190.34	0.00	1.00
	0111570201	-2.53 ± 0.07	-251.18	1.04	5.9×10^{-1}
IC 4329A	0147440101	-1.15 ± 0.05	-954.57	0.00	1.00
MRK 509	0130720101	-0.85 ± 0.11	-130.142	0.00	1.00
	0130720201	-0.91 ± 0.08	-249.775	0.00	1.00
	0306090201	-0.87 ± 0.06	-630.80	0.00	1.00
	0306090301	-0.85 ± 0.07	-440.28	0.00	1.00
	0306090401	-0.85 ± 0.07	-432.47	0.00	1.00
	0601390201	-0.91 ± 0.07	-407.42	0.00	1.00
	0601390301	-0.76 ± 0.06	-581.46	0.00	1.00
	0601390401	-0.96 ± 0.06	-651.77	0.00	1.00
	0601390501	-1.04 ± 0.06	-503.24	0.00	1.00
	0601390601	-1.05 ± 0.06	-466.01	0.00	1.00
	0601390701	-1.13 ± 0.07	-388.38	0.00	1.00
	0601390801	-1.06 ± 0.07	-368.39	0.00	1.00
	0601390901	-0.97 ± 0.06	-514.00	0.00	1.00
	0601391001	-1.63 ± 0.06	-529.11	2.07	3.56×10^{-1}
	0601391101	-0.96 ± 0.07	-350.44	0.00	1.00
NGC 7469	0112170301	-1.04 ± 0.12	-98.10	0.00	1.00
	0207090101	-1.16 ± 0.06	-538.46	0.00	1.00
	0207090201	-1.22 ± 0.07	-322.59	0.00	1.00

Table 5.4: Results from the PSD fit with a power law model. Columns 1 – 6 give the object name, its observation I.D., the slope α which is the only parameter used in this model, the AIC value corresponding to the particular parameter value for which the log likelihood S is a minimum, the difference Δ_i which is used to calculate the likelihood and the relative likelihood which quantifies the probability of the power law model being chosen over the null model as a best fit PSD model.

Object	Observation ID	Bending power law model parameters		AIC	Δ_i	Relative Likelihood (RL)
		T_{Ben} (s)	α		= AIC_i-AIC_{Null}	
MRK 335	0101040101	2701^{+940}_{-555}	-2.30 ± 0.11	-154.43	23.64	7.35×10^{-6}
	0306870101	3055^{+470}_{-360}	-2.40 ± 0.06	-639.36	63.40	1.71×10^{-14}
	0600540501	10656^{+14187}_{-3873}	-1.60 ± 0.08	-294.19	53.83	2.04×10^{-12}
	0600540601	7979^{+3118}_{-1751}	-1.50 ± 0.04	-817.03	145.79	2.20×10^{-32}
Q 0056-363	0205680101	370^{+8}_{-7}	-1.60 ± 0.05	-864.88	7.78	2.05×10^{-2}
	0401930101	517^{+20}_{-19}	-1.30 ± 0.09	-233.44	0.00	1.00
Fairall 9	0101040201	871^{+77}_{-64}	-1.00 ± 0.08	-186.59	6.71	3.48×10^{-2}
	0605800401	11103^{+12969}_{-3888}	-1.00 ± 0.06	-789.23	94.95	3.58×10^{-19}
3C 120	0152840101	10760^{+12568}_{-3767}	-1.00 ± 0.06	-873.04	85.73	2.42×10^{-19}
ARK 120	0147190101	3075^{+154}_{-390}	-1.00 ± 0.05	-798.37	51.34	7.10×10^{-12}
MRK 79	0502091001	1429^{+117}_{-100}	-1.00 ± 0.07	-368.79	21.25	2.43×10^{-5}
MCG-5-23-16	0302850201	7106^{+3681}_{-1808}	-1.40 ± 0.06	-665.06	68.99	1.05×10^{-15}
NGC 3516	0107460601	1957^{+175}_{-150}	-3.00 ± 0.06	-303.85	47.33	5.28×10^{-11}
	0107460701	1445^{+107}_{-94}	-1.00 ± 0.05	-909.70	61.91	3.59×10^{-14}
	0401210401	7891^{+6098}_{-2395}	-2.30 ± 0.11	-153.13	27.55	1.04×10^{-6}
	0401210501	5399^{+2343}_{-1205}	-1.90 ± 0.09	-273.30	32.68	8.00×10^{-8}
	0401210601	4959^{+2274}_{-1187}	-2.00 ± 0.08	-289.66	44.77	1.90×10^{-10}
	0401211001	5583^{+2451}_{-1305}	-2.20 ± 0.10	-211.91	29.64	3.67×10^{-7}
NGC 3783	0112210101	5643^{+4304}_{-1704}	-1.30 ± 0.12	-146.74	18.80	8.26×10^{-5}
	0112210201	6648^{+4879}_{-1977}	-1.40 ± 0.09	-239.19	31.23	1.66×10^{-7}
	0112210501	14178^{+25249}_{-5535}	-1.30 ± 0.06	-820.01	100.00	1.93×10^{-22}
NGC 4051	0157560101	2460^{+486}_{-348}	-3.00 ± 0.12	-77.72	13.65	1.09×10^{-3}
	0606320101	2063^{+397}_{-287}	-3.00 ± 0.09	-108.40	21.59	2.05×10^{-5}
	0606320201	1741^{+301}_{-224}	-3.00 ± 0.09	-88.72	22.87	1.08×10^{-5}
	0606321601	2179^{+352}_{-266}	-2.90 ± 0.06	-178.88	57.58	3.14×10^{-13}
NGC 4151	0402660101	430^{+16}_{-15}	-1.20 ± 0.09	-280.37	0.02	9.91×10^{-1}
	0402660201	3736^{+1694}_{-889}	-1.50 ± 0.09	-284.348	34.69	2.93×10^{-8}
MRK 766	0096020101	3066^{+904}_{-569}	-2.40 ± 0.11	-104.37	20.47	3.60×10^{-5}
	0109141301	3541^{+735}_{-520}	-2.20 ± 0.06	-574.40	86.92	1.34×10^{-19}
	0304030301	4954^{+1726}_{-1017}	-2.20 ± 0.07	-349.63	68.94	1.07×10^{-15}
	0304030401	2679^{+438}_{-330}	-3.00 ± 0.07	-364.17	52.01	5.09×10^{-12}
	0304030501	2169^{+305}_{-238}	-3.00 ± 0.06	-433.83	54.33	1.59×10^{-12}
	0304030601	3783^{+1004}_{-656}	-2.20 ± 0.06	-408.18	70.27	5.50×10^{-16}
	0304030701	2735^{+936}_{-555}	-2.50 ± 0.12	-84.94	20.04	4.45×10^{-5}
MCG-6-30-15	0029740101	2869^{+537}_{-391}	-3.00 ± 0.08	-284.61	43.57	3.57×10^{-10}
	0029740701	2766^{+416}_{-319}	-3.00 ± 0.06	-563.17	70.65	4.55×10^{-16}
	0029740801	5179^{+1635}_{-1002}	-2.20 ± 0.06	-482.26	86.79	1.42×10^{-19}
	0111570101	2924^{+930}_{-568}	-2.60 ± 0.07	-156.93	33.41	5.56×10^{-8}
	0111570201	2137^{+398}_{-290}	-2.60 ± 0.07	-221.77	30.45	2.44×10^{-7}
IC 4329A	0147440101	4400^{+1097}_{-732}	-1.10 ± 0.06	-886.42	68.15	1.59×10^{-15}
MRK 509	0130720101	2144^{+384}_{-283}	-1.00 ± 0.14	-122.35	7.80	2.03×10^{-2}
	0130720201	831^{+49}_{-42}	-3.00 ± 0.11	-239.18	10.59	5.01×10^{-3}
	0306090201	2570^{+400}_{-305}	-1.00 ± 0.07	-594.80	36.00	1.53×10^{-8}
	0306090301	748^{+42}_{-48}	-1.10 ± 0.08	-429.11	11.17	3.76×10^{-3}
	0306090401	8069^{+8535}_{-2639}	-1.10 ± 0.08	-393.05	39.42	2.76×10^{-7}
	0601390201	2601^{+525}_{-374}	-1.00 ± 0.08	-382.51	24.92	3.89×10^{-6}
	0601390301	889^{+55}_{-49}	-1.00 ± 0.07	-565.95	15.50	4.31×10^{-4}
	0601390401	383^{+12}_{-10}	-2.70 ± 0.07	-639.68	12.09	2.37×10^{-3}
	0601390501	7021^{+7572}_{-2399}	-1.00 ± 0.08	-459.11	44.13	2.61×10^{-10}
	0601390601	8223^{+10583}_{-2961}	-1.00 ± 0.08	-426.45	39.55	2.58×10^{-9}
	0601390701	8263^{+8659}_{-2797}	-1.10 ± 0.09	-354.16	34.21	3.72×10^{-8}
	0601390801	9206^{+12610}_{-3372}	-1.10 ± 0.09	-354.16	34.21	3.72×10^{-8}
	0601390901	2752^{+645}_{-439}	-1.00 ± 0.08	-480.44	33.56	5.15×10^{-8}
	0601391001	4403^{+1938}_{-945}	-1.10 ± 0.08	-493.99	37.19	8.41×10^{-9}
	0601391101	4902^{+1901}_{-1071}	-1.10 ± 0.08	-493.99	37.19	8.41×10^{-9}
NGC 7469	0112170301	6640^{+9566}_{-2465}	-1.40 ± 0.15	-88.50	9.60	8.23×10^{-3}
	0207090101	8779^{+8484}_{-2893}	-1.20 ± 0.07	-488.24	50.22	1.25×10^{-11}
	0207090201	7379^{+3989}_{-1917}	-1.60 ± 0.07	-292.18	30.42	2.48×10^{-7}

Table 5.5: Results from the PSD fit with a bending power law model. Columns 1 – 7 give the object name, its observation I.D., the bend timescale in s (converted to temporal domain from a bend frequency in the binned periodogram), the slope α of the power law region at frequencies lower than the bend frequency, the AIC value, the difference Δ_i which is used to calculate the likelihood and the relative likelihood which quantifies the probability of the bending power law model being chosen over the null model as a best fit PSD model.

Object	Observation ID	Broken power law model parameters			AIC	Δ_i	Relative Likelihood (RL)
		T_{Brk} (s)	α_{Hi}	α_{Low}		= AIC_i-AIC_{Null}	
MRK 335	0101040101	3527^{+1423}_{-787}	-2.00 ± 0.08	-1.00 ± 0.06	-173.28	4.78	9.15×10^{-2}
	0306870101	4262^{+833}_{-599}	-2.00 ± 0.05	-1.00 ± 0.03	-698.85	3.92	1.41×10^{-1}
	0600540501	9025^{+6914}_{-2730}	-1.70 ± 0.06	-1.00 ± 0.04	-340.83	7.19	2.75×10^{-2}
	0600540601	7285^{+2181}_{-1365}	-1.60 ± 0.03	-1.00 ± 0.02	-953.12	9.70	7.84×10^{-3}
Q 0056-363	0205680101	740^{+31}_{-29}	-1.00 ± 0.04	-0.30 ± 0.03	-872.66	0.00	1.00
	0401930101	866^{+53}_{-48}	-1.20 ± 0.07	-0.20 ± 0.05	-232.49	0.95	6.22×10^{-1}
Fairall 9	0101040201	1173^{+139}_{-113}	-1.00 ± 0.08	-0.50 ± 0.06	-190.02	3.28	1.94×10^{-1}
	0605800401	8587^{+5524}_{-2415}	-1.1 ± 0.04	-1.00 ± 0.03	-874.18	0.00	1.00
3C 120	0152840101	9891^{+8726}_{-3157}	-1.00 ± 0.05	-1.00 ± 0.03	-958.77	0.00	1.00
ARK 120	0147190101	3075^{+545}_{-403}	-1.00 ± 0.05	-0.90 ± 0.03	-844.42	5.29	7.09×10^{-2}
MRK 79	0502091001	1843^{+200}_{-163}	-1.00 ± 0.06	-0.60 ± 0.04	-383.91	6.13	4.66×10^{-2}
MCG-5-23-16	0302850201	7254^{+3257}_{-1716}	-1.40 ± 0.05	-1.00 ± 0.03	-732.71	1.34	5.13×10^{-1}
NGC 3516	0107460601	3830^{+676}_{-500}	-1.80 ± 0.05	-1.00 ± 0.03	-350.41	0.00	1.00
	0107460701	1834^{+183}_{-153}	-1.00 ± 0.04	-0.70 ± 0.03	-961.53	10.08	6.47×10^{-2}
	0401210401	8812^{+6337}_{-2599}	-2.20 ± 0.08	-1.00 ± 0.06	-172.55	8.13	1.71×10^{-2}
	0401210501	6238^{+2508}_{-1390}	-1.80 ± 0.07	-1.00 ± 0.05	-299.72	6.27	4.36×10^{-2}
	0401210601	5664^{+2722}_{-1261}	-1.90 ± 0.06	-1.00 ± 0.04	-332.71	1.72	4.22×10^{-1}
	0401211001	6651^{+3043}_{-1589}	-2.00 ± 0.08	-1.00 ± 0.05	-235.21	6.34	4.20×10^{-2}
NGC 3783	0112210101	4878^{+2409}_{-1911}	-1.40 ± 0.09	-1.00 ± 0.06	-160.84	4.70	9.53×10^{-3}
	0112210201	5939^{+2928}_{-1474}	-1.50 ± 0.07	-1.00 ± 0.05	-264.472	5.95	5.11×10^{-2}
	0112210501	11353^{+9886}_{-3606}	-1.40 ± 0.04	-1.00 ± 0.029	-913.03	6.98	3.05×10^{-3}
NGC 4051	0157560101	3882^{+1083}_{-695}	-2.20 ± 0.09	-1.00 ± 0.06	-90.10	1.26	5.33×10^{-1}
	0606320101	3067^{+784}_{-519}	-2.30 ± 0.07	-1.00 ± 0.05	-129.60	0.39	8.21×10^{-1}
	0606320201	2396^{+506}_{-355}	-2.50 ± 0.07	-1.00 ± 0.05	-111.51	0.08	9.61×10^{-1}
	0606321601	3403^{+805}_{-547}	-2.20 ± 0.05	-1.00 ± 0.03	-236.46	0.00	1.00
NGC 4151	0402660101	588^{+28}_{-26}	-2.50 ± 0.07	-0.20 ± 0.05	-280.38	0.00	1.00
	0402660201	4317^{+2038}_{-1049}	-1.40 ± 0.07	-1.00 ± 0.05	-314.96	4.08	1.30×10^{-1}
MRK 766	0096020101	4195^{+1499}_{-874}	-2.00 ± 0.09	-1.00 ± 0.06	-119.85	4.99	8.23×10^{-2}
	0109141301	5069^{+1441}_{-918}	-1.80 ± 0.04	-1.00 ± 0.03	-660.15	1.17	5.56×10^{-1}
	0304030301	5632^{+1992}_{-1167}	-2.10 ± 0.05	-1.00 ± 0.04	-411.175	7.40	2.47×10^{-1}
	0304030401	3939^{+882}_{-609}	-2.40 ± 0.05	-1.00 ± 0.04	-416.17	0.00	1.00
	0304030501	2960^{+516}_{-382}	-2.50 ± 0.05	-1.00 ± 0.03	-488.16	0.00	1.00
	0304030601	5041^{+1678}_{-1008}	-1.90 ± 0.05	-1.00 ± 0.03	-477.54	0.92	6.3×10^{-1}
	0304030701	3388^{+1227}_{-711}	-2.20 ± 0.09	-1.00 ± 0.06	-99.91	5.08	7.9×10^{-2}
MCG-6-30-15	0111570101	3695^{+1341}_{-777}	-2.30 ± 0.07	-1.00 ± 0.05	-185.82	4.52	1.04×10^{-3}
	0111570201	3181^{+806}_{-535}	-2.40 ± 0.07	-1.00 ± 0.05	-252.21	0.00	1.00
	0029740101	3918^{+912}_{-623}	-2.50 ± 0.06	-1.00 ± 0.04	-324.67	3.50	1.73×10^{-1}
	0029740701	3865^{+742}_{-535}	-2.50 ± 0.05	-1.00 ± 0.03	-632.34	1.48	4.78×10^{-1}
	0029740801	5941^{+1958}_{-1180}	-2.10 ± 0.04	-1.00 ± 0.03	-564.11	4.94	8.45×10^{-2}
IC 4329A	0147440101	4665^{+1263}_{-820}	-1.10 ± 0.04	-1.00 ± 0.03	-949.53	5.04	8.05×10^{-2}
MRK 509	0130720101	2855^{+744}_{-489}	-1.00 ± 0.11	-0.90 ± 0.07	-125.79	4.35	1.13×10^{-1}
	0130720201	2504^{+504}_{-359}	-1.00 ± 0.08	-0.80 ± 0.06	-245.79	3.99	1.36×10^{-1}
	0306090201	3040^{+601}_{-431}	-1.00 ± 0.05	-0.90 ± 0.04	-625.50	5.30	7.10×10^{-2}
	0306090301	1074^{+99}_{-83}	-1.00 ± 0.06	-0.50 ± 0.04	-437.29	2.99	2.24×10^{-1}
	0306090401	6961^{+4288}_{-1921}	-1.20 ± 0.06	-1.00 ± 0.04	-427.16	5.31	7.05×10^{-2}
	0601390201	3082^{+800}_{-527}	-1.00 ± 0.07	-1.00 ± 0.05	-403.09	4.33	1.15×10^{-1}
	0601390301	1200^{+100}_{-86}	-1.00 ± 0.06	-0.50 ± 0.04	-576.85	4.60	1.00×10^{-1}
	0601390401	1044^{+84}_{-73}	-1.00 ± 0.05	-0.50 ± 0.04	-650.54	1.23	5.40×10^{-1}
	0601390501	6752^{+5890}_{-2146}	-1.00 ± 0.06	-1.00 ± 0.04	-498.77	4.47	1.07×10^{-1}
	0601390601	6248^{+4151}_{-1783}	-1.10 ± 0.06	-1.00 ± 0.04	-461.38	4.63	9.87×10^{-2}
	0601390701	6998^{+4557}_{-1979}	-1.20 ± 0.07	-1.00 ± 0.05	-383.37	5.01	8.18×10^{-2}
	0601390801	7615^{+5990}_{-2328}	-1.10 ± 0.07	-1.00 ± 0.05	-363.79	4.60	1.00×10^{-1}
	0601390901	2964^{+784}_{-430}	-1.00 ± 0.06	-1.00 ± 0.04	-509.73	4.27	1.18×10^{-1}
	0601391001	4508^{+1966}_{-1050}	-1.1 ± 0.06	-1.00 ± 0.04	-531.18	0.00	1.00
	0601391101	5847^{+2923}_{-1462}	-1.00 ± 0.07	-1.00 ± 0.05	-346.718	3.72	1.55×10^{-1}
NGC 7469	0112170301	5546^{+3799}_{-1603}	-1.50 ± 0.12	-1.00 ± 0.08	-95.84	2.26	3.24×10^{-1}
	0207090101	7455^{+4437}_{-2026}	-1.30 ± 0.06	-1.00 ± 0.04	-533.01	5.45	6.56×10^{-2}
	0207090201	7885^{+3786}_{-1931}	-1.60 ± 0.07	-1.00 ± 0.05	-319.29	3.30	1.92×10^{-1}

Table 5.6: Results from the PSD fit with a broken power law model. Columns 1 – 8 give the object name, its observation I.D., the break timescale in s (converted to temporal domain from a break frequency in the binned periodogram), the slope $\alpha_{\rm Hi}$ of the power law region at frequencies higher than the break frequency, the slope $\alpha_{\rm Hi}$ of the power law region at frequencies lower than the break frequency, the AIC value, the difference Δ_i which is used to calculate the likelihood and the relative likelihood which quantifies the probability of the broken power law model being chosen over the null model as a best fit PSD model.

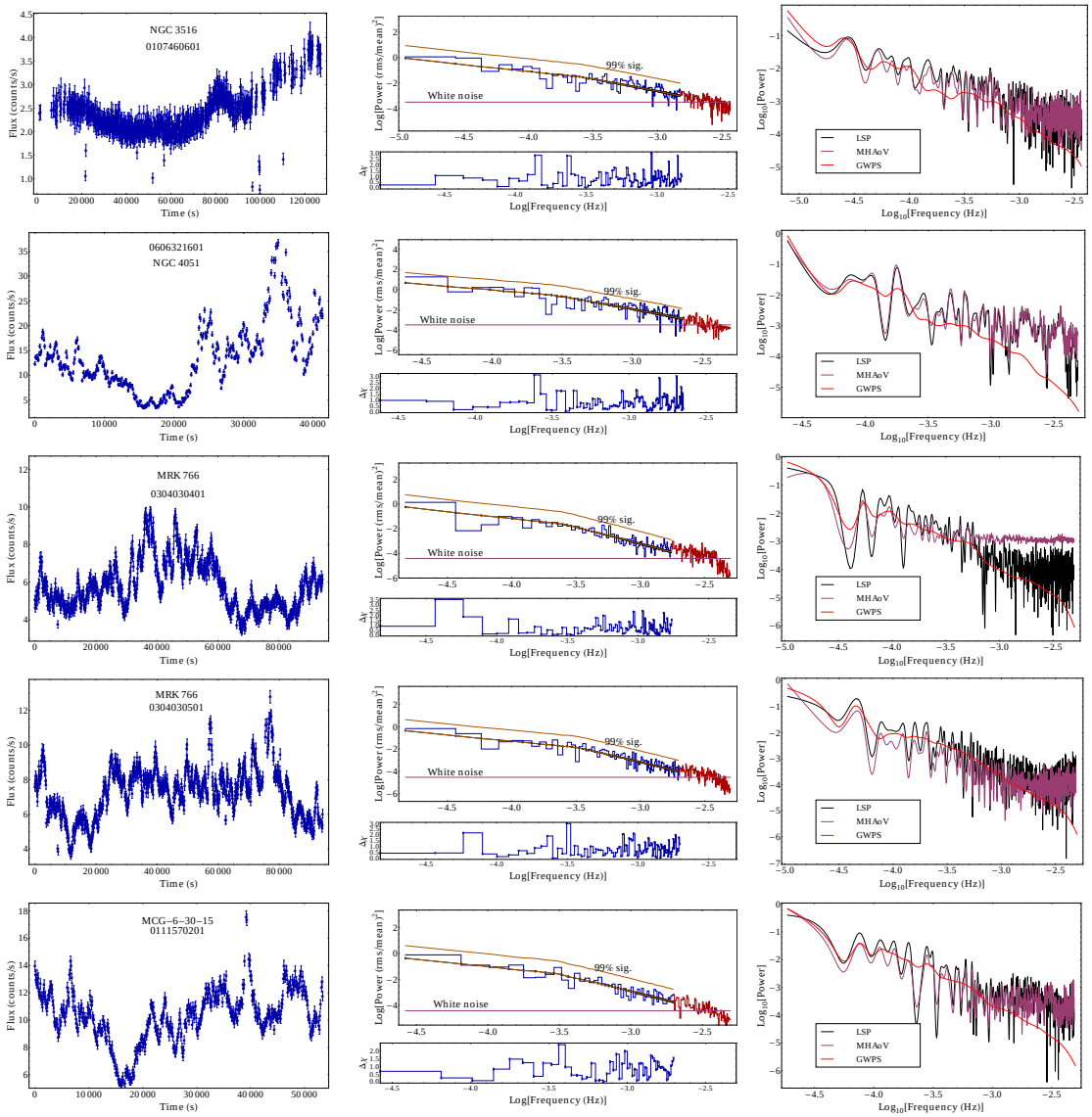

Figure 5.11: Left plot: X-ray light curve (0.3 keV to 10 keV) of the AGN. Middle plot: binned periodogram: fit portion is in blue and white noise region is in red. The best fit is the power law with Lorentzian QPO model and the residue $\Delta\chi$ =(data-model)/σ is shown below it. Right plot: LSP, MHAoV periodogram and global wavelet power spectrum results.

Chapter 6

Theoretical models of disk variability

6.1 Introduction

Rapid short timescale variability with small to large amplitude fluctuations which are generally aperiodic e.g. [3] are observed in light curves from active galactic nuclei (AGN) spanning a wide range of wavelengths from optical to ultra-violet (UV) and X-rays as discussed in Chapter 1.

Phenomenological models of timing properties of variability in optical/UV and X-ray emission from AGN are based on disk based orbital signatures from regions in the near vicinity of the central black hole [75, 74, 76, 77]. Gravitational and Doppler redshift, time delay and light bending introduce their collective signature on outward bound emission. Observables which include light curves and their power spectral density are simulated considering all these effects and intrinsic disk based emission and then compared with observational data in these bands. The development of a power law shape of the measured power spectral density and theoretical constraints on it slope between -1.4 and -2.1 [77] are well supported by observational studies in these wavelengths e.g. [203]. The main general relativistic components used in these models include the geometry or disk structure, Doppler shift due to material on the disk moving away and towards the observer line of sight, gravitational redshift due to the curved spacetime surrounding the black hole and time delay also due to the curved spacetime as well as due to the disk being inclined towards the observer line of sight. Light bending effects have been considered recently in phenomenological models of variable emission from orbital features in Keplerian orbits around Schwarzschild black holes [78, 204], Kerr black holes [205] and from the inner region hosting the disk and the developing jet around Schwarzschild black holes [101] in the context of simulating light curves and power spectra. A summary of the developments in the phenomenological modelling of variability in optical/UV and X-ray emission from AGN is presented in Table 6.1.

In the following sections of this chapter, we present a complete description of the formalism used in constructing the phenomenological models in Kerr geometry for various observers, showing the reduction or simplification to one of the above cases summarized in Table 6.1. We first describe briefly the Kerr metric, its properties and use it to place lower limits on the emission region and upper limits on the black hole mass assuming that the emission signature is from an orbital feature

Reference	Effects considered	Application and results
Wiita (1991) Schwarzschild (disk model) X-rays	Hotspot in Keplerian motion Co-rotating observer Gravitational and Doppler shifts Time delay	Intrinsic variability: evolution of hotspots g-factor Light curves and power spectra Power law slope for power spectrum
Zhang & Bao (1991) Schwarzschild (disk model) X-rays	Hotspot in Keplerian motion Co-rotating observer Gravitational and Doppler shifts Time delay	Intrinsic variability: evolution of hotspots g-factor Light curves and power spectra Power law slope for power spectrum
Abramowicz et al. (1991) Schwarzschild (disk model) X-rays	Hotspot in Keplerian motion Co-rotating observer Gravitational and Doppler shifts Time delay Power law slope dependent on spot evolution	Intrinsic variability: evolution of hotspots Rotation of spots, angle to observer los g-factor Light curves and power spectra
Bao (1992) Schwarzschild (disk model) X-rays	Hotspot in Keplerian motion Co-rotating observer Gravitational and Doppler shifts Time delay	Intrinsic variability: evolution of hotspots Overall variability: rotation of spots, angle to observer los Analytic expression for impact factor Analytic expression for solid angle and flux at observer Light curves and power spectra
Mangalam & Wiita (1993) Schwarzschild (disk model) Optical/UV	Orbital features in Keplerian motion Co-rotating observer Gravitational and Doppler shifts Time delay α and β disks	Intrinsic variability: evolution of hotspots Orbital features and their evolution g-factor Light curves and power spectra Statistical study of simulated power spectra and light curves Simulated power law slope between -1.4 and -2.0
Zycki & Niedzwiecki (2005) Kerr (disk model) X-rays	Flares in Keplerian motion Co-rotating observer Gravitational and Doppler shifts	Intrinsic variability: evolution of hotspots Overall variability: rotation of spots, angle to observer los g-factor Light curves and power spectra
Pechacek et al. (2005) Schwarzschild (disk model) X-rays	Hotspot in Keplerian motion Local static observer Gravitational and Doppler shifts Light bending using approximation in [79]	g-factor g with aberration effects
Pechacek et al. (2006) Schwarzschild (disk model) X-rays	Hotspot in Keplerian motion in a narrow ring Local static observer frame Gravitational and Doppler shifts Light bending using approximation in [79] Time delay due to disk orientation, spot motion and light bending	Variability due to orbiting features g-factor g with aberration effects Light curves and a QPO profiled power spectrum
Mangalam & Mohan (2013) Kerr (disk) and Schwarzschild (jet) Optical/UV X-rays	Orbital features in Keplerian motion Local static observer frame Gravitational and Doppler shifts Light bending using approximation in [79] Time delay due to disk orientation, spot motion and light bending Kinematic motion of orbital features in jet	Variability due to orbiting features g-factor g with aberration effects Light curves Evolution of the QPO

Table 6.1: Summary of theoretical models of variability in X-ray and optical/UV from disk based orbital processes.

in §6.2. Then, the derivation of the four-velocity of the bulk-flowing plasma is first calculated in the local relativistic frames in §6.3. This is followed by the derivation of the four-momentum of the null geodesics in the Kerr metric in §6.4. The derived four-velocity of the bulk flowing plasma and the four-momentum of the null geodesics are put to use in §6.5 where the effective redshift factor g is expressed in terms of these quantities. The description of variability can be simplified by expressing all physical quantities in the description of variability in terms of the emission angles $\hat{\theta}$ and $\hat{\phi}$. The procedure to carry this out is described in §6.6 where the emission angles are related to the initial emission null vectors as observed in the local relativistic observer frames. The impact parameter, Carter's constant and hence the effective redshift factor are expressed in terms of the emission angles as observed in these frames in §6.7. This is shown reduce to known results for the cases of the co-rotating observer or a local non-rotating observer in Schwarzschild geometry (local static frame). In our model, we calculate the g factor in the LNRF which directly corresponds to the observers frame. We derive a relation between the emission angles $\hat{\theta}$ and $\hat{\phi}$ in §6.8, using the impact parameter and Carter's constant which are expressed in terms of the null vectors for the LRF and the LNRF where radial inflow is present and for the CRF and LNRF where only azimuthal flow is present. Constraints on the region of emission and range of allowed angles such that the null ray would reach the observer are calculated using the effective potential and the relationship between the null emission vectors in §6.9. The dependence of the azimuthal emission angle $\hat{\phi}$ on the time delay is presented in §6.10 such that the effective redshift factor g can be finally expressed in terms of the proper time. Simulated light curves are then presented in §6.11.

6.2 Kerr geometry and relevant properties

The physics of the flow and the emission are described in the Kerr metric expressed by the general line element e.g. [61],

$$ds^2 = -e^{2\nu}dt^2 + e^{2\psi}(d\phi - \omega dt)^2 + e^{2\mu_1}dr^2 + e^{2\mu_2}d\theta^2 \tag{6.1}$$

All above quantities are expressed in geometrized units where Newton's constant $G = 1$ and the velocity of light in vacuum $c = 1$. In the Boyer-Lindquist coordinates (t,r,θ,ϕ), the line element describes the spacetime around a rotating black hole with a specific angular momentum or spin of $a = J/M$ and mass M. The covariant and contravariant components of the metric, expressed in these coordinates are given by

$$\begin{aligned} g_{tt} = (-e^{2\nu} + \omega^2 e^{2\psi}),\ g^{tt} = -e^{-2\nu} \\ g_{\phi\phi} = e^{2\psi},\ g^{\phi\phi} = -e^{-2\psi} + \omega^2 e^{-2\psi} \\ g_{rr} = e^{2\mu_1},\ g^{rr} = e^{-2\mu_1} \\ g_{\theta\theta} = e^{2\mu_2},\ g^{\theta\theta} = e^{-2\mu_2} \\ g_{\phi t} = g_{t\phi} = -\omega e^{2\psi},\ g^{\phi t} = g^{t\phi} = -\omega e^{-2\nu} \end{aligned} \tag{6.2}$$

where the coefficients used in the metric components and in the line element are given by

$$\begin{aligned} e^{2\nu} &= \frac{\Sigma\Delta}{A} \\ e^{2\psi} &= \frac{A\sin^2\theta}{\Sigma} \\ e^{2\mu_1} &= \frac{\Sigma}{\Delta} \\ e^{2\mu_2} &= \Sigma \end{aligned} \tag{6.3}$$

and

$$\begin{aligned} \omega &= 2Mar/A \\ \Delta &= r^2 + a^2 - 2Mr \\ A &= (r^2+a^2)^2 - \Delta a^2 \sin^2\theta \\ \Sigma &= r^2 + a^2\cos^2\theta. \end{aligned} \tag{6.4}$$

Using the above expressions, the line element can be expressed as

$$\begin{aligned} ds^2 &= -\left(1 - \frac{2Mr}{\Sigma}\right)dt^2 + \frac{r^2+a^2+2Ma^2r\sin^2\theta}{\Sigma}\sin^2\theta d\phi^2 \\ &+ \frac{4Mar\sin^2\theta}{\Sigma}dtd\phi - \frac{\Sigma}{\Delta}dr^2 - \Sigma d\theta^2 \end{aligned} \tag{6.5}$$

The line element reduces to the Schwarzschild metric when we set $a = 0$ as the cross term $dtd\phi = 0$ due to $\omega = 0$. Further, for $r \gg M$ and $r \gg a$, i.e. at large distances from the black hole, the line element reduces to

$$ds^2 = -\left(1 - \frac{2M}{r}\right)dt^2 + \left(1 + \frac{2M}{r}\right)dr^2 + r^2(d\theta + \sin^2\theta d\phi^2) \tag{6.6}$$

which is the static weak field line element. Thus the Kerr metric is asympotically flat. From the form of the line element, the Kerr metric is independent of changes in ϕ and t coordinates. Hence, there exist two Killing vectors corresponding to these symmetries, $\zeta^\alpha = (1,0,0,0)$ and $\eta^\alpha = (0,0,0,1)$. These can be used to describe a stationary, axisymmetric observer. Unlike the Schwarzschild metric, the Kerr metric is not spherically symmetric due to the dependence of the metric coefficients on θ.

6.3 Reference frames and the bulk flow velocity

We make use of a set of orthonormal frames in order to describe the geometry of the flow and the null trajectories. These help in simplifying the description and the inferences one may draw from the results. The orthonormal nature of each frame allows one to treat these as local relativistic frames and hence perform a Lorentz transformation to describe the relationship of physical quantitites

measured in these frames. These frames include the local non-rotating frame (LNRF) or the zero angular momentum frame (ZAMO) which is the frame of a local stationery observer, the co-rotating frame (CRF) which is the frame co-rotating with the fluid on the disk and the local rest frame (LRF) which is co-rotating and radially infalling along with the fluid on the disk. The following quantites are calculated: the contravariant and covariant four-velocities, the tetrads used by an observer in that frame for measurements, the orthogonal three-velocity obtained by projecting the four-velocity into the local orthogonal tetrad frame. The LNRF reduces to the frame of the distant observer at large r, which is the correct frame for practical purposes. Using the multiple reference frames, once can derive the four-velocity of the bulk flow in the Boyer-Lindquist coordinates.

The contravariant four-velocity of the emitting source (on time-like trajectories) is given by

$$u^\alpha = (u^t, u^r, u^\theta, u^\phi) \tag{6.7}$$

Since $u.u = -1$ for time-like trajectories, this identity can be used to evaluate the components of the four-velocity

$$u.u = u^\alpha u_\alpha = u^\alpha u^\beta g_{\alpha\beta} = -1 \tag{6.8}$$

For the case of the emitting source being confined to a disk, $u^\theta = 0$. Further, if the source is on Keplerian orbits around the black hole, its angular velocity $\Omega = \dfrac{u^\phi}{u^t}$. Using these simplifications, the four-velocity reduces to

$$u^\alpha = (u^t, u^r, 0, \Omega u^t). \tag{6.9}$$

Using the identity in eqn. (6.8),

$$(u^t)^2 g_{tt} + 2\Omega (u^t)^2 g_{\phi t} + (u^r)^2 g_{rr} + \Omega^2 (u^t)^2 g_{\phi\phi} = -1 \tag{6.10}$$

From the above equation, it can be inferred that u^r and u^t are related. The covariant four-velocity can be evaluated from the contravariant four velocity using the metric coefficients

$$u_\beta = u^\alpha g_{\alpha\beta}. \tag{6.11}$$

The orthogonal three-velocity in a specific local relativistic frame such as the LNRF, CRF or LRF can be evaluated once the observed four-velocity and tetrads in that frame are specificed using

$$v^{(a)} = \frac{u^\alpha e^{(a)}_\alpha}{u^\alpha e^{(t)}_\alpha} = \frac{u_\alpha e^\alpha_{(a)}}{u_\alpha e^\alpha_{(t)}} = v_{(a)} \tag{6.12}$$

where the tetrads e_α and e^α are the orthogonal unit vectors used by an observer in the desired frame and $a = 1, 2, 3$ is used to represent the space coordinates.

The physics of the flow is evaluated in the Boyer-Linquist frame where the four-velocity is given by eqn. 6.9. In each of the local relativistic frames, the tetrads which include the unit direction vectors and the one-forms in that frame are first developed. The tetrads are useful when the description of the flow or the emission and the null geodesics must be projected into the frame

of the local relativistic observer. Then, the four-velocity of the flow is assembled in stages in the Boyer-Lindquist frame using the LNRF, CRF and finally the LRF frame. In each of the frames, the orthogonal three-velocity of the flow as measured by each corresponding observer is derived and used in some cases to obtain the components of the flow four-velocity. The transformation of tetrads between the LNRF, CRF and LRF are presented in [206].

6.3.1 Local non-rotating frame (LNRF)

An observer in this frame posseses zero angular momentum $l = 0$ and thus the azimuthal component of the four-velocity, $u_\phi = 0$. Thus, $u^\phi = (-g_{\phi t}/g_{\phi\phi})u^t = \omega u^t$. Thus, the observer orbits the black hole at an angular velocity ω, being dragged by the rotating black hole. This observer is similar to the stationary observer in Schwarzschild spacetime as when the black hole spin $a = 0$, $\omega = 0$. Also, at large distances r, for a given black hole mass and spin, $\omega \propto r^{-3}$, thus tending to 0 reducing the frame to the stationary Schwarzschild observer.

The tetrads in terms of the matrix notation are

$$e^{(a)}_\alpha = \begin{pmatrix} e^\nu & 0 & 0 & 0 \\ 0 & e^{\mu_1} & 0 & 0 \\ 0 & 0 & e^{\mu_2} & 0 \\ -\omega e^\psi & 0 & 0 & e^\psi \end{pmatrix}$$

$$e^\alpha_{(a)} = \begin{pmatrix} e^{-\nu} & 0 & 0 & \omega e^{-\nu} \\ 0 & e^{-\mu_1} & 0 & 0 \\ 0 & 0 & e^{-\mu_2} & 0 \\ 0 & 0 & 0 & e^{-\psi} \end{pmatrix}$$

which are obtained by writing the metric in a tetrad notation. It is first necessary to describe the four-velocity of the LNRF observer for the four-velocity of the flow in the Boyer-Lindquist frame to be constructed in stages. The four velocity of a time-like observer in the LNRF is given by

$$u^\alpha = u^t(1, 0, 0, \omega) \tag{6.13}$$

Using eqn. (6.8),

$$(u^t)^2 g_{tt} + 2u^t u^\phi g_{\phi t} + (u^\phi)^2 g_{\phi\phi} = -1 \tag{6.14}$$

Solving this, we obtain $u^t = e^{-\nu}$ and hence the four-velocity of the LNRF observer is given by:

$$u^\alpha = e^{-\nu}(1, 0, 0, \omega) \tag{6.15}$$

We can now calculate the three-velocity of the LNRF observer using the orthogonal tetrads obtained above. The radial component, the polar or co-latitudinal component and the azimuthal

component of the three-velocity are given by

$$v^{(r)} = \frac{u^r e_r^{(r)}}{u^t e_t^{(t)} + u^\phi e_\phi^{(t)}} = 0 = v_{(r)}. \tag{6.16}$$

$$v^{(\theta)} = \frac{u^\theta e_\theta^{(\theta)}}{u^t e_t^{(t)} + u^\phi e_\phi^{(t)}} = 0 = v_{(\theta)} \tag{6.17}$$

$$v^{(\phi)} = \frac{u^t e_t^{(\phi)} + u^\phi e_\phi^{(\phi)}}{u^t e_t^{(t)} + u^\phi e_\phi^{(t)}} = 0 = v_{(\phi)}. \tag{6.18}$$

Thus, the three-velocity, measured using the projection of the four-velocity into the orthogonal tetrad frame for an LNRF observer is 0.

$$v^{(a)} = (v^{(r)}, v^{(\theta)}, v^{(\phi)}) = (0, 0, 0) \tag{6.19}$$

6.3.2 Co-rotating frame (CRF)

The observer in this frame co-rotates with the fluid which is in a Keplerian orbit with angular velocity Ω. If bulk radial inflow of the orbiting plasma is absent, the co-rotating frame can be used to describe the four-velocity of the flow. The tetrads in this frame can be obtained by an azimuthal Lorentz boost to the LNRF tetrads. The tetrads in terms of the matrix notation are

$$e_\alpha^{(a)}(CRF) = \Lambda^a{}_b(\phi)\ e_\alpha^{(b)}(LNRF) \tag{6.20}$$

$$e_\alpha^{(a)} = \begin{pmatrix} \gamma_\phi & 0 & 0 & -\gamma_\phi\beta_\phi \\ 0 & 1 & 0 & 0 \\ 0 & 0 & 1 & 0 \\ -\gamma_\phi\beta_\phi & 0 & 0 & \gamma_\phi \end{pmatrix} \begin{pmatrix} e^\nu & 0 & 0 & 0 \\ 0 & e^{\mu_1} & 0 & 0 \\ 0 & 0 & e^{\mu_2} & 0 \\ -\omega e^\psi & 0 & 0 & e^\psi \end{pmatrix}$$

$$e_\alpha^{(a)} = \begin{pmatrix} \gamma_\phi(e^\nu + \beta_\phi\omega e^\psi) & 0 & 0 & -\gamma_\phi\beta_\phi e^\psi \\ 0 & e^{\mu_1} & 0 & 0 \\ 0 & 0 & e^{\mu_2} & 0 \\ -\gamma_\phi(\beta_\phi e^\nu + \omega e^\psi) & 0 & 0 & \gamma_\phi e^\psi \end{pmatrix}$$

$$e_{(a)}^\alpha(CRF) = \Lambda_a{}^b(\phi)\ e_{(b)}^\alpha(LNRF) \tag{6.21}$$

$$e_{(a)}^\alpha = \begin{pmatrix} \gamma_\phi & 0 & 0 & \gamma_\phi\beta_\phi \\ 0 & 1 & 0 & 0 \\ 0 & 0 & 1 & 0 \\ \gamma_\phi\beta_\phi & 0 & 0 & \gamma_\phi \end{pmatrix} \begin{pmatrix} e^{-\nu} & 0 & 0 & \omega e^{-\nu} \\ 0 & e^{-\mu_1} & 0 & 0 \\ 0 & 0 & e^{-\mu_2} & 0 \\ 0 & 0 & 0 & e^{-\psi} \end{pmatrix}$$

$$e^{\alpha}_{(a)} = \begin{pmatrix} \gamma_\phi e^{-\nu} & 0 & 0 & \gamma_\phi(\omega e^{-\nu} + \beta_\phi e^{-\psi}) \\ 0 & e^{\mu_1} & 0 & 0 \\ 0 & 0 & e^{\mu_2} & 0 \\ \gamma_\phi \beta_\phi e^{-\nu} & 0 & 0 & \gamma_\phi(\beta_\phi \omega e^{-\nu} + e^{-\psi}) \end{pmatrix}$$

The four velocity of a time-like trajectory in of a CRF observer expressed in the Boyer-Lindquist frame is then given by

$$u^\alpha = u^t(1, 0, 0, \Omega). \tag{6.22}$$

Using eqn. (6.8),

$$(u^t)^2 g_{tt} + 2u^t u^\phi g_{\phi t} + (u^\phi)^2 g_{\phi\phi} = -1. \tag{6.23}$$

Solving this, we obtain $u^t = \left(e^{2\nu} - (\Omega - \omega)^2 e^{2\psi}\right)^{-1/2}$ due to which the four-velocity of the bulk flow is given by

$$u^\alpha = \left(e^{2\nu} - (\Omega - \omega)^2 e^{2\psi}\right)^{-1/2} (1, 0, 0, \Omega). \tag{6.24}$$

The orthogonal three-velocity of the CRF with respect to the LNRF observer is obtained by projecting the four-velocity calculated into the LNRF tetrad frame. The radial component, the polar or co-latitudinal component and the azimuthal component of the three-velocity are given by

$$v^{(r)} = \frac{u^r e^{(r)}_r}{u^t e^{(t)}_t + u^\phi e^{(t)}_\phi} = 0 = v_{(r)}. \tag{6.25}$$

$$v^{(\theta)} = \frac{u^\theta e^{(\theta)}_\theta}{u^t e^{(t)}_t + u^\phi e^{(t)}_\phi} = 0 = v_{(\theta)} \tag{6.26}$$

$$v^{(\phi)} = \frac{u^t e^{(\phi)}_t + u^\phi e^{(\phi)}_\phi}{u^t e^{(t)}_t + u^\phi e^{(t)}_\phi} = (\Omega - \omega) e^{\psi - \nu} = v_{(\phi)}. \tag{6.27}$$

Thus, the LNRF observer sees the CRF frame with an azimuthal motion

$$v^{(a)} = (v^{(r)}, v^{(\theta)}, v^{(\phi)}) = (0, 0, (\Omega - \omega) e^{\psi - \nu}) \tag{6.28}$$

The azimuthal orthogonal velocity $v^\phi = \beta_\phi = (\Omega - \omega)e^{\psi-\nu}$ with an associated Lorentz factor $\gamma_\phi = (1 - \beta^2_\phi)^{-1/2}$. The time component of the fluid four-velocity is then given by $u^t = \gamma_\phi e^{-\nu}$ and hence, the four-velocity is given by

$$u^\alpha = \gamma_\phi e^{-\nu}(1, 0, 0, \Omega) \tag{6.29}$$

6.3.3 Local rest frame (LRF)

The flow could possess radial motion in addition to azimuthal motion. An observer in the LNRF observes the LRF moving with a Kelperian orbit of the fluid with an angular velocity Ω and a

radial velocity u^r. The tetrads in this frame can be obtained by a radial Lorentz boost to the CRF tetrads. The tetrads in terms of the matrix notation are

$$e^{(a)}_{\alpha}(LRF) = \Lambda^{a}{}_{b}(r)\; e^{(b)}_{\alpha}(CRF) \tag{6.30}$$

$$e^{(a)}_{\alpha} = \begin{pmatrix} \gamma_r & -\gamma_r\beta_r & 0 & 0 \\ -\gamma_r\beta_r & \gamma_r & 0 & 0 \\ 0 & 0 & 1 & 0 \\ 0 & 0 & 0 & 1 \end{pmatrix} \begin{pmatrix} \gamma_\phi(e^\nu + \beta_\phi\omega e^\psi) & 0 & 0 & -\gamma_\phi\beta_\phi e^\psi \\ 0 & e^{\mu_1} & 0 & 0 \\ 0 & 0 & e^{\mu_2} & 0 \\ -\gamma_\phi(\beta_\phi e^\nu + \omega e^\psi) & 0 & 0 & \gamma_\phi e^\psi \end{pmatrix}$$

$$e^{(a)}_{\alpha} = \begin{pmatrix} \gamma_r\gamma_\phi(e^\nu + \beta_\phi\omega e^\psi) & \gamma_r\beta_r e^{-mu_1} & 0 & -\gamma_r\gamma_\phi\beta_\phi e^\psi \\ -\gamma_r\gamma_\phi\beta_r(e^\nu + \beta_\phi\omega e^\psi) & \gamma_r e^{\mu_1} & 0 & \gamma_r\gamma_\phi\beta_r\beta_\phi e^\psi \\ 0 & 0 & e^{\mu_2} & 0 \\ -\gamma_\phi(\beta_\phi e^\nu + \omega e^\psi) & 0 & 0 & \gamma_\phi e^\psi \end{pmatrix}$$

$$e^{\alpha}_{(a)}(CRF) = \Lambda_{a}{}^{b}(r)\; e^{\alpha}_{(b)}(LNRF) \tag{6.31}$$

$$e^{\alpha}_{(a)} = \begin{pmatrix} \gamma_r & \gamma_r\beta_r & 0 & 0 \\ \gamma_r\beta_r & \gamma_r & 0 & 0 \\ 0 & 0 & 1 & 0 \\ 0 & 0 & 0 & 1 \end{pmatrix} \begin{pmatrix} \gamma_\phi e^{-\nu} & 0 & 0 & \gamma_\phi(\omega e^{-\nu} + \beta_\phi e^{-\psi}) \\ 0 & e^{\mu_1} & 0 & 0 \\ 0 & 0 & e^{\mu_2} & 0 \\ \gamma_\phi\beta_\phi e^{-\nu} & 0 & 0 & \gamma_\phi(\beta_\phi\omega e^{-\nu} + e^{-\psi}) \end{pmatrix}$$

$$e^{\alpha}_{(a)} = \begin{pmatrix} \gamma_r\gamma_\phi e^{-\nu} & \gamma_r\beta_r e^{-\mu_1} & 0 & \gamma_r\gamma_\phi(\omega e^{-\nu} + \beta_\phi e^{-\psi}) \\ \gamma_r\gamma_\phi\beta_r e^{-\nu} & \gamma_r e^{\mu_1} & 0 & \gamma_r\gamma_\phi\beta_r(\omega e^{-\nu} + \beta_\phi e^{-\psi}) \\ 0 & 0 & e^{\mu_2} & 0 \\ \gamma_\phi\beta_\phi e^{-\nu} & 0 & 0 & \gamma_\phi(\beta_\phi\omega e^{-\nu} + e^{-\psi}) \end{pmatrix}$$

The four-velocity of a time-like observer in the LRF is given by

$$u^\alpha = (u^t, u^r, 0, \Omega u^t). \tag{6.32}$$

Using eqn. (6.8),

$$(u^t)^2 g_{tt} + 2u^t u^\phi g_{\phi t} + (u^\phi)^2 g_{\phi\phi} + (u^r)^2 g_{rr} = -1. \tag{6.33}$$

Solving this, we obtain

$$u^t = \left(\frac{1 + (u^r)^2 e^{2\mu_1}}{e^{2\nu} - (\Omega - \omega)^2 e^{2\psi}}\right)^{1/2} \tag{6.34}$$

using which the four-velocity of the bulk flow is given by

$$u^\alpha = \left(\left(\frac{1 + (u^r)^2 e^{2\mu_1}}{e^{2\nu} - (\Omega - \omega)^2 e^{2\psi}}\right)^{1/2}, u^r, 0, \Omega\left(\frac{1 + (u^r)^2 e^{2\mu_1}}{e^{2\nu} - (\Omega - \omega)^2 e^{2\psi}}\right)^{1/2}\right). \tag{6.35}$$

The radial component of the orthgonal three-velocity v^r evaluated by an observer in the LRF would be 0. Imposing this condition, we obtain the relation

$$v^{(r)} = \frac{u^r e_r^{(r)} + u^t e_t^{(r)} + u^\phi e_\phi^{(r)} +}{u^t e_t^{(t)} + u^r e_r^{(t)} + u^\phi e_\phi^{(t)}} = 0 = v_{(r)}. \tag{6.36}$$

The polar or co-latitudinal component and the azimuthal component of the three-velocity are given by

$$v^{(\theta)} = \frac{u^\theta e_\theta^{(\theta)}}{u^t e_t^{(t)} + u^\phi e_\phi^{(t)}} = 0 = v_{(\theta)}, \tag{6.37}$$

$$v^{(\phi)} = \frac{u^t e_t^{(\phi)} + u^\phi e_\phi^{(\phi)}}{u^t e_t^{(t)} + u^\phi e_\phi^{(t)}} = (\Omega - \omega)e^{\psi-\nu} = v_{(\phi)}. \tag{6.38}$$

The azimuthal orthogonal velocity is $v^\phi = \beta_\phi = (\Omega - \omega)e^{\psi-\nu}$ and the associated Lorentz factor is $\gamma_\phi = (1 - \beta_\phi^2)^{-1/2}$. The radial orthogonal velocity is $v^r = \beta_r$ and the associated Lorentz factor $\gamma_r = (1 - \beta_r^2)^{-1/2}$.

The imposed condition in eqn. (6.36) simplifies to

$$\frac{u^r}{u^t} = \frac{\beta_r}{\gamma_\phi} e^{\mu_1 - \nu}. \tag{6.39}$$

Using u^t derived in eqn. (6.34), we can then express the radial component of the flow four-velocity as

$$u^r = \gamma_r \beta_r \sqrt{\Delta/r^2}. \tag{6.40}$$

Now, using eqn. (6.39), u^t can be written as

$$u^t = \sqrt{A/(\Delta r^2)}\gamma_\phi \gamma_r, \tag{6.41}$$

and the azimuthal component of the flow four-velocity can be written as

$$u^\phi = \Omega\sqrt{A/(\Delta r^2)}\gamma_\phi \gamma_r \tag{6.42}$$

Thus, the general four-velocity of the bulk flow is given by

$$u^\alpha = (\sqrt{A/(\Delta r^2)}\gamma_\phi \gamma_r, \gamma_r \beta_r \sqrt{\Delta/r^2}, 0, \Omega\sqrt{A/(\Delta r^2)}\gamma_\phi \gamma_r) \tag{6.43}$$

6.4 Null geodesics and the four-momentum in Boyer-Lindquist coordinates

The conserved quantities for the Kerr metric include the total energy $\varepsilon = -p_t$, the azimuthal angular momentum $l = p_\phi$ and Carter's constant $Q = p_\theta^2 + \cos^2\theta(-a^2\varepsilon^2 + l^2/\sin^2\theta)$. The null

geodesics and the associated covariant components of the four-momentum are derivable from these general conditions [207]. The contravariant components of the four-momentum are obtained using

$$p^{\alpha} = p_{\beta} g^{\beta\alpha} \tag{6.44}$$

The time component is given by

$$p^{t} = p_{t} g^{tt} + p_{\phi} g^{\phi t} \implies \Sigma p^{t} - a(a\varepsilon \sin^{2}\theta - l) + \frac{r^{2}+a^{2}}{\Delta} T. \tag{6.45}$$

The radial component is given by

$$p^{r} = p_{r} g^{rr} = e^{-\mu_{1}} p_{r}. \tag{6.46}$$

The polar component, using the Carter's constant Q can be written as

$$p^{\theta} = p_{\theta} g^{\theta\theta} = e^{-\mu_{2}} (Q - \cos^{2}\theta(-a^{2}\varepsilon^{2} + l^{2}/\sin^{2}\theta))^{1/2} \tag{6.47}$$

and the azimuthal component, using the angular momentum $l = p_{\phi}$ can be written as

$$p^{\phi} = p_{t} g^{\phi t} + p_{\phi} g^{\phi\phi} \implies \Sigma p^{\phi} = \frac{aT}{\Delta} - (a\varepsilon - l/\sin^{2}\theta) \tag{6.48}$$

where $T = (r^{2}+a^{2})\varepsilon - al$.

For null geodesics, the following condition

$$p.p = p^{\alpha} p_{\alpha} = p^{t} p_{t} + p^{r} p_{r} + p^{\theta} p_{\theta} + p^{\phi} p_{\phi} = 0 \tag{6.49}$$

is used to solved for the contravariant radial component of the null four-momentum, p^{r}, in terms of the above contravariant time, polar and azimuthal components:

$$\Sigma p^{r} = (T^{2} - \Delta((l - a\varepsilon)^{2} + Q))^{1/2} \tag{6.50}$$

If we introduce the impact factor $\lambda = l/\varepsilon$ and rescale the Carter's constant $q^{2} = Q/\varepsilon^{2}$, the terms used to express the radial and polar components of the four momentum can be written as

$$T^{2} - \Delta((l - a\varepsilon)^{2} + Q) = \varepsilon((r^{2} + a^{2} - \lambda)^{2} - \Delta((\lambda - a)^{2} + q^{2})) = \varepsilon R \tag{6.51}$$

and

$$Q + \cos^{2}\theta(a^{2}\varepsilon^{2} - l^{2}/\sin^{2}\theta) = \varepsilon(q^{2} + \cos^{2}\theta(a^{2}\varepsilon^{2} - \lambda^{2}/\sin^{2}\theta) = \varepsilon\Theta \tag{6.52}$$

Thus, the covariant components of the four-momentum can be calculated to be,

$$p_{\alpha} = (p_{t}, p_{r}, p_{\theta}, p_{\phi}) = \varepsilon(-1, R^{1/2}/\Delta, \Theta^{1/2}, \lambda) \tag{6.53}$$

6.5 Effective redshift factor

The effective redshift factor g is the ratio of observed to emitted energy of the photon and is given by,

$$g = \frac{E_{\rm observed}}{E_{\rm emitted}} = \frac{p_\alpha(\infty)u^\alpha(\infty)(t+\tau)}{p_\alpha u^\alpha(t)} \tag{6.54}$$

where τ is the travel time of the emitted photon. The four-momentum of the null geodesics is given by eqn. (6.53) and the four-velocity of the flow is given by eqn. (6.43). Using these in the above equation, the general expression for the effective redshift factor includes effects due to Doppler shift, gravitational redshift, azimuthal and radial bulk inflow

$$g = \sqrt{\frac{r^2\Delta}{A}}\frac{1}{\gamma_\phi\gamma_r}\left(1 - \frac{\beta_r}{\gamma_\phi}\sqrt{\frac{R}{A}} - \lambda\Omega\right)^{-1} \tag{6.55}$$

The effective redshift factor $g = g(\beta_r, \lambda, q, r, a)$.

6.6 Emission vectors and emission angles

The parameters λ and q can be expressed in terms of the initial emission angles of the photon $(\tilde{\theta}, \tilde{\phi})$ where $\tilde{\theta}$ is the polar or co-latitudinal angle between the local normal and the emission direction and $\tilde{\phi}$ is the azimuthal angle which describes the position of emission of the radiation. The emission four-vector of the emerging radiation from a source orbiting on the disk is given by,

$$n^\alpha = \sin\tilde{\theta}\cos\tilde{\phi}\ e^\alpha_{(r)} + \cos\tilde{\phi}\ e^\alpha_{(\theta)} - \sin\tilde{\theta}\sin\tilde{\phi}\ e^\alpha_{(\phi)} \tag{6.56}$$

The tetrads $e^\alpha_{(a)}$ describe the frame in which the emission is viewed by the corresponding observer. The orthogonal three-velocity vectors for the null rays can be obtained by projecting the emission four-vector n^α into the desired frame by the corresponding observer. These components can be evaluated using

$$n^{(a)} = n^\alpha e^\alpha_{(a)} \tag{6.57}$$

and

$$n^{(a)} = n_{(a)} = \frac{p^\alpha e^{(a)}_\alpha}{p^\alpha e^{(t)}_\alpha} = \frac{p_\alpha e^\alpha_{(a)}}{p_\alpha e^\alpha_{(t)}} \tag{6.58}$$

The orthogonal three-velocities of the null geodesics as measured by an observer in the LNRF are

$$n^{(\phi)} = \frac{p_\alpha e^\alpha_{(\phi)}}{p_\alpha e^\alpha_{(t)}} = \frac{p_t e^t_{(\phi)} + p_\phi e^\phi_{(\phi)}}{p_t e^t_{(t)} + p_\phi e^\phi_{(t)}} = -\frac{\lambda e^{\nu-\psi}}{1-\lambda\omega} = n_{(\phi)} \tag{6.59}$$

and

$$n^{(\theta)} = \frac{p_\alpha e^\alpha_{(\theta)}}{p_\alpha e^\alpha_{(t)}} = \frac{p_\theta e^\theta_{(\theta)}}{p_t e^t_{(t)} + p_\phi e^\phi_{(t)}} = -\frac{\Theta^{1/2} e^{\nu-\mu_2}}{1-\lambda\omega} = n_{(\theta)} \tag{6.60}$$

where $n^{(\phi)}$ and $n^{(\theta)}$ in eqns. (6.59) & (6.60) are the azimuthal and polar components of the null orthogonal three-velocities as observed in the LNRF. The orthogonal three-velocities of the null geodesics as measured by an observer in the LRF are

$$n^{(\phi)} = \frac{p_\alpha e^\alpha_{(\phi)}}{p_\alpha e^\alpha_{(t)}} = \frac{p_t e^t_{(\phi)} + p_\phi e^\phi_{(\phi)}}{p_t e^t_{(t)} + p_\phi e^\phi_{(t)}} = \frac{\beta_\phi(1-\lambda\omega) - \lambda e^{\nu-\psi}}{\gamma_r(1-\lambda\Omega - \frac{R^{1/2}}{\Delta}\frac{\beta_r}{\gamma_r} e^{\nu-\mu_1})} = n_{(\phi)} \tag{6.61}$$

$$n^{(\theta)} = \frac{p_\alpha e^\alpha_{(\theta)}}{p_\alpha e^\alpha_{(t)}} = \frac{p_\theta e^\theta_{(\theta)}}{p_t e^t_{(t)} + p_\phi e^\phi_{(t)}} = -\frac{\Theta^{1/2} e^{\nu-\mu_2}}{\gamma_r\gamma_\phi(1-\lambda\Omega - \frac{R^{1/2}}{\Delta}\frac{\beta_r}{\gamma_r} e^{\nu-\mu_1})} = n_{(\theta)} \tag{6.62}$$

where $n^{(\phi)}$ and $n^{(\theta)}$ in eqns. (6.61) & (6.62) are the azimuthal and polar components of the null orthogonal three-velocities as observed in the LRF. If we make the assumption, $\beta_r = 0$, i.e., there is no radial component of the flow, then the LRF reduces to the CRF and the three-velocities calculated above reduce to

$$n^{(\phi)} = \frac{\beta_\phi(1-\lambda\omega) - \lambda e^{\nu-\psi}}{1-\lambda\Omega} \tag{6.63}$$

$$n^{(\theta)} = \frac{\Theta^{1/2} e^{\nu-\mu_2}}{\gamma_\phi(1-\lambda\Omega)} \tag{6.64}$$

6.7 g factor in each local relativistic frame

The orthogonal emission three-velocities of null geodesics, derived in the previous section are first expressed in terms of the emission angles $\tilde{\theta}$ and $\tilde{\phi}$ using which one can then write an expression for the g factor in eqn. (6.55) in each local relativistic frame as a function of these angles. For an observer in the LRF possessing the LRF tetrads, the radial component of the orthogonal three-velocity of the null geodesics is given by

$$n^{(r)} = n^\alpha e^{(r)}_\alpha(LRF) = \sin\tilde{\theta}\cos\tilde{\phi}. \tag{6.65}$$

The polar component is given by

$$n^{(\theta)} = n^\alpha e^{(\theta)}_\alpha(LRF) = \cos\tilde{\theta}, \tag{6.66}$$

and the azimuthal component is given by

$$n^{(\phi)} = n^\alpha e^{(\phi)}_\alpha(LRF) = -\sin\tilde{\theta}\sin\tilde{\phi}. \tag{6.67}$$

The azimuthal component of the three-velocity $n^{(\phi)}$ for an observer in the LRF, expressed in

terms of the impact parameter and Carter's constant is given by eqn. (6.61). Re-expressing it in terms of λ and using eqn. (6.67),

$$\lambda = \frac{-\sin\tilde{\theta}\sin\tilde{\phi}\gamma_r(1-\sqrt{\frac{R}{A}}\frac{\beta_r}{\gamma_\phi})-\beta_\phi}{-\gamma_r\Omega\sin\tilde{\theta}\sin\tilde{\phi}-\beta_\phi\omega-\frac{\Sigma\sqrt{\Delta}}{A\sin\theta}} \tag{6.68}$$

Using the above expression in eqn. (6.55), the g factor can be written as

$$g = -\sqrt{\frac{r^2\Delta}{A}}\frac{1}{\gamma_r\gamma_\phi}\left(\frac{\gamma_r\Omega\sin\tilde{\theta}\sin\tilde{\phi}+\beta_\phi\omega+\frac{\Sigma\sqrt{\Delta}}{A\sin\theta}}{\Omega\beta_\phi-(\beta_\phi\omega+\frac{\Sigma\Delta}{A\sin\theta})(1-\frac{R}{A}\frac{\beta_\phi}{\gamma_\phi})}\right). \tag{6.69}$$

The g factor above can be completely expressed in terms of the emission angles when R is expressed in terms of the angles by solving Eqns. (6.62) & (6.66)

$$\begin{aligned} R^{1/2} &= \frac{\frac{1-\lambda\omega}{\Delta}\sqrt{A}\beta_r\gamma_\phi\gamma_r^2}{1+\frac{\beta_r^2\gamma_r^2}{\Delta}\cos^2\tilde{\theta}} \\ &\pm \frac{(\frac{(1-\lambda\omega)^2}{\Delta^2}A\beta_r^2\gamma_\phi^2\gamma_r^4-(1+\frac{\beta_r^2\gamma_r^2}{\Delta}\cos^2\tilde{\theta})(-(r^2+a^2-\lambda a)^2+\Delta(\lambda-a)^2+\frac{A}{\Delta}\cos^2\tilde{\theta}\gamma_r^2\gamma_\phi^2(1-\lambda\Omega)^2))))}{1+\frac{\beta_r^2\gamma_r^2}{\Delta}\cos^2\tilde{\theta}} \end{aligned} \tag{6.70}$$

As $R=(r^2+a^2-\lambda)^2-\Delta((\lambda-a)^2+q^2)$, q can then be expressed in terms of λ and $\tilde{\theta}$ as:

$$q^2 = (r^2+a^2-\lambda a)^2/\Delta-(\lambda-a)^2-R(\lambda,\tilde{\theta})/\Delta \tag{6.71}$$

With the above expression, the eqn. (6.68) is solved for $\lambda=\lambda(\theta,\phi)$ as $q=q(\lambda,\theta)$ from eqn. (6.71) and $R=R(\lambda,\theta)$ from eqn. (6.71). The g factor in eqn. (6.69) can then be expressed in terms of $\tilde{\theta}$ and $\tilde{\phi}$.

For an observer in the CRF possessing the CRF tetrads, the radial component, the polar component and the azimuthal components of the orthogonal three-velocity of the null geodesics are given by

$$n^{(r)} = n^\alpha e_\alpha^{(r)}(CRF) = \sin\tilde{\theta}\cos\tilde{\phi}. \tag{6.72}$$

$$n^{(\theta)} = n^\alpha e_\alpha^{(\theta)}(CRF) = \cos\tilde{\theta} \tag{6.73}$$

$$n^{(\phi)} = n^\alpha e_\alpha^{(\phi)}(CRF) = -\sin\tilde{\theta}\sin\tilde{\phi} \tag{6.74}$$

The azimuthal component of the three-velocity $n^{(\phi)}$ for an observer in the CRF, expressed in terms of the impact parameter and Carter's constant is given by eqn. (6.63). Re-expressing it in terms of λ and using eqn. (6.74),

$$\lambda = \frac{\sin\tilde{\theta}\sin\tilde{\phi}+\beta_\phi}{\Omega\sin\tilde{\theta}\sin\tilde{\phi}+\beta_\phi\omega+\frac{\Sigma\sqrt{\Delta}}{A\sin\theta}} \tag{6.75}$$

The expression for the effective redshift factor (6.69) simplifies to,

$$g = -\sqrt{\frac{r^2\Delta}{A}}\frac{1}{\gamma_\phi}\frac{\Omega\sin\tilde{\theta}\sin\tilde{\phi}+\beta_\phi\omega+\frac{\Sigma\sqrt{\Delta}}{A\sin\theta}}{\Omega\beta_\phi-\left(\beta_\phi\omega+\frac{\Sigma\Delta}{A\sin\theta}\right)} \tag{6.76}$$

As the g factor from the above equation depends only on λ, it can be cast in terms of the emission angles $\tilde{\theta}$ and $\tilde{\phi}$ using eqn. (6.75). If we assume that the null geodesics are restricted to equatorial orbits ($\theta = \pi/2$) and the underlying geometry is Schwarzschild ($a = 0$), the following simplifications follow: $\Omega = M^{1/2}r^{-3/2}$, $\omega = 0$, $\beta_\phi = \Omega e^{\psi-\nu} = M^{1/2}/\sqrt{r-2M}$ and hence, $\gamma_\phi = \sqrt{\frac{r-2M}{r-3M}}$. These can be used to simplify the g factor from eqn. (6.76) to be

$$g = \sqrt{\frac{r-2M}{r(r-3M)}}(M^{1/2}\sin\tilde{\theta}\sin\tilde{\phi}+\sqrt{r-2M}) \tag{6.77}$$

which is the effective redshift factor obtained for a Schwarzschild CRF observer as calculated in [76] and subsequent papers. As noted in [78], an observer in the CRF (also applicable to the LRF) is co-rotating with the flow with the consequence that the physics in this frame not accounting for aberration effects due to the Keplerian motion of the emitter.

For an observer in the CRF possessing the CRF tetrads, the radial component of the orthogonal three-velocity of the null geodesics is given by:

$$n^{(r)} = n^\alpha e^{(r)}_\alpha(LNRF) = \sin\tilde{\theta}\cos\tilde{\phi}. \tag{6.78}$$

The polar component is given by

$$n^{(\theta)} = n^\alpha e^{(\theta)}_\alpha(LNRF) = \cos\tilde{\theta} \tag{6.79}$$

and the azimuthal component is given by

$$n^{(\phi)} = n^\alpha e^{(\phi)}_\alpha(LNRF) = -\sin\tilde{\theta}\sin\tilde{\phi} \tag{6.80}$$

The azimuthal component of the three-velocity $n^{(\phi)}$ for an observer in the CRF, expressed in terms of the impact parameter and Carter's constant is given by eqn. (6.59). Re-expressing it in terms of λ and using eqn. (6.80)

$$\lambda = -\frac{\sin\tilde{\theta}\sin\tilde{\phi}}{\omega\sin\tilde{\theta}\sin\tilde{\phi}+\frac{\Sigma\sqrt{\Delta}}{A\sin\theta}} \tag{6.81}$$

Using this in the expression for the effective redshift factor from eqn. (6.55),

$$g = \sqrt{\frac{r^2\Delta}{A}}\frac{1}{\gamma_r\gamma_\phi}\left(\frac{\omega\sin\tilde{\theta}\sin\tilde{\phi}+\frac{\Sigma\sqrt{\Delta}}{A\sin\theta}}{(1-\frac{\beta_r}{\gamma_\phi}\sqrt{\frac{R}{A}})(\omega\sin\tilde{\theta}\sin\tilde{\phi}+\frac{\Sigma\sqrt{\Delta}}{A\sin\theta})+\Omega\sin\tilde{\theta}\sin\tilde{\phi}}\right) \tag{6.82}$$

Solving eqn. (6.60) for q, we can write it in terms of λ and $\tilde{\theta}$ as

$$q^2 = \frac{A}{\Delta}(1-\lambda\omega)^2\cos^2\tilde{\theta} - \cos^2\theta(a^2 - \lambda^2/\sin^2\theta) \tag{6.83}$$

The above is used in eqn. (6.82) to describe the g factor in terms of $\tilde{\theta}$ and $\tilde{\phi}$. For a flow without radial motion ($\beta_r = 0$; $\gamma_r = 1$), the g factor in eqn. (6.82) simplifies to

$$g = -\sqrt{\frac{r^2\Delta}{A}}\frac{1}{\gamma_\phi}\frac{A\sin\theta}{\Sigma\sqrt{\Delta}}\frac{\frac{\Sigma\sqrt{\Delta}-n^\phi\omega}{A\sin\theta}}{n^\phi\beta_\phi + 1} \tag{6.84}$$

Further, if we assume that photon orbits are restricted to equatorial orbits ($\theta = \pi/2$) and the underlying geometry is Schwarzschild ($a = 0$), the following simplifications can be made: $\Omega = M^{1/2}r^{-3/2}$, $\omega = 0$, $\beta_\phi = \Omega e^{\psi-\nu} = M^{1/2}/\sqrt{r-2M}$ and hence, $\gamma_\phi = \sqrt{\frac{r-2M}{r-3M}}$ as obtained earlier. These can be used to write the g factor in eqn. (6.84) as

$$g = \sqrt{\frac{(r-2M)(r-3M)}{r}}\frac{1}{\sqrt{r-2M} - M^{1/2}\sin\tilde{\theta}\sin\tilde{\phi}} \tag{6.85}$$

which is the g factor obtained for a Schwarzschild LNRF observer as calculated in [78]. The above expression for the redshift factor accounts for aberration of the observed emission due to the rotation of the disk.

6.8 Relationship between the emission angles $\tilde{\theta}$ and $\tilde{\phi}$

The emission angles $\tilde{\theta}$ and $\tilde{\phi}$ can be related using the developed formalism from the reference frames which relates the emission vectors as viewed by the local relativistic observers. The evaluation of the g factor which depended on β_r, $\tilde{\theta}$ and $\tilde{\phi}$ can be made to depend only on β_r and any one of the emission angles, simplifying the description of the variability.

For the assumption that the emission occurs with the angles $\tilde{\theta}$ and $\tilde{\phi}$ as seen by an observer in the LRF, the orthogonal three-velocity vectors of the null rays in the LRF can be projected using the LNRF tetrads into the LNRF

$$n^{(a)}(LNRF) = n^\alpha(LRF)e^{(a)}_\alpha(LNRF) \tag{6.86}$$

The radial component of the orthogonal three-velocity in the LNRF is evaluated to be

$$n^{(r)}(LNRF) = \gamma_r n^{(r)}(LRF) = \gamma_r \sin\tilde{\theta}\cos\tilde{\phi}. \tag{6.87}$$

The polar component is given by

$$n^{(\theta)}(LNRF) = n^{(\theta)}(LRF) = \cos\tilde{\theta} \tag{6.88}$$

and the azimuthal component can be evaluated to be

$$n^{(\phi)}(LNRF) = \gamma_\phi n^{(\phi)}(LRF) = -\gamma_\phi \sin\tilde{\theta}\sin\tilde{\phi} \tag{6.89}$$

The angles $\tilde{\theta}$ and $\tilde{\phi}$ can be related in two cases, with and without radial motion of the emitting source. The eqn. (6.81) relates the impact factor λ to the emission three-velocity in the LNRF and the eqn. (6.75) relates λ to the emission three-velocity in the CRF. Equating these and using the relation obtained in eqn. (6.89) above, we obtain,

$$\sin\tilde{\theta}\sin\tilde{\phi} = \frac{(1-\gamma_\phi) \pm ((1-\gamma_\phi)^2 + 4\gamma_\phi\beta_\phi^2\frac{\Sigma^2\Delta}{A^2\sin^2\theta})^{1/2}}{2\gamma_\phi\beta\phi\frac{\Sigma\sqrt{\Delta}}{A\sin\theta}} \tag{6.90}$$

From the above expression, we can obtain $\tilde{\theta} = \tilde{\theta}(\tilde{\phi})$. For the source possessing an inflowing radial velocity, the following procedure is adopted: the eqn. (6.68) relates the impact factor λ to the emission three-velocity in the LRF. Using eqn.(6.71) in this renders $\lambda = \lambda(\tilde{\theta}, \tilde{\phi})$. The eqn. (6.81) relates the impact factor λ to the emission three-velocity in the LNRF. Equating the $\lambda(\tilde{\theta}, \tilde{\phi})$ from the LRF to that from the LNRF, we obtain $\tilde{\theta} = \tilde{\theta}(\tilde{\phi})$. This can also used to then evaluate $\lambda(\tilde{\phi})$ and in eqn. (6.71) to determine $q(\tilde{\phi})$.

6.9 Constraints on r, $\tilde{\theta}$ and $\tilde{\phi}$

It was pointed out in the previous section that the relationship between the emission angles $\tilde{\theta}$ and $\tilde{\phi}$ can be used to reduce the number of parameters in the evaluation of the effective redhsift factor g. In this section, we calculate certain conditions which can be used to constrain the allowed extent of r, $\tilde{\theta}$ and $\tilde{\phi}$.

6.9.1 Effective potential and constraints on r

From eqn. (6.53), the radial component of the contravariant four-momentum is given by

$$\Sigma p^r = \varepsilon R^{1/2} \tag{6.91}$$

Expanding R and using the definition of $\lambda = l/\varepsilon$,

$$\left(\frac{p^r}{l}\right)^2 = \frac{r^4}{\Sigma^2\lambda^2} - V_{\rm eff}(\lambda, q, r, a, \theta) \tag{6.92}$$

where $V_{\rm eff}(\lambda, q, r, a, \theta)$ is the effective potential and is given by

$$V_{\rm eff} = \frac{1}{\Sigma^2}\left(r^2\left(1 - \frac{a^2-q^2}{\lambda^2}\right) - 2Mr\left(\left(1-\frac{a}{\lambda}\right)^2 + \frac{q^2}{\lambda^2}\right) + \frac{a^2q^2}{\lambda^2}\right) \tag{6.93}$$

If we make an assumption that null trajectories are restricted to the equatorial plane ($\theta = \pi/2$),

then $p^\theta = 0$ and $q = 0$; $\Sigma = r^2$. Using these in eqn. (6.92), the equation reduces to

$$\left(\frac{p^r}{l}\right)^2 = \frac{1}{\lambda^2} - V_{\rm eff}(\lambda, r, a) \tag{6.94}$$

and the effective potential is now given by

$$V_{\rm eff} = \frac{1}{r^2}\left(1 - \frac{a^2}{\lambda^2} - \frac{2M}{r}\left(1 - \frac{a}{\lambda}\right)^2\right) \tag{6.95}$$

If we make a further assumption that the geometry is Schwarzschild, the Eqns. (6.94) & (6.95) further reduce to the familiar expression e.g. [**?**] for Schwarzschild geometry,

$$\left(\frac{p^r}{l}\right)^2 = \frac{1}{\lambda^2} - V_{\rm eff}(r) \tag{6.96}$$

$$V_{\rm eff} = \frac{1}{r^2}\left(1 - \frac{2M}{r}\right) \tag{6.97}$$

The extrema of the effective potential from eqn. (6.93) can be determined by the expression $\frac{\partial V_{\rm eff}}{\partial r} = 0$. This leads to the cubic equation

$$\begin{aligned} r^3\left(1 - \frac{a^2 - q^2}{\lambda^2}\right) - 3Mr^2\left(\left(1 - \frac{a}{\lambda}\right)^2 + \frac{q^2}{\lambda^2}\right) \\ + a^2 r\left(\frac{q^2}{\lambda^2}(1 + \sin^2\theta) - \left(1 - \frac{a^2 - q^2}{\lambda^2}\right)\cos^2\theta\right) \\ + Ma^2\cos^2\theta\left(\left(1 - \frac{a}{\lambda}\right)^2 + \frac{q^2}{\lambda^2}\right) = 0 \end{aligned} \tag{6.98}$$

Solving the above cubic equation, one can obtain $r_{\rm TP} = r_{\rm TP}(\lambda, q)$ where $r_{\rm TP}$ is the radial distance to the turning point where the effective potential is extremal. Using the obtained $r_{\rm TP}$, one can then determine the extrema of the potential by using it in eqn. (6.93).

For the case of only equatorial null orbits, $q = 0$ and $\theta = \pi/2$. Hence, the cubic equation above reduces to

$$r\left(1 - \frac{a^2}{\lambda^2}\right) - 3M\left(1 - \frac{a}{\lambda}\right)^2 = 0 \tag{6.99}$$

which can be used to solve for $r_{\rm TP}$

$$r_{\rm TP} = 3M\frac{1 - a/\lambda}{1 + a/\lambda} \tag{6.100}$$

If we are searching for a maxima for the effective potential $V_{\rm eff}$, then, the above solution for $r_{\rm TP}$ represents the radius at which the maximum occurs. Further, the maximum of the potential implies the existence of an unstable circular photon orbit at $r_{\rm TP}$. If we set $a = 0$ in the expression for $r_{\rm TP}$ in eqn. (6.100), it reduces to the familiar $r_{\rm TP} = 3M$ for Schwarzschild geometry. Using

$r_{\rm TP}$ from eqn. (6.100) in the expression for the effective potential in eqn. (6.95), we obtain

$$V_{\rm eff} = \frac{1}{27M^2}\frac{(1+a/\lambda)^3}{(1-a/\lambda)} \tag{6.101}$$

which reduces to the familiar $V_{\rm eff} = \dfrac{1}{27M^2}$ for $a = 0$. Now, using the result from eqn. (6.101) in the expression for circular orbits

$$\left(\frac{p^r}{l}\right)^2 = 0 = \frac{1}{\lambda^2} - V_{\rm eff} = \lambda^3 + 3a\lambda^2 + 3\lambda(a^2 - 9M^2) + a(a^2 + 27M^2) \tag{6.102}$$

we can solve the above to obtain the impact factor at which this special turning point occurs

$$\lambda_{\rm TP} = -a + 3\sqrt{3}M \tag{6.103}$$

The above $\lambda_{\rm TP}$ can be used to determine $r_{\rm TP}$

$$r_{\rm TP} = (3M - 2a/\sqrt{3}) \tag{6.104}$$

6.9.2 Constraints on the azimuthal emission angle $\tilde{\phi}$

If one expresses $\tilde{\theta}$ in terms of the azimuthal angle $\tilde{\phi}$ using the relations derived in the previous section for either a source with or without radial inflow, the allowable extent of $\tilde{\phi}$ can be derived in terms of the radial coordinate r and the BH spin a.

The radial component of the orthogonal three-velocity of the photon as measured in the LNRF is given by

$$n^{(r)} = n_{(r)} = \frac{p_\alpha e^\alpha_{(r)}}{p_\alpha e^\alpha_{(t)}} = \frac{p_r e^r_{(r)}}{p_t e^t_{(t)} + p_\phi e^\phi_t} = -\frac{R^{1/2} e^{\nu-\mu_1}}{\Delta(1-\lambda\omega)} \tag{6.105}$$

In eqn. (6.87), $n^{(r)}$ is measured by an observer in the LNRF where the emission angles $\tilde{\theta}$ and $\tilde{\phi}$ are native to the LRF. This equation when combined with eqn. (6.105) gives

$$n^{(r)} = \gamma_r \sin\tilde{\theta}\cos\tilde{\phi} = -\frac{\sqrt{R/A}}{1-\lambda\omega} \tag{6.106}$$

In eqn. (6.89), $n^{(\phi)}$ is measured by an observer in the LNRF where the emission angles $\tilde{\theta}$ and $\tilde{\phi}$ are native to the LRF. This equation when combined with eqn. (6.59) gives

$$n^{(\phi)} = -\gamma_\phi \sin\tilde{\theta}\sin\tilde{\phi} = -\frac{\lambda\Sigma\sqrt{\Delta}}{A\sin\theta(1-\lambda\omega)} \tag{6.107}$$

The expressions for $n^{(r)}$ and $n^{(\phi)}$ in eqns. (6.106) & (6.107) as obtained above can be used to

express the azimuthal emission angle $\tilde{\phi}$

$$\tan\tilde{\phi} = \frac{\gamma_r}{\gamma_\phi}\frac{\lambda\Sigma}{\sin\theta}\sqrt{\frac{\Delta}{Ar}} \tag{6.108}$$

For equatorial null orbits ($\theta = \pi/2$), this reduces to

$$\tan\tilde{\phi} = \frac{\gamma_r}{\gamma_\phi}\ \lambda r^2\Delta^{1/2}((r^2+a^2)^2 - a^2\Delta)^{-1/2}((r^2+a^2-\lambda a)^2 - \Delta(\lambda-a)^2)^{-1/2}. \tag{6.109}$$

One can use the $\lambda_{\rm TP}$ from eqn. (6.103) in the above equation to obtain $\tilde{\phi} = \tilde{\phi}(r,a)$. If we assume that there is no bulk radial flow and that the geometry is Schwarzschild ($\gamma_r = 1$ and $a = 0$), then, the above expression reduces further to

$$\tan\tilde{\phi} = \frac{1}{\gamma_\phi}\frac{1}{r}\left(1-\frac{2M}{r}\right)^{1/2}\left(\frac{1}{27M^2} - \frac{1}{r^2}\left(1-\frac{2M}{r}\right)\right)^{-1/2} \tag{6.110}$$

If we assume that the emission angles were native to a LNRF observer as opposed to the LRF observer described above, the expression above reduces to

$$\tan\tilde{\phi} = \frac{1}{r}\left(1-\frac{2M}{r}\right)^{1/2}\left(\frac{1}{27M^2} - \frac{1}{r^2}\left(1-\frac{2M}{r}\right)\right)^{-1/2} \tag{6.111}$$

which is the familiar expression for the relation between $\tilde{\phi}$ and r, e.g. [**?**].

6.9.3 Allowed $\tilde{\phi}$

For $r = r_{\rm TP} = (3M - 2a/\sqrt{3})$, $\tilde{\phi} = \pi/2$. i.e. if the emission occurs from a distance $r = r_{\rm TP}$, it can be emitted upto an azimuthal angle of $\pi/2$ in order that it is on an unstable circular orbit. A small perturbation from this would either send it into the black hole or it could escape from the vicinity of the black hole. For $r < r_{\rm TP}$ at a given a, $\tilde{\phi}$ decreases until $\tilde{\phi} = 0^\circ$ at $r = M$ ($a = M$). As this limit approaches, only the purely radial emission can escape.

6.10 Time delay and the temporal dependence of physical quantities

It is a geometrical effect which depends on the disk orientation along the observer line of sight, the azimuthal position of the emitting orbital feature on the disk or jet and light bending due to the curved spacetime. Consider the distribution of orbital features on a circle of constant radius in a face-on disk. If all these features emit radiation at a given time, they will arrive at detector at the same time subject to them not interacting with the medium in between on their journey to the detector. A perturbed configuration due to spatially and kinematically distributed emitting sources or a finite orientation of the disk will tend to break this symmetry. In an inclined disk,

even if all features at the same radial position emit radiation at the same time, the arrival times of the radiation will differ due to the inclination resulting in the photon having to traverse through a lesser or an additional amount of distance to reach the observer depending on the azimuthal position of the source.

If $\tilde{\phi}/\Omega$ is the time of emission of a photon from a position r, the time of emission of the next photon is,

$$t = \tilde{\phi}/\Omega + \Delta t \tag{6.112}$$

Where t is the coordinate time in the LRF and Δt is the coordinate time elapsed between the emission events and is given by:

$$\Delta t = (\Delta t_0 - \Delta t_0(\lambda = 0)) + (\Delta\phi - \Delta\phi(\lambda = 0))/\Omega \tag{6.113}$$

The constituents $\Delta\tau_0$ and $\Delta\phi$ in the above expression are integrals and the entire expression can be written as

$$\begin{aligned}
\Delta t &= \int_{\pi/2}^{i} \Omega \left(\frac{a(\lambda - a\sin^2\theta)}{\Theta^{1/2}} + \frac{\lambda - a\sin^2\theta}{\Theta^{1/2}\sin^2\theta} \right. \\
&+ \left. \Omega \frac{a^2\sin^2\theta}{(q^2 + a^2\cos^2\theta)^{1/2}} + \frac{a}{(q^2 + a^2\cos^2\theta)^{1/2}} \right) d\theta \\
&+ \int_{r}^{\infty} \Omega \left(\frac{(r^2 + a^2)(r^2 + a^2 - \lambda a)^2}{\Delta R^{1/2}} + \frac{a(r^2 + a^2 - \lambda a)}{\Delta R^{1/2}} \right. \\
&- \left. \Omega \frac{(r^2 + a^2)^2}{\Delta(A - \Delta q^2)^{1/2}} - \frac{a(r^2 + a^2)}{\Delta(A - \Delta q^2)^{1/2}} \right) dr
\end{aligned} \tag{6.114}$$

In the above equation, the quantities λ and q can be expressed in terms of the azimuthal emission angle $\hat{\phi}$ as derived in the earlier sections. Then, one must solve the equation iteratively in order to obtain $\hat{\phi} = \hat{\phi}(t)$.

The coordinate time lapse in the LRF is converted to the proper time lapse in the LNRF as $u^t = \dfrac{dt}{d\tau}$ where u^t is the time component of the four-velocity of the bulk flow. Thus,

$$\tau = \int \frac{dt}{u^t_s} = \frac{\gamma_r\gamma_\phi}{\sqrt{\Sigma\Delta/A}} \tag{6.115}$$

Using the above transformation, one can obtain $\hat{\phi} = \hat{\phi}(\tau)$ using which the impact factor $\lambda = \lambda(\tau)$ and hence the effective redshift factor $g = g(\tau)$ can be evaluated.

6.11 Results

To illustrate the shape of the PSD and the QPO properties for a non-rotating as well as maximally rotating black hole, single component ($r = 6\ M$) simulations are carried out for $\beta_r = 0$, $a = 0$ and $r = 6\ M$. The light curve and the analysis results are plotted in Fig. 6.1. The light curve shows a

tight, gradual spread in individual features. The periodogram is fit with a power law model with a slope -2.05 and a QPO peaked at 2764 s clearly stands out with a statistical significance $> 99.99\%$. The QPO is also observed in the wavelet analysis where a peak at 2438 s is inferred. A second set of simulations are carried out for with $\beta_r = 0$, $a = 0.998$ and $r = 6\ M$. The light curve and the analysis results are plotted in Fig. 6.2. The periodogram is fit with a power law model with slope -2.27 and a QPO with a peak at 2108 s is seen. The wavelet analysis also indicates a QPO at 2307 s which lasts throughout the observation duration.

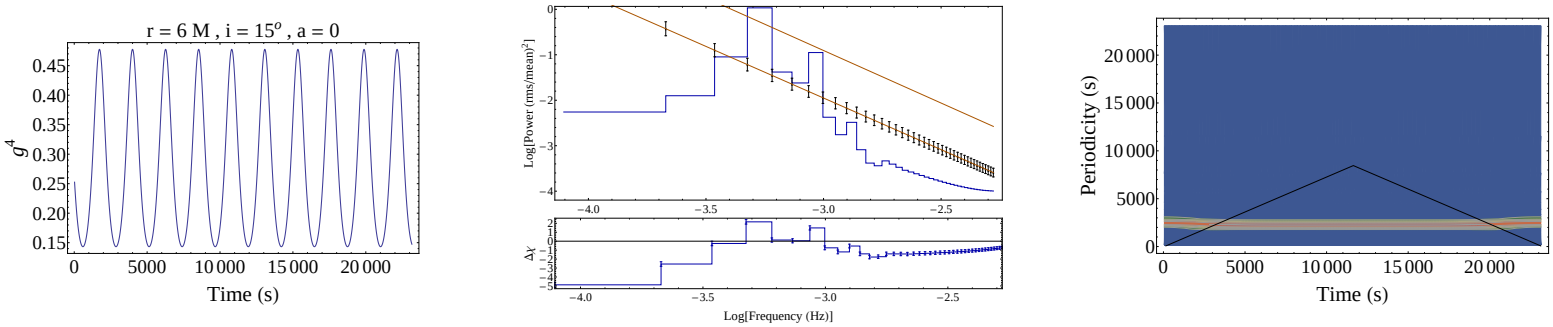

Figure 6.1: Left plot: light curve for the bulk flow variability model with parameters $\beta_r = 0$, $a = 0$ and $r = 6\ M$; middle plot: power spectral density of the combined light curve fit with a power law with a slope -2.05. The lower power law is the fit model and the upper one is the 99% significance contour; A QPO peaked at 2764 s rises above this; right plot: wavelet analysis of the combined light curve indicating a QPO at 2438 s.

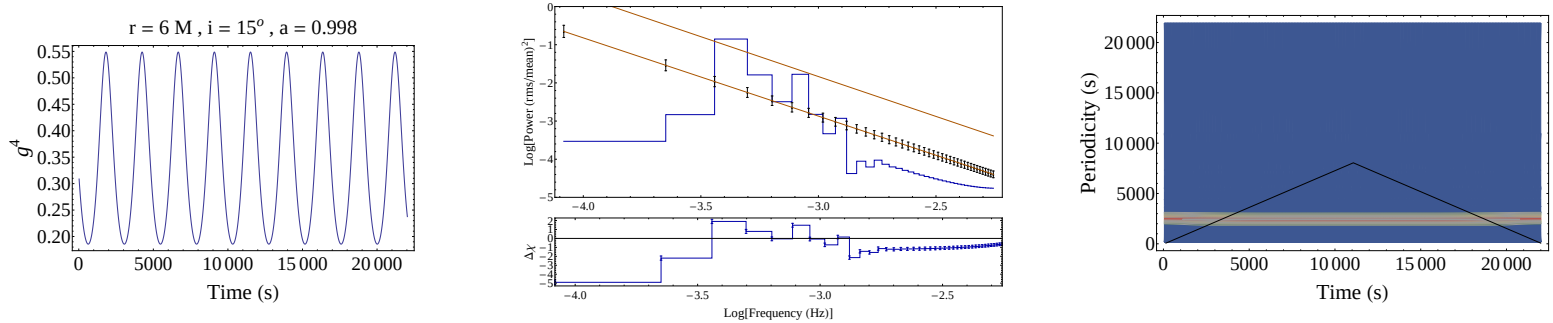

Figure 6.2: Left plot: light curve for the bulk flow variability model with parameters $\beta_r = 0$, $a = 0.998$ and $r = 6\ M$; middle plot: power spectral density of the combined light curve fit with a power law with a slope -2.27. The lower power law is the fit model and the upper one is the 99% significance contour; A QPO peaked at 2108 s rises above this; right plot: wavelet analysis of the combined light curve indicating a QPO at 2307 s.

Results for bulk flow parameters of $\beta_r = 0$, $a = 0$ and $r = 6M$ to $14M$ are plotted in Figs. 6.3, 6.4 and 6.5. The parameters $\beta_r = 0$, $a = 0.998$ and $r = 6M$ to $14M$ are then used for a second set of simulations plotted in Figs. 6.6, 6.7 and 6.8. The overall combined light curve, taken to be the mean of the individual light curves are plotted in Figs. 6.9 and 6.10. Individual light curves from the above figures indicate a QPO in the range of $\sim$ 1000 s and 10000 s. Though, these features are smoothed out in the combined light curves where they are diluted, broad and short lived as seen in the wavelet plots. The entire region in individual light curves is dominated by the Doppler component. The PSD shape is characterized in general by a power law with or without a broad QPO for the combined light curves. The PSD is fit with a power law shape. For the first set of simulations, the slope is found to range between -2.51 for that obtained from the combined light curve of $r = 9\ M$ to $11\ M$ and -4.5 for that obtained from the combined light curve of $r = 6\ M$ to $8\ M$. The combined light curve from $r = 6\ M$ to $14\ M$ gives a flatter power law slope of -2.75. For the second set of simulations, the slope is found to range between -2.5 for that obtained from the combined light curve of $r = 6\ M$ to $8\ M$ and -3.51 for that obtained from the combined light curve of $r = 9\ M$ to $11\ M$. As the region of interest is small, spanning only $\sim 10\ M$, it is likely to flatten with a larger size of the emission region.

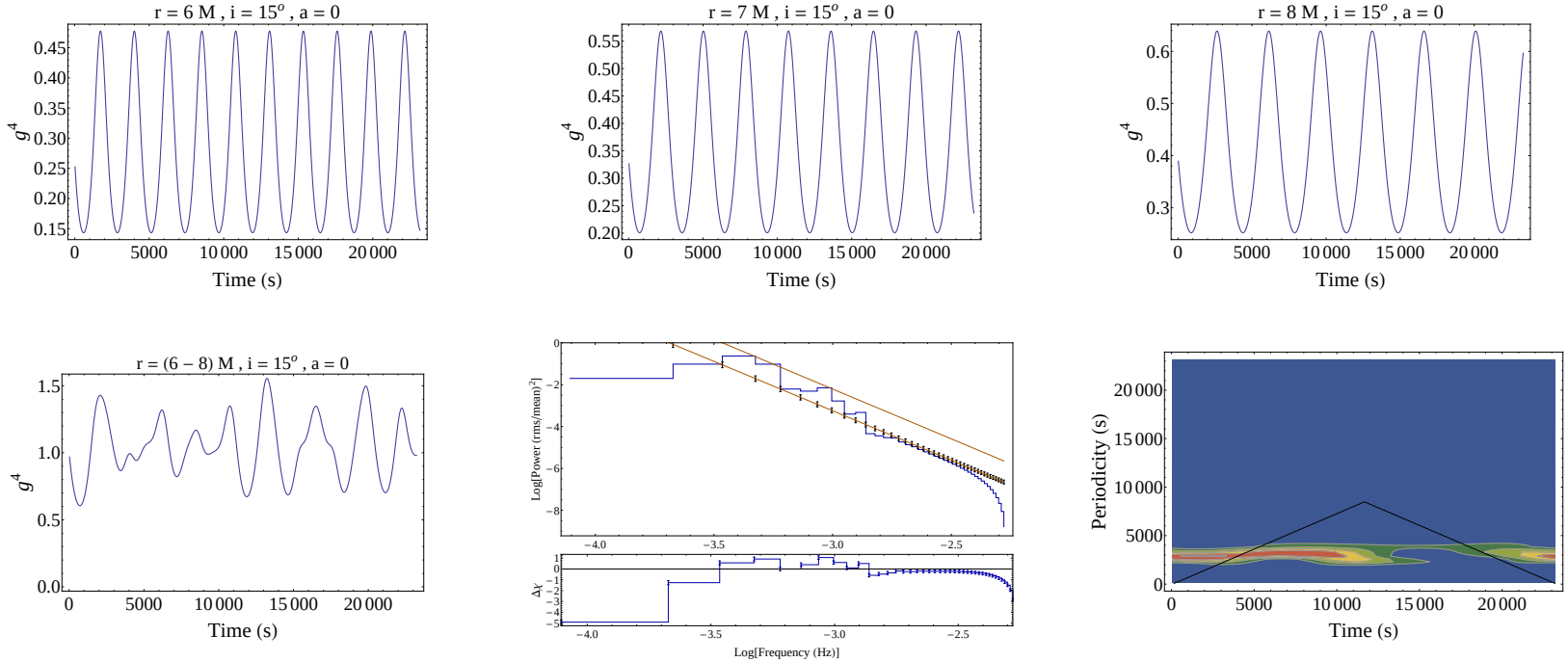

Figure 6.3: First row: simulated light curves for the bulk flow variability model with parameters $\beta_r = 0$, $a = 0$ and $r = 6\ M$ to $8\ M$. Second row: left plot: combined mean light curve for $r = 6\ M$ to $8\ M$; middle plot: power spectral density of the combined light curve fit with a power law with a slope -4.5. The lower power law is the fit model and the upper one is the 99% significance contour; right plot: wavelet analysis of the combined light curve indicating a QPO at 2860 s.

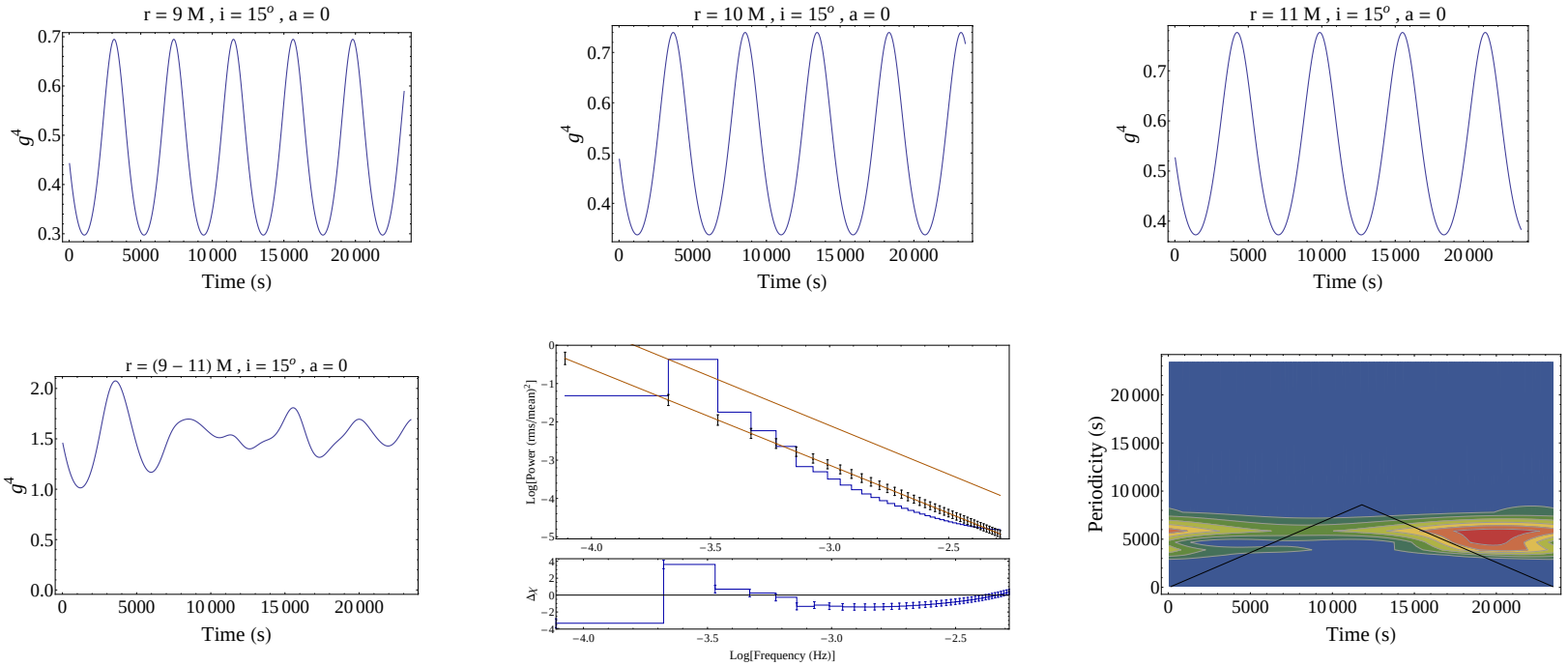

Figure 6.4: First row: simulated light curves for the bulk flow variability model with parameters $\beta_r = 0$, $a = 0$ and $r = 9\ M$ to 11 M. Second row: left plot: combined mean light curve for $r = 9\ M$ to 11 M; middle plot: power spectral density of the combined light curve fit with a power law with a slope -2.51. The lower power law is the fit model and the upper one is the 99% significance contour; right plot: wavelet analysis of the combined light curve indicating the absence of any QPO.

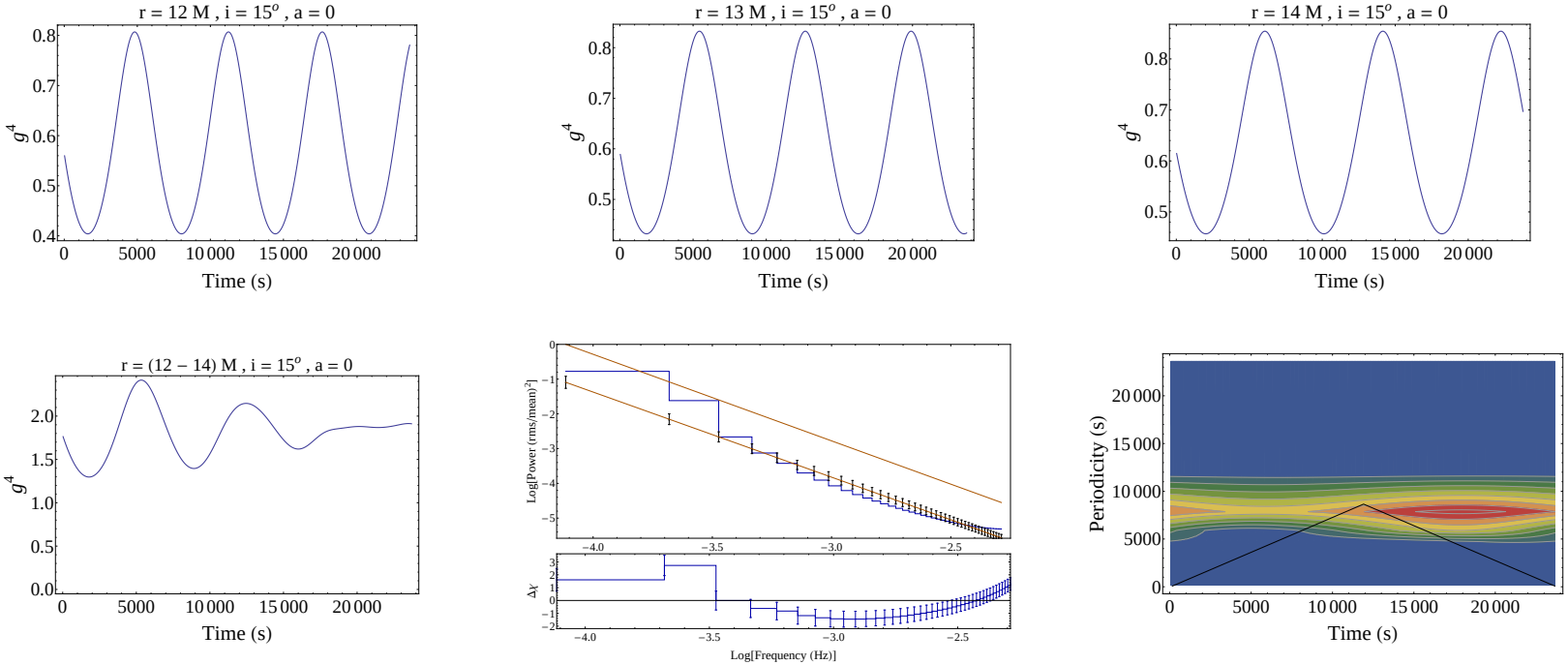

Figure 6.5: First row: simulated light curves for the bulk flow variability model with parameters $\beta_r = 0$, $a = 0$ and $r = 12\ M$ to $14\ M$. Second row: left plot: combined mean light curve for $r = 12\ M$ to $14\ M$; middle plot: power spectral density of the combined light curve fit with a power law with a slope -2.45. The lower power law is the fit model and the upper one is the 99% significance contour; right plot: wavelet analysis of the combined light curve indicating the absence of any QPO.

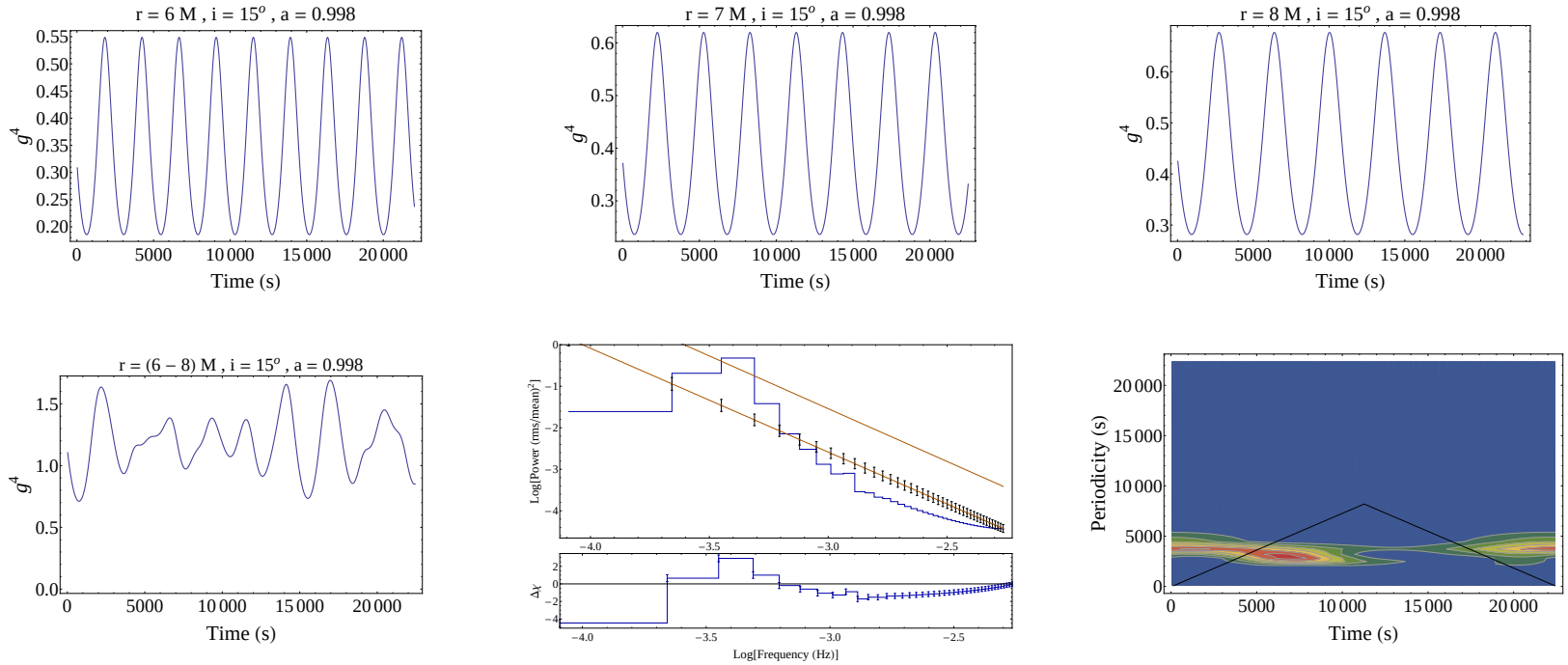

Figure 6.6: First row: simulated light curves for the bulk flow variability model with parameters $\beta_r = 0$, $a = 0.998$ and $r = 6\ M$ to $8\ M$. Second row: left plot: combined mean light curve for $r = 6\ M$ to $9\ M$; middle plot: power spectral density of the combined light curve fit with a power law with a slope -2.29. The lower power law is the fit model and the upper one is the 99% significance contour. A QPO peaked at 2816 s rises above this; right plot: wavelet analysis of the combined light curve indicating a QPO of 3726 s.

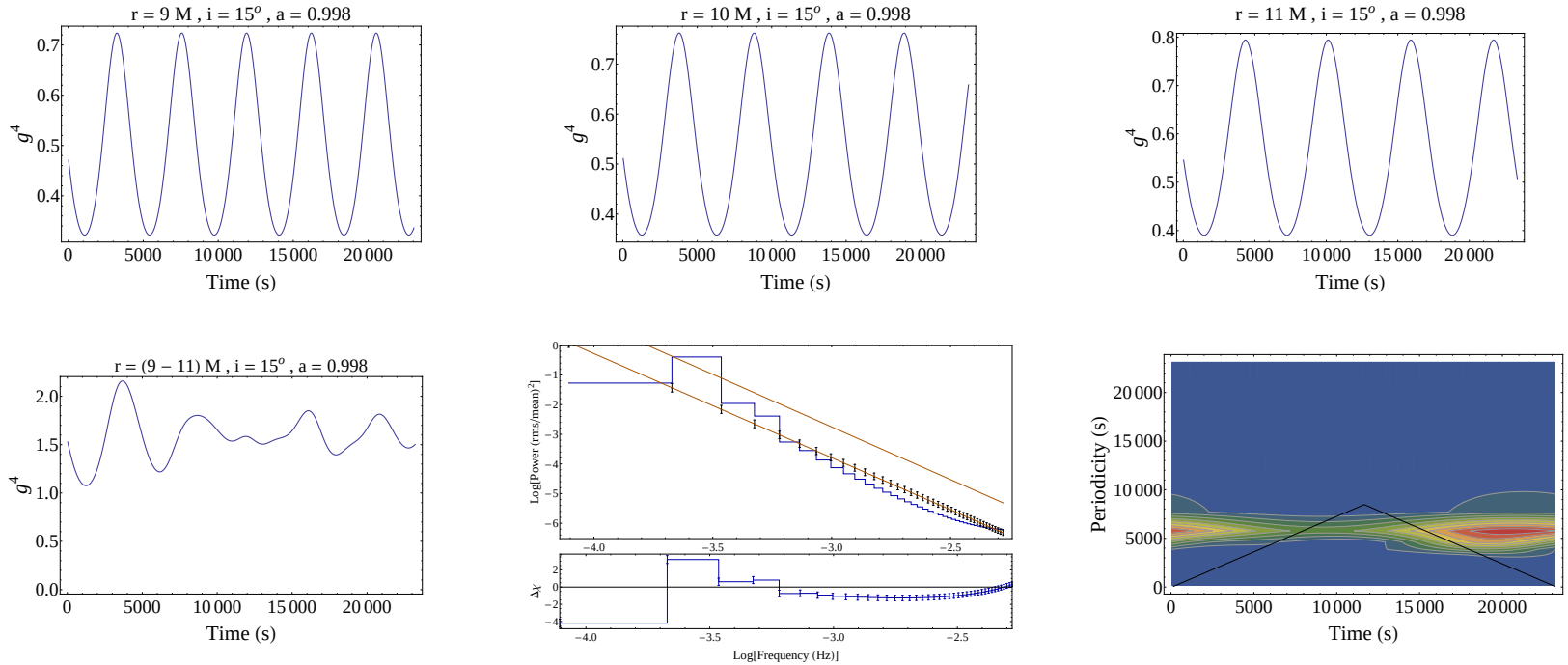

Figure 6.7: First row: simulated light curves for the bulk flow variability model with parameters $\beta_r = 0$, $a = 0.998$ and $r = 9\ M$ to 11 M. Second row: left plot: combined mean light curve for $r = 9\ M$ to 11 M; middle plot: power spectral density of the combined light curve fit with a power law with a slope -3.51. The lower power law is the fit model and the upper one is the 99% significance contour; right plot: wavelet analysis of the combined light curve indicating the absence of any QPO.

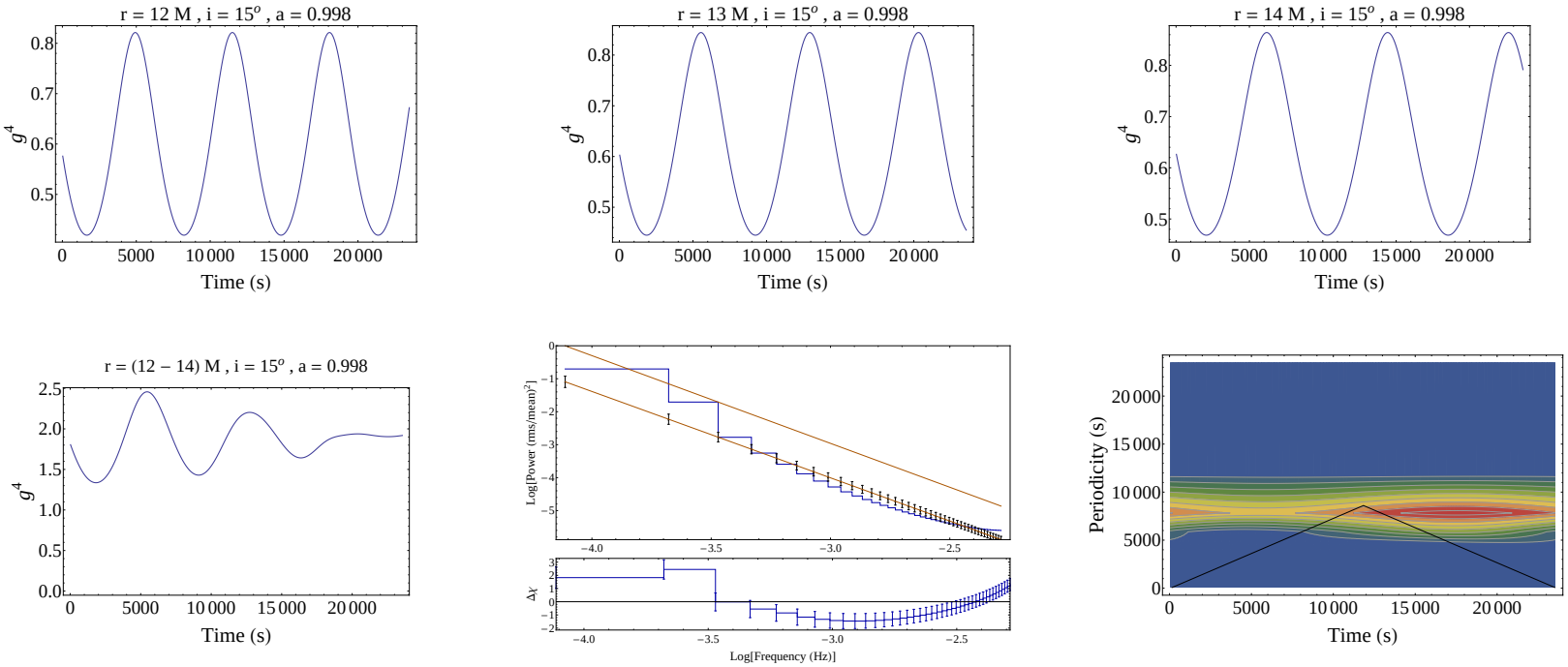

Figure 6.8: First row: simulated light curves for the bulk flow variability model with parameters $\beta_r = 0$, $a = 0.998$ and $r = 12\ M$ to 14 M. Second row: left plot: combined mean light curve for $r = 12\ M$ to 14 M; middle plot: power spectral density of the combined light curve fit with a power law with a slope -2.62. The lower power law is the fit model and the upper one is the 99% significance contour; right plot: wavelet analysis of the combined light curve indicating the absence of any QPO.

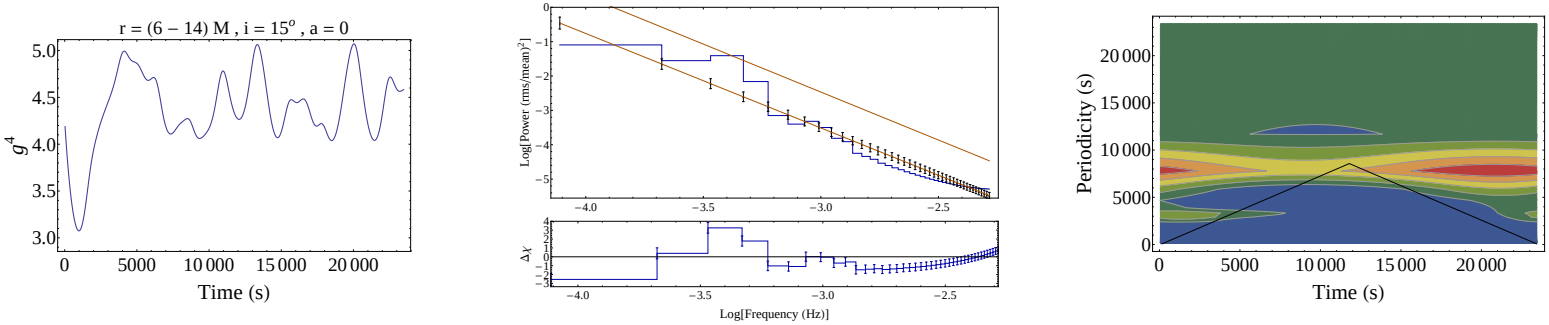

Figure 6.9: Left plot: combined light curve for the bulk flow variability model with parameters $\beta_r = 0$, $a = 0$ and $r = 6\ M$ to $14\ M$; middle plot: power spectral density of the combined light curve fit with a power law with a slope -2.75. The lower power law is the fit model and the upper one is the 99% significance contour; right plot: wavelet analysis of the combined light curve indicating the absence of any QPO.

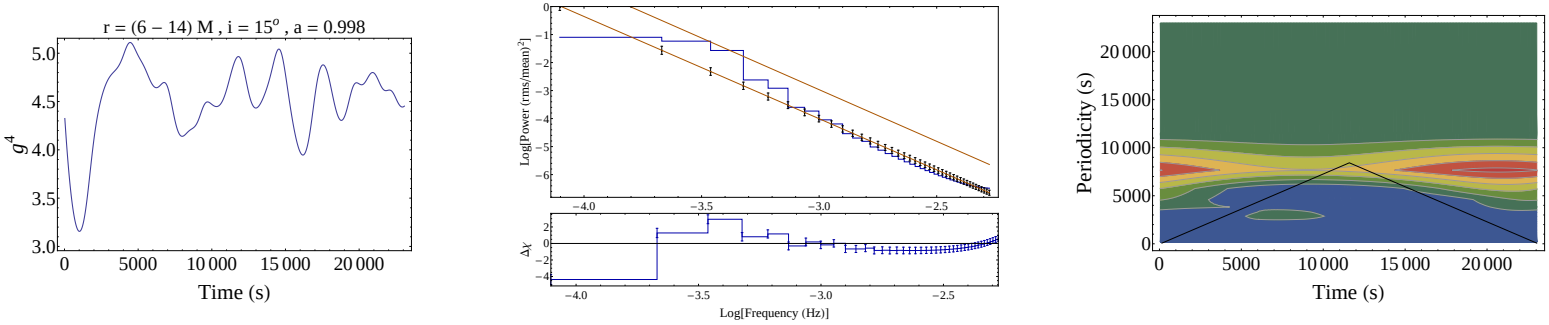

Figure 6.10: Left plot: combined light curve for the bulk flow variability model with parameters $\beta_r = 0$, $a = 0.998$ and $r = 6\ M$ to $14\ M$; middle plot: power spectral density of the combined light curve fit with a power law with a slope -3.65. The lower power law is the fit model and the upper one is the 99% significance contour; right plot: wavelet analysis of the combined light curve indicating the absence of any QPO.

6.12 Conclusions

1. A disk variability model based on a bulk flow confined to the accretion disk was presented.
2. The g factor was calculated in Kerr geometry and the following effects were included: gravitational and Doppler shifts, aberration, time delay and radial motion.
3. The impact parameter and Carter's constant were expressed in terms of the initial photon emission angles.
4. A relationship between the emission angles was then used to express g as a function of only the azimuthal angle and hence, the proper time.
5. Simulations were carried out assuming only azimuthal motion and choices of parameters such as the BH spin a and the radius of emission r.
6. A strong QPO was inferred in the single component light curve with time-scales are in the range $\sim$ 1000 s - 10000 s.
7. A natural power law shaped PSD with a typical slope of -2.5 along with the weak to strong emerged from the simulations.
8. The model thus offers a natural explanation for the development of a power law PSD shape with a QPO without any appeal to procedures that force their appearance in the PSD.

Chapter 7

Theoretical models of jet variability

7.1 Introduction

The inner region consisting of the disk and the developing jet is one dominated by effects due to plasma flow, magnetic field structures, differential rotation of the disk and radiative structuring and the flow velocity field and magnetic fields are dominated by the azimuthal component. The poloidal components are non-zero owing to vertical structuring, random motions, radiation pressure and dynamo action in the disk. If the magnetic field structure is well developed, the rotating field lines could be rooted with footpoints on the disk. The magnetic field strength generated by dynamo action in the inner disk is expected to be in equipartition with the gas pressure e.g. [85], allowing for a reasonably well developed vertically structuring in the field [208]. As jets are believed to originate in the immediate vicinity of the central black hole, it could be expected that they carry ejected material from the disk into an ordered flow along the vertically structured rotating field lines, possibly through advection e.g. [97] which would contribute to the loss of angular momentum in addition to magnetized winds and structured magnetic field lines e.g. [209] and the disk viscosity [60] allowing for the in-spiralling of disk material.

In the hydrodynamics approach to jet launching, the flow is described in terms of fluid equations of motion and possible methods of its expulsion from the disk are through advection and by means of non-axisymmetric shocks on the disk e.g. [133] possessing a poloidal component. The flow distribution in velocity and physical extent is expected to be spread e.g. [210] due to a number of instabilities likely to be present in the inner region and due to the action of the central potential. It would thus not be accelerated to relativistic velocities and would manifest as winds which can contribute to the collimation of the developing jet e.g. [211].

In the magneto-hydrodynamic (MHD) approach, multiple issues such as acceleration of the flow to relativistic velocities, collimation, confinement and the expectation of wide range of observed total luminosity can be addressed. Early formulations based on a relativistic treatment of ideal MHD e.g. [212] indicated that at large distances (compared to the light cylinder radius), the total energy is dominated by the Poynting flux as opposed to being constituted by mass loading. This has led to full general relativistic treatments of the flow in this region studied by means of numerical

simulations e.g. [213, 214, 215] with a similar conclusion. Further, the Poynting flux in the inner jet is traced from its inception either along rotating magnetic field lines threading the disk [209] or magnetic fields threading the ergosphere of a rotating black hole [216] to large distances ($r \sim 10^4\ r_g$) in order to study the evolution of the physical parameters such as bulk Lorentz factor, jet opening angle, magnetic field strength and overall energetics.

Simplified models treating the flow in terms of test particles (bead on a wire models) assume their ballistic motion along open magnetic field structures e.g. [208] where there is an initial centrifugal acceleration of the flow which dies down as its velocity reaches the local Alfven speed. Confinement at this stage is brought about by the co-rotation enforced by the rotating magnetic field lines in the expanding region of the jet. For radiation pressure dominated disks, there is a combination of acceleration from the centrifugal force action and the radiation pressure from the disk based outward flux [90]. Variability in the emission is expected from the inner jet at this stage, when the material has not yet attained asymptotic relativistic velocities (such as those close to the light cylinder and beyond) and the flow is constrained by the expanding vertical magnetic field component. Emission in AGN such as blazars is observed in a wide variety of wavelengths ranging from radio to optical to Gamma-rays e.g. [217] and can be inferred in many cases to arise from the jet.

Variability is often observed in emission from AGN with strong jet components such as blazars, inferred from the domination of synchrotron processes in radio to optical light curves and spectra from regions at parsec scales as well as close to the base of the jet e.g. [121, 98]. Theoretical models are often applicable to emission from regions which are some distance away from the central region where structures are resolvable. Some of these include Doppler beaming of a stream or blobs of plasma accelerated to relativistic velocities along helical paths, the entire structure being oriented in a direction very close to the observer line of sight [93, 94, 95] observed recently in the blazar BL Lacertae [122], shocks propagating along the relativistic jet [91] which explains the variability in some blazars e.g. [123, 124]. Relativistic aberration effects due to small deviations from linearity in the propagating shock front could also lead to variability in overall flux and polarization [92]. Rapid variability has been observed in TeV emission from blazars [4], the time-scales of which are a few times or much shorter than the light crossing time. Explanations have invoked instabilities in the jet e.g. [125, 126] as well as the presence of layering in the jet with randomly oriented substructures contributing to the overall observation [127, 128].

A study aimed at the relation between the disk corona and the inner jet [218] indicates that jet and thermal Comptonization model fits to the radio to X-ray spectra of X-ray binaries are in close agreement. The inner jet appears to be intrinsically linked to the corona as spectral characteristics of its emissions are the same as that from a Comptonized corona. VLBI observations at 1.3 mm are able to clearly resolve structures and study the emission from the inner jet of M87 [219]. A direct scaling relation between the angular size and the distance to the object indicates that the region of emission is very compact, even inside of the ISCO ($5.5 \pm 0.4\ R_{Sch}$) implying that its source on the disk are likely to be on prograde orbits around the Kerr black hole. These and similar studies indicate that there is a strong connection between the inner region very close to the ISCO

and the emerging jet. It is also likely that perturbations produced in disks can be advected into these relativistic jets and amplified there via Doppler boosting e.g. [97]. Hence, it is important to study inner region in the immediate vicinity of the BH composed of the putative disk as well as the developing jet with footpoints on the disk both from a theoretical as well as an observational point of view.

Variability due to orbital signatures in the inner region is possible only if the flow is mass dominated at these scales. Poynting flux can still develop in the inner jet (spine) to further accelerate the mass loaded in the sheath through radiation pressure and magnetic field pressure and tension based contributions to the developing kinetic energy of the jet. Ejected material may not be able to travel to large distances (few light cylinders) due to inertial effects, interaction with external earlier expelled gas and Compton drag from radiation pressure, at which time the flow becomes Poynting flux dominated, consistent with numerical simulations and the observation of bright radio cores e.g. [219] possibly due to particle based synchrotron radiation. Quasi-periodic variability can be caused due to the orbital motion of the flow along helical trajectories which get beamed when their local angle is close to the angle to the observer line of sight in the inner region where the jet is just developing. This effect is expected to last for a few cycles.

There is thus a necessity for more advanced models which possess a realistic treatment of the emission source kinematics and the null geodesics in curved space-time as the inner jet region is close to the central black hole. In §7.2, we propose a simple kinematical model where a funnel shaped structure which could approximate a stable magnetic field structure with footpoints on the disk describes the jet geometry. Results from the analysis of simulated light curves include addressing the QPO phenomenon, its evolution and the shape of the power spectral density for multiple emitting regions. The model discussed is used to simulate light curves and power spectral densities which can be generated for a wide range of parameters and are presented in §7.3.

7.2 Variability models

We propose a model of variability in the emission from this inner region consisting of the disk and the emerging jet. Novel properties of this model are the inclusion of structure in the direction locally normal to the disk approximating the emergence of the jet which points towards a unifying view of emission from the inner region. This structure is treated in a funnel geometry and cylindrical geometry in order that the results be applicable to physically relevant situations in a variety of AGN showing jet based variability where the disk inclination angle is small and the emission is beamed due to the relativistic motion of blobs with an angle very close to the observer line of sight e.g. [14]. This treatment can be applied to AGN such as Seyferts and NLS1s indicating strong disk based emission and possible spectral lines as well as blazars where emission is dominated by the jet. Some of the issues that can be addressed by this model include shapes and broad trends introduced by micro-variability and conditions for the presence and sustenance of a QPO due to orbital motion of the emitting source. The model is constructed assuming a background Schwarzschild geometry

with the line element

$$ds^2 = -(1-2M/r)dt^2 + \frac{dr^2}{(1-2M/r)} + r^2(d\theta^2 + \sin^2\theta d\phi^2) \tag{7.1}$$

Where (r, θ, ϕ) are the spherical polar coordinates and $M = GM_{BH}/c^2$ is the gravitational mass in units of length. The covariant components of the metric, expressed in these coordinates are given by

$$\begin{aligned} g_{tt} &= -(1-2M/r) \\ g_{\phi\phi} &= r^2\sin^2\theta \\ g_{rr} &= \frac{1}{1-2M/r} \\ g_{\theta\theta} &= r^2 \end{aligned} \tag{7.2}$$

The metric is spherically symmetric unlike the Kerr metric which only obeys axial symmetry. The conserved quantities for the Schwarzschild metric include: total energy $\varepsilon = -p_t$ and the azimuthal angular momentum $l = p_\phi$. If we introduce the impact factor $\lambda = l/\varepsilon$, the contravariant components of the four-momentum for null geodesics can be written as

$$p^\alpha = \varepsilon\left(\frac{1}{1-2M/r}, \left(1 - \frac{\lambda}{r^2\sin^2\theta}(1-2M/r)\right)^{1/2}, 0, \frac{\lambda}{r^2\sin^2\theta}\right) \tag{7.3}$$

With p^α being evaluated using $p^\alpha = p_\beta g^{\alpha\beta}$ and p^r being evaluated using the relation

$$p.p = p^\alpha p^\beta g_{\alpha\beta} = (p^t)^2 g_{tt} + (p^r)^2 g_{rr} + (p^\phi)^2 g_{\phi\phi} = 0 \tag{7.4}$$

Assuming that the emitter is located at a radial distance R from the central BH emits a photon at an angle α with respect to the radial vector. It then undergoes bending due to the curvature effects to emerge at a final angle ψ with respect to the radial vector. The relationship between ψ and α can be determined by solving and combining

$$\psi = \int_R^\infty \frac{dr}{r}(1/\lambda^2 - 1/r^2(1-2M/r))^{-\frac{1}{2}} \tag{7.5}$$

and

$$\sin\alpha = \frac{\lambda}{R}(1-2M/R)^{\frac{1}{2}}. \tag{7.6}$$

This light bending effect can be approximated fairly accurately by a simple analytic expression [79]

$$1 - \cos\alpha = (1-\cos\psi)(1-2M/R) \tag{7.7}$$

and is illustrated in Fig. 7.1.

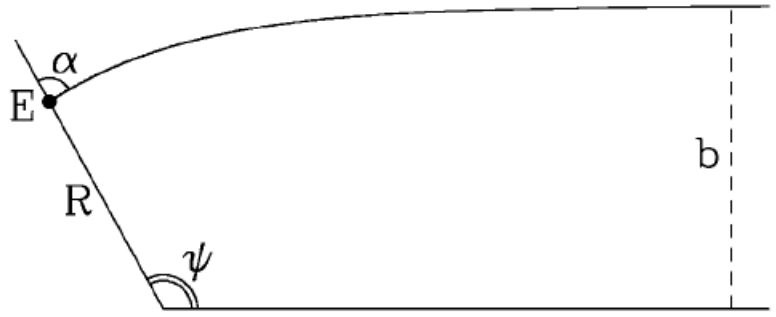

Figure 7.1: Illustration of light bending with the initial angle (α) and final angle (ψ) of the emitted photon from [79].

The travel time will be different for photons emitted from different R. It is required to account for these differences in path length which will lead to an array of arrival times. The travel time can be obtained from the integral

$$\Delta t = \int_R^\infty \frac{dr}{1-2M/r}\left(\left(1-\frac{b^2}{r^2}(1-2M/r)\right)^{-\frac{1}{2}}-1\right) \tag{7.8}$$

The time delay due to orientation effects and the effect of light bending can be approximated [204] as

$$\Delta t = \frac{R-1}{2}(1-\cos\psi) - \ln\left(\frac{1+\cos\psi}{2}\right) \tag{7.9}$$

Assuming a funnel shaped geometry with the parametrization

$$x = \rho_o(1+k(1-e^{-\alpha z}))\cos\phi;\ y = \rho_o(1+k(1-e^{-\alpha z}))\sin\phi;\ z = p\phi;\ \Omega = (\rho_o)^{-\frac{3}{2}} \tag{7.10}$$

with a footpoint radius (between the normal axis and the source starting position on the disk) ρ_o, a normalizing factor $k = (\rho_{max}-\rho_o)/\rho_o$, where ρ_{max} is the cylindrical distance between the normal axis and the final source position and the pitch distance of the helix p. We first calculate the velocity components in spherical geometry. From $r = \sqrt{x^2+y^2+z^2}$,

$$v_S^r = \frac{v_S^\phi}{r}(p^2\phi + \alpha k p e^{-\alpha p\phi}(1+k(1-e^{-\alpha p\phi}))) \tag{7.11}$$

From $\theta = \cos^{-1}\frac{z}{r}$,

$$v_S^\theta = -\frac{pv_S^\phi}{r\sqrt{1-p^2\phi^2/r^2}}\left(1-\frac{\phi}{r^2}(p^2\phi+\alpha kpe^{-\alpha p\phi}(1+k(1-e^{-\alpha p\phi})))\right) \tag{7.12}$$

. The calculation of v_S^ϕ involves the time delay as $\phi = \Omega(t+\Delta t)$. Using the expression in eqn. 7.9,

$$v_S^\phi = \frac{\Omega}{A} \tag{7.13}$$

where

$$\begin{aligned} A &= 1-\Omega\left(\frac{1-\cos\phi\sin i}{2}\right)\left(\frac{1}{r}\left(p^2\phi+\alpha pe^{-\alpha p\phi}\rho_f^2(1+k(1-e^{-\alpha p\phi}))\right)\right) \\ &- \Omega\sin\phi\sin i\left(\frac{r-1}{2}+(1+\cos\phi\sin i)^{-1}\right) \end{aligned} \tag{7.14}$$

For the description of the fluid four-velocity, one must account for the Lorentz boosts due to the radial motion and the θ-motion in order to describe the kinematics in its local rest frame. The four-velocity is then given by

$$u_S^\alpha = u_s^t(1,\gamma_r v_S^r,\gamma_r\gamma_\theta v_S^\theta, v_S^\phi), \tag{7.15}$$

where $\gamma_r = \frac{1}{\sqrt{1-(v_S^r)^2}}$ and $\gamma_\theta = \frac{1}{\sqrt{1-(v_S^\theta)^2}}$ are the Lorentz factors due to radial and θ motions. Since $u.u = -1$ for time-like trajectories, this identity can be used to evaluate the components of the four-velocity

$$u.u = u_S^\alpha u_S^\beta g_{\alpha\beta} = -1. \tag{7.16}$$

for which

$$u_S^t = (1-2M/r-v^2)^{1/2} \tag{7.17}$$

where v^2 is the total velocity of the flow and is given by

$$v^2 = \gamma_r^2(v_S^r)^2/(1-2M/r) - \gamma_r^2\gamma_\theta^2 r^2(v_S^\theta)^2 + r^2\sin^2\theta(v_S^\phi)^2. \tag{7.18}$$

The quantity u_S^t is the inverse of γ_{jet} which can be evaluated at the Alven point from angular momentum conservation. For a cylindrical geometry ($\alpha = 0$, $k = 0$) which is a special case of the funnel geometry, the above relations reduce to

$$x = \rho_o\cos\phi;\ y = \rho_o\sin\phi;\ z = p\phi;\ \Omega = (\rho_o)^{-\frac{3}{2}} \tag{7.19}$$

$$\begin{aligned} A &= 1-\Omega\left(\frac{1-\cos\psi}{2}\right)(p^2\phi/r) \\ &- \Omega\sin\phi\sin i\left(\frac{r-1}{2}+(1+\cos\phi\sin i)^{-1}\right) \end{aligned} \tag{7.20}$$

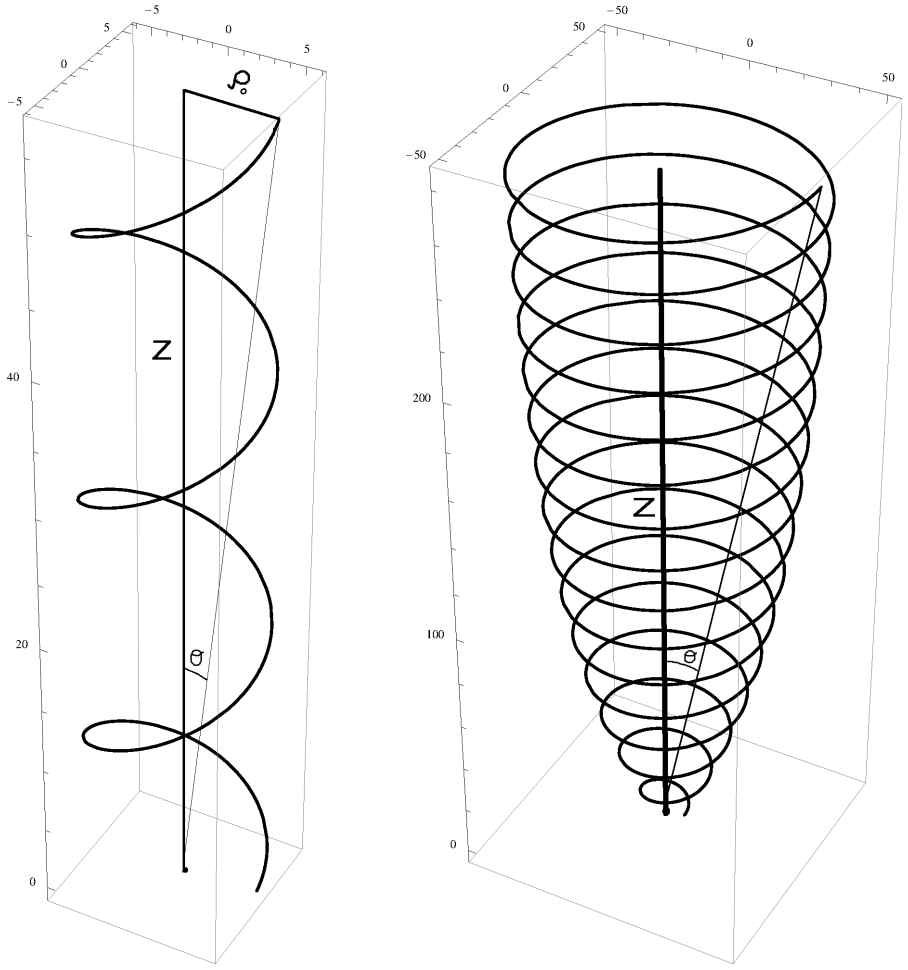

Figure 7.2: Simple schematics showing broadly, time-like trajectories in the jet geometries. Left plot: cylindrical model with constant radius ρ_o. Right plot: expanding funnel model with an initial footpoint radius ρ_o and final radius ρ_{max}. The flow would be along the helical shaped field lines.

The cylindrical and funnel geometries are illustrated in Fig. 7.2 and the emission geometry for the funnel model in Fig. 7.3.

The coordinate time is converted to the proper time as $u^t_s = \dfrac{dt}{d\tau}$. Thus,

$$\tau = \int \frac{dt}{u^t_s} \tag{7.21}$$

The effective redshift factor g is the ratio of observed to emitted energy of the photon and is given by,

$$g = \frac{E_{\rm observed}}{E_{\rm emitted}} = \frac{p^\alpha(\infty) u^\beta_S(\infty) g_{\alpha\beta}}{p^\alpha u^\beta_S g_{\alpha\beta}} \tag{7.22}$$

The four-momentum of the null geodesics is given by eqn. (7.3) and the four-velocity of the flow is given by eqn. (7.15). Using these in the above equation, the effective redshift factor is given by,

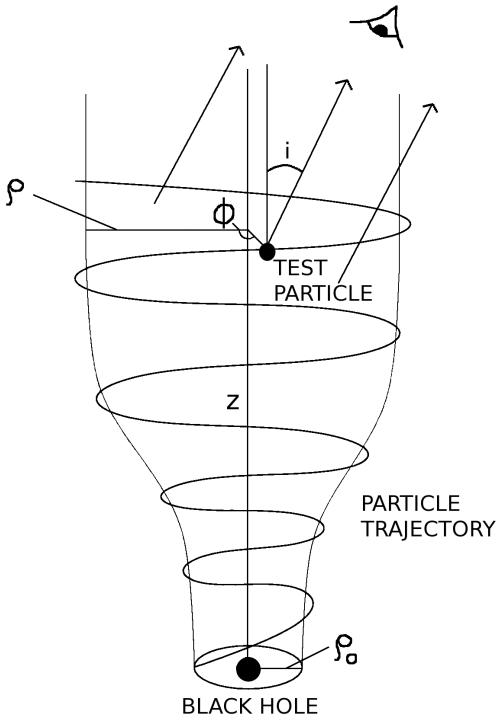

Figure 7.3: Helical trajectory of an emitting test particle in Schwarzschild geometry, constrained along rotating magnetic field lines with footpoints on a Keplerian disk (at cylindrical radius ρ_o) and asymptotically bound by a cylinder of radius ρ at large z.

$$g = \left(u_s^t \left(1 - \frac{\Omega}{A}(B + \lambda) \right) \right)^{-1} \tag{7.23}$$

where

$$B = \left(1 - \frac{\lambda^2}{r^2 \sin^2\theta}(1 - 2M/r) \right)^{\frac{1}{2}} \frac{(p^2\phi + \alpha p e^{-\alpha p \phi} \rho_f^2 (1 + k(1 - e^{-\alpha p \phi}))}{r(1 - 2M/r)} \tag{7.24}$$

Thus, the effective redshift factor g depends on the parameters of the funnel model which include (α, k, p) and the azimuthal coordinate ϕ. As $\phi = \Omega t$ where t is the coordinate time, once (α, k, p) are fixed, t is converted to the proper time τ using Eqn. 7.21 in order to obtain $g = g(\tau)$. The quantity I_ν/ν^3 where I_ν is the intensity of emitted radiation of frequency ν is conserved. Thus, the intensity observed $I_{\rm obs}$ can be related to the intensity emitted $I_{\rm em}$ through the relation,

$$\frac{I_{\rm obs}}{I_{\rm em}} = g^4 \tag{7.25}$$

The quantity $g^4(\tau)$ being a function of arrival time of the photon thus represents the expected light curve.

7.3 Results and discussion

To illustrate the clear visibility of a QPO during the beaming phase, induced due to the flow velocity and the details of the geometry, a single component ($r = 6\ M$) simulation is carried out for the funnel shape with $\alpha = 0.1$, $k = 1$, $p = 0.55$ and $r = 6\ M$. The light curve and the analysis results are plotted in Fig. 7.4. The light curve shows a clear beamed portion with an increased amplitude lasting for 3 - 4 cycles. The periodogram is fit with a power law model for the PSD shape and a QPO peaked at 0.39 days clearly stands out with a statistical significance $> 99.99\%$. Interestingly as expected, the QPO feature lasts strongly only for the first ~ 1.7 days. At large distances, $\gamma_{jet} \sim (1 - v_S^2)^{-1/2}$ where the fluid velocity being close to c will lead to $\gamma_{jet} \sim 2$ - 4.

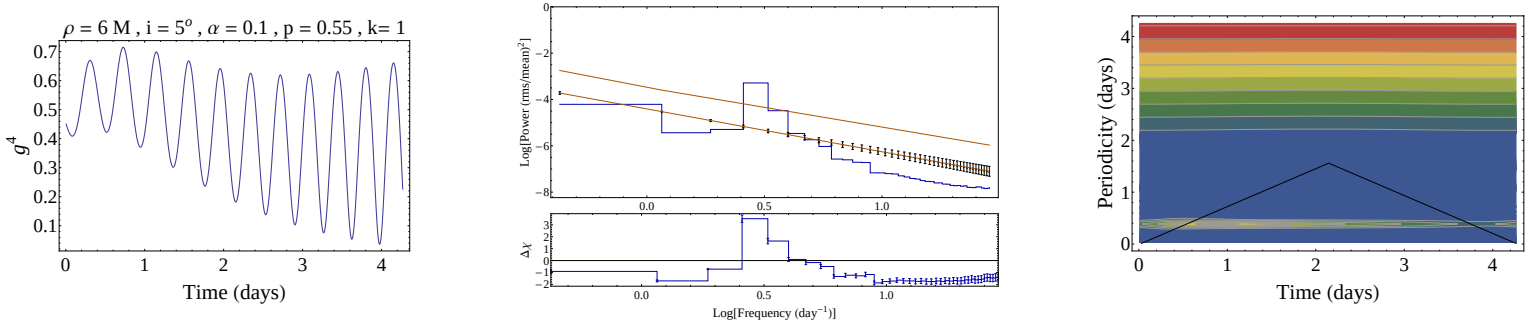

Figure 7.4: Left plot: light curve for the funnel model with parameters $\alpha = 0.1$, $k = 1$ and $p = 0.55$ and $r = 6\ M$; middle plot: power spectral density of the combined light curve fit with a power law with a slope -1.85 with a QPO peaked at 0.39 days for which the statistical significance > 99.99 %; right plot: wavelet analysis of the combined light curve indicating a strong QPO at 0.39 days lasting for ~ 1.7 days after which it dies down.

Simulations are carried out for a given set of funnel shape parameters to illustrate the light curves, their properties, the presence and evolution of the QPO and a time series analysis of the combined light curve (determination of the power spectral density with significance testing and the wavelet analysis). The funnel shape parameters $\alpha = 0.1$, $k = 1$ and $p = 0.55$ are chosen for the funnel model, illustrated in Figs. 7.6, 7.7 and 7.8. The funnel shape parameters $\alpha = 0.1$, $k = 1.2$ and $p = 0.55$ are chosen for the funnel model, illustrated in Figs. 7.9, 7.10 and 7.11. The parameters $\alpha = 0$, $k = 0$ and $p = 0.55$ are chosen to describe the effects in the cylindrical model, illustrated in Fig. 7.5.

The funnel shape parameters $\alpha = 0.1$, $k = 1$ and $p = 0.55$ are chosen for the funnel model and the light curves are simulated for $r = 6\ M$ to $14\ M$ with the combined light curve and analysis presented in Fig. 7.12. The parameters $\alpha = 0.1$, $k = 1.2$ and $p = 0.55$ are then also used for a second set of simulations with the funnel model. These light curves are also simulated for $r = 6\ M$ to $14\ M$ and the combined light curve and results are plotted in Fig. 7.13. Individual light curves from the simulations indicate a QPO evolving between $\sim$ 0.5 days and 2 days. Though, these features are smoothed out in the combined light curves where they are diluted, broad and short lived as seen in the wavelet plots. Beaming lasts for a short duration of 2 - 4 cycles at the start of the source motion as expected to occur when the relativistic fluid is emitting in a direction close to the observer line of sight. It is during this portion that the QPO feature is captured as seen by the wavelet analysis. The later region is dominated by the Doppler component regime purely due to the helical motion of the emitter in both models. The beamed emission will occur in the region beyond the acceleration region for motion is close to the observer line of sight. This depends on the details of the geometry. Beaming is more pronounced in the funnel model: (maximum flux of beamed portion)/(maximum of the Doppler component)$\sim$ 2.

The PSD shape is characterized in general by a power law with or without a broad QPO for the combined light curves. The PSD is fit with a power law shape. For the first set of simulations, the slope is found to range between -2.12 for that obtained from the combined light curve of $r = 12\ M$ to $14\ M$ and -2.80 for that obtained from the combined light curve of $r = 9\ M$ to $11\ M$. The combined light curve from $r = 6\ M$ to $14\ M$ gives a steeper power law slope of -3.0. For the second set of simulations, the slope is found to range between -2.28 for that obtained from the combined light curve of $r = 12\ M$ to $14\ M$ and -2.84 for that obtained from the combined light curve of $r = 9\ M$ to $11\ M$. A general trend of steeper slopes with increased size of emission region can be inferred from this. The power law fit is found to be a poor indicator of the PSD for this combined light curve as it indicates a steep slope of -3.0, due to the complex shape of the PSD. Though, as the region of interest is small, spanning only $\sim 10\ M$, it is likely to flatten with a larger size of the emission region.

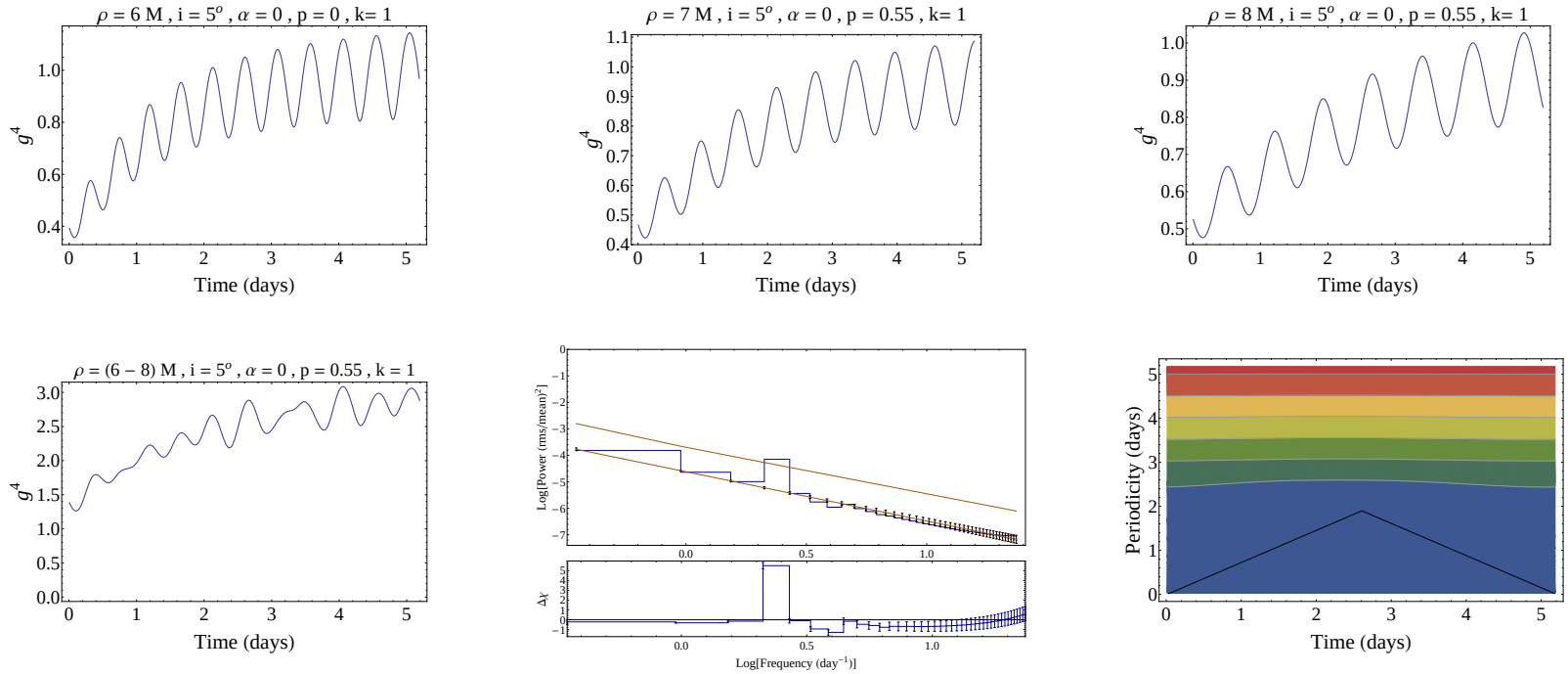

Figure 7.5: First row: simulated light curves for the cylinder model with parameters $\alpha = 0$, $k = 0$ and $p = 0.55$. Second row: left plot: combined mean light curve for $r = 6\ M$ to $8\ M$ indicating an upward trend; middle plot: power spectral density of the combined light curve fit with a power law with a slope -1.85. The lower power law is the fit model and the upper one is the 99% significance contour. A QPO peaked at 0.47 days rises above this; right plot: wavelet analysis of the combined light curve not indicating any QPO.

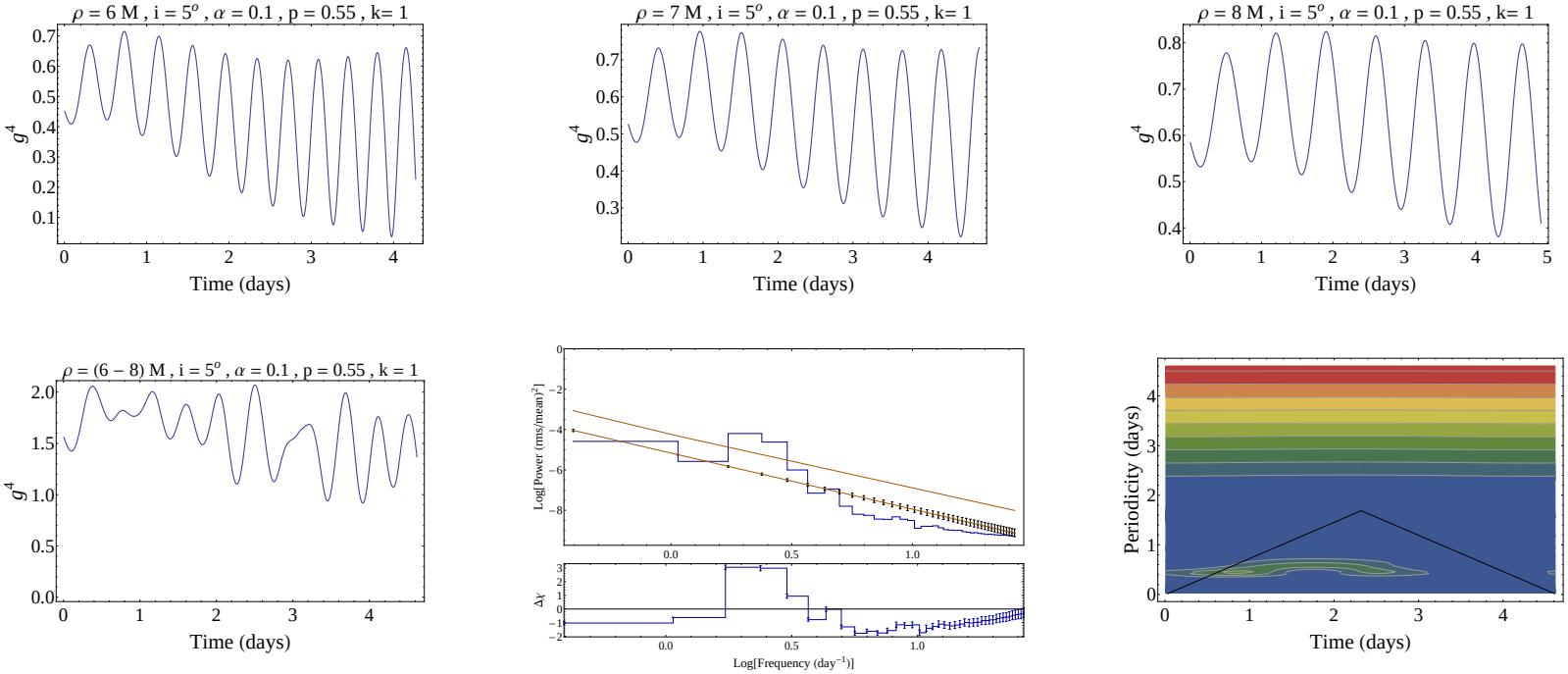

Figure 7.6: First row: simulated light curves for the funnel model with parameters $\alpha = 0.1$, $k = 1$ and $p = 0.55$. Second row: left plot: combined mean light curve for $r = 6\ M$ to $8\ M$ indicating a beamed portion gradually falling into the Doppler regime; middle plot: power spectral density of the combined light curve fit with a power law with a slope -2.77. The lower power law is the fit model and the upper one is the 99% significance contour. A QPO peaked at 0.51 days rises above this; right plot: wavelet analysis of the combined light curve indicating a QPO at 0.47 days which lasts upto ~ 3 days.

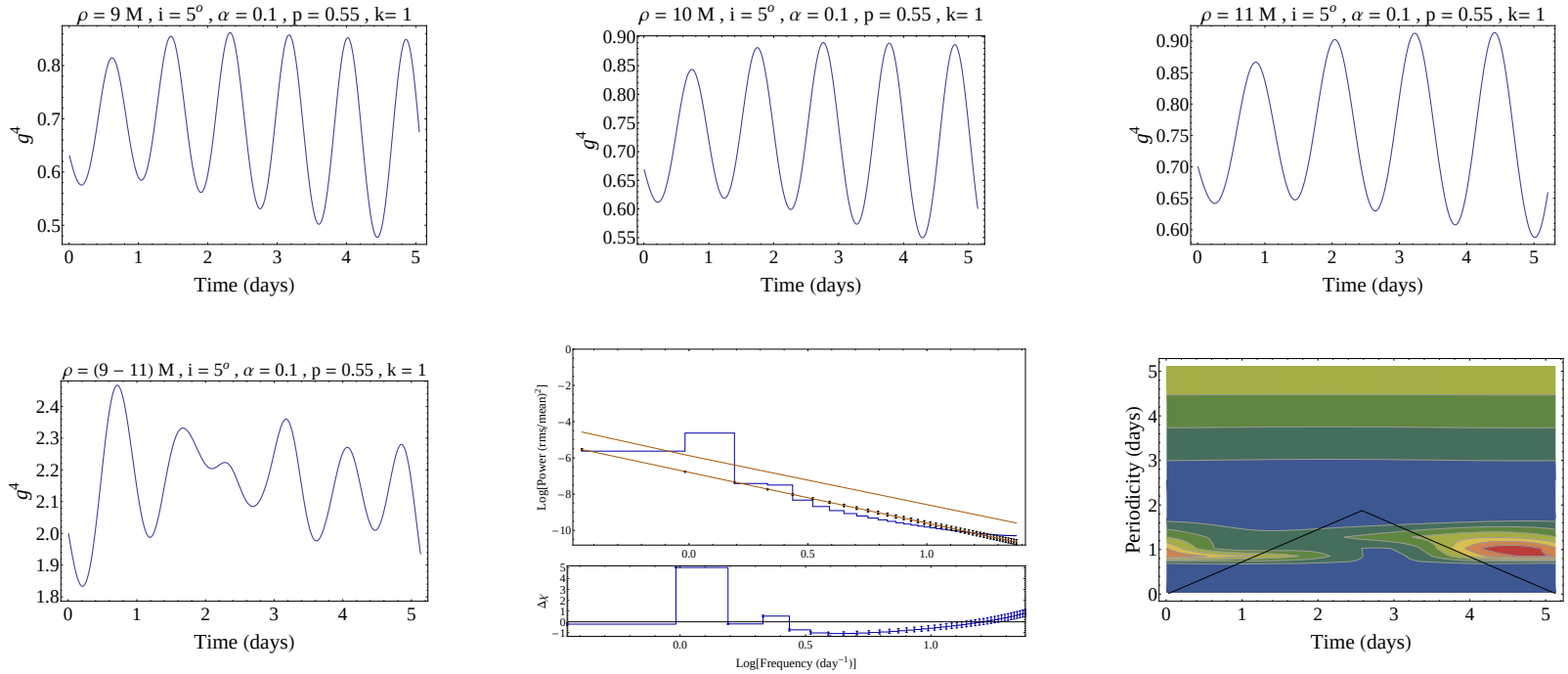

Figure 7.7: First row: simulated light curves for the funnel model with parameters $\alpha = 0.1$, $k = 1$ and $p = 0.55$. Second row: left plot: combined mean light curve for $r = 9\ M$ to $11\ M$ indicating a beamed portion gradually falling into the Doppler regime; middle plot: power spectral density of the combined light curve fit with a power law with a slope -2.80. The lower power law is the fit model and the upper one is the 99% significance contour. A QPO peaked at 1.04 days rises above this; right plot: wavelet analysis of the combined light curve indicating a QPO at 0.85 days near the edge.

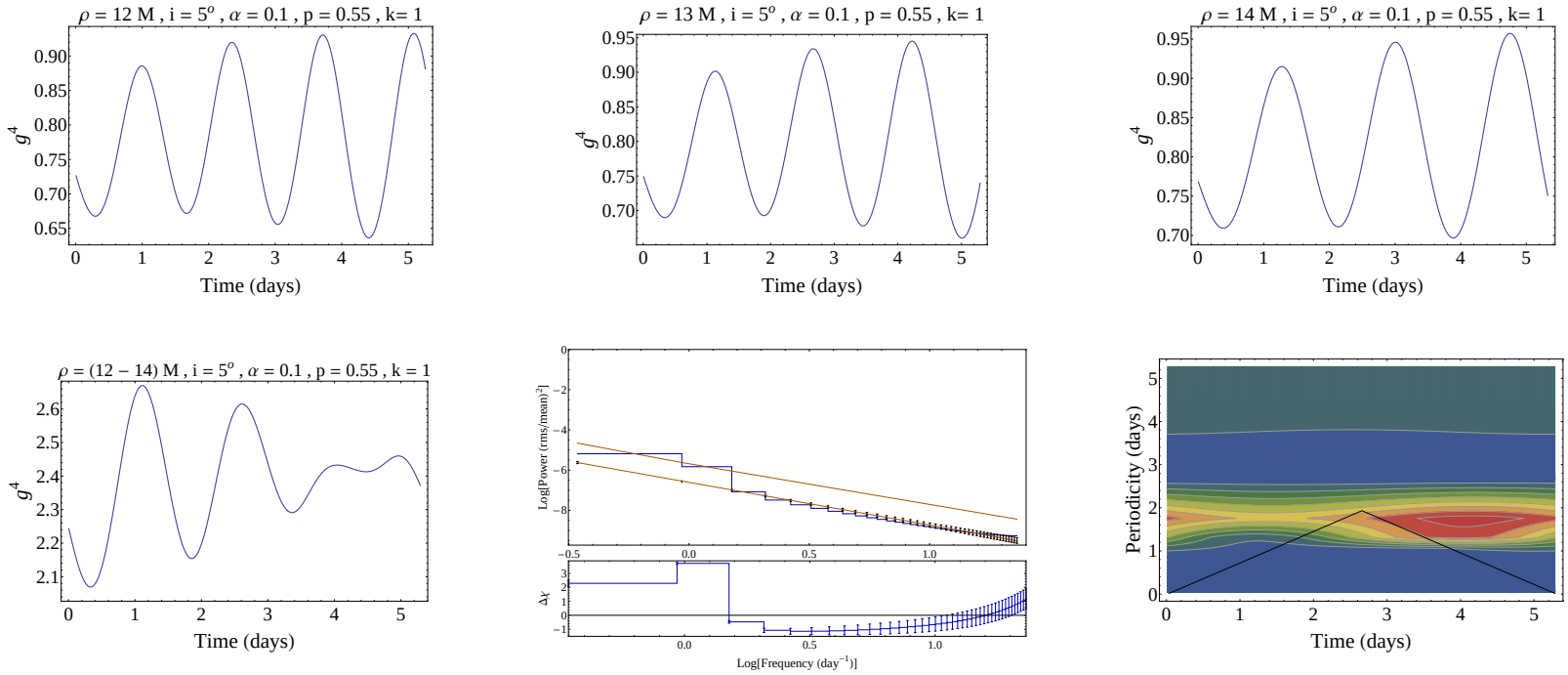

Figure 7.8: First row: simulated light curves for the funnel model with parameters $\alpha = 0.1$, $k = 1$ and $p = 0.55$. Second row: left plot: combined mean light curve for $r = 12\ M$ to $14\ M$ indicating a beamed portion gradually falling into the Doppler regime; middle plot: power spectral density of the combined light curve fit with a power law with a slope -2.12. The lower power law is the fit model and the upper one is the 99% significance contour; right plot: wavelet analysis of the combined light curve indicating the absence of any QPO.

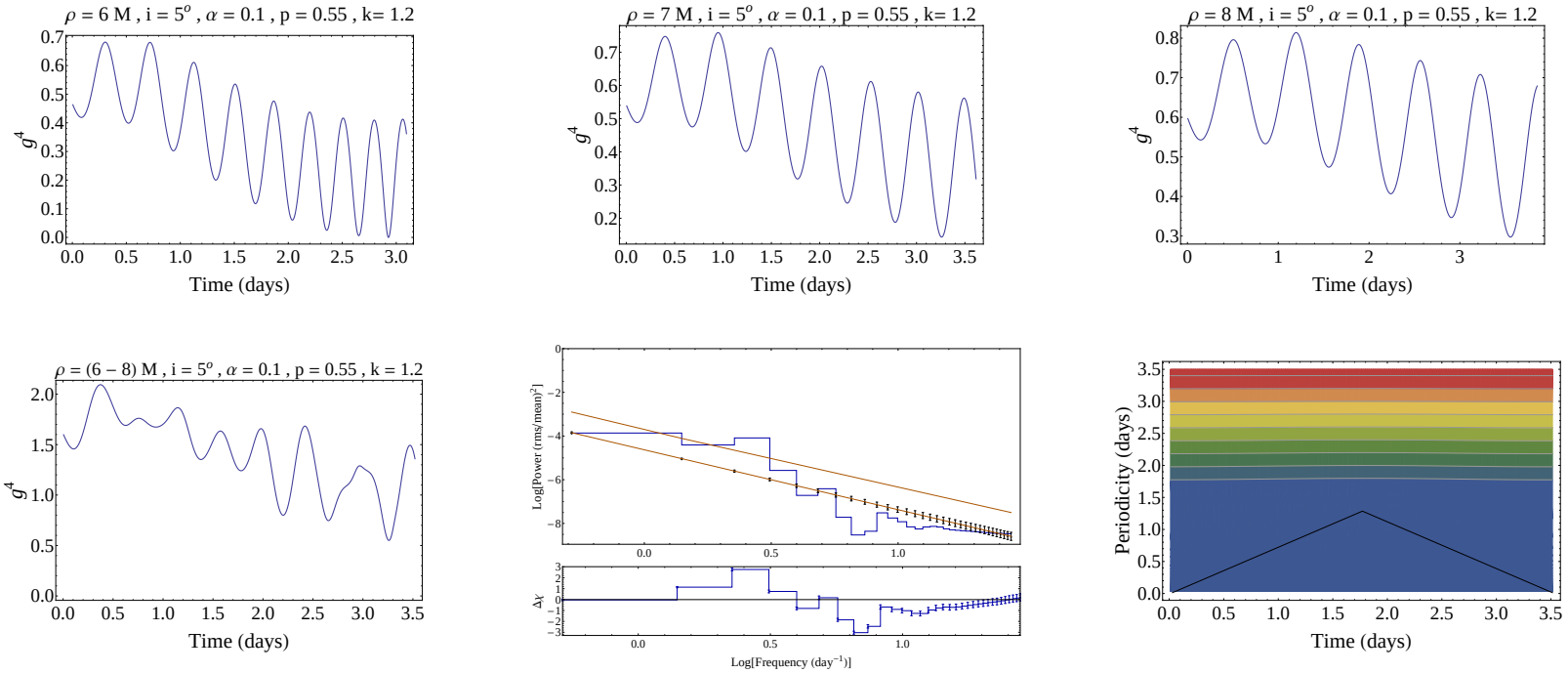

Figure 7.9: First row: simulated light curves for the funnel model with parameters $\alpha = 0.1$, $k = 1.2$ and $p = 0.55$. Second row: left plot: combined mean light curve for $r = 6\ M$ to $8\ M$ indicating a beamed portion gradually falling into the Doppler regime; middle plot: power spectral density of the combined light curve fit with a power law with a slope -2.74. The lower power law is the fit model and the upper one is the 99% significance contour. A QPO peaked at 0.44 days rises above this; right plot: wavelet analysis of the combined light curve indicating the absence of any QPO possibly due to a decreased signal strength.

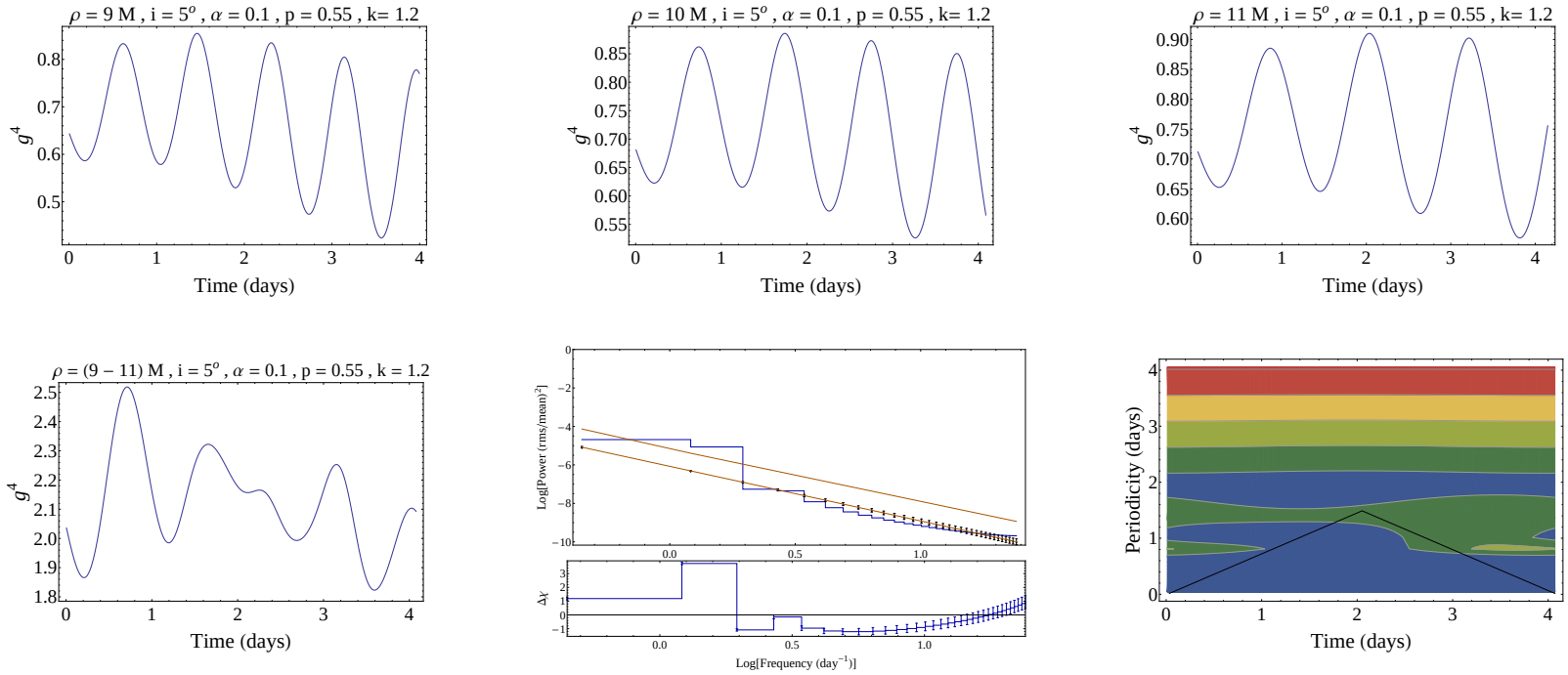

Figure 7.10: First row: simulated light curves for the funnel model with parameters $\alpha = 0.1$, $k = 1.2$ and $p = 0.55$. Second row: left plot: combined mean light curve for $r = 9\ M$ to $11\ M$ indicating a beamed portion gradually falling into the Doppler regime; middle plot: power spectral density of the combined light curve fit with a power law with a slope -2.84. The lower power law is the fit model and the upper one is the 99% significance contour; right plot: wavelet analysis of the combined light curve indicating the absence of any QPO.

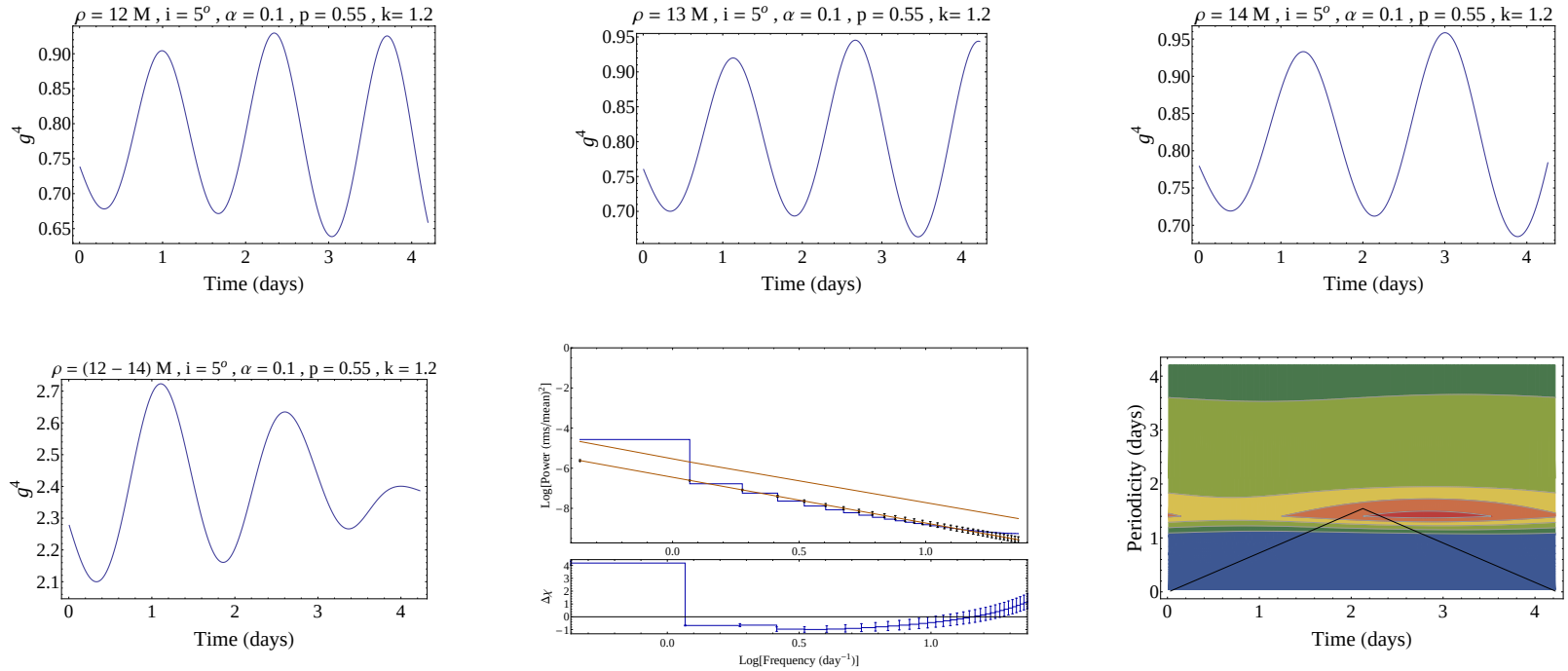

Figure 7.11: First row: simulated light curves for the funnel model with parameters $\alpha = 0.1$, $k = 1.2$ and $p = 0.55$. Second row: left plot: combined mean light curve for $r = 12\ M$ to $14\ M$ indicating a beamed portion gradually falling into the Doppler regime; middle plot: power spectral density of the combined light curve fit with a power law with a slope -2.28. The lower power law is the fit model and the upper one is the 99% significance contour; right plot: wavelet analysis of the combined light curve indicating the absence of any QPO.

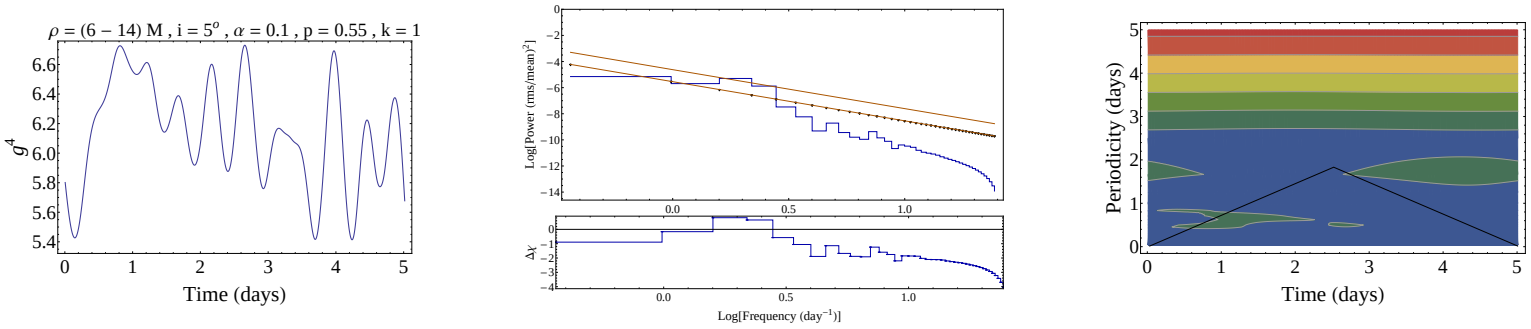

Figure 7.12: Left plot: combined mean light curve for the funnel model with parameters $\alpha = 0.1$, $k = 1$ and $p = 0.55$ and $r = 6$ M to 14 M; middle plot: power spectral density of the combined light curve fit with a power law with a slope -3.0. The lower power law is the fit model and the upper one is the 99% significance contour; right plot: wavelet analysis of the combined light curve indicating the absence of any QPO.

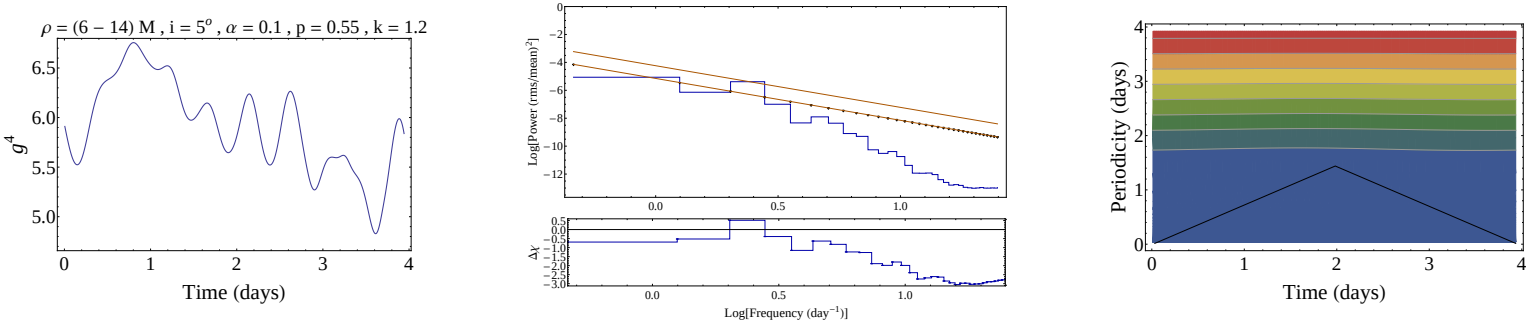

Figure 7.13: Left plot: combined mean light curve for the funnel model with parameters $\alpha = 0.01$, $k = 1$ and $p = 0.55$ and $r = 6$ M to 14 M; middle plot: power spectral density of the combined light curve fit with a power law with a slope -3.0. The lower power law is the fit model and the upper one is the 99% significance contour; right plot: wavelet analysis of the combined light curve indicating the absence of any QPO.

7.4 Conclusions

1. A jet variability model based on a bulk flow along helical trajectories on a funnel surface was presented.

2. The g factor was calculated in Schwarzschild geometry and the following effects were included: gravitational and Doppler shifts, aberration, light bending and time delay.

3. Simulations were carried out for suitable choice of geometrical parameters.

4. A beamed portion was observed lasting between 3-4 cycles at the start of the single component simulations. Inferred time-scales are in the range $\sim$ 0.5 days - 2 days.

5. Earlier special relativistic results treating jets in a magnetized geometry e.g. [93] are consistent with our general relativistic results.

6. A natural power law shaped PSD with a typical slope of -2.5 along with a weak to strong QPO emerges from the simulations.

7. The emergent QPO is strong in the beamed portion. An observer inferring this from observations of blazars or other jet dominated AGN could then attribute the QPO to orbital signatures in the jet.

Chapter 8

Summary and future work

8.1 Summary of results

In Chapter 2, we developed a suite of time series analysis techniques to extract information from a wide variety of input light curves. The suite consists of the periodogram, Lomb-Scargle periodogram, multi-harmonic analysis of variance periodogram and the wavelet analysis. Descriptive properties of the light curve such as its mean, variance and fractional root mean square variance are discussed. Then, the light curve (which could be mean subtracted or de-trended) is analyzed using the analysis suite to determine the PSD shape (periodogram); presence of a quasi-periodic oscillation (periodogram, LSP and MHAoV); times of existence, duration and number of cycles of the QPO (wavelet analysis); evolution of the QPO during the observation duration (wavelet analysis). The definitions, evaluation frequencies and properties to compare the techniques both from a detection as well as statistical points of view were discussed. A description of the statistical properties of each technique was then presented.

In Chapter 3, we described the methodology followed in the analysis of light curves. This included a description of parametric models of the periodogram and the statistical fit to it (parameter estimation and model selection) using the AIC and relative likelihood. This procedure was demonstrated for the X-ray light curve of REJ 1034+396. Analytic significance testing and MC simulations based significance testing were then described followed by a set of numerical experiments which compared and contrasted the best features of each analysis technique and provided criteria for selection of any interesting QPO feature. Finally, a data characterization and search strategy was presented which is used in the identification of interesting features and extraction of a large set of information from observed light curves.

In Chapter 4, analysis suite developed in Chapter 2 and the data characterization-search strategy from Chapter 3 were applied to analyze optical and X-ray light curves of blazars. In the X-ray data, 80 % of the blazars show a broken power law but are ruled out based on strict statistical considerations. Optical light curves of S5 0716+714 show a power law PSD with slope ranging between -1.86 (1999 - 2003 data) and -2.21 (2012 campaign data). This could be interpreted in terms of a larger emission region, possible in the context of an expanding jet. A possible QPO

reported in [131] for an X-ray LC of 3C 273 was ruled out based on our statistical analysis. A weak time-scale of $\sim$ 1 day is seen in the optical light curve of S5 0716+714 from the campaign study. The typical aperiodic variability time-scales over $\sim$ 1 day are consistent with expectations from orbital signatures in jets.

In Chapter 5, we developed a theoretical description of the high frequency break, measured in short duration light curves followed by a model for the quality factor Q of a QPO for bulk flowing fluid confined to a disk. We then analyzed short duration ($\sim$ 1 day) X-ray light curves (0.3 keV to 10 keV) from a set of Sy1 and NLSy1 galaxies which have known measurements of black hole mass and spin as reported in literature. A statistically significant high frequency break is inferred in 4 of 58 data sets (7 %). The high frequency break model is applied to infer additional constraints on the black hole mass and spin. In NGC 3516, a lower limit to the black hole spin of ≥ 0.30 is revised to a well constrained ≥ 0.80. In the three other data sets, only two of the constraints intersect (spin and break timescale). An upper limit to the BH mass of 57.2 M_6, 57.6 M_6 and 18.2 M_6 can be inferred for a maximally spinning BH for NGC 4051, MRK 766 and MCG-6-30-15 respectively. The Q-factor model is applied to an X-ray light curve of REJ 1034+396. The power law with a Lorentzian QPO model was the best fit PSD shape with $Q = \pm$ 6.5. The inferred BH mass assuming that the QPO is from an orbital signature is between 10^6 $M_\odot$ and 5×10^7 $M_\odot$, determined for a Schwarzschild BH and a maximally spinning Kerr BH respectively. Using the value of Q, the QPO is likely to arise from $\sim$ 11 M.

In Chapter 6, a disk based variability model (in Kerr geometry) of bulk flow confined to an accretion disk is presented. The g-factor is derived and expressed in the LNRF which is the correct frame describing a distant observer. The g-factor is calculated as a function of the initial emission angles of photons. Preliminary simulations are carried out for the single and multiple emitting components with a power law PSD shape emerging along with a weak to strong QPO. Time-scales inferred are $\sim$ few hours, highlighting the correspondence with dynamic processes.

In Chapter 7, a jet based variability model (in Schwarzschild geometry) of bulk flow in a funnel shaped geometry is presented. The presence and evolution of a QPO, its time-scale and the PSD shape expected are discussed in the context of optical and X-ray emission from blazar. Preliminary simulations are carried out for certain values of the funnel shape parameters for the single and multiple emitting components. Time-scales inferred are $\sim$ 1 day - few days, highlighting the correspondence with helical motion of orbital signatures in the jet. In the single component simulation ($r = 6$ M), a beamed portion is observed in the light curve. A QPO of 0.39 days is strong and stands out clearly in the periodogram. In the wavelet analysis, the QPO is strong only during the first $\sim$ 2 days which coincides with the beaming portion. A QPO (with 5-6 cycles) of $\sim$ 1 day could be identified if observations of jet dominated AGN such as blazars are carried out for campaigns lasting a few days to a month. Our general relativistic results confirm simulations indicating similar variability in BL Lacs reported for special relativistic plasma motion in magnetized jets e.g. [93].

8.2 Novel aspects and their impact

1. The statistical techniques and the analysis methodology developed in Chapters 2 and 3 extract the maximum possible information from an observed AGN light curve (variability properties, QPO and its evolution, PSD shapes and characteristic time-scales) through the use of multiple techniques, each with their unique advantages. We ensure that the strict statistical significance testing (analytic and MC simulations) criteria are met when quoting a result, making them highly reliable. This procedure can also be extended to timing analysis in X-ray binaries.

2. The data search characterization and search strategy formulated in Chapter 3 is applicable to a variety of light curves (even or unevenly sampled), providing a method of extracting all information on the light curve and any possible QPO as described above.

3. The periodogram fit procedure we use does not resort to any numerical differentiation scheme e.g. [113] which may introduce possible artefacts of particular methods used in carrying it out. The fit procedure and model selection can be extended to any physically motivated PSD model. Our PSD model selection and significance testing using MC simulations use the AIC, thus giving smaller fit errors. This helps in reducing computation time drastically compared to that developed using the χ^2 fit [115]. If we must perform PSD model selection for 4 competing models (such as used here), using only the MC simulations, a typical computation must run through a parameter space consisting of 10 variables, each with added complexity. If the time taken for a single parameter model is t, the total time $\geq 10\ t$ where t depends on the number of points in the light curve. In our procedure, this total time is reduced to $\sim$ 3 - 4 t due to MC simulations only used partially.

4. Our analysis is well suited to study light curves from both ground based as well as space based instruments in multiple wavelengths as it can be applied regardless of the sampling type (even or unven). This has not been carried out before as previous studies tend to use only a single technique such as the periodogram e.g. [115, 132] or the wavelet analysis e.g. [131] which can only yield limited information.

5. The mass M_{BH} and spin a of super-massive black holes reported in literature are further constrained with the break frequency model (Chapter 5) using orbital signatures in light curves. The region from which the QPO emerges is constrained to be $\sim$ 11 M for REJ 1034+396 using the quality factor Q model (Chapter 5). QPO time-scales inferred from the disk model (Chapter 6) are $\sim$ 1000 - 10000 s and that from the jet model (Chapter 7) are $\sim$ 0.5 days - 2 days. These time-scales, obtained from general relativistic simulations are in agreement with observed expectations.

6. The g-factor in the disk model (Chapter 6) is calculated for a LNRF observer and includes the effects of gravitational and Doppler shifts, aberration and time delay on a bulk flow in

Kerr geometry. A summary of the development of disk based variability models is presented in Table 6.1 of Chapter 6.

7. The g-factor in the jet model (Chapter 7) is calculated for a local static observer in Schwarzschild spacetime and includes the effects of gravitational and Doppler shifts, aberration, light bending and time delay on a bulk flow along helical trajectories in a funnel geometry.

8. In the disk and jet models, there is a natural development of a power law shape with slopes in the range $\sim$ -1.5 to -3 in the simulated PSD along with a weak to strong QPO, attributable to orbital signatures; the strength of which depends on the number of orbital features- a single feature results in a strong QPO which becomes weaker for multiple emitters. Thus, we need not appeal to any intrinsic variability process such as the disk based flare-avalanche model [205], self-organized criticality models e.g. [220], shocks in jet [91] or the disk oscillations based features [80]. Further, in these models and other models of intrinsic variability, the power law PSD shape does not emerge naturally. In the case of the disk and jet models presented here, the PSD shape is accounted for by the combination of the Doppler and relativistic effects (including light bending) and time delay that modulates the light curve.

8.3 Future work

1. Development of analytic significance formulae for the LSP, MHAoV and wavelet analysis and a comparison with MC simulations based results.

2. A self consistent detailed physical model involving disk and jet mass and angular momentum equations for predicting the evolution of BH mass and spin as a function of the accretion rate, the jet power, the total kinetic luminosity and others factors.

3. Calculation of the quality factor Q from the inclusion of vertical motion of the bulk flow.

4. A more comprehensive statistical study of light curves and PSD shapes simulated from the developed disk and jet variability models, exploring a larger parameter space as well as a comparison with observational results to constrain geometrical and physical parameters.

5. Extension of developed disk variability model to include light bending in Kerr geometry, using elliptical integrals for null trajectories e.g. [221].

6. Extension of developed jet variability model to Kerr geometry including light bending and a comparison with the Schwarzschild case.

7. Calculation of relativistically broadened emission line profiles and their variations due to time variability of the g factor. This formulation will address the development of the double horned asymmetric profile shape.

8. Realistic models of the jet involving magnetic field geometry as determined by the relativistic Grad-Shafranov equation.

Bibliography

[1] A. A. Abdo *et al.*, *ApJ,* **716**, 30 (2010).

[2] A. Koratkar and O. Blaes, *Pub. Astron. Soc. Pac.,* **111**, 1 (1999).

[3] R. F. Mushotzky, C. Done, and K. A. Pounds, *Ann.Rev. Astron. Astrophys.,* **31**, 717 (1993).

[4] F. Aharonian *et al.*, *Astrophys. J. Lett.,* **664**, L71 (2007).

[5] S. P. Gupta *et al.*, New Astronomy **17**, 8 (2012).

[6] M. Böttcher *et al.*, *ApJ,* **596**, 847 (2003).

[7] H. Gaur *et al.*, *Mon. Not. Roy. Astron. Soc.,* **425**, 3002 (2012).

[8] B.-R. Liu *et al.*, *Astron. Astrophys.,* **555**, A134 (2013).

[9] E. S. Perlman, D. E. Harris, J. A. Biretta, W. B. Sparks, and F. D. Macchetto, *Astrophys. J. Lett.,* **599**, L65 (2003).

[10] B. Rani, P. J. Wiita, and A. C. Gupta, *ApJ,* **696**, 2170 (2009).

[11] P. Lachowicz, A. C. Gupta, H. Gaur, and P. J. Wiita, *Astron. Astrophys.,* **506**, L17 (2009).

[12] S. Kaspi *et al.*, *ApJ,* **533**, 631 (2000).

[13] J. H. Krolik, *Active galactic nuclei : from the central black hole to the galactic environment* (, 1999).

[14] A. B. Pushkarev, Y. Y. Kovalev, M. L. Lister, and T. Savolainen, *Astron. Astrophys.,* **507**, L33 (2009).

[15] R. A. Perley, J. W. Dreher, and J. J. Cowan, *Astrophys. J. Lett.,* **285**, L35 (1984).

[16] J. Frank, A. King, and D. J. Raine, *Accretion Power in Astrophysics: Third Edition* (, 2002).

[17] D. E. Osterbrock, *Astrophysics of gaseous nebulae and active galactic nuclei* (, 1989).

[18] A. S. Bennett, *Mon. Not. Roy. Astron. Soc.,* **125**, 75 (1962).

[19] J. D. H. Pilkington and J. F. Scott, *Memoirs of the Royal Astronomical Society,* **69**, 183 (1965).

[20] J. F. R. Gower, P. F. Scott, and D. Wills, *Memoirs of the Royal Astronomical Society,* **71**, 49 (1967).

[21] K. I. Kellermann, R. Sramek, M. Schmidt, D. B. Shaffer, and R. Green, *Astronom. J.,* **98**, 1195 (1989).

[22] B. L. Fanaroff and J. M. Riley, *Mon. Not. Roy. Astron. Soc.,* **167**, 31P (1974).

[23] J. Heidt and S. J. Wagner, *Astron. Astrophys.,* **305**, 42 (1996).

[24] A. C. Gupta, U. C. Joshi, and J. H. Fan, *Astrophys. Spa. Sci.,* **282**, 655 (2002).

[25] J. H. Fan *et al.*, *Astron. Astrophys.,* **381**, 1 (2002).

[26] J. T. Stocke *et al.*, *ApJ, Suppl.,* **76**, 813 (1991).

[27] M. J. M. Marcha, I. W. A. Browne, C. D. Impey, and P. S. Smith, *Mon. Not. Roy. Astron. Soc.,* **281**, 425 (1996).

[28] C. M. Urry, Advances in Space Research **21**, 89 (1998).

[29] Ž. Ivezić *et al.*, *Astronom. J.,* **124**, 2364 (2002).

[30] Gopal-Krishna, A. Mangalam, and P. J. Wiita, *Astrophys. J. Lett.,* **680**, L13 (2008).

[31] A. Tchekhovskoy, R. Narayan, and J. C. McKinney, *ApJ,* **711**, 50 (2010).

[32] R. Antonucci, *Ann.Rev. Astron. Astrophys.,* **31**, 473 (1993).

[33] C. M. Urry and P. Padovani, *Pub. Astron. Soc. Pac.,* **107**, 803 (1995).

[34] R. R. J. Antonucci and J. S. Miller, *ApJ,* **297**, 621 (1985).

[35] J. S. Miller and R. W. Goodrich, *ApJ,* **355**, 456 (1990).

[36] A. P. Marscher, Astronomische Nachrichten **327**, 217 (2006).

[37] B. Czerny and M. Elvis, *ApJ,* **321**, 305 (1987).

[38] R. Schödel *et al.*, *Nature,* **419**, 694 (2002).

[39] M. Miyoshi *et al.*, *Nature,* **373**, 127 (1995).

[40] G. Lodato and G. Bertin, *Astron. Astrophys.,* **398**, 517 (2003).

[41] C. Y. Kuo *et al.*, *ApJ,* **727**, 20 (2011).

[42] L. Ferrarese and H. Ford, *Space Sci. Rev.,* **116**, 523 (2005).

[43] H. C. Ford *et al.*, *Astrophys. J. Lett.,* **435**, L27 (1994).

[44] R. J. Harms *et al.*, *Astrophys. J. Lett.,* **435**, L35 (1994).

[45] F. Macchetto *et al.*, *ApJ,* **489**, 579 (1997).

[46] L. Ferrarese and H. C. Ford, *ApJ,* **515**, 583 (1999).

[47] A. Marconi *et al.*, *Astron. Astrophys.,* **448**, 921 (2006).

[48] J. Kormendy and D. Richstone, *Ann.Rev. Astron. Astrophys.,* **33**, 581 (1995).

[49] K. Gebhardt *et al.*, *Astrophys. J. Lett.,* **539**, L13 (2000).

[50] L. Ferrarese and D. Merritt, *Astrophys. J. Lett.,* **539**, L9 (2000).

[51] P. F. Hopkins, L. Hernquist, T. J. Cox, B. Robertson, and E. Krause, *ApJ,* **669**, 45 (2007).

[52] B. M. Peterson, *Pub. Astron. Soc. Pac.,* **105**, 247 (1993).

[53] H. Netzer and B. M. Peterson, Reverberation Mapping and the Physics of Active Galactic Nuclei, in *Astronomical Time Series*, edited by D. Maoz, A. Sternberg, and E. M. Leibowitz, volume 218 of *Astrophysics and Space Science Library*, p. 85, 1997.

[54] B. M. Peterson *et al.*, *ApJ,* **613**, 682 (2004).

[55] M. Gierliński, M. Middleton, M. Ward, and C. Done, *Nature,* **455**, 369 (2008).

[56] G. Bao and E. Ostgaard, *Astrophys. J. Lett.,* **422**, L51 (1994).

[57] A. C. Fabian, Astronomische Nachrichten **327**, 943 (2006).

[58] A. C. Fabian, M. J. Rees, L. Stella, and N. E. White, *Mon. Not. Roy. Astron. Soc.,* **238**, 729 (1989).

[59] Y. Tanaka *et al.*, *Nature,* **375**, 659 (1995).

[60] N. I. Shakura and R. A. Sunyaev, *Astron. Astrophys.,* **24**, 337 (1973).

[61] I. D. Novikov and K. S. Thorne, Astrophysics of black holes., in *Black Holes (Les Astres Occlus)*, edited by C. Dewitt and B. S. Dewitt, pp. 343–450, 1973.

[62] B. Paczyński and P. J. Wiita, *Astron. Astrophys.,* **88**, 23 (1980).

[63] D. L. Meier, *Astrophys. J. Lett.,* **548**, L9 (2001).

[64] M. A. Abramowicz, B. Czerny, J. P. Lasota, and E. Szuszkiewicz, *ApJ,* **332**, 646 (1988).

[65] A. M. Beloborodov, *Mon. Not. Roy. Astron. Soc.,* **297**, 739 (1998).

[66] A. Sądowski, *ApJ, Suppl.,* **183**, 171 (2009).

[67] R. Narayan and I. Yi, *Astrophys. J. Lett.,* **428**, L13 (1994).

[68] F. Yuan, S. Markoff, and H. Falcke, *Astron. Astrophys.,* **383**, 854 (2002).

[69] Q. Wu, F. Yuan, and X. Cao, *ApJ,* **669**, 96 (2007).

[70] E. Quataert, T. Di Matteo, R. Narayan, and L. C. Ho, *Astrophys. J. Lett.,* **525**, L89 (1999).

[71] M. A. Abramowicz and P. C. Fragile, Living Reviews in Relativity **16**, 1 (2013).

[72] D. Grupe, S. Komossa, K. M. Leighly, and K. L. Page, *ApJ, Suppl.,* **187**, 64 (2010).

[73] C. S. Reynolds and M. A. Nowak, *Physics Reports,* **377**, 389 (2003).

[74] P. J. Wiita, H. R. Miller, M. T. Carini, and A. Rosen, Microvariability in Blazars via Accretion Disk Instabilities., in *IAU Colloq. 129: The 6th Institute d'Astrophysique de Paris (IAP) Meeting: Structure and Emission Properties of Accretion Disks*, edited by C. Bertout, S. Collin-Souffrin, and J. P. Lasota, p. 557, 1991.

[75] M. A. Abramowicz, G. Bao, A. Lanza, and X.-H. Zhang, *Astron. Astrophys.,* **245**, 454 (1991).

[76] X.-H. Zhang and G. Bao, *Astron. Astrophys.,* **246**, 21 (1991).

[77] A. V. Mangalam and P. J. Wiita, *ApJ,* **406**, 420 (1993).

[78] T. Pecháček, M. Dovčiak, V. Karas, and G. Matt, *Astron. Astrophys.,* **441**, 855 (2005).

[79] A. M. Beloborodov, *Astrophys. J. Lett.,* **566**, L85 (2002).

[80] C. A. Perez, A. S. Silbergleit, R. V. Wagoner, and D. E. Lehr, *ApJ,* **476**, 589 (1997).

[81] A. S. Silbergleit, R. V. Wagoner, and M. Ortega-Rodríguez, *ApJ,* **548**, 335 (2001).

[82] R. V. Wagoner, *Astrophys. J. Lett.,* **752**, L18 (2012).

[83] A. Merloni, M. Vietri, L. Stella, and D. Bini, *Mon. Not. Roy. Astron. Soc.,* **304**, 155 (1999).

[84] A. Ingram, C. Done, and P. C. Fragile, *Mon. Not. Roy. Astron. Soc.,* **397**, L101 (2009).

[85] A. Brandenburg, A. Nordlund, R. F. Stein, and U. Torkelsson, *ApJ,* **446**, 741 (1995).

[86] H. C. Spruit, Magnetohydrodynamic jets and winds from accretion disks, in *NATO ASIC Proc. 477: Evolutionary Processes in Binary Stars*, edited by R. A. M. J. Wijers, M. B. Davies, and C. A. Tout, pp. 249–286, 1996.

[87] A. V. Mangalam and K. Subramanian, *ApJ, Suppl.,* **90**, 963 (1994).

[88] A. V. Mangalam and K. Subramanian, *ApJ,* **434**, 509 (1994).

[89] L. Mestel, *Mon. Not. Roy. Astron. Soc.,* **122**, 473 (1961).

[90] X. Cao, *Mon. Not. Roy. Astron. Soc.,* **426**, 2813 (2012).

[91] A. P. Marscher and W. K. Gear, *ApJ,* **298**, 114 (1985).

[92] Gopal-Krishna and P. J. Wiita, *Astron. Astrophys.,* **259**, 109 (1992).

[93] M. Camenzind and M. Krockenberger, *Astron. Astrophys.,* **255**, 59 (1992).

[94] W. Steffen, J. A. Zensus, T. P. Krichbaum, A. Witzel, and S. J. Qian, *Astron. Astrophys.,* **302**, 335 (1995).

[95] F. M. Rieger, *Astrophys. J. Lett.,* **615**, L5 (2004).

[96] M. Chiaberge, A. Celotti, A. Capetti, and G. Ghisellini, *Astron. Astrophys.,* **358**, 104 (2000).

[97] P. J. Wiita, Accretion Disks, Jets and Blazar Variability, in *Blazar Variability Workshop II: Entering the GLAST Era*, edited by H. R. Miller, K. Marshall, J. R. Webb, and M. F. Aller, volume 350 of *Astronomical Society of the Pacific Conference Series*, p. 183, 2006.

[98] A. C. Gupta *et al.*, *Mon. Not. Roy. Astron. Soc.,* **425**, 1357 (2012).

[99] S. Vaughan, R. Edelson, R. S. Warwick, and P. Uttley, *Mon. Not. Roy. Astron. Soc.,* **345**, 1271 (2003).

[100] P. Mohan, A. Mangalam, H. Chand, and A. C. Gupta, Journal of Astrophysics and Astronomy **32**, 117 (2011).

[101] A. Mangalam and P. Mohan, Journal of Astrophysics and Astronomy (In press) (2013).

[102] I. E. Papadakis and A. Lawrence, *Mon. Not. Roy. Astron. Soc.,* **261**, 612 (1993).

[103] S. Vaughan, *Astron. Astrophys.,* **431**, 391 (2005).

[104] J. H. Horne and S. L. Baliunas, *ApJ,* **302**, 757 (1986).

[105] N. R. Lomb, *Astrophys. Spa. Sci.,* **39**, 447 (1976).

[106] J. D. Scargle, *ApJ,* **263**, 835 (1982).

[107] W. H. Press and G. B. Rybicki, *ApJ,* **338**, 277 (1989).

[108] A. Schwarzenberg-Czerny, *Astrophys. J. Lett.,* **460**, L107 (1996).

[109] P. Lachowicz, A. A. Zdziarski, A. Schwarzenberg-Czerny, G. G. Pooley, and S. Kitamoto, *Mon. Not. Roy. Astron. Soc.,* **368**, 1025 (2006).

[110] C. Torrence and G. P. Compo, Bulletin of the American Meteorological Society **79**, 61 (1998).

[111] M. Farge, Annual Review of Fluid Mechanics **24**, 395 (1992).

[112] P. Mohan, A. Mangalam, and S. Chattopadhyay, Journal of Astrophysics and Astronomy (In press) (2013).

[113] D. Barret and S. Vaughan, *ApJ,* **746**, 131 (2012).

[114] K. P. Burnham and D. R. Anderson, Sociological Methods & Research .

[115] P. Uttley, I. M. McHardy, and I. E. Papadakis, *Mon. Not. Roy. Astron. Soc.,* **332**, 231 (2002).

[116] R. A. Remillard and J. E. McClintock, *Ann.Rev. Astron. Astrophys.,* **44**, 49 (2006).

[117] M. A. Nowak, *Mon. Not. Roy. Astron. Soc.,* **318**, 361 (2000).

[118] S. Vaughan and P. Uttley, *Mon. Not. Roy. Astron. Soc.,* **362**, 235 (2005).

[119] W. H. Press, S. A. Teukolsky, W. T. Vetterling, and B. P. Flannery, *Numerical recipes in C++ : the art of scientific computing* (, 2002).

[120] J. Timmer and M. Koenig, *Astron. Astrophys.,* **300**, 707 (1995).

[121] S. J. Wagner *et al.*, *Astronom. J.,* **111**, 2187 (1996).

[122] A. P. Marscher *et al.*, *Nature,* **452**, 966 (2008).

[123] S. J. Qian *et al.*, *Astron. Astrophys.,* **241**, 15 (1991).

[124] V. A. Hagen-Thorn *et al.*, *ApJ,* **672**, 40 (2008).

[125] M. C. Begelman, A. C. Fabian, and M. J. Rees, *Mon. Not. Roy. Astron. Soc.,* **384**, L19 (2008).

[126] P. Subramanian, A. Shukla, and P. A. Becker, *Mon. Not. Roy. Astron. Soc.,* **423**, 1707 (2012).

[127] D. Giannios, D. A. Uzdensky, and M. C. Begelman, *Mon. Not. Roy. Astron. Soc.,* **402**, 1649 (2010).

[128] R. Narayan and T. Piran, *Mon. Not. Roy. Astron. Soc.,* **420**, 604 (2012).

[129] F. Montagni *et al.*, *Astron. Astrophys.,* **451**, 435 (2006).

[130] A. C. Gupta, A. K. Srivastava, and P. J. Wiita, *ApJ,* **690**, 216 (2009).

[131] C. Espaillat, J. Bregman, P. Hughes, and E. Lloyd-Davies, *ApJ,* **679**, 182 (2008).

[132] O. González-Martín and S. Vaughan, *Astron. Astrophys.,* **544**, A80 (2012).

[133] S. K. Chakrabarti and P. J. Wiita, *ApJ,* **411**, 602 (1993).

[134] M. Cappi *et al.*, *Mon. Not. Roy. Astron. Soc.,* **271**, 438 (1994).

[135] C. M. Raiteri *et al.*, *Astron. Astrophys.,* **402**, 151 (2003).

[136] W. Bian and Y. Zhao, *ApJ,* **591**, 733 (2003).

[137] R. Nesci *et al.*, *Astronom. J.,* **130**, 1466 (2005).

[138] C. S. Stalin *et al.*, *Mon. Not. Roy. Astron. Soc.,* **366**, 1337 (2006).

[139] A. C. Gupta *et al.*, *Astronom. J.,* **136**, 2359 (2008).

[140] T. Hovatta, H. J. Lehto, and M. Tornikoski, *Astron. Astrophys.,* **488**, 897 (2008).

[141] C. Villforth *et al.*, *Mon. Not. Roy. Astron. Soc.,* **397**, 1893 (2009).

[142] B. Rani, A. C. Gupta, U. C. Joshi, S. Ganesh, and P. J. Wiita, *Astrophys. J. Lett.,* **719**, L153 (2010).

[143] B. Rani *et al.*, *Astron. Astrophys.,* **552**, A11 (2013).

[144] J. Heidt and S. J. Wagner, *Astron. Astrophys.,* **329**, 853 (1998).

[145] D. Watson *et al.*, *Astron. Astrophys.,* **418**, 459 (2004).

[146] A. Kraus *et al.*, *Astron. Astrophys.,* **401**, 161 (2003).

[147] A. Malizia *et al.*, *ApJ,* **519**, 637 (1999).

[148] C. M. Raiteri *et al.*, *Astron. Astrophys. Suppl.,* **127**, 445 (1998).

[149] A. Quirrenbach *et al.*, *Astron. Astrophys.,* **258**, 279 (1992).

[150] A. Okudaira, H. Tabara, T. Kato, and M. Inoue, *Pub. Astron. Soc. Japan,* **45**, 153 (1993).

[151] A. Quirrenbach *et al.*, *Astron. Astrophys. Suppl.,* **141**, 221 (2000).

[152] E. P. Bozyan, P. D. Hemenway, and A. N. Argue, *Astronom. J.,* **99**, 1421 (1990).

[153] C. Lloyd, *Mon. Not. Roy. Astron. Soc.,* **209**, 697 (1984).

[154] A. J. Pica *et al.*, *Astronom. J.,* **96**, 1215 (1988).

[155] S. Soldi *et al.*, *Astron. Astrophys.,* **486**, 411 (2008).

[156] J. H. Fan *et al.*, *Astron. Astrophys.,* **462**, 547 (2007).

[157] K. Hayashida, S. Miyamoto, S. Kitamoto, H. Negoro, and H. Inoue, *ApJ,* **500**, 642 (1998).

[158] J. Kataoka *et al.*, *Mon. Not. Roy. Astron. Soc.,* **336**, 932 (2002).

[159] R. Mukherjee *et al.*, *ApJ,* **490**, 116 (1997).

[160] V. Beckmann *et al.*, *Astron. Astrophys.,* **475**, 827 (2007).

[161] A. R. G. Mead *et al.*, *Astron. Astrophys. Suppl.,* **83**, 183 (1990).

[162] C. D. Impey and S. Tapia, *ApJ,* **354**, 124 (1990).

[163] C. M. Raiteri *et al.*, *Astron. Astrophys.,* **377**, 396 (2001).

[164] G. E. Romero, S. A. Cellone, J. A. Combi, and I. Andruchow, *Astron. Astrophys.,* **390**, 431 (2002).

[165] R. Sagar, C. S. Stalin, Gopal-Krishna, and P. J. Wiita, *Mon. Not. Roy. Astron. Soc.,* **348**, 176 (2004).

[166] S. L. O'dell *et al.*, *ApJ,* **326**, 668 (1988).

[167] J. F. Salgado *et al.*, *ApJ, Suppl.,* **120**, 77 (1999).

[168] G. E. Romero *et al.*, *Astron. Astrophys.,* **326**, 77 (1997).

[169] B. Peng, A. Kraus, T. P. Krichbaum, and A. Witzel, *Astron. Astrophys. Suppl.,* **145**, 1 (2000).

[170] C. Barbieri, G. Romano, and M. Zambon, *Astron. Astrophys. Suppl.,* **31**, 401 (1978).

[171] R. A. Edelson, *Astronom. J.,* **94**, 1150 (1987).

[172] B. J. Wills, D. Wills, M. Breger, R. R. J. Antonucci, and R. Barvainis, *ApJ,* **398**, 454 (1992).

[173] J.-H. Fan *et al.*, *Pub. Astron. Soc. Japan,* **60**, 707 (2008).

[174] T. Maccacaro, B. Garilli, and S. Mereghetti, *Astronom. J.,* **93**, 1484 (1987).

[175] A. R. Patrick, J. N. Reeves, A. P. Lobban, D. Porquet, and A. G. Markowitz, *Mon. Not. Roy. Astron. Soc.,* **416**, 2725 (2011).

[176] F. Haardt and L. Maraschi, *Astrophys. J. Lett.,* **380**, L51 (1991).

[177] F. Haardt, L. Maraschi, and G. Ghisellini, *Astrophys. J. Lett.,* **432**, L95 (1994).

[178] T. J. Turner, I. M. George, K. Nandra, and D. Turcan, *ApJ,* **524**, 667 (1999).

[179] A. Markowitz and R. Edelson, *ApJ,* **547**, 684 (2001).

[180] A. Markowitz and R. Edelson, *ApJ,* **617**, 939 (2004).

[181] P. Barr and R. F. Mushotzky, *Nature,* **320**, 421 (1986).

[182] A. Lawrence and I. Papadakis, *Astrophys. J. Lett.,* **414**, L85 (1993).

[183] R. Smith and S. Vaughan, *Mon. Not. Roy. Astron. Soc.,* **375**, 1479 (2007).

[184] F. Panessa *et al.*, *Mon. Not. Roy. Astron. Soc.,* **417**, 2426 (2011).

[185] D. Grupe and S. Mathur, *Astrophys. J. Lett.,* **606**, L41 (2004).

[186] J. M. Miller, *Ann.Rev. Astron. Astrophys.,* **45**, 441 (2007).

[187] A. J. Young, R. R. Ross, and A. C. Fabian, *Mon. Not. Roy. Astron. Soc.,* **300**, L11 (1998).

[188] L. W. Brenneman and C. S. Reynolds, *ApJ,* **652**, 1028 (2006).

[189] I. de La Calle Pérez *et al.*, *Astron. Astrophys.,* **524**, A50 (2010).

[190] A. R. Patrick *et al.*, *Mon. Not. Roy. Astron. Soc.,* **426**, 2522 (2012).

[191] M. A. Abramowicz *et al.*, *Astron. Astrophys.,* **521**, A15 (2010).

[192] A. Markowitz *et al.*, *ApJ,* **593**, 96 (2003).

[193] I. E. Papadakis, *Mon. Not. Roy. Astron. Soc.,* **348**, 207 (2004).

[194] M. Nikolajuk, I. E. Papadakis, and B. Czerny, *Mon. Not. Roy. Astron. Soc.,* **350**, L26 (2004).

[195] X.-L. Zhou, S.-N. Zhang, D.-X. Wang, and L. Zhu, *ApJ,* **710**, 16 (2010).

[196] D. Porquet and J. N. Reeves, *Astron. Astrophys.,* **408**, 119 (2003).

[197] E. Oliva, L. Origlia, J. K. Kotilainen, and A. F. M. Moorwood, *Astron. Astrophys.,* **301**, 55 (1995).

[198] B. De Marco *et al.*, *Mon. Not. Roy. Astron. Soc.,* **431**, 2441 (2013).

[199] I. M. McHardy, K. F. Gunn, P. Uttley, and M. R. Goad, *Mon. Not. Roy. Astron. Soc.,* **359**, 1469 (2005).

[200] A. Markowitz, *ApJ,* **698**, 1740 (2009).

[201] D. J. Walton, E. Nardini, A. C. Fabian, L. C. Gallo, and R. C. Reis, *Mon. Not. Roy. Astron. Soc.,* **428**, 2901 (2013).

[202] L. C. Gallo *et al.*, *Mon. Not. Roy. Astron. Soc.,* **411**, 607 (2011).

[203] H. Gaur, A. C. Gupta, P. Lachowicz, and P. J. Wiita, *ApJ,* **718**, 279 (2010).

[204] T. Pecháček, M. Dovčiak, and V. Karas, Astronomische Nachrichten **327**, 957 (2006).

[205] P. T. Życki and A. Niedźwiecki, *Mon. Not. Roy. Astron. Soc.,* **359**, 308 (2005).

[206] Y.-F. Yuan, X. Cao, L. Huang, and Z.-Q. Shen, *ApJ,* **699**, 722 (2009).

[207] J. M. Bardeen, W. H. Press, and S. A. Teukolsky, *ApJ,* **178**, 347 (1972).

[208] H. C. Spruit, ArXiv Astrophysics e-prints (1996).

[209] R. D. Blandford and D. G. Payne, *Mon. Not. Roy. Astron. Soc.,* **199**, 883 (1982).

[210] P. J. Wiita, ArXiv Astrophysics e-prints (2001).

[211] H. Sol, G. Pelletier, and E. Asseo, *Mon. Not. Roy. Astron. Soc.,* **237**, 411 (1989).

[212] M. Camenzind, *Astron. Astrophys.,* **156**, 137 (1986).

[213] S. Koide, K. Shibata, and T. Kudoh, *ApJ,* **522**, 727 (1999).

[214] C. F. Gammie, J. C. McKinney, and G. Tóth, *ApJ,* **589**, 444 (2003).

[215] J. C. McKinney, *Mon. Not. Roy. Astron. Soc.,* **368**, 1561 (2006).

[216] R. D. Blandford and R. L. Znajek, *Mon. Not. Roy. Astron. Soc.,* **179**, 433 (1977).

[217] A. A. Abdo *et al.*, *ApJ,* **726**, 43 (2011).

[218] S. Markoff, M. A. Nowak, and J. Wilms, *ApJ,* **635**, 1203 (2005).

[219] S. S. Doeleman *et al.*, Science **338**, 355 (2012).

[220] S. Mineshige, M. Takeuchi, and H. Nishimori, *Astrophys. J. Lett.,* **435**, L125 (1994).

[221] S. Chandrasekhar, *The mathematical theory of black holes* (, 1983).